

**ENHANCED BACKSCATTERING OF  
SEISMIC WAVES FROM IRREGULAR  
INTERFACES**

by

Craig A. Schultz

B.S., University of California (1989)

Submitted to the Department of Earth, Atmospheric, and Planetary  
Sciences

in partial fulfillment of the requirements for the degree of

Doctor of Philosophy

at the

MASSACHUSETTS INSTITUTE OF TECHNOLOGY

May 1994

© Massachusetts Institute of Technology 1994

All rights reserved

Signature of Author .....  
Department of Earth, Atmospheric, and Planetary Sciences

March 18, 1994

Certified by .....  
M. Nafi Toksöz

Professor of Geophysics

Thesis Supervisor

Accepted by .....  
Thomas H. Jordan

Chairman, Department of Earth, Atmospheric, and Planetary  
Sciences

**WITHDRAWN**  
MASSACHUSETTS INSTITUTE  
OF TECHNOLOGY  
**FROM**  
MIT LIBRARIES  
1994  
Lindgren



# ENHANCED BACKSCATTERING OF SEISMIC WAVES FROM IRREGULAR INTERFACES

by

Craig A. Schultz

Submitted to the Department of Earth, Atmospheric, and Planetary Sciences  
on March 18, 1994, in partial fulfillment of the  
requirements for the degree of  
Doctor of Philosophy

## Abstract

In this thesis I study the general scattering of seismic waves from highly irregular, 2-D elastic interfaces and show that the "enhanced backscattering" or "retroreflectance" of seismic waves, which has been previously identified in optics, exists. Theoretically, using the Somigliana identity and the extinction theorem, exact integral expressions are obtained for the scattered seismic displacement produced when a P, SV, or SH wave of general form is incident on a highly irregular, 2-D elastic interface. The scattered pressure over a fluid-solid boundary is also obtained by coupling Green's second integral theorem with the Somigliana identity. The final coupled pair of inhomogeneous integral equations are solved numerically and, unlike most numerical approaches, the curvature of the interface is included in the formulation. Comparisons between this Somigliana approach and the discrete wavenumber (DWN) approach show that the Somigliana approach is accurate up to the 45° slopes tested. Comparisons with finite-difference and DWN algorithms also show that the Somigliana algorithm is more computationally efficient for the statistical analyses carried out in this thesis.

Utilizing the Somigliana approach, the final scattered energy is expressed in terms of a deterministic reflection coefficient. Averaging over hundreds of realizations of scattering from an irregular interface with given statistical properties a mean reflection coefficient is determined, therefore describing the average amplitude distribution for waves propagating away from the interface. The total, coherent, and incoherent contribution to this mean reflection coefficient are determined. This statistical analysis shows that for interfaces with a large impedance contrast and large slopes, an enhancement of energy scattered towards the source, otherwise known as 'retrore-

flectance' or 'enhanced backscattering', is observed in the incoherent component. The retroreflective properties of the interface are characterized by varying the height and length of irregularities with respect to the incident wavelength and varying the incident angle and impedance contrast at the interface. In general, the width of the retroreflective peak was found to increase as the ratio between the incident wavelength and the mean free path of the interface is increased, thus tying the retroreflective properties directly to the interface statistics. The retroreflective peak height also decreases dramatically with a decrease in impedance contrast and an increase in the incident angle. Finally, the absence of retroreflectance for specific conversions in the P-SV case gives strong support to the optical hypothesis of 'time-reversed paths'.

Experimentally, using our in-house ultrasonic water tank, acoustic energy scattered from a fluid-solid boundary is studied in detail. A glass etching process which utilizes numerically generated photoresist templates allows for the fabrication of a 3-D glass surface which is characterized by approximately Gaussian statistics. We find that our 2-D numerical reflection coefficients can give insight into the experimentally observed 3-D scattering. The 2-D numerical results predict the presence of enhanced backscattering and the experimental results strongly support the existence of this coherent scattering phenomenon. In terms of the diffuse reflection coefficient, the numerical results predict the asymmetry and general trend of the observed amplitude distributions. Strikingly, however, as the incident angle is increased, backscattering from the numerical 2-D interface appears to decrease more slowly than for the 3-D interface, suggesting an inherent difference between 2-D and 3-D scattering mechanisms.

Seismic retroreflectance and general scattering can also give insight into the crustal scattering problem. Scattering, from both an irregular Moho discontinuity and a high impedance intracrustal boundary, is shown to be consistent with a preliminary analysis of P coda energy observed at NORESS, FINESA, ARCESS, and NYNEX arrays. General backscattering and retroreflectance of energy from irregular topography and intracrustal interfaces may also provide a mechanism whereby various phases can be retropropagated laterally in the crust. Preliminary evidence for retropropagation is discussed. We find that further investigation into the role that irregular interfaces play (including free surface topography) in the generation of P coda and S coda at regional distances is well warranted.

Thesis Supervisor: M. Nafi Toksöz  
Title: Professor of Geophysics

## Acknowledgments

I would like to thank my advisor, Prof. M. Nafi Toksöz, for his considerable input into my research. His ability to see directly to the heart of a question and his ability to think critically has been a model which I have and always will try to follow. I have enjoyed working with him on this research and I hope we can continue to work together in the future.

The Earth Resources Laboratory has been a place which has always stimulated new and interesting ideas. I have enjoyed working with both the staff and students there. I thank the students for their enthusiasm and willingness to discuss my ideas and projects. I would specifically like to thank Dr. Zenya Zhu for his insights into the engineering side of ultrasonic testing. His input in building the piezo-film transducer introduced in this paper, not to mention his continual advice on how to obtain better controlled experiments in the lab, were critical in obtaining the highest quality experimental results. I would also like to thank Matthijs Haartsen, Rick Bennett, Bob Cicerone, and Joe Matarese for their valuable discussions both on this research and also on technical aspects of the computing facilities on campus. Ted Charrette was indispensable in the use of the nCUBE Parallel computing facilities. I also want to thank Xiaoming Tang for sharing his experience in water tank experiments and Ningya Cheng for his help on 3-D finite-difference modeling. Finally, Arcangelo Sena, my officemate, was a great source of knowledge on theoretical matters. In addition, Anita Killian, Sara Brydges, Naida Buckingham, Liz Henderson, and Sue Turbak were always helpful in administrative matters.

I wish to thank both Dr. Ross Hill at Chevron in La Habra and Prof. A.A. Maradudin at the University of California in Irvine for introducing me first to the idea of enhanced backscattering. The help of Dr. Anton Dainty at Phillips Laboratory in the analysis of array data has been indispensable.

On the international side, I would like to particularly thank Prof. Michel Bouchon and Prof. Michel Campillo for their very valuable input on the Boundary Integral techniques. I would also like to thank them for their enthusiasm and love for geophysics which I must say, is highly contagious. I am indebted to Michel Bouchon for his invitation to study in France for 5 months. In addition, I owe him a great deal for the times he pulled me away from my desk on weekends "pour aller faire du ski de fond sur le Vercors".

My final thanks on a professional level go to a someone who has had the greatest impact on me, both as a person and as a scientist. Prof. Shawn Biehler at the University of California in Riverside has given me continual input and has always

been there for support. He has inspired me to do good solid science and to try my best to fully understand at a basic level the problem at hand.

My greatest thanks go to my wife Susan, whose support, enthusiasm, and level headedness helped carry me through my years at MIT. It is impossible to express the deep appreciation and respect I have for her. I must also give a great deal of thanks to my parents who have always been there for me. Their steady and unwavering support has always helped me to go forward.

This research was partially funded by the Defense Advanced Research Projects Agency through contract number F29601-91-K-DB15 administered by Phillips Laboratory of the Air Force Systems Command. The author was a National Science Foundation Fellow for three years (1989-1992) and a Chevron Fellow for one year (1993).

# Contents

<b>1</b>	<b>Introduction</b>	<b>11</b>
<b>2</b>	<b>Analysis of Full Waveform Approaches</b>	<b>18</b>
2.1	Summary . . . . .	18
2.2	Introduction . . . . .	19
2.3	The Direct Somigliana Approach: P–SV Case . . . . .	21
2.3.1	General Numerical Approach . . . . .	25
2.3.2	The Green’s Function in Cylindrical Coordinates . . . . .	27
2.3.3	Evaluation of Matrix Elements Near Singularities . . . . .	29
2.4	BIE–DWN Formulation . . . . .	34
2.5	BIE–DWN Comparison with the Somigliana Approach . . . . .	39
2.5.1	Accuracy of the Somigliana Technique . . . . .	39
2.5.2	Periodicity Limitations in DWN Formulation . . . . .	41
2.6	BIE–DWN Comparison with FD . . . . .	42
2.6.1	2–D Finite Difference Formulation . . . . .	43
2.6.2	General Comparison . . . . .	45

2.7	Discussion and Conclusions . . . . .	49
<b>3</b>	<b>Enhanced Backscattering of Seismic Waves from a Highly Irregular, Random Interface: SH-Case</b>	<b>63</b>
3.1	Summary . . . . .	63
3.2	Introduction . . . . .	64
3.3	Theory . . . . .	66
3.3.1	Numerical Formulation: SH-case . . . . .	71
3.4	Numerical Results . . . . .	73
3.4.1	Dependence of Scattering on Properties . . . . .	77
3.5	Discussions and Conclusions . . . . .	80
<b>4</b>	<b>Enhanced Backscattering of Seismic Waves from a Highly Irregular, Random Interface: P-SV case</b>	<b>91</b>
4.1	Summary . . . . .	91
4.2	Introduction . . . . .	92
4.3	Representation of the Scattered Energy . . . . .	94
4.3.1	The Scattered Field in Cartesian Coordinates . . . . .	94
4.3.2	Incident Beam . . . . .	96
4.3.3	The Differential Reflection Coefficient . . . . .	97
4.4	Numerical Results . . . . .	100
4.4.1	Soil-Basement Interface . . . . .	105
4.4.2	Mohorovičić Discontinuity . . . . .	107
4.4.3	Scattering Mechanisms . . . . .	109

4.4.4	Accuracy of Statistical Averages . . . . .	115
4.5	Discussion and Conclusions . . . . .	117
<b>5</b>	<b>Experimental Study of Scattering from a Highly Irregular, Acoustic-Elastic Interface</b>	<b>139</b>
5.1	Summary . . . . .	139
5.2	Introduction . . . . .	140
5.3	Theory . . . . .	144
5.3.1	Numerical Analysis . . . . .	149
5.4	Experimental Procedure . . . . .	150
5.4.1	Random Interface Generation . . . . .	151
5.4.2	The Scattering Instrumentation . . . . .	153
5.5	Surface Scattering Measurements . . . . .	156
5.5.1	Case: $\lambda = 0.71a$ . . . . .	159
5.5.2	Case: $\lambda = 2.14a$ . . . . .	161
5.5.3	Piezo-Film Measurements . . . . .	163
5.5.4	General Discussion . . . . .	163
5.6	Conclusions . . . . .	167
<b>6</b>	<b>Application to the Earth</b>	<b>194</b>
6.1	Abstract . . . . .	194
6.2	Introduction . . . . .	195
6.3	Crustal Scattering . . . . .	198

6.3.1	The Nature of Regional P Coda . . . . .	198
6.3.2	F–K Analysis . . . . .	200
6.3.3	The Role of an Irregular Moho . . . . .	202
6.3.4	The Role of Near Surface Intracrustal Layers . . . . .	204
6.4	Retropropagating Lg Waves . . . . .	206
6.4.1	General Mechanism . . . . .	208
6.5	Ocean Bottom Topography . . . . .	210
6.6	Discussion and Conclusions . . . . .	216
<b>7</b>	<b>General Discussion</b>	<b>237</b>
7.1	Conclusions . . . . .	237
7.2	Future Work . . . . .	243
<b>A</b>	<b>Key of Variables, Symbols, and Constants: P–SV case</b>	<b>247</b>
<b>B</b>	<b>Numerical Formulation: Acoustic–Elastic Case</b>	<b>250</b>
<b>C</b>	<b>Ultrasonic Design</b>	<b>253</b>
C.1	Ultrasonic Water Tank Design . . . . .	253
C.2	Piezo–film Receiver . . . . .	254
<b>D</b>	<b>F–K Analysis of Ultrasonic Data</b>	<b>257</b>
<b>E</b>	<b>2–D vs 3–D Acoustic–Elastic Comparison</b>	<b>259</b>

# Chapter 1

## Introduction

The scattering of seismic waves from rough interfaces and volume heterogeneities has become a subject of wide interest. Although the effects of this scattering can often be identified on seismograms, the exact nature of wave interaction with irregular boundaries is difficult to assess. In this thesis, we quantitatively analyze the nature of scattering from highly irregular surfaces by directly solving for a mean reflection coefficient over the boundary. We specifically study interface irregularities which are comparable in size to the incident wavelength. Although analysis in this region is difficult, it is essential for the complete modeling of broadband seismograms which include waves scattered from heterogeneities of all sizes.

A number of theoretical approaches have been utilized to help understand the rough-surface-scattering problem. Until the recent advent of digital computers, most theoretical approaches directly modeled a specific geometry of interest with varying degrees of approximation. The initial study of the scattering from corrugated interfaces was performed for the acoustic case by Rayleigh (1894). Subsequent studies involved implementing similar approximate approaches in more general cases, requir-

ing properties, such as the overall interface topography (amplitude and slope), to be small compared to the incident wavelength (Asano, 1960 1966; Abubaker, 1962ab). These studies have effectively shown, with a fair amount of algebra, that corrugations with lateral length less than the incident wavelength can noticeably decrease reflected P and SV wave amplitudes and can generate diffracted waves whose amplitude and phase depend strongly on the angle of incidence and the size of the corrugation. In addition, these approximate studies were very effective in demonstrating that as corrugations become smaller relatively to the incident wavelength, energy incident over a wide range of angles can become partially trapped in the form of head waves and interface waves. More recently, Prange and Toksöz (1990), using the perturbation technique of Kennett (1972), demonstrated similar amplitude variations from random 3-D surfaces. Techniques such as the Kirchhoff technique (requiring small slopes) have also been implemented (Ogilvy, 1987).

Many boundaries in the crust and mantle present geometrical irregularities which are similar in size (both horizontally and vertically) to an incoming wavelength. In these instances the above approximate techniques, which require small perturbations, break down and full-waveform techniques must be implemented which model completely a wave's interaction with large interface topography. These techniques must include multiple scattering, interface wave propagation, and wave conversions. The boundary integral techniques have been effectively used in this area. The discrete-wavenumber technique used by Bouchon (1985), Campillo (1987), Paul and Campillo (1988), Gaffet and Bouchon (1989), and Bouchon *et al.* (1989) solves the boundary integral equation by using boundary conditions to directly invert for a body force distribution along the interface. Generally, the discrete wavenumber technique is considered an indirect approach as it does not require specific evaluation of integrals over singularities. A second computationally efficient approach solves the boundary integral problem directly by numerically integrating along the interface, using the elastic representation theorem (e.g. Aki and Richards, 1980). This requires explicit

analytic integration over the singularities. These Somigliana techniques, as we will refer to them (*see* Sanchez–Sesma and Campillo, 1991), have been effectively used by Kawase (1988), Kawase and Aki (1989), and Sanchez–Sesma and Campillo (1991) to study the effect of alluvial valleys and surface topography on the propagation of surface waves. In addition, hybrid techniques, which combine the discrete–wavenumber and the Somigliana techniques, have been developed in many of the above studies. The Somigliana approach is generally a more efficient computational technique. However, the periodicity assumed with the discrete–wavenumber technique is not present and integral truncation along the boundary must be dealt with directly.

The finite–difference (FD) approach has also become effective in studying diffractions from a corrugated interface. Although grid memory requirements and dispersion effects limit finite–difference models to small regions, this approach has been successfully used to model energy diffracted at highly irregular interfaces (Lavender and Hill, 1985; Dougherty and Stephen, 1991). In addition, unlike the boundary integral techniques, lateral velocity variations can be easily incorporated (*e.g.* Stephen, 1984 1988). However, the finite–difference technique, as we will show, is too computationally intensive for the large number of simulations required in this thesis.

Since many boundaries within the Earth and at the free–surface are extremely irregular over significant distances, a statistical description of the interface has been recently utilized to investigate the more complex seismic scattering which results. Paul and Campillo (1988) applied the discrete–wavenumber technique to determine the average amplitude distribution obtained when a wave reflects from a long, statistically distributed chain of small irregularities simulating the Moho discontinuity. This approach demonstrated many scattering trends, including the conversion of waves incident at most angles to post–critical shear energy, possibly explaining some of the long wave trains observed in seismic studies of the continental crust. Prange and Toksöz (1990) also used a statistical description of interface irregularities in their

study of diffraction from a 3-D distribution of irregularities.

A great number of statistical studies of scattering from rough interfaces can be found in the optical literature. O'Donnell and Mendez (1987) first conducted systematic experimental studies of scattering from highly irregular metallic interfaces with a Gaussian distribution of 3-D irregularities. By illuminating thousands of irregularities along a metallic plate with a finite width laser beam and then recording the far-field scattered power, an average power distribution of the scattered field was obtained. This work dramatically demonstrated that scattered energy varies strongly as a function of interface geometry, material properties, and the incident wave angle. "Enhanced backscattering" or "retroreflectance" was identified as a prominent part of the scattered field. Maradudin *et al.* (1990ab), using Green's second integral theorem, obtained exact integral expressions for the scattered field resulting from an incident finite-beam. Averaging over thousands of numerical surface realizations, each containing a few irregularities with the same statistical properties, scattering distributions similar in nature to the above experimental results, were obtained. In addition, using single- and double-scattering approximations, Maradudin *et al.* (1990a) demonstrated that enhanced backscattering appears first in the double-scattering approximation, supporting the idea that multiple scattering and time-reversed paths are responsible for this retroreflectance.

This idea of time-reversed paths is straightforward (O'Donnell and Mendez, 1987; Maradudin *et al.*, 1990b). Consider for instance, a wave traveling into a valley of the irregular interface. If the valley sides are steep enough, a double-scattered path can be found, allowing the wave to travel back towards the source. In this case, a wave traveling from the source along the time-reversed path can also send energy back to the source with the same phase, causing constructive interference in the direction of the source. Since the surface is random, all other paths cancel each other at least partially, while the constructive interference of the time-reversed paths allows

additional energy to return in the direction of the source.

In terms of electron and photon scattering, there has been a great deal of research into the localization and coherent scattering which results from disordered systems. John (1991) gives a good review of these studies. Initially, it was found that an electron moving in a potential  $V(\underline{x})$  is localized when the potential becomes very deep relative to the electrons energy (Anderson localization). The degree to which this localization takes place has a dramatic affect on the solids ability to conduct electricity since the localization can strongly affect the electrons ability to move through the system. In the case of monochromatic electromagnetic waves, comparisons between the Schrödinger equation and the wave equation for disordered systems show that the localization of light can occur strongly when the incident wavelength is on the same order as the distance a wave travels between individual scatterers. In the case of acoustic waves, there has been limited investigations into localization and coherent backscattering effects due to disordered systems. The recent study of Bayer and Niederdränk (1993) has shown that strongly heterogeneous media, such as random distributions of brass rods (2-D) and random distributions of gravel (3-D) can create weak localization effects. Coherent backscattering, which is a precursor to localization, was studied in a narrow region about the backscattering direction where a simple diffusion model predicted the results well. Theoretical work has also been done on the localization of acoustic waves, where Kirkpatrick (1985) has shown that, similar to monochromatic electromagnetic waves, all states are localized for dimension,  $d \leq 2$ . Although, this work may have implications for seismic scattering in an inhomogeneous crust, Condat and Kirkpatrick (1987) have shown that the localization of waves in an acoustic medium is very difficult to achieve unless extremely strong scatterers are present. Crustal localization, therefore, is likely far smaller than the effects shown in these results. In terms of elastic backscattering by irregular interfaces, the author has found very little previous research into possible coherent scattering effects.

This thesis studies scattering from highly irregular interfaces in five parts. In Chapter 2 we extend the optical approach of Maradudin *et al.* (1990a) to the general case of P–SV scattering from a highly irregular 2–D interface. The accuracy of this direct approach is first determined through direct comparisons with the boundary Integral Equation–Discrete Wavenumber (BIE–DWN) approach. Further comparisons are then made with this discrete wavenumber (DWN) approach to determine the advantages and disadvantages of each approach. The robust, staggered grid FD approach of Virieux (1986) is then further investigated to determine its applicability to this study. After demonstrating the numerous advantages of the Somigliana approach over these other full waveform techniques, we utilize this approach to study the scattered energy. In Chapter 3, scattering is analyzed in the simplest case of an SH wave, incident on a highly irregular 2–D elastic interface. Statistical reflection coefficients are evaluated for random interfaces with Gaussian statistics. The statistics and material properties along the interface are then varied over a full range of values to determine the properties of enhanced backscattering along with scattering properties, both in the forward and back scattering directions. Chapter 4 extends the reflection coefficient approach of Chapter 3 to the 2–D case of P–SV scattering. Utilizing the formulations in Chapter 2, scattering from both an irregular Moho discontinuity and an irregular soil–basement interface are investigated in detail. In Chapter 5, an experimental and theoretical study of scattering from a characterized fluid–solid interface are presented. The fabrication of the well controlled, characterized irregular interface is described in detail and the final measured statistics are compared with the objective statistics. The general amplitude distribution of energy scattered from this interface is then investigated both numerically and experimentally, and a partially transparent receiver is constructed to better constrain the retroreflective properties of the interface. In Chapter 6, the reflection coefficients presented in Chapter 4 are used to determine whether scattering from irregularities in the crust is consistent with P coda energy recorded at NORESS, FINESA, and ARCESS. We also discuss

the potential for retropropagating shear energy in the crust, which might result from diffraction at near surface crustal boundaries and at an irregular free surface. Finally, the potential role of multiple scattering by both ocean bottom topography, an irregular CMB, and rough ice cover is discussed. We show that, although these cases are very involved, the reflection coefficient analysis in the previous chapters may be useful for investigating the role of general scattering in many of these regions.

# Chapter 2

## Analysis of Full Waveform Approaches

### 2.1 Summary

In this chapter we develop an efficient boundary integral algorithm, which allows for the statistical analysis of seismic scattering in later chapters. Specifically, we combine the seismic representation theorem and the extinction theorem to model scattering of P and SV waves which are incident on a highly irregular 2-D interface, separating two semi-infinite, elastic halfspaces. Exact integral expressions are derived and an efficient numerical formulation allows for a compact analytic representation, which includes the curvature of the interface. The accuracy and efficiency of this Somigliana approach is then determined through direct comparisons with the Boundary Integral Equation–Discrete Wavenumber representation (BIE-DWN) approach in the frequency domain. We find that the Somigliana and BIE–DWN approaches match well up to the forty–five degree slopes tested. We show that our direct approach also

has distinct advantages over the BIE–DWN approach in the frequency domain, since periodic effects which create spurious peaks in the solution are avoided. Although there are advantages and disadvantages to both of these approaches, we find that the DWN approach is essentially a time–domain approach (where these periodic effects can be successfully removed) and must be used with caution in the frequency domain. The accuracy and efficiency of the time–domain finite difference (FD) approach of Virieux (1986) is also investigated to determine its applicability to this study. Given the advantages of the DWN approach in the time domain, we extend the BIE–DWN approach to the case of an acoustic–elastic interface for comparisons. We find that with a 15 point per wavelength (PPW) discretization criterion, micro-roughness on the FD grid results in numerical noise. This is accompanied by both large amplitude and phase errors. As the FD grid sampling is increased to 30 PPW, we find that the FD solution does converge towards the DWN solution. However, the FD grid becomes too large and the algorithm too computationally intensive to verify absolute convergence.

After comparing these various approaches with the Somigliana approach, we find that the scattered field calculated with the direct Somigliana approach is the most appropriate for the frequency domain, statistical analysis presented in this thesis.

## **2.2 Introduction**

A study of scattering from irregular interfaces may help our understanding of the nonuniform, low amplitude arrivals which tend to complicate seismograms. A number of numerical approaches have been shown to be effective in identifying the energy diffracted from irregular interfaces, including all wave conversions and all orders of multiple scattering. As discussed in Chapter 1, the direct and indirect boundary

integral techniques and the finite-difference (FD) technique rank among the most commonly used approaches. We will show, however, that for the case of two homogeneous media separated by an irregular interface, the advantages of the boundary integral techniques far outweigh their limitations. These approaches can give more accurate solutions with less memory requirements and a much faster run time than the more commonly used FD approaches. In addition, the results do not suffer from dispersion effects when waves are propagated over large distances.

In the first section of this chapter we take the space domain, boundary integral approach of Maradudin *et al.* (1990a), used to study optical scattering of p-polarized waves from a 2-D irregular, vacuum-dielectric contact, and extend it to the case of seismic scattering. Specifically, this approach is applied to the case of P and SV waves diffracted from a highly irregular, 2-D random interface. An approach similar to this has been developed by Sanchez-Sesma and Campillo (1991) to model the generation and distortion of surface waves by surface topography. Our approach differs from this approach in several ways. First, instead of making the standard assumption that the interface elements are plane, we allow the interface element to retain each of its higher derivatives. We find that for first order accuracy, the solution should retain additional curvature terms. Secondly, our solutions are fully analytic, requiring no numerical integration (Gaussian integration schemes, etc.) for the final solution. The remaining differences are discussed in Chapters 3 and 4.

In the second section of this chapter, we focus our attention on the accuracy of the Somigliana approach. Comparisons are made with one recently developed boundary integral approaches for modeling irregular interfaces, the Boundary Integral Equation-Discrete Wavenumber Representation [BIE-DWN] technique. Bouchon (1985) and Campillo and Bouchon (1985) initiated this technique. Paul and Campillo (1988) applied this technique to determine the generalized reflection coefficients for elastic P-SV waves diffracted from a corrugated Moho discontinuity.

Bouchon *et al.* (1989) later developed this technique for the two-dimensional SH-case, where multiple layers are incorporated. We begin with a brief summary of the full elastic, 2-D BIE-DWN approach. Given a steeply sloping sinusoidal interface, the Somigliana results are then compared directly with the BIE-DWN results to determine the accuracy of our approach. We then investigate the potential pitfalls associated with using the BIE-DWN approach for a frequency domain analysis.

In the third section of this chapter, we show that the boundary integral approaches can be more accurate and efficient than the commonly used FD approaches, when modeling a smoothly varying, irregular interface which separates two homogeneous halfspaces. Direct comparisons are made with the commonly used velocity-stress FD technique of Virieux (1986). To obtain an upper bound on the accuracy of the FD technique comparisons are made over a fluid solid-boundary. Dougherty and Stephen (1991) have evaluated the accuracy of this technique with indirect reciprocity tests and have already shown the slow convergence on an accurate solution. In this section, we take a more direct approach and compare the forward solutions directly with BIE-DWN results to show the numerical limitations of this FD technique. One should note that a list of abbreviations and symbols is given in Appendix A for easy reference.

## 2.3 The Direct Somigliana Approach: P-SV Case

In this section we introduce the notation which will be used throughout this study. We use a 2-D Cartesian coordinate system  $(x_1, x_3)$ , with properties invariant in the  $x_2$ -direction. The irregular surface is specified by a function of one coordinate

$$x_3 = \zeta(x_1), \tag{2.1}$$

and we assume that the interface has a mean height of zero. In this case, the unit normal at the interface can be written as

$$\hat{n}(x_1) = N\underline{n}(x_1) = [(\zeta'(x_1))^2 + 1]^{-\frac{1}{2}}[-\zeta'(x_1), 1], \quad (2.2)$$

where the prime represents differentiation with respect to  $x_1$  and  $N$  normalizes the normal vector  $\underline{n}(x_1)$ .

Consider now two homogeneous, isotropic, elastic media separated by a 2-D welded boundary with the plane of incidence in the  $x_1x_3$ -plane, as shown in Figure 2-1. If no source regions are present in either volume, the Helmholtz potentials for displacement in an infinite whole space satisfy the partial differential equations

$$\begin{aligned} \left(\frac{\partial^2}{\partial x_1^2} + \frac{\partial^2}{\partial x_3^2} + \frac{\omega^2}{\alpha^{(l)2}}\right)\phi^{(l)}(\underline{\mathbf{x}}|\omega) &= 0, \\ \left(\frac{\partial^2}{\partial x_1^2} + \frac{\partial^2}{\partial x_3^2} + \frac{\omega^2}{\beta^{(l)2}}\right)\underline{\psi}^{(l)}(\underline{\mathbf{x}}|\omega) &= 0, \end{aligned} \quad (2.3)$$

where  $\omega$  is the angular frequency,  $\phi^{(l)}(\underline{\mathbf{x}}|\omega)$  and  $\underline{\psi}^{(l)}(\underline{\mathbf{x}}|\omega)$  are the dilational and rotational displacement potentials for the wave,  $\alpha^{(l)}$  and  $\beta^{(l)}$  are the P and SV wave velocities, respectively, and  $l$  identifies the volume 1 or 2. Given these potentials, the Helmholtz relation gives the vector displacement at any point in the media

$$\underline{\mathbf{u}}^{(l)}(\underline{\mathbf{x}}|\omega) = \underline{\nabla}\phi^{(l)}(\underline{\mathbf{x}}|\omega) + \underline{\nabla} \times \underline{\psi}^{(l)}(\underline{\mathbf{x}}|\omega), \quad (2.4)$$

where  $\underline{\psi}^{(l)}(\underline{\mathbf{x}}|\omega) = (0, \psi_2^{(l)}(\underline{\mathbf{x}}|\omega), 0)$ . Given a source region, the displacement satisfies the partial differential equations

$$(\lambda^{(l)} + \mu^{(l)})u_{j,ij}^{(l)}(\underline{\mathbf{x}}|\omega) + \mu^{(l)}u_{i,jj}^{(l)}(\underline{\mathbf{x}}|\omega) + f_i^{(l)}(\underline{\mathbf{x}}|\omega) + \rho^{(l)}\omega^2 u_i^{(l)}(\underline{\mathbf{x}}|\omega) = 0, \quad (2.5)$$

in each medium, where  $f_i(\underline{\mathbf{x}}|\omega)$  is the body force per unit volume,  $\mu^{(l)}$  and  $\lambda^{(l)}$  are the Lamé parameters, and the Einstein summation convention is implied (where  $u_{i,jk}$  corresponds to a spatial derivative in the  $x_j$  and  $x_k$  directions). The Green's functions in this paper are defined by a unit line force acting at the point  $\underline{\mathbf{x}}' = (x'_1, x'_3)$  in the

$x_i$ -direction with  $f_i(\underline{x}|\omega) = \hat{Q}_i \delta(x_1 - x'_1) \delta(x_3 - x'_3)$ , where  $\delta(x)$  is the Dirac delta function. For these isotropic solids, stresses are related to displacements through the constitutive relation

$$\tau_{ij}^{(l)}(\underline{x}|\omega) = \lambda^{(l)} u_{k,k}^{(l)}(\underline{x}|\omega) \delta_{ij} + \mu^{(l)} (u_{i,j}^{(l)}(\underline{x}|\omega) + u_{j,i}^{(l)}(\underline{x}|\omega)), \quad (2.6)$$

where  $\delta_{ij}$  is the Kronecker identity tensor and  $\tau_{ij}^{(l)}(\underline{x}|\omega)$  is the elastic stress tensor.

The total scattered displacement at any point within these volumes can be expressed exactly in terms of the Somigliana representation theorem (*e.g.*, *elastic representation theorem*, Aki and Richards, 1980). Simplifying this theorem to a 2-D case gives a set of four integral equations

$$\begin{aligned} H[1]u_n^{(1)}(\underline{x}|\omega) &= \int_V f_p^{(1)}(\underline{\eta}|\omega) G_{np}^{(1)}(\underline{x}; \underline{\eta}) dV(\underline{\eta}) \\ &+ \int_S dS(\underline{x}') \{ [c_{ijpq}^{(1)} \hat{n}_j(\underline{x}') \partial G_{np}^{(1)}(\underline{x}; \underline{x}') / \partial x'_q] u_i^{(1)}(\underline{x}'|\omega) \\ &- G_{np}^{(1)}(\underline{x}; \underline{x}') T_p^{(1)}(\underline{u}^{(1)}(\underline{x}'), \hat{n}|\omega) \}, \end{aligned} \quad (2.7)$$

$$\begin{aligned} H[2]u_n^{(2)}(\underline{x}|\omega) &= \int_V f_p^{(2)}(\underline{\eta}|\omega) G_{np}^{(2)}(\underline{x}; \underline{\eta}) dV(\underline{\eta}) \\ &- \int_S dS(\underline{x}') \{ [c_{ijpq}^{(2)} \hat{n}_j(\underline{x}') \partial G_{np}^{(2)}(\underline{x}; \underline{x}') / \partial x'_q] u_i^{(2)}(\underline{x}'|\omega) \\ &- G_{np}^{(2)}(\underline{x}; \underline{x}') T_p^{(2)}(\underline{u}^{(2)}(\underline{x}'), \hat{n}|\omega) \}, \end{aligned} \quad (2.8)$$

where  $T_p^{(l)}(\underline{x}|\omega)$  is the traction vector along the interface and we have assumed all surfaces are far enough away that only the boundary,  $S(\underline{x})$ , separating the two volumes contributes to the final displacement.  $G_{np}(\underline{x}; \underline{x}')$  is a Green's function giving the  $n$ -component of displacement at  $\underline{x}$  resulting from a point force in the  $p$ -direction at  $\underline{x}'$ ,  $c_{ijpq}$  is the elasticity tensor, and  $H[i]$  is a function which takes a value of 0 or 1 depending on whether the point  $\underline{x}$  lies outside or inside the volume of interest,  $i$ , respectively. It has been assumed here that the displacement,  $u_n^{(l)}(\underline{x})$ , has a sinusoidal dependence on time

$$\underline{u}^{(l)}(\underline{x}|t) = (u_1^{(l)}(\underline{x}|\omega), 0, u_3^{(l)}(\underline{x}|\omega)) \exp(-i\omega t). \quad (2.9)$$

This time dependence will be implied throughout the remainder of this chapter to simplify the notation.

We now obtain integral equations valid for the model geometry of Figure 2-1. Assuming that the external forcing function,  $f_i^{(l)}(\underline{\mathbf{x}})$ , forms the incident wave in the upper medium, the volume integral in (2.7) and (2.8) can be represented in the upper medium by

$$\int_V f_p^{(1)}(\underline{\boldsymbol{\eta}}) G_{np}^{(1)}(\underline{\mathbf{x}}; \underline{\boldsymbol{\eta}}) dV(\underline{\boldsymbol{\eta}}) = u_n^{(1)}(\underline{\mathbf{x}})_{incid}, \quad (2.10)$$

and set to zero in the lower medium. The boundary conditions now allow the coupling of the two volumes along the boundary  $\zeta(x_1)$ . For an elastic medium, the boundary conditions can be written in general as a continuity of displacement and traction at the interface

$$\begin{aligned} T_i^{(1)}(\underline{\mathbf{x}})|_{x_3=\zeta(x_1)} &= T_i^{(2)}(\underline{\mathbf{x}})|_{x_3=\zeta(x_1)}, \\ u_i^{(1)}(\underline{\mathbf{x}})|_{x_3=\zeta(x_1)} &= u_i^{(2)}(\underline{\mathbf{x}})|_{x_3=\zeta(x_1)}. \end{aligned} \quad (2.11)$$

To obtain a final pair of coupled relations, we choose our volume of interest as volume 1 and substitute the volume integral (2.10) into the integral equations (2.7) and (2.8). Substituting the proper boundary conditions (2.11), while allowing  $x_3 \rightarrow \zeta^+(x_1)$ , these coupled integrals take the final form

$$\begin{aligned} u_n^{(1)}(\underline{\mathbf{x}}) &= u_n^{(1)}(\underline{\mathbf{x}})_{incid} \\ &+ \int_{-\infty}^{+\infty} dx'_1 [T_i^{n(1)}(\underline{\mathbf{x}}|x'_1) D_i(x'_1) - D_p^{n(1)}(\underline{\mathbf{x}}|x'_1) T_p(x'_1)], \end{aligned} \quad (2.12)$$

$$0 = - \int_{-\infty}^{+\infty} dx'_1 [T_i^{n(2)}(\underline{\mathbf{x}}|x'_1) D_i(x'_1) - \frac{\mu^{(1)}}{\mu^{(2)}} D_p^{n(2)}(\underline{\mathbf{x}}|x'_1) T_p(x'_1)], \quad (2.13)$$

where we define

$$\begin{aligned} T_i^{n(l)}(\underline{\mathbf{x}}|\underline{\mathbf{x}}') &= c_{ijpq}^{(l)} \hat{n}_j(\underline{\mathbf{x}}') \partial G_{np}^{(l)}(\underline{\mathbf{x}}; \underline{\mathbf{x}}') / \partial x'_q, \\ D_p^{n(l)}(\underline{\mathbf{x}}|\underline{\mathbf{x}}') &= \mu^{(l)} G_{np}^{(l)}(\underline{\mathbf{x}}; \underline{\mathbf{x}}'), \end{aligned} \quad (2.14)$$

with

$$c_{ijpq} = \lambda \delta_{ij} \delta_{pq} + \mu (\delta_{ip} \delta_{jq} + \delta_{iq} \delta_{jp}),$$

and  $\underline{x}' = (x_1', \zeta(x_1'))$ . The four unknown source strength functions, which we eventually solve, can be written as a function of  $x_1$  alone

$$\begin{aligned} D_i(x_1) &= u_i^{(1)}(\underline{x})|_{x_3=\zeta(x_1)}, \\ T_p(x_1) &= \frac{1}{\mu^{(1)}} c_{pqij}^{(1)} n_j(\underline{x}) u_{i,q}^{(1)}(\underline{x})|_{x_3=\zeta(x_1)}, \end{aligned} \quad (2.15)$$

where we have normalized the unknown traction with respect to the rigidity of the upper medium to ensure that the final numerical inversions are well-conditioned.

Now that the final coupled set of integral equations have been derived, the scattered field can be expressed specifically in terms of known Green's functions.

### 2.3.1 General Numerical Approach

We begin by summarizing the general numerical approach and giving a brief review of the representation of the 2-D Green's functions in cylindrical coordinates for a homogeneous, isotropic elastic medium. We present the limiting approach used to approximate the coupled surface integrals and the final approximations are then given.

We can numerically solve the coupled integral equations (2.12) and (2.13) by dividing them into a finite sum of integrals, each integrated over a smaller segment of the interface. An analytic approximation to these integrals then allows for numerical evaluation of the total scattered displacement. We begin by assuming that only a finite segment of the interface

$$-L/2 \leq x \leq L/2, \quad (2.16)$$

is excited by the incident wave. The integrals in (2.12) and (2.13) can then be approximated by integrating over this finite interval, provided that the majority of multiple scattering is restricted to this region. This approximation then contributes negligible error to the final solution. Now, replacing the infinite interval of integration

by the finite interval  $(-L/2, L/2)$ , and separating each integral into a finite sum over  $N$  smaller integrals (this  $N$  should not be confused with the normalization in 2.2), the final displacement can be expressed as

$$u_n^{(1)}(\underline{x}) = u_n^{(1)}(\underline{x})_{incid} + \sum_{n=1}^N \int_{x_n - \frac{\Delta x}{2}}^{x_n + \frac{\Delta x}{2}} dx'_1 [T_i^{n(1)}(\underline{x}|x'_1)D_i(x'_1) - D_p^{n(1)}(\underline{x}|x'_1)T_p(x'_1)], \quad (2.17)$$

where each contributing integral is evaluated over an element with length defined by  $\Delta x = \frac{L}{N}$ . In this case, each interval of integration is centered about a corresponding point

$$x_n = -\frac{L}{2} + (n - \frac{1}{2})\Delta x, \quad n = 1, 2, \dots, N, \quad (2.18)$$

where the  $n$  which corresponds to the component of displacement should not be confused with this element index  $n$ . If we assume that the source strength functions,  $D_i(x'_1)$  and  $T_p(x'_1)$ , are slowly varying functions with respect to  $x'_1$ , these functions can be removed from each integral over  $\Delta x$ , giving

$$u_n^{(1)}(\underline{x}) = u_n^{(1)}(\underline{x})_{incid} + \sum_{n=1}^N \{D_i(x_n) \int_{x_n - \frac{\Delta x}{2}}^{x_n + \frac{\Delta x}{2}} dx'_1 T_i^{n(1)}(\underline{x}|x'_1) - T_p(x_n) \int_{x_n - \frac{\Delta x}{2}}^{x_n + \frac{\Delta x}{2}} dx'_1 D_p^{n(1)}(\underline{x}|x'_1)\},$$

where the functions  $D_i(x_n)$  and  $T_p(x_n)$  take on values at the discrete points  $x_n$ .

A final coupled set of integral equations can now be obtained for the upper medium by evaluating the displacement at each point,  $x_m$ , along the interface. This gives  $2N$  linear equations

$$u_n^{(1)}(x_m) = u_n^{(1)}(x_m)_{incid} + \sum_{n=1}^N [D_i(x_n)T_{i0}^{n(1)}(x_m|x_n) - T_p(x_n)D_{p0}^{n(1)}(x_m|x_n)], \quad (2.19)$$

where

$$T_{i0}^{n(1)}(x_m|x_n) = \int_{x_n - \frac{\Delta x}{2}}^{x_n + \frac{\Delta x}{2}} dx'_1 T_i^{n(1)}(x_m|x'_1), \quad (2.20)$$

$$D_{p0}^{n(1)}(x_m|x_n) = \int_{x_n - \frac{\Delta x}{2}}^{x_n + \frac{\Delta x}{2}} dx'_1 D_p^{n(1)}(x_m|x'_1),$$

and we have let  $x_1 = x_m$  as  $x_3 \rightarrow \zeta^+(x_1)$ . Similarly, in the lower medium this gives  $2N$  additional equations

$$0 = - \sum_{n=1}^N [D_i(x_n) T_{i0}^{n(2)}(x_m|x_n) - \epsilon_o T_p(x_n) D_{p0}^{n(2)}(x_m|x_n)], \quad (2.21)$$

where

$$T_{i0}^{n(2)}(x_m|x_n) = \int_{x_n - \frac{\Delta x}{2}}^{x_n + \frac{\Delta x}{2}} dx'_1 T_i^{n(2)}(x_m|x'_1), \quad (2.22)$$

$$D_{p0}^{n(2)}(x_m|x_n) = \int_{x_n - \frac{\Delta x}{2}}^{x_n + \frac{\Delta x}{2}} dx'_1 D_p^{n(2)}(x_m|x'_1),$$

with  $\epsilon_o = (\mu^{(1)}/\mu^{(2)})$ . These integrals are also evaluated in the limit as the point of evaluation,  $x_m$ , approaches the interface from above. Equations (2.19) and (2.21) now represent a  $4N$  by  $4N$  coupled system of linear equations which can be solved using standard techniques, given that the integrals over  $\Delta x$  can be evaluated.

### 2.3.2 The Green's Function in Cylindrical Coordinates

We now evaluate the integral equations (2.20) and (2.22) with the use of cylindrical Green's functions. Mathematically, these Green's functions, expressed in terms of first, second, and third order Hankel functions, allow analytic evaluation of the integrands near singularities by use of descending series approximations. In addition, these Hankel functions are computed rapidly through polynomial approximations. This extra computational efficiency is necessary for the thousands of surface realizations required in our statistical approach.

The Green's tensor for a 2-D, homogeneous, isotropic medium can be written in cylindrical coordinates as

$$G_{ij}(\underline{x}; \underline{x}') = \frac{i}{4\mu} \left[ \delta_{ij} H_0(k_\beta r) - \frac{\delta_{ij}}{k_\beta r} \left\{ H_1(k_\beta r) - \left(\frac{\beta}{\alpha}\right) H_1(k_\alpha r) \right\} \right. \\ \left. + \gamma_i \gamma_j \left\{ H_2(k_\beta r) - \left(\frac{\beta}{\alpha}\right)^2 H_2(k_\alpha r) \right\} \right], \quad (2.23)$$

where  $\gamma_l$  is the direction cosine calculated from the source point  $x'_l$  to the point of evaluation  $x_l$ ,  $H_m(k_p r) = H_m^{(1)}(k_p r)$  is the Hankel function of  $m$ th order and first kind, and the radial distance  $r = \sqrt{(x_1 - x'_1)^2 + (x_3 - x'_3)^2}$  (e.g. Singh and Sikka, 1988). Substituting the Green's function (2.23) into the expression for the traction term (2.14), the traction at a point can now be expressed in terms of Hankel functions

$$T_i^n(\underline{x}|\underline{x}') = \frac{ik_\beta}{8} \left[ \left(\frac{\beta}{\alpha}\right)^3 \left\{ \left(\frac{2\lambda}{\mu} n_i \gamma_n + \Sigma n_i \gamma_n\right) H_1(k_\alpha r) \right. \right. \\ \left. \left. + (\Sigma n_i \gamma_n - 4\gamma_i (n_j \gamma_j) \gamma_n) H_3(k_\alpha r) \right\} \right. \\ \left. + (\Sigma n_i \gamma_n - 2n_i \gamma_n) H_1(k_\beta r) \right. \\ \left. - (\Sigma n_i \gamma_n - 4\gamma_i (n_j \gamma_j) \gamma_n) H_3(k_\beta r) \right], \quad (2.24)$$

where  $\underline{n}$  is evaluated at the point  $\underline{x}'$ . This expression includes the shorthand form

$$\Sigma n_i \gamma_n = n_i \gamma_n + n_n \gamma_i + \delta_{ni} \gamma_j n_j. \quad (2.25)$$

The integrals in (2.19) and (2.21) can now be explicitly approximated for small  $k\Delta x$ . The integration is straight-forward when evaluating the effect of one element centered at  $x_n$  on another element centered at  $x_m$  ( $x_m \neq x_n$ ), since no singularities are encountered along the path of integration. Thus, the first order approximation becomes a simple multiplication of (2.23) and (2.24) by  $\Delta x$ . However, integrating to determine the effect of an element on itself is a more involved matter because singularities must be dealt with explicitly in the integration.

### 2.3.3 Evaluation of Matrix Elements Near Singularities

In this section we extend the limiting technique of Maradudin *et al.* (1990a) to the analytic formulation of the integrals

$$T_{i0}^{n(l)}(x_m|x_n) = \int_{x_n - \frac{\Delta x}{2}}^{x_n + \frac{\Delta x}{2}} dx'_1 T_i^{n(l)}(x_m|x'_1), \quad (2.26)$$

$$D_{p0}^{n(l)}(x_m|x_n) = \int_{x_n - \frac{\Delta x}{2}}^{x_n + \frac{\Delta x}{2}} dx'_1 D_p^{n(l)}(x_m|x'_1),$$

allowing for an explicit representation of these integrals as  $k\Delta x$  becomes very small. This is accomplished by expanding the integrands in an infinite series in terms of  $\Delta x$ . The element length  $\Delta x$  is then taken small enough that only the first order terms in this expansion need to be included for an accurate solution.

Consider first the case  $m \neq n$ . No singularities are encountered in the interval of integration and the first order  $\Delta x$  term can be easily evaluated by assuming that the integrand is constant over the element interval, giving

$$T_{i0}^{n(l)}(x_m|x_n) = \Delta x T_i^{n(l)}(x_m|x_n), \quad (2.27)$$

$$D_{p0}^{n(l)}(x_m|x_n) = \Delta x D_p^{n(l)}(x_m|x_n),$$

which can be evaluated using (2.24) and the normalized Green's function (2.23). Calculating the diagonal matrix elements,  $T_{0i}^{n(l)}(x_m|x_m)$  and  $D_{0p}^{n(l)}(x_m|x_m)$ , is a more involved matter as singularities must be dealt with explicitly in the interval of integration. However, these singularities can be dealt with directly by using a limiting process where we compute the effect of an element at some point  $x_3$  above the interface as that point approaches the element from the upper medium. This is accomplished by letting  $x_3 = \zeta(x_1) + \epsilon$  and integrating all terms corresponding to first order in  $\Delta x$  in the limit as  $\epsilon \rightarrow 0^+$ . To expand each term in the integral in a series, we make the change of variable  $x'_1 = x_m + u$

$$T_{i0}^{n(l)}(x_m|x_m) = \int_{-\frac{\Delta x}{2}}^{\frac{\Delta x}{2}} du T_i^{n(l)}(x_m|x_m + u), \quad (2.28)$$

$$D_{p0}^{n(l)}(x_m|x_m) = \int_{-\frac{\Delta x}{2}}^{\frac{\Delta x}{2}} du D_p^{n(l)}(x_m|x_m + u),$$

where  $u$  is the horizontal distance from the singularity of the given element. Using Taylor series expansions, both the surface normal vector and the direction cosines can be written in terms of the variable  $u$

$$\begin{aligned} \underline{n}(x_n) &= (-\zeta'(x_n), 1) \\ &\approx (-\zeta'(x_n) - \zeta''(x_n)u - \frac{1}{2}\zeta'''(x_n)u^2, 1) + O(u^3), \\ \underline{\gamma}(x_m|x_n)r &= (x_m - x_n, \zeta(x_m) - \zeta(x_n)) \\ &\approx (-u, \epsilon - \zeta'(x_m)u - \frac{1}{2}\zeta''(x_m)u^2) + O(u^3). \end{aligned} \quad (2.29)$$

In a similar manner the radius vector can now be approximated by the expression

$$\begin{aligned} r &= [(x_m - x_n)^2 + (\zeta(x_m) - \zeta(x_n))^2]^{\frac{1}{2}} \\ &\approx [\gamma_m^2 u^2 - 2\zeta'(x_m)\epsilon u + \epsilon^2]^{\frac{1}{2}}, \end{aligned} \quad (2.30)$$

with  $\gamma_m = \sqrt{(1 + (\zeta'(x_m))^2)}$ . The Hankel functions can now be expanded in terms of descending series about the singular point  $r = 0$ , giving the pertinent relationships (Abramowitz and Stegun, 1964)

$$\begin{aligned} \frac{1}{r^2}[H_2(k_\beta r) - (\frac{\beta}{\alpha})^2 H_2(k_\alpha r)] &\approx -\frac{i}{\pi} \frac{1}{r^2} M_2, \\ \frac{1}{r^3}[H_3(k_\beta r) - (\frac{\beta}{\alpha})^3 H_3(k_\alpha r)] &\approx -\frac{i}{\pi} [\frac{2}{k_\beta} \frac{M_2}{r^4} + \frac{k_\beta}{4} \frac{M_4}{r^2}], \end{aligned} \quad (2.31)$$

where

$$\begin{aligned} LN_p &= \ln\left(\frac{\gamma k_p r}{2e}\right) + \frac{1}{2} - \frac{i\pi}{2}, \\ M_2 &= 1 - \left(\frac{\beta}{\alpha}\right)^2, \\ M_4 &= 1 - \left(\frac{\beta}{\alpha}\right)^4, \end{aligned}$$

with  $\gamma = 1.7810724$  corresponding to Euler's constant and  $\alpha$  and  $\beta$  corresponding to the velocities of the respective medium. Substituting the above expressions into

the explicit representation of the displacement and traction, (2.23) and (2.24), respectively, the integral equations, (2.28), can be evaluated by direct integration. Canceling singular terms which are first order in  $\Delta x$ , these integrals can be expressed as

$$\begin{aligned}
D_{10}^{3(l)}(x_m|x_m) &= D_{30}^{1(l)}(x_m|x_m) = \lim_{\epsilon \rightarrow 0^+} \frac{M_2 \zeta'(x_m)}{2\pi} \int_0^{\frac{\Delta x}{2}} du \frac{u^2}{r^2}, \\
D_{10}^{1(l)}(x_m|x_m) &= \lim_{\epsilon \rightarrow 0^+} \frac{1}{2\pi} \left\{ \int_0^{\frac{\Delta x}{2}} du \left( -2 \ln \left( \frac{\gamma k_\beta \gamma_m u}{2} \right) + i\pi \right. \right. \\
&\quad \left. \left. + [LN_\beta - \left( \frac{\beta}{\alpha} \right)^2 LN_\alpha] + M_2 \int_0^{\frac{\Delta x}{2}} du \frac{u^2}{r^2} \right\}, \\
D_{30}^{3(l)}(x_m|x_m) &= \lim_{\epsilon \rightarrow 0^+} \frac{1}{2\pi} \left\{ \int_0^{\frac{\Delta x}{2}} du \left( -2 \ln \left( \frac{\gamma k_\beta \gamma_m u}{2} \right) + i\pi \right. \right. \\
&\quad \left. \left. + [LN_\beta - \left( \frac{\beta}{\alpha} \right)^2 LN_\alpha] + M_2 (\zeta'(x_m))^2 \int_0^{\frac{\Delta x}{2}} du \frac{u^2}{r^2} \right\},
\end{aligned} \tag{2.32}$$

which upon evaluation gives the cross terms

$$D_{10}^{3(l)}(x_m|x_m) = D_{30}^{1(l)} = \frac{M_2}{4\pi} \zeta'(x_m) \gamma_m^{-2} \Delta x, \tag{2.33}$$

and the diagonal terms

$$\begin{aligned}
D_{10}^{1(l)}(x_m|x_m) &= \frac{\Delta x}{4\pi} \left[ i\pi H_0 \left( \frac{k_\beta \gamma_m \Delta x}{2e} \right) \right. \\
&\quad \left. + \left[ \ln \left( \frac{\gamma k_\beta \gamma_m \Delta x}{4e^2} \right) - \left( \frac{\beta}{\alpha} \right)^2 \ln \left( \frac{\gamma k_\alpha \gamma_m \Delta x}{4e^2} \right) \right] \right. \\
&\quad \left. + \frac{M_2}{2} (1 - i\pi) + M_2 \gamma_m^{-2} \right] \\
&\approx \frac{\Delta x}{4\pi} \left[ i\pi H_0 \left( \frac{k_\beta \gamma_m \Delta x}{2e} \right) - \frac{i\pi}{2} \left[ H_0 \left( \frac{k_\beta \gamma_m \Delta x}{2e^2} \right) \right. \right. \\
&\quad \left. \left. - \left( \frac{\beta}{\alpha} \right)^2 H_0 \left( \frac{k_\alpha \gamma_m \Delta x}{2e^2} \right) \right] + \frac{M_2}{2} + M_2 \gamma_m^{-2} \right],
\end{aligned} \tag{2.34}$$

$$\begin{aligned}
D_{30}^{3(l)}(x_m|x_m) &= \frac{\Delta x}{4\pi} \left[ i\pi H_0 \left( \frac{k_\beta \gamma_m \Delta x}{2e} \right) \right. \\
&\quad \left. + \left[ \ln \left( \frac{\gamma k_\beta \gamma_m \Delta x}{4e^2} \right) - \left( \frac{\beta}{\alpha} \right)^2 \ln \left( \frac{\gamma k_\alpha \gamma_m \Delta x}{4e^2} \right) \right] \right. \\
&\quad \left. + \frac{M_2}{2} (1 - i\pi) + (\zeta'(x_m))^2 M_2 \gamma_m^{-2} \right] \\
&\approx \frac{\Delta x}{4\pi} \left[ i\pi H_0 \left( \frac{k_\beta \gamma_m \Delta x}{2e} \right) - \frac{i\pi}{2} \left[ H_0 \left( \frac{k_\beta \gamma_m \Delta x}{2e^2} \right) \right. \right. \\
&\quad \left. \left. - \left( \frac{\beta}{\alpha} \right)^2 H_0 \left( \frac{k_\alpha \gamma_m \Delta x}{2e^2} \right) \right] + \frac{M_2}{2} + M_2 (\zeta'(x_m))^2 \gamma_m^{-2} \right],
\end{aligned} \tag{2.35}$$

where we have approximated the natural logs by Hankel functions in the last step, using the same descending series approximations presented above.

The traction of one element on itself is expressed by evaluating the traction integrals (2.28) over their singularities. Rearranging expression (2.24) and substituting the expansions (2.31), the final contribution can be evaluated algebraically with some effort. We summarize the process here by stating that, following the cancellation of singular terms, the finite integrals which contribute to the final expressions become

$$\begin{aligned}
I_1 &= \lim_{\epsilon \rightarrow 0^+} \int_{-\frac{\Delta x}{2}}^{\frac{\Delta x}{2}} du \frac{\epsilon}{r^2} = \pi, \\
I_2 &= \lim_{\epsilon \rightarrow 0^+} \int_{-\frac{\Delta x}{2}}^{\frac{\Delta x}{2}} du \frac{u}{r^2} = \zeta'(x_m) \gamma_m^{-2} \pi, \\
I_3 &= \lim_{\epsilon \rightarrow 0^+} \int_{-\frac{\Delta x}{2}}^{\frac{\Delta x}{2}} du \frac{u^2}{r^2} = \gamma_m^{-2} \Delta x, \\
I_4 &= \lim_{\epsilon \rightarrow 0^+} \int_{-\frac{\Delta x}{2}}^{\frac{\Delta x}{2}} du \frac{\epsilon u^2}{r^4} = \frac{\pi}{2}, \\
I_5 &= \lim_{\epsilon \rightarrow 0^+} \int_{-\frac{\Delta x}{2}}^{\frac{\Delta x}{2}} du \frac{\epsilon^2 u}{r^4} = \frac{\pi}{2} \zeta'(x_m), \\
I_6 &= \lim_{\epsilon \rightarrow 0^+} \int_{-\frac{\Delta x}{2}}^{\frac{\Delta x}{2}} du \frac{u^4}{r^4} = \gamma_m^{-4} \Delta x, \\
I_7 &= \lim_{\epsilon \rightarrow 0^+} \int_{-\frac{\Delta x}{2}}^{\frac{\Delta x}{2}} du \frac{\epsilon^3}{r^4} = \frac{\pi \gamma_m^2}{2},
\end{aligned} \tag{2.36}$$

where, using the fact that

$$\frac{\lambda}{\mu} = \frac{\alpha^2}{\beta^2} - 2, \tag{2.37}$$

the final first order approximations in  $\Delta x$  can be written as

$$\begin{aligned}
T_{10}^{3(l)}(x_m|x_m) &= -\frac{1}{2\pi} \left[ +\frac{3}{2} \left(\frac{\beta}{\alpha}\right)^2 \zeta''(x_m) \zeta'(x_m) \gamma_m^{-2} \Delta x - M_2 \zeta'(x_m) \zeta''(x_m) \gamma_m^{-4} \Delta x \right], \\
T_{30}^{1(l)}(x_m|x_m) &= -\frac{1}{2\pi} \left[ -\frac{3}{2} \left(\frac{\beta}{\alpha}\right)^2 \zeta''(x_m) \zeta'(x_m) \gamma_m^{-2} \Delta x - M_2 \zeta'(x_m) \zeta''(x_m) \gamma_m^{-4} \Delta x \right], \\
T_{10}^{1(l)}(x_m|x_m) &= \frac{1}{2} + \frac{1}{2\pi} \left[ \frac{1}{2} \left(\frac{\beta}{\alpha}\right)^2 \zeta''(x_m) \gamma_m^{-2} \Delta x + M_2 \zeta''(x_m) \gamma_m^{-4} \Delta x \right], \\
T_{30}^{3(l)}(x_m|x_m) &= \frac{1}{2} + \frac{1}{2\pi} \left[ \frac{1}{2} \left(\frac{\beta}{\alpha}\right)^2 \zeta''(x_m) \gamma_m^{-2} \Delta x + M_2 (\zeta'(x_m))^2 \zeta''(x_m) \gamma_m^{-4} \Delta x \right].
\end{aligned} \tag{2.38}$$

Each of the approximations above can now be substituted into the coupled matrix equations (2.19) and (2.21) to give the complete solution good to first order in  $\Delta x$ . Note that, if the surface element is assumed plane (without curvature), the solution for  $m = n$  reduces to the case of Sánchez-Sesma and Campillo (1991). Each cross-term vanishes and the diagonal terms become equivalent to one-half the identity tensor. Although the sample interval required for a convergent solution depends on the interface geometry, we find that for the interfaces in this study, the final Somigliana solution converges for a sampling of approximately 5 discrete points per minimum wavelength. In addition, the computation of matrix elements is extremely rapid due to the polynomial approximation of the Hankel functions. Therefore, the computational time required for this algorithm is almost completely the time required to solve the final system of linear equations. This time can be further reduced by direct application of techniques such as the biconjugate gradient approach with a preconditioned matrix. Therefore, this approach is extremely efficient as the computational demand approaches a frequency squared dependence.

Numerically, the slope and curvature of the interface,  $\zeta'(x_1)$  and  $\zeta''(x_1)$ , were calculated both with finite differencing and Fourier differentiation algorithms. Comparisons between the results for various interface irregularities showed that with the coarser grids, a second-order finite differencing technique in space resulted in numerical noise. Therefore, the Fourier differencing approach is implemented. The interface, along with additional damped segments at the ends of the interface, are transformed to the wavenumber domain. The interface is then differentiated and transformed back to the space domain where the undamped section of the interface is then selected. This more elegant approach gives a very good approximation to the derivatives and minimal numerical noise in all cases studied.

## 2.4 BIE–DWN Formulation

In order to determine the accuracy of the Somigliana approach and its efficiency for a statistical analysis in the frequency domain, we summarize the formulation of the Boundary Integral Equation-Discrete Wavenumber Technique (BIE–DWN) for a 2–D elastic–elastic boundary. We then generalize this DWN approach to an acoustic–elastic configuration as shown in Figure 2-2, which later in this chapter allows for a determination of the accuracy and efficiency of the FD approach in modeling irregular boundaries.

The model geometry is the same as the two layered system introduced in the last section, where, in this case, the surface separates a lower elastic medium either from an upper acoustic or upper elastic medium. The compressional and shear wave velocities are again denoted by  $\alpha^{(l)}$  and  $\beta^{(l)}$  with  $l = 1, 2$  corresponding to the upper or lower layer, respectively, where  $\beta^{(l)}$  is nonexistent in the case of the acoustic medium. The source can be located in either the upper or lower medium. Even though we present a two layer system, more layers can be included by converting the linear equations presented below into a layered matrix form (Bouchon *et al.*, 1989).

We begin by considering a monochromatic incident plane wave in the upper medium, where any source can be constructed by a superposition of these plane waves. In this case any observable such as displacement or stress can be expressed as

$$\underline{\mathbb{P}}(x_1, x_3|\omega) = e^{i\omega t} \int_{-\infty}^{\infty} p(k, x_3) e^{-ikx_1} dk, \quad (2.39)$$

where  $\omega$  is the angular frequency. Given this linear transformation, the Helmholtz potentials for the displacement in an infinite whole space again satisfy the partial differential equations, (2.3), where in the acoustic case,  $\underline{\psi}^{(l)}$  is nonexistent since the medium can not support shear motions. Given these potentials, the Helmholtz relation, (2.4), gives the vector displacement at any point in the media.

In this section we follow the boundary approach initiated by Bouchon (1985) and Campillo and Bouchon (1985) for the study of SH wave scattering and later adapted by Paul and Campillo (1988) to P–SV waves diffracted at an interface. Scattered waves are represented in both media by the superposition of body forces  $F^{(i)}(x_1, x_3)$  which are distributed along the interface,  $\zeta(x_1)$ . The magnitude of each force is determined by the continuity conditions at the interface. These continuity, or boundary, conditions can be written as

$$\begin{aligned}\hat{\boldsymbol{n}} \cdot \boldsymbol{u}^{(1)}(\boldsymbol{x})|_{x_3=\zeta(x_1)} &= \hat{\boldsymbol{n}} \cdot \boldsymbol{u}^{(2)}(\boldsymbol{x})|_{x_3=\zeta(x_1)}, \\ \hat{\boldsymbol{n}} \cdot \boldsymbol{T}^{(1)}(\boldsymbol{x})|_{x_3=\zeta(x_1)} &= \hat{\boldsymbol{n}} \cdot \boldsymbol{T}^{(2)}(\boldsymbol{x})|_{x_3=\zeta(x_1)}, \\ 0 &= \hat{\boldsymbol{n}} \times \boldsymbol{T}^{(2)}(\boldsymbol{x})|_{x_3=\zeta(x_1)},\end{aligned}\tag{2.40}$$

in the acoustic–elastic case, and as

$$\begin{aligned}\boldsymbol{u}^{(1)}(\boldsymbol{x})|_{x_3=\zeta(x_1)} &= \boldsymbol{u}^{(2)}(\boldsymbol{x})|_{x_3=\zeta(x_1)}, \\ \boldsymbol{T}^{(1)}(\boldsymbol{x})|_{x_3=\zeta(x_1)} &= \boldsymbol{T}^{(2)}(\boldsymbol{x})|_{x_3=\zeta(x_1)},\end{aligned}\tag{2.41}$$

in the elastic–elastic case, with

$$T_i^{(l)}(\boldsymbol{x}) = \tau_{i1}^{(l)}(\boldsymbol{x})n_1 + \tau_{i2}^{(l)}(\boldsymbol{x})n_2,$$

where  $\boldsymbol{u}^{(l)}(\boldsymbol{x}) = (u_1(\boldsymbol{x}), u_3(\boldsymbol{x}))$  represents the displacement and  $\tau_{ij}^{(l)}(\boldsymbol{x})$  represents the stress tensor in the corresponding medium. The stresses can be determined with the constitutive relation, (2.6), for an isotropic medium.

The exact form of the scattered displacement in both media can now be expressed with a different form of the elastic representation theorem, (2.12), giving

$$\begin{aligned}u_1^{(1)}(\boldsymbol{x})_{scat} &= \int_{\zeta} [F_V^{(1)}(\boldsymbol{x}') \partial G_{1q}^{(1)}(\boldsymbol{x}; \boldsymbol{x}') / \partial x'_q] dl, \\ u_3^{(1)}(\boldsymbol{x})_{scat} &= \int_{\zeta} [F_V^{(1)}(\boldsymbol{x}') \partial G_{3q}^{(1)}(\boldsymbol{x}; \boldsymbol{x}') / \partial x'_q] dl,\end{aligned}\tag{2.42}$$

in the acoustic medium, and

$$\begin{aligned} u_1^{(l)}(\underline{\mathbf{x}})_{scat} &= \int_{\zeta} [F_1^{(l)}(\underline{\mathbf{x}}') G_{11}^{(l)}(\underline{\mathbf{x}}; \underline{\mathbf{x}}') + F_3^{(l)}(\underline{\mathbf{x}}') G_{31}^{(l)}(\underline{\mathbf{x}}; \underline{\mathbf{x}}')] dl, \\ u_3^{(l)}(\underline{\mathbf{x}})_{scat} &= \int_{\zeta} [F_1^{(l)}(\underline{\mathbf{x}}') G_{13}^{(l)}(\underline{\mathbf{x}}; \underline{\mathbf{x}}') + F_3^{(l)}(\underline{\mathbf{x}}') G_{33}^{(l)}(\underline{\mathbf{x}}; \underline{\mathbf{x}}')] dl, \end{aligned} \quad (2.43)$$

in the corresponding elastic medium. We have used a notation similar to that of Paul and Campillo (1988) where  $G_{ij}^{(l)}(\underline{\mathbf{x}}; \underline{\mathbf{x}}')$  represents the Green's function tensor in each medium,  $F_V^{(1)}(\underline{\mathbf{x}})$  and  $F_i^{(l)}(\underline{\mathbf{x}})$  represent the strength of a dilatational line source and a line force,  $u_i^{(l)}(\underline{\mathbf{x}})_{scat}$  represents the scattered displacement in the corresponding medium, and  $dl$  refers to an infinitesimal length along the interface.

To solve equations (2.42) and (2.43) we convert them into a system of linear equations which can be solved numerically. Replacing the continuous integral by a sum over an infinite number of discrete points along the interface, the integral equations, (2.42) and (2.43), can be converted to the discrete form

$$\begin{aligned} u_1^{(1)}(\underline{\mathbf{x}})_{scat} &= \sum_{m=-\infty}^{\infty} [F_V^{(1)}(x_m, \zeta(x_m)) \partial G_{1q}^{(1)}(\underline{\mathbf{x}}; x_m, \zeta(x_m)) / \partial x'_q], \\ u_3^{(1)}(\underline{\mathbf{x}})_{scat} &= \sum_{m=-\infty}^{\infty} [F_V^{(1)}(x_m, \zeta(x_m)) \partial G_{3q}^{(1)}(\underline{\mathbf{x}}; x_m, \zeta(x_m)) / \partial x'_q], \end{aligned} \quad (2.44)$$

for the acoustic medium, and

$$\begin{aligned} u_1^{(l)}(\underline{\mathbf{x}})_{scat} &= \sum_{m=-\infty}^{\infty} [F_1^{(l)}(x_m, \zeta(x_m)) G_{11}^{(l)}(\underline{\mathbf{x}} | x_m, \zeta(x_m)) \\ &\quad + F_3^{(l)}(x_m, \zeta(x_m)) G_{31}^{(l)}(\underline{\mathbf{x}} | x_m, \zeta(x_m)), \\ u_3^{(l)}(\underline{\mathbf{x}})_{scat} &= \sum_{m=-\infty}^{\infty} [F_1^{(l)}(x_m, \zeta(x_m)) G_{13}^{(l)}(\underline{\mathbf{x}} | x_m, \zeta(x_m)) \\ &\quad + F_3^{(l)}(x_m, \zeta(x_m)) G_{33}^{(l)}(\underline{\mathbf{x}} | x_m, \zeta(x_m)), \end{aligned} \quad (2.45)$$

for the corresponding elastic medium.

The terms in (2.44) and (2.45) can be expanded using a plane wave decomposition of the respective Green's functions. Assuming that the model is periodic along the

x-axis with length  $L$ , we can work in the frequency–horizontal wavenumber domain, using the Green’s functions presented by Bouchon and Aki (1977). Implementing this Discrete Wavenumber representation requires discretizing the interface into a finite number of points,  $N$ . Requiring  $N$  to equal  $2M + 1$ , with  $M$  an integer, and expanding the Green’s functions we can explicitly express the horizontal displacements in (2.44) and (2.45) as

$$u_1^{(1)}(\underline{x})_{scat} = \frac{1}{2L\alpha^{(1)2}\rho^{(1)}} \left\{ \sum_{m=-M}^M F^{(1)}(x_m, \zeta(x_m))_v \right. \\ \left. \times \sum_{p=-M}^M \left[ \frac{k}{k_3^{\alpha(1)}} e^{-ik_{3p}^{\alpha(1)}|x_3-\zeta(x_m)|} \right] e^{-ik_p(x-x_m)} \right\}, \quad (2.46)$$

in the acoustic medium, and

$$u_1^{(l)}(\underline{x})_{scat} = \frac{-i}{2L\omega^2\rho^{(l)}} \left\{ \sum_{m=-M}^M F_1^{(l)}(x_m, \zeta(x_m)) \right. \\ \times \sum_{p=-M}^M \left[ \left( \frac{k_p}{k_{3p}^{\alpha(l)}} \right)^2 e^{-ik_{3p}^{\alpha(l)}|x_3-\zeta(x_m)|} + k_{3p}^{\beta(l)} e^{-ik_{3p}^{\beta(l)}|x_3-\zeta(x_m)|} \right] \\ \times e^{-ik_p(x-x_m)} + \sum_{m=-M}^M F_3^{(l)}(x_m, \zeta(x_m)) \operatorname{sgn}(x_3 - \zeta(x_3)) \\ \times \sum_{p=-M}^M k_p \left[ e^{-ik_{3p}^{\alpha(l)}|x_3-\zeta(x_m)|} - e^{-ik_{3p}^{\beta(l)}|x_3-\zeta(x_m)|} \right] \\ \left. \times e^{-ik_p(x-x_m)} \right\}, \quad (2.47)$$

for the respective full elastic medium, where

$$\begin{aligned} k_{3p}^{\alpha(1)} &= \left( \frac{\omega^2}{\alpha^{(1)2}} - k_p^2 \right)^{\frac{1}{2}} \quad \text{for } \operatorname{Im}(k_{3p}^{\alpha(1)}) < 0, \\ k_{3p}^{\beta(1)} &= \left( \frac{\omega^2}{\beta^{(1)2}} - k_p^2 \right)^{\frac{1}{2}} \quad \text{for } \operatorname{Im}(k_{3p}^{\beta(1)}) < 0, \\ k_{3p}^{\alpha(2)} &= \left( \frac{\omega^2}{\alpha^{(2)2}} - k_p^2 \right)^{\frac{1}{2}} \quad \text{for } \operatorname{Im}(k_{3p}^{\alpha(2)}) < 0, \\ k_{3p}^{\beta(2)} &= \left( \frac{\omega^2}{\beta^{(2)2}} - k_p^2 \right)^{\frac{1}{2}} \quad \text{for } \operatorname{Im}(k_{3p}^{\beta(2)}) < 0, \\ k_p &= \frac{2\pi p}{L}. \end{aligned} \quad (2.48)$$

The vertical displacements can be derived in a similar manner. As a result of this formalism, the interface is summed over  $N$  equally spaced points  $\{x_m\}$ , defined by

$$x_m = (m - 1)\Delta x \quad m = 1, 2, \dots, N,$$

where  $\Delta x = \frac{L}{N}$  defines the interface sample interval along the  $x_1$ -coordinate axis. Note that in (2.46) and (2.47) the truncation of the wavenumber series results from the wavenumber periodicity implied by the discretization of the interface at a constant  $\Delta x$  interval. This resulting finite sum over  $k_p$  avoids singularities at the point where each force is applied along the interface.

To solve for the final scattered displacement in both media we require that the displacement and tractions satisfy the proper boundary conditions at the interface. Therefore, combining the horizontal and vertical displacements in both media with the continuity conditions (2.40) we find that

$$A_{scat}^{(1)}(x_r, \zeta(x_r)) - A_{scat}^{(2)}(x_r, \zeta(x_r)) = -A_{source}^{(1)}(x_r, \zeta(x_r)), \quad 1 \leq r \leq 2M + 1, \quad (2.49)$$

where A refers to the normal displacement, normal traction, and tangential traction along the interface for the acoustic-elastic case, and the displacement and traction in the elastic case. A final system of linear equations is formed. The size of the system is  $3N \times 3N$  and  $4N \times 4N$  in the acoustic-elastic and elastic-elastic cases, respectively. Using LU-decomposition techniques, these equations can be stably inverted to give the strength of the fictitious source distributions along the interface. Since each fictitious point along the interface is coupled with another, this technique gives a full scattered solution at all points in both media and includes all multiple scattered waves and interface waves.

To determine a time-domain solution the scattered displacement is solved at multiple frequencies. The final seismogram is then formed by a transformation from the frequency to the time domain. Since this is a periodic medium of length L, source periodicity must be removed. This effect is reduced by adding a small constant imaginary part,  $\omega_I$ , to the frequency domain solution

$$\omega = \omega_R - i\omega_I, \quad (2.50)$$

which essentially attenuates the energy from sources other than the source of interest.

By multiplying the time domain solution by an exponential term

$$\underline{u}(\underline{x}, t) = \underline{u}(\underline{x}, t)_{atten} e^{+w_I t}, \quad (2.51)$$

this attenuation is later removed from the final time domain solution (Bouchon and Aki, 1977).

## 2.5 BIE–DWN Comparison with the Somigliana Approach

In order to verify the accuracy of the Somigliana algorithm, we compare this technique with the Boundary Integral Equation–Discrete Wavenumber (BIE–DWN) approach, presented above. The DWN technique above is formulated in the spatial wavenumber domain and contains periodicity over the integration length,  $L$ . Unfortunately, in the frequency domain, this periodicity often results in Bragg scattering and is difficult to remove from the results because the frequency domain solution is ambiguous in time. Interference from this periodicity appears to exist in the results of Paul and Campillo (1988), where distinct diagonal signatures appear on average reflection coefficients. The Somigliana approach assumes no periodicity and does not suffer from this Bragg scattering.

### 2.5.1 Accuracy of the Somigliana Technique

Interference from periodicity must be modeled directly when comparing the Somigliana and BIE–DWN approaches. Figures 2-4 shows the horizontal and vertical displacements recorded a distance  $\frac{a}{2}$  above one cycle of a sinusoidal interface with a cycle length,  $a = L$ , as shown in Figure 2-3a. The upper elastic medium has a P wave

velocity of  $2000m/s$  and density of 2.0. The remaining velocities are given by the relation  $\alpha^{(2)} = 2\alpha^{(1)}$ ,  $\alpha^{(l)} = \sqrt{3}\beta^{(l)}$  and  $\rho^{(2)} = 1.18\rho^{(1)}$ . DWN periodicity requires the interface to take the form of an infinite sinusoid with wavelength  $a$ . Given a normally incident, monochromatic P wave with wavelength,  $\lambda_o = \frac{a}{3}$ , Figure 2-4a shows the displacements calculated over the interface with a maximum slope of  $30^\circ$ . The displacements calculated with the Somigliana approach over five cycles of the sinusoidal interface clearly converge on the DWN solution. Figure 2-4b shows the displacements recorded over an interface with a maximum  $45^\circ$  slope. The Somigliana solution again converges on the DWN solution, but only after the periodic contribution from eleven cycles of the interface have been included.

This comparison shows that the Somigliana algorithm presented in this study accurately models slopes greater than  $45^\circ$  and accurately includes the large amount of interference resulting from multiple scattering and conversion at the interface. In addition, the Somigliana approach does not suffer from periodic interference and can actually be used to better understand periodic interference in DWN solutions. We examine this periodic contribution.

Although the Somigliana approach does not suffer from periodicity, it does suffer from edge effects due to the finite interval of integration,  $L$ , in the space domain. Before making any further comparisons, we must first identify the length of integration required to remove the edge diffractions from the final solution. Figure 2-5 shows the resulting vertical and horizontal displacement recorded a distance  $\frac{a}{2}$  over a five cycle interface where the seismic data is again recorded over the central cycle, trough to trough. The length of integration beyond the five cycles is then increased by adding an additional flat section as shown in Figure 2-3b. The final solutions are compared with the case in which a total length of fifteen cycles ( $45\lambda_o$ ) is integrated, and the edges of the incident wave are tapered with the aid of the Gaussian beam approximation, which is developed in Chapter 4. This tapering reduces the amplitude at the corners

to essentially zero, removing the diffractive edge effects, while leaving the majority of the incident plane wave undisturbed. The results show that in the worst case scenario, where a wave is incident at the critical angles, a total integration length of at least  $33\lambda_o$  and preferably  $45\lambda_o$  is required to reduce the edge effects. This large length of integration is an upper bound on the required length of integration, since at these critical angles energy can travel for some distance along the interface to reach the receiver array.

### 2.5.2 Periodicity Limitations in DWN Formulation

To understand how the potential contribution of energy from periodicity can affect the frequency domain solution, we now look at the larger incident angles where Bragg scattering is the strongest. Figure 2-3b shows the sinusoidal model where the horizontal and vertical displacements are recorded over the sinusoidally periodic interface with a  $30^\circ$  maximum slope. Figure 2-5 shows the final displacement measured with the DWN approach a distance  $\frac{a}{2}$  above the continuously sinusoidal interface. Shown also is the displacement calculated with the Somigliana approach which includes various degrees of periodicity. Finite sinusoids with five, eleven, and 34 periodic cycles are modeled. To avoid edge effects in the five and eleven cycle cases the interface was integrated out to 15 cycles by attaching a flat layer as shown in Figure 2-3b. It is clear from the results that significant vertical contributions from further than six cycles ( $18\lambda_o$ ) away are affecting the displacements observed over the central basin. The vertical displacement clearly converges by 34 cycles, however, the horizontal displacement does not completely converge. This suggests that diffracted P wave energy from further than 17 cycles ( $51\lambda_o$ ) away are significantly distorting the results. Also apparent is the creation and destruction of peaks in the recorded displacement as more periodic cycles are included. The most dramatic change is observed in the vertical displacement for  $30^\circ$ -incidence, at a normalized distance of 0.12 and 0.25, where a

distinct peak and valley disappear almost completely from the data as more periodic cycles are included.

Even though a sinusoid is a worst case scenario of periodic contributions, it is clear from the examples above that extreme care must be taken when working in the frequency domain with a periodic model. Interference from this periodicity can contribute additional energy to the results, even when the periodic portions of the interface are many wavelengths away. As a result, this periodic energy can be difficult to identify and almost impossible to separate in frequency domain solutions. In the reflection coefficient work of Paul and Campillo (1988) clear diagonal signatures are present, most likely resulting from this Bragg scattering. In addition, it is difficult, if not impossible, to determine whether many signatures on the reflection coefficients are real or the result of periodic contributions. We emphasize that the DWN approach is a time domain approach since periodic contributions can often be removed once the solution is transformed, using multiple frequencies, into the time domain. A time window and periodicity length that does not include contributions from the periodic interface elements can also be chosen, although this approach does increase the computational demand on the algorithm.

We now turn to the time domain, DWN solution to determine the accuracy and efficiency of one of the more commonly used finite-difference approaches.

## **2.6 BIE-DWN Comparison with FD**

In this section, we look at the accuracy and efficiency of using the FD approach to model scattering from irregular interfaces and determine whether they can compete with the boundary integral approaches summarized above. Although the FD algorithm has the advantage of being straightforward to code and implement, we show

that to obtain proper accuracy, the technique can be computationally intensive and too demanding for a statistical analysis used later in this thesis. We choose to study one of the most problematic of the FD boundaries, the acoustic–elastic boundary since the computational requirements for modeling this boundary can give an upper bound on the computational requirements for modeling the less problematic, elastic–elastic interface. Accurate modeling of an acoustic–elastic boundary is also important for direct comparisons with ultrasonic experiments conducted later in this study.

Previous work by Dougherty and Stephen (1991) has shown that the velocity–stress finite–difference technique can kinematically model scattering from sinusoidal ocean bottom topography. The technique’s accuracy was further studied using reciprocity arguments, showing that the introduction of a finite–grid introduces micro–roughness to the a smoothly varying interface, creating additional scattered energy. As a result, grid sampling had to be increased to at least 60 points per wavelength (PPW) to completely remove this numerical noise from a smoothly varying, sinusoidal interface. In this section, we go one step further and directly compare the amplitude and phase of the results generated by the BIE-DWN technique above with the FD approach of Virieux (1986) for a grid sampling of both 15 PPW and 30 PPW. Based on these results we evaluate the accuracy and efficiency of this approach.

### **2.6.1 2–D Finite Difference Formulation**

Modeling a sharp ocean bottom interface that separates two media with widely varying material properties has a number of inherent difficulties. Two difficulties in particular arise with a ‘non-staggered’ finite–difference (FD) scheme, where stress and displacement are calculated at the same points on the finite grid. First, a boundary condition with continuous normal stress and displacement must be applied explicitly. For a non-staggered grid this boundary condition must be set up artificially by the

programmer. These methods suffer because the form of the boundary conditions is difficult to code for rough interfaces, becoming extremely involved. The second difficulty is that large impedance contrasts can cause large instabilities at the interface, rendering many results useless. Stephen (1988a) gives a good summary of these difficulties. Fortunately, by choosing a staggered grid, these two problems are overcome naturally by offsetting horizontal and vertical displacement grids. In this case the internal interfaces are not treated with explicit boundary conditions. Instead, the interface is represented naturally with changes of the elastic parameters, making implementation of the algorithm very straight-forward. The algorithm, thus, requires only four explicit boundary conditions; namely, the four edges of the discrete FD grid (Virieux, 1984; Virieux, 1986).

In this study we extend the stable staggered-grid, FD approach of Virieux (1986) to a second-order, displacement-stress formulation. In this case horizontal and vertical displacements are offset. The tangential stress components are then offset from both the remaining components of the stress tensor and the displacements. We find that this staggered scheme is stable for the acoustic-elastic boundaries encountered in this study. First-order absorbing boundaries developed by Lindman (1975) and later introduced to geophysics by Randall (1989) are implemented along each edge of the rectangular grid. These boundaries give reflected amplitudes less than one percent the incident wave amplitude at all angles less than  $90^\circ$ . Since the Lindman boundary conditions become unstable at an acoustic-elastic interface and the boundary computations for an elastic medium are larger than for an acoustic medium, the elastic medium is completely surrounded by water so that acoustic absorbing boundary can be implemented on all sides of the grid. As a result, the elastic volume with any arbitrary shape is completely submerged in the acoustic medium. Since most of the incident energy is reflected from the upper surface of the aluminum block and very little energy penetrates the block, this approach gives an accurate model of reflection by the upper interface. In general, this algorithm also has the added advantage of

completely modeling the solid models submerged in the our in-house ultrasonic water tank. This algorithm was adapted to our in-house nCUBE2 multiple instruction, multiple data, parallel processor.

## 2.6.2 General Comparison

Comparisons between the DWN and FD techniques were made for a dilatational line source located above the interface, in the fluid. The source time function is a Ricker wavelet pressure pulse which is generated in the time domain. The BIE-DWN technique requires the application of an attenuation factor to the source pulse

$$S(t)_{atten} = e^{-\omega t} S(t), \quad (2.52)$$

where the attenuated function,  $S(t)_{atten}$ , is transformed into the frequency domain and multiplied with the Green's function for the interface of interest. The final solution is transformed back to the time domain and multiplied by the exponential factor introduced at the end of Section 2.4. In the FD approach, the source function is calculated analytically and administered as a function of time at the source location. This is one distinct disadvantage to the FD approach. The boundary integral approaches require the source function only after the Green's function for the medium has been determined. Therefore, many source functions can be convolved with little additional computation. The FD approach requires the source function initially, thus more rigorous techniques must be implemented to introduce another source wavelet.

In both the BIE-DWN and FD techniques, the discretization intervals are chosen as a function of the source wavelength. In the BIE-DWN algorithm the discretization interval of the interface source distribution,  $\Delta x$ , is varied at each frequency for computational efficiency. Tests have shown that the final solution converges to a consistent solution for a sample rate of at least 3 points per incident wavelength.

This is consistent with the work of Bouchon (1985) and Paul and Campillo (1988). As a result, the number of operations increases slightly faster than the cube of the wavelength. In the FD technique, grid size is chosen as a function of the smallest source wavelength. Stability and the reduction of grid dispersion require at least a 10 PPW discretization (Kelly *et al.*, 1976). As the frequency of the source is increased, the computational demand increases with the square of the frequency at each time step, rapidly making higher frequency models more computationally demanding and memory intensive than smaller models. Table I gives a summary of the FD grid parameters for the models studied, while Table II gives the BIE-DWN parameters.

**Table I: Finite difference**

PPW	$\Delta x$ (m)= $\Delta z$ (m)	$\Delta t$ (ms)	Total Range (km)	Total Depth (km)
15	7.50	.57	3.60	3.049
30	3.75	.31	3.60	3.049

**Table II: BIE-DWN**

L (km)	T (s)	$\omega_I$ ( $\frac{rad}{s}$ )	$\Delta x$ (km)
5	2.048	$\frac{2\pi}{L}$	3 PPW

The two different models tested in this section are shown in Figure 2-7. In each case, the fluid is given the properties of water with a P-wave velocity of 1500 m/s and a density of 1.0. The underlying elastic medium has a P-wave velocity of 3100 m/s, a SV-wave velocity of 1600 m/s, and a density of 2.7. The first model tested is the simple horizontal interface shown in Figure 2-7a. This model is used directly to

verify the accuracy of each algorithm, given a 1-D configuration. The second model presented is an ocean bottom with single sinusoid depression (Fig. 2-7b). The basin measures 1 km from edge to edge and is defined by its maximum slope, which we set at  $30^\circ$ . This model is used to verify the accuracy of each algorithm, given a highly irregular deterministic geometry.

In the plane layer case the Ricker wavelet source is given a 0–30 Hz frequency range and 18.5 Hz peak amplitude. Figure 2-8 gives the results calculated with both the BIE-DWN and FD algorithms along with the results of a plane layered reflectivity algorithm which we coded in the form of Müller (1985). In each case, three different receiver positions are shown, corresponding to a normal reflection (Fig. 2-8a), a reflection at the critical angle (Fig. 2-8b), and a wide angle reflection (Fig. 2-8c). Several important points can be made from these results. First, as expected, the BIE-DWN technique is indistinguishable from the reflectivity result in all cases. Second, the FD technique, with only 15 PPW, also models the direct wave, reflected wave, and head wave well in both phase and amplitude. Although the FD wavelet is slightly broader in time, due to a combination of source implementation and grid dispersion, the accuracy is more than sufficient for this study. Figure 2-9 shows the displacement, again measured over a plane interface, but with the interface and receiver array rotated by  $30^\circ$  on the FD grid, so that the acoustic-elastic interface no longer aligns with the grid coordinates. The grid sampling has been increased to 30 PPW to increase the accuracy of the code. In this case we see that the FD grid poorly predicts the displacement at larger offsets. Micro-roughness due to the grid appears to introduce additional phases in the reflected pulse and, in post-critical reflection (Fig 2-9c), larger amplitudes.

In the case of the sinusoidal basin, shown in Figure 2-7, a Ricker wavelet source function with a 0–15 Hz frequency range and 9 Hz peak amplitude is introduced into the fluid. Figures 2-11 and 2-12 compare the results of the BIE-DWN and FD

approaches for a grid sample rate of 15 PPW and 30 PPW. FD snap shots taken at four different times during the waves propagation over the sinusoidal ocean basin, are shown in Figure 2-10. In Figures 2-10ab the incident wave can be seen impinging on the basin, followed at later times by the reflected butterfly pattern in Figures 2-10cd. Referring back to the seismic traces in Figure 2-11, we see that although kinematically the reflected waves match the BIE–DWN results, the FD approach predicts reflected amplitudes which are again too large. Detailed phase variations in the reflected wave also tend to be smoothed over in the FD results. Upon increasing the grid sample interval to 30 PPW, Figure 2-12 shows that the FD results match more closely the BIE–DWN solution. Although amplitudes are still overpredicted, the phases are much closer. In addition, the noise resulting from the micro-roughness of the boundary is greatly reduced. This reduction is most clearly seen when comparing Figures 2-11cd and Figures 2-12cd at later times. Unfortunately, even with this increase in accuracy, the Virieux (1986) scheme still gives poor amplitude and phase information for a smoothly varying fluid–elastic interface for grid sampling as high as 30 PPW. Head wave propagation and wide angle reflections are most influenced by grid microroughness as the amplitude and phase of these waves are continually mispredicted.

Based on these results we conclude that for layers with simple velocity variations, boundary integral approaches are more efficient and accurate for modeling scattering from smoothly varying ocean floor topography. The 60 PPW FD discretization, required to completely remove numerical noise and obtain higher accuracy, results in both large memory requirements and a high computational demand. In fact, a 60 PPW model was not computationally feasible on our nCUBE parallel computer due to memory limitations. As a result, the final convergence of the FD solution to the BIE–DWN solution could not be verified.

## 2.7 Discussion and Conclusions

In this chapter we have developed an efficient boundary integral approach which can rapidly model the complete solution for scattering from an irregular interface separating two homogeneous, elastic media. The Somigliana approach is a direct approach which integrates over singularities explicitly and obtains additional accuracy by including curvature terms in the final solution. We have shown that the results of this Somigliana approach matched the results of the BIE–DWN approach well up to the  $45^\circ$  slopes tested, strongly supporting the accuracy of both algorithms in modeling multiple scattering and wave conversions at an irregular interface. Further comparisons have shown that the BIE–DWN approach does have the limitation of periodicity in the frequency domain, resulting in Bragg scattering effects. These periodic contributions can be difficult to separate from the final solution and can result in the appearance of fictitious peaks in the final displacement recorded over the interface. The Somigliana approach avoids these edge effects, and given its added efficiency, we find it to be a preferable approach for a frequency domain analyses.

Extending the BIE–DWN approach to a fluid–solid interface allowed for direct comparisons with the commonly used staggered grid, velocity–stress, FD algorithm presented by Virieux (1986). Final comparisons showed that the FD results approach the BIE–DWN results only as the grid resolution is increased up to 30 PPW. Absolute convergence on the BIE–DWN solution was difficult to determine directly, as the memory requirement for larger grid sizes was not feasible on our parallel computer. We find that the FD approach does have the ability to couple distributed inhomogeneities and irregular interfaces with little additional effort, but one must consider the inaccuracies in both amplitude and phase which accompany a coarser grid. In addition to these inaccuracies, the FD approach is most suited for a time domain approach, and is difficult to implement for a frequency domain analysis since it requires

a broadband incident wavelet and differencing in time.

Turning to the boundary integral approaches, we conclude that, for a frequency domain analysis, the Somigliana approach is much more efficient than the BIE–DWN approach. Although the 5 points per wavelength sample rate required for the Somigliana approach is finer than the 3 point per wavelength criterion of the BIE–DWN approach, the time gained with the analytic approximations makes this Somigliana algorithm far more efficient than the DWN approach. The computational demand associated with the evaluation of matrix coefficients in the DWN approach increases faster than the cube of the angular frequency (even after numerous steps are taken to optimize the code) on account of a direct sum over interface elements, which includes the rigorous computation of complex exponential functions. The Somigliana approach, on the other hand, uses simple polynomial expansions and mathematically avoids a direct sum over interface elements, reducing the computational time of the algorithm almost completely to the time required to solve the matrix equation. Utilizing the biconjugate gradient approach, the time for solving the system of linear equations can be reduced to almost a frequency squared dependence, making the direct Somigliana approach far more efficient than the DWN approach.

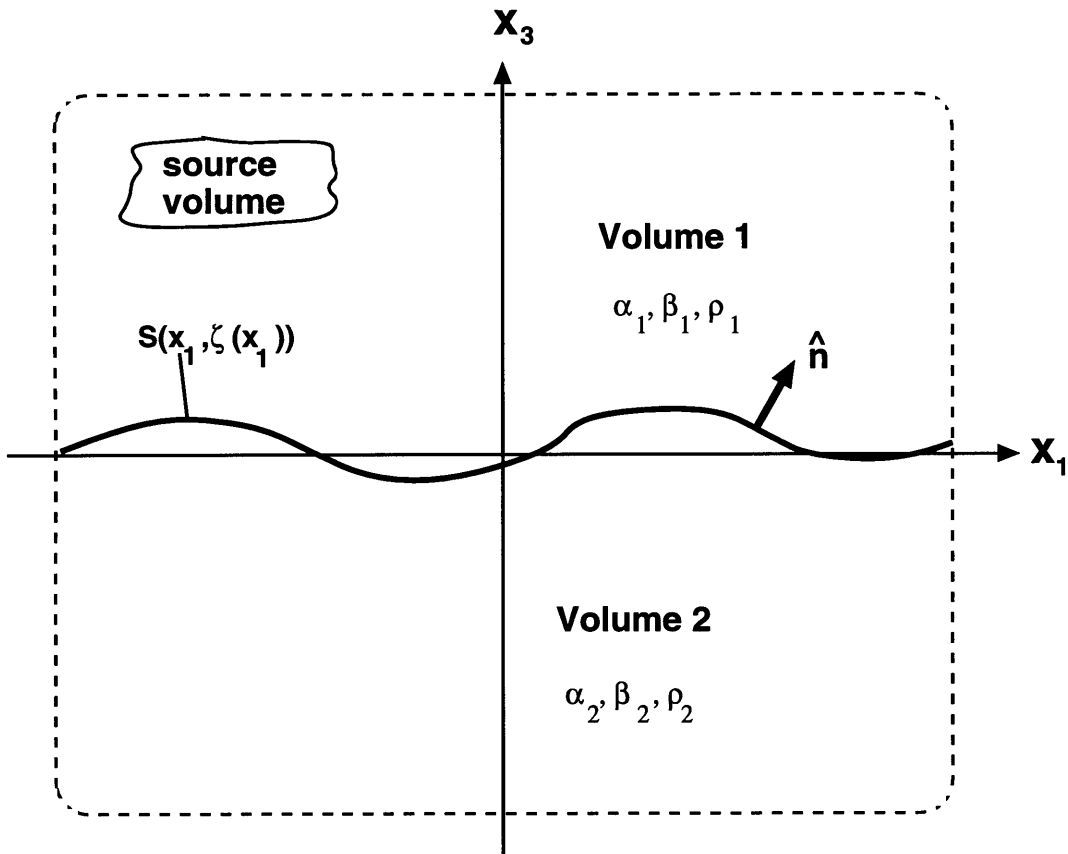


Figure 2-1: Geometry used to develop a surface integral representation of the scattered displacement, resulting when both a P and SV wave are incident on the irregular surface,  $S(x'_1, \zeta(x'_1))$ . We assume that no energy is contributed from the dashed surfaces.

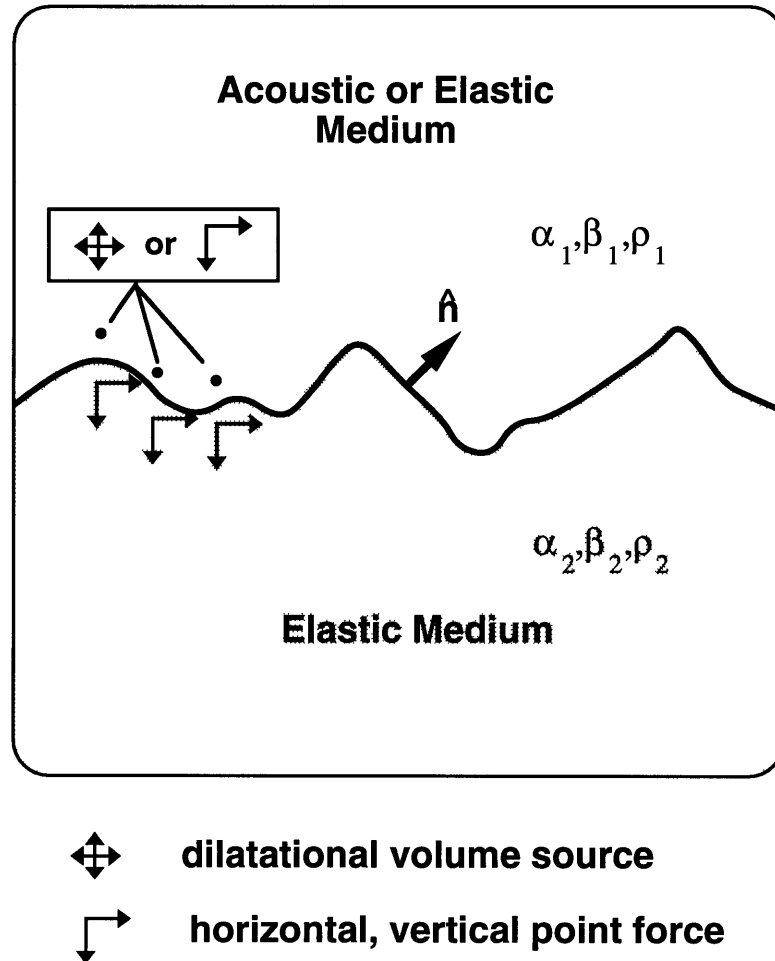


Figure 2-2: The general model configuration used to formulate the BIE-DWN algorithm. The source is positioned in either medium and a distribution of secondary sources is placed along the interface in both media. The secondary line sources are dilatational in the fluid, and horizontal and vertical point forces in the corresponding elastic medium. Boundary conditions are then used to determine the strength of these sources.

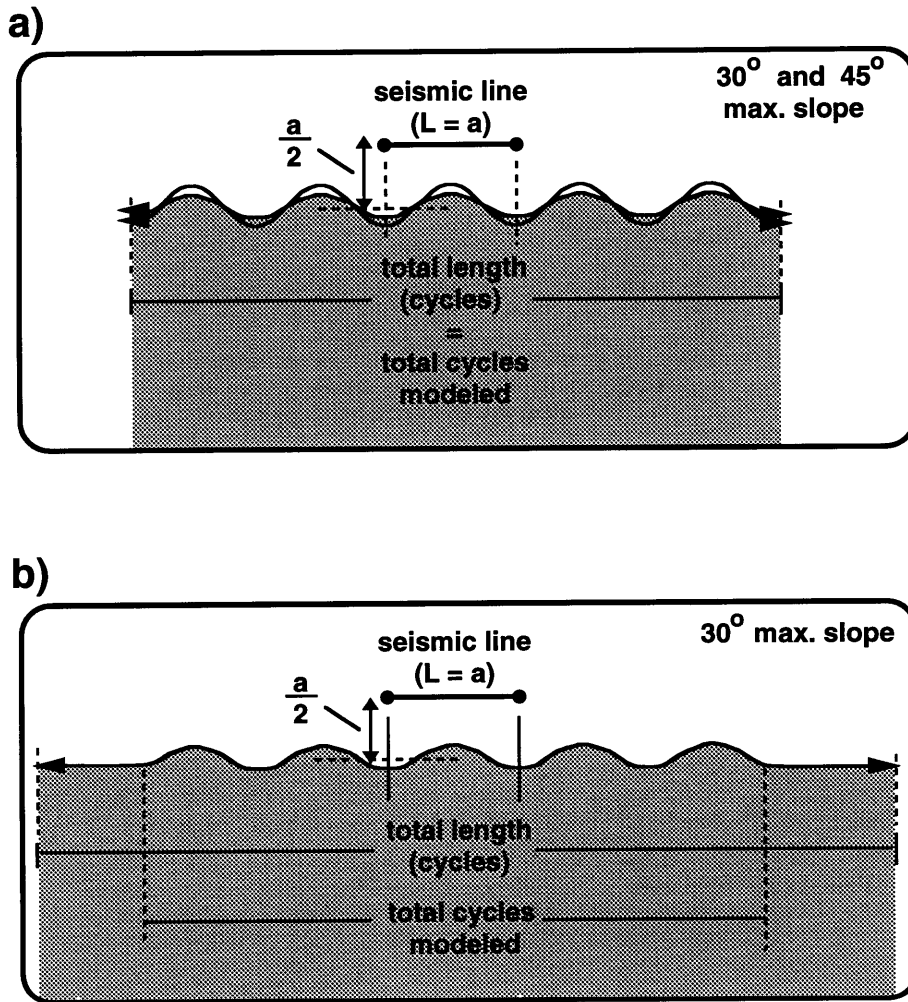


Figure 2-3: Shown are the periodic sinusoidal models utilized to (a) verify the accuracy of the Somigliana approach and to (b) investigate the contribution from periodic effects in the BIE-DWN approach. The displacement is calculated a distance  $\frac{a}{2}$  above the central sinusoid of the interface.

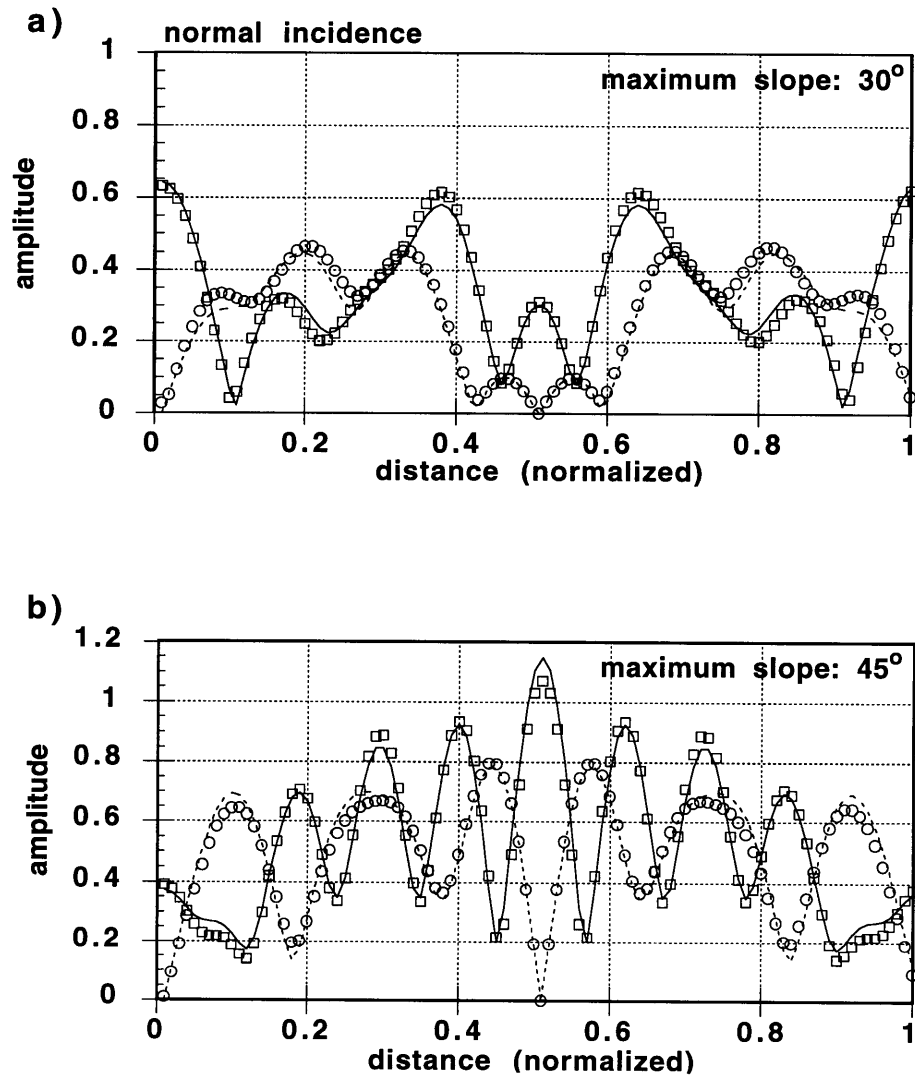


Figure 2-4: Comparison of the displacement measured over an elastic interface with the sine wave geometry given a normally incident plane wave. Interfaces with a maximum slope of (a)  $30^\circ$  and (b)  $45^\circ$  are shown. The horizontal (dashed line) and vertical displacement (solid line) calculated with the DWN technique are compared to the horizontal (circle) and vertical displacements (square) calculated with the Somigliana approach.

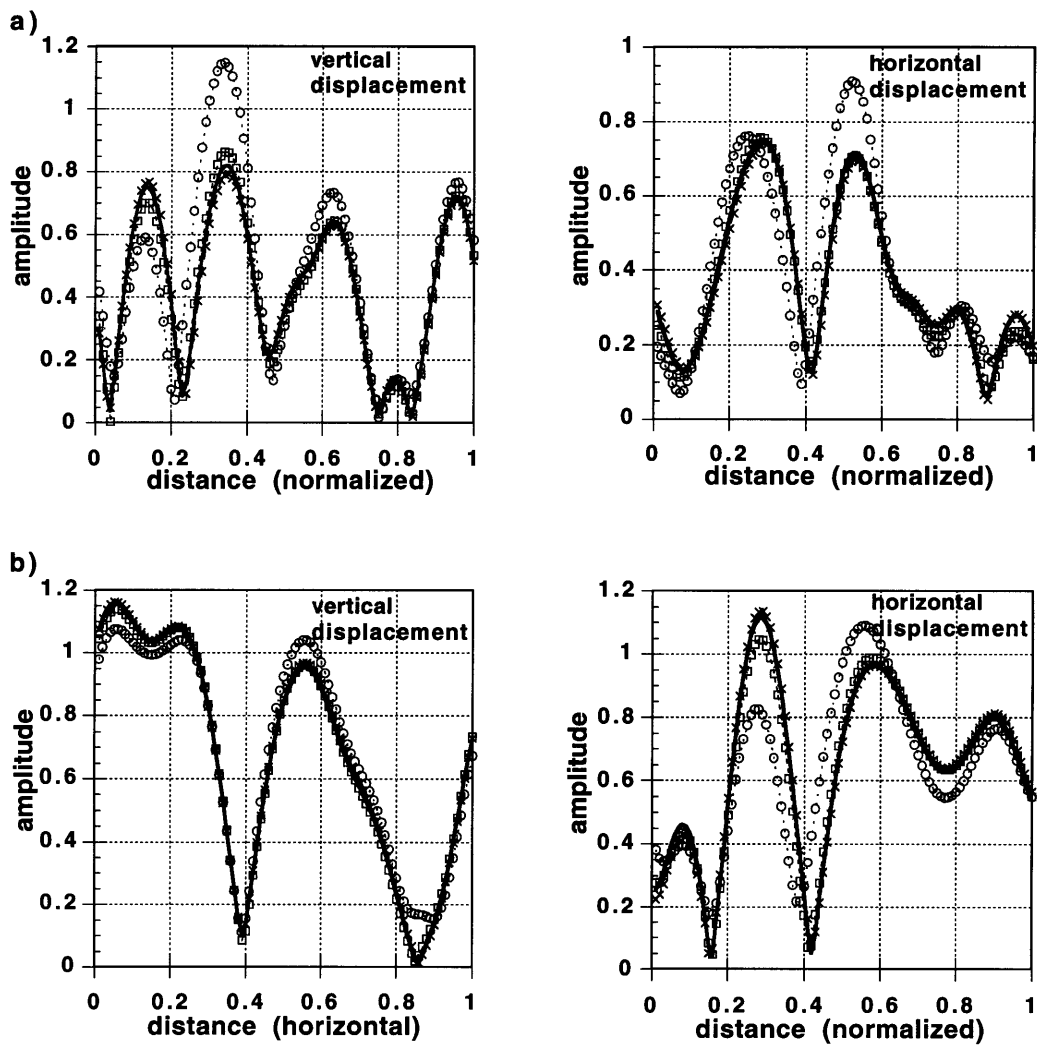


Figure 2-5: Comparisons of vertical and horizontal displacements calculated over a five-cycle sinusoidal interface with a maximum slope of  $30^\circ$  using the Somigliana approach. A plane wave with  $\lambda_o = \frac{8}{3}$  is incident at both (a)  $30^\circ$  and (b)  $60^\circ$ . Each curve corresponds to an overall integration length,  $L$ , of five (circle), eleven (square), and fifteen (cross) cycles. The case of a damped incident plane (solid line) wave is also shown.

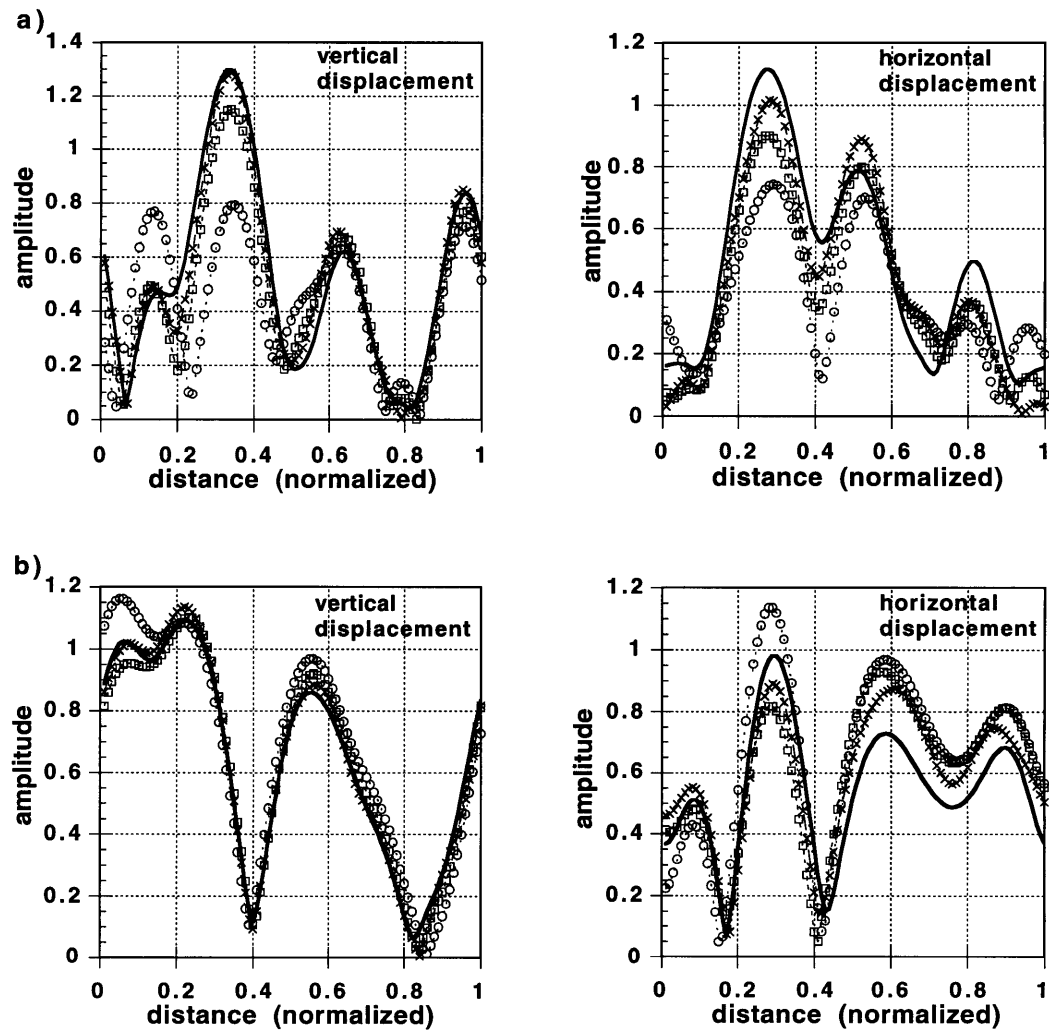


Figure 2-6: Comparison of vertical and horizontal displacements calculated over a sinusoidal interface with a maximum slope of  $30^\circ$  using both DWN (solid line) and Somigliana (symbols) approaches. A plane wave with  $\lambda = \frac{a}{2}$  is incident at both (a)  $30^\circ$  incidence and (b)  $60^\circ$  incidence. The displacements calculated with the Somigliana approach are shown for five (circles), eleven (squares), and 34 (crosses) irregularities. The DWN approach assumes an infinite number of irregularities.

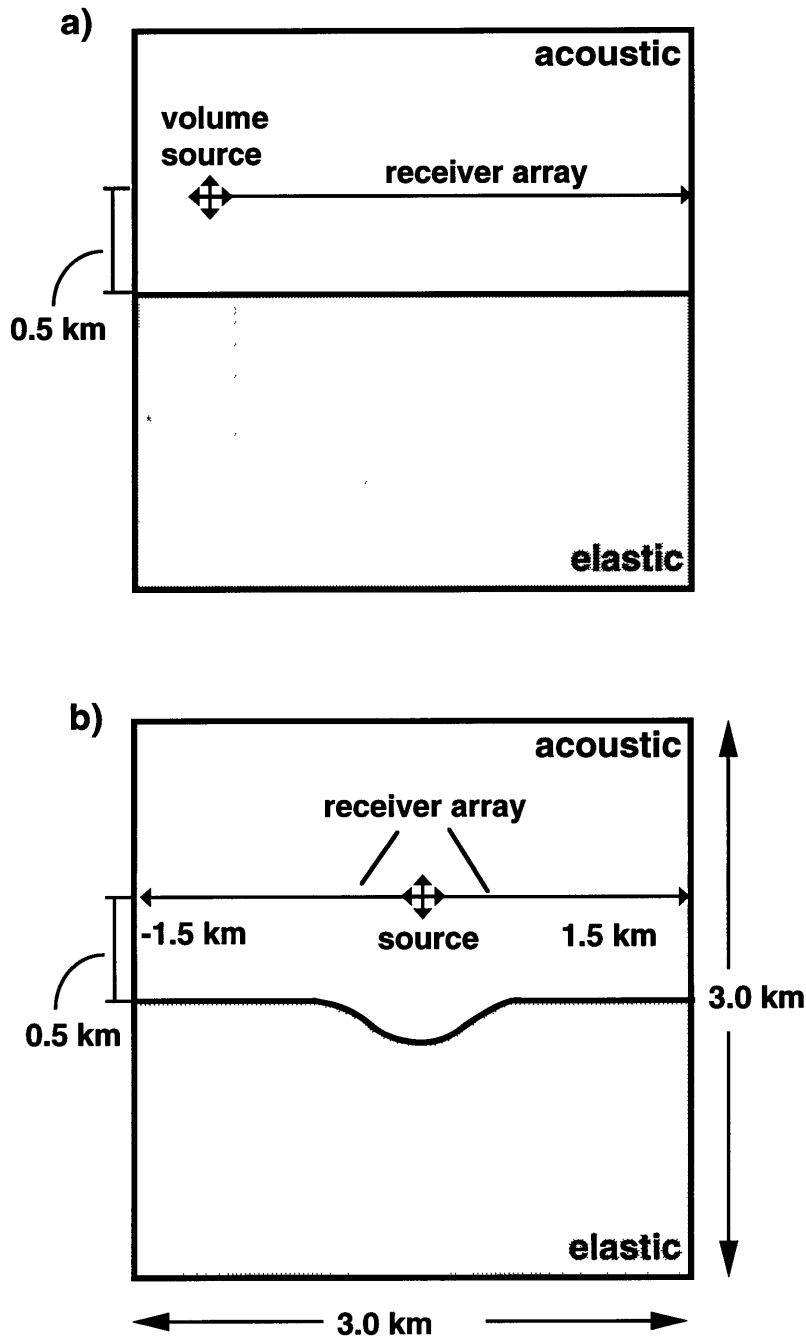


Figure 2-7: The two ocean bottom models used for comparisons between FD and BIE-DWN approaches in the time domain where the source and receiver array are both located 0.5 km above the plane portions of the interface. The first model (a) is a plane interface. The second model (b) is an ocean basin model having a single cycle of a sinusoid with a maximum slope of 30°.

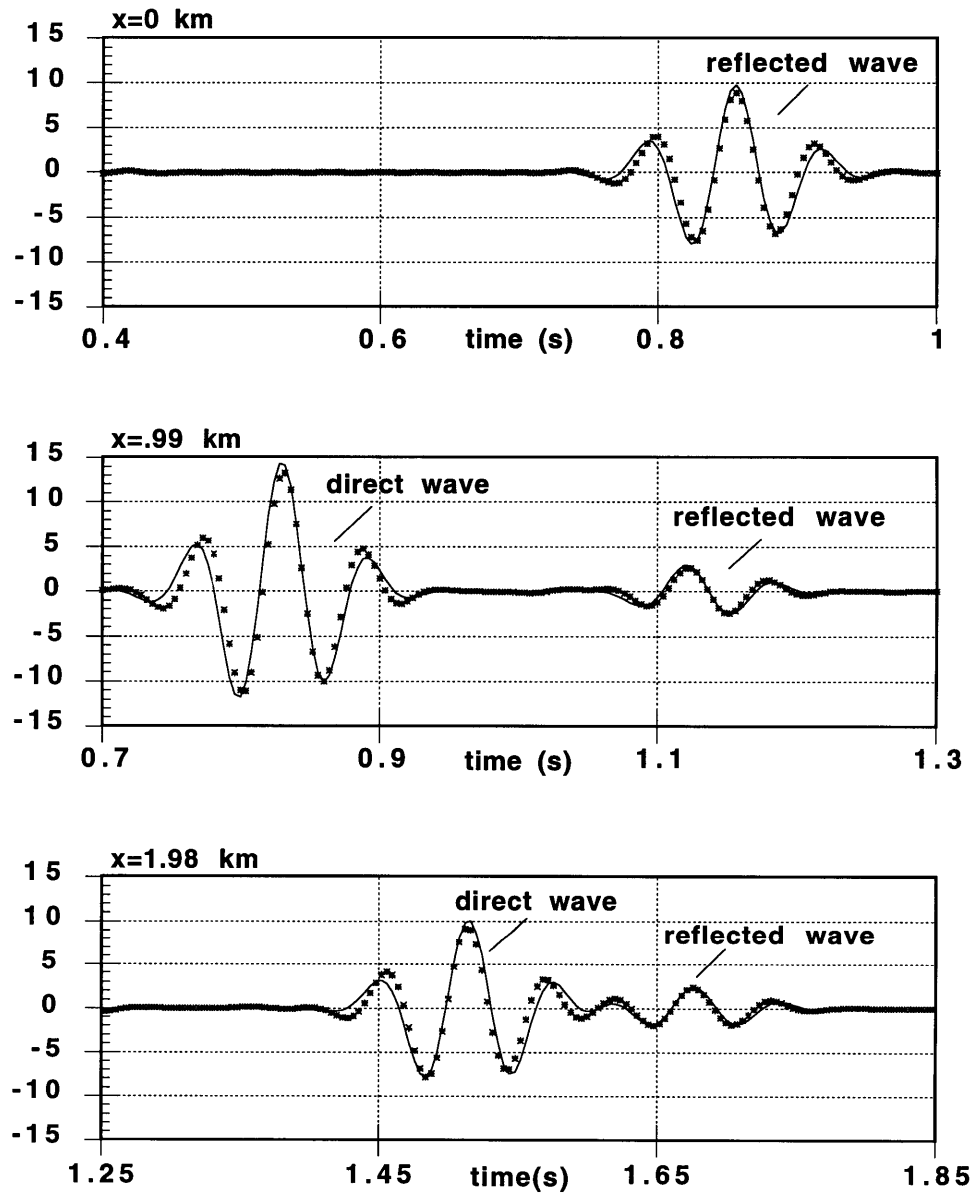


Figure 2-8: Comparison of displacements calculated with the FD (solid line), BIE-DWN (cross), and reflectivity (plus) techniques over the plane acoustic-elastic interface. In this case, the BIE-DWN results fall directly on the reflectivity results.

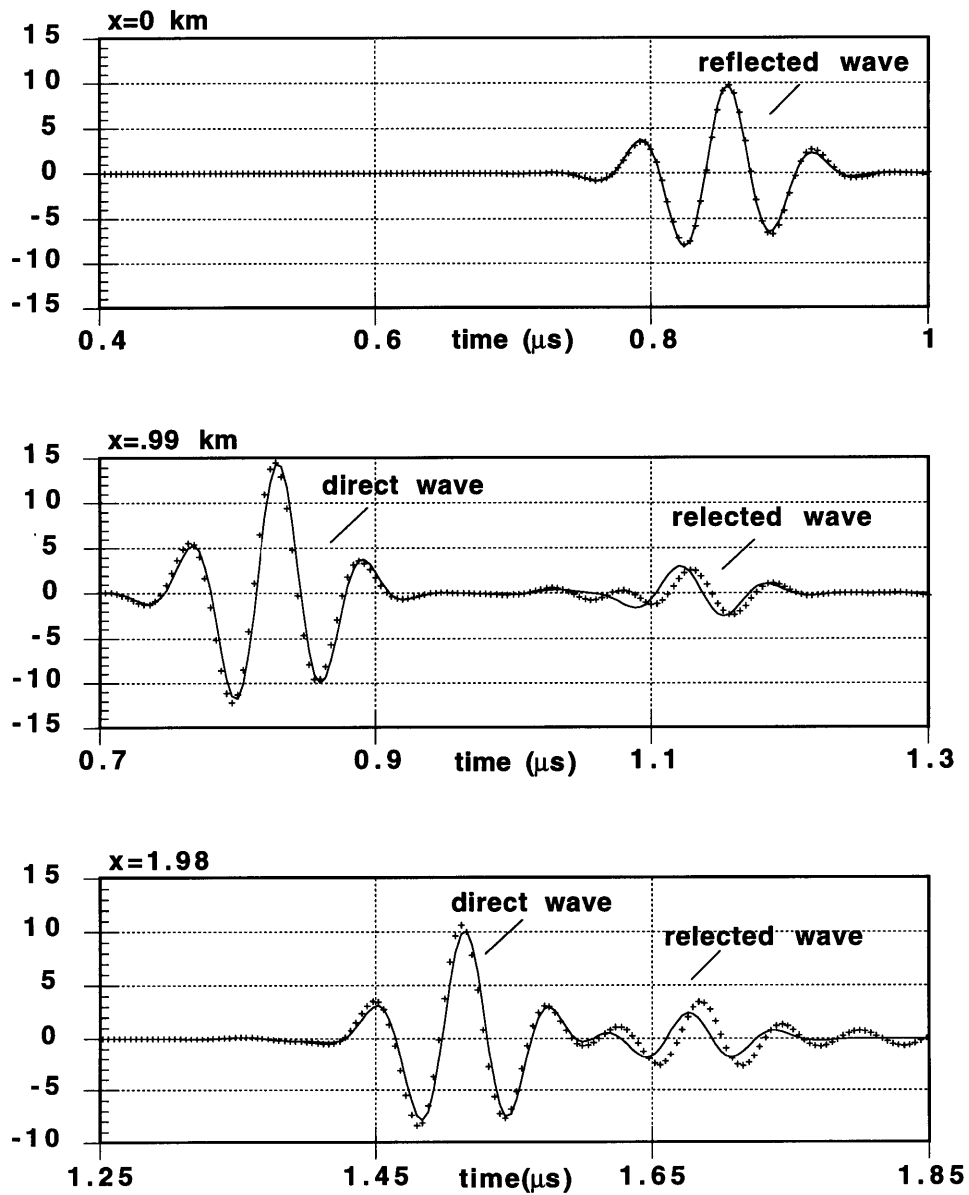
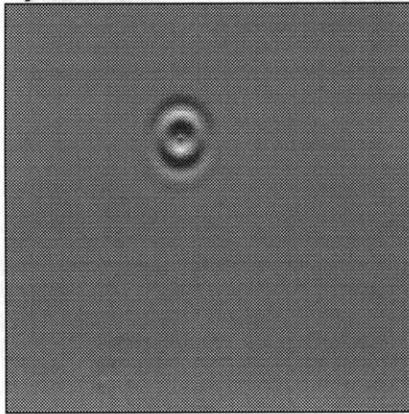
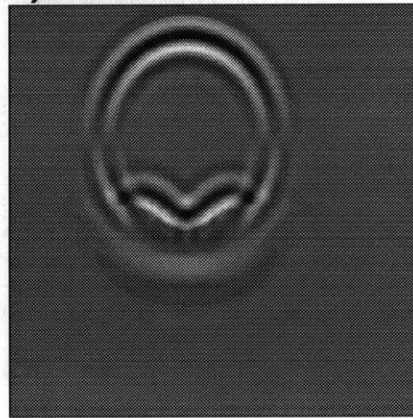


Figure 2-9: Comparison of displacements calculated with the FD (cross) and reflectivity (solid line) techniques over the plane acoustic-elastic interface which is rotated by  $30^\circ$  on the finite-difference grid.

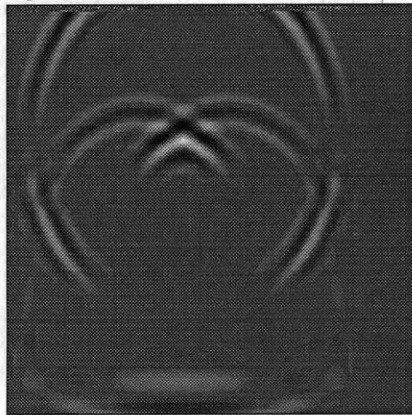
**a)  $t=0.41\text{ s}$**



**b)  $t=0.82\text{ s}$**



**c)  $t=1.23\text{ s}$**



**d)  $t=1.64\text{ s}$**

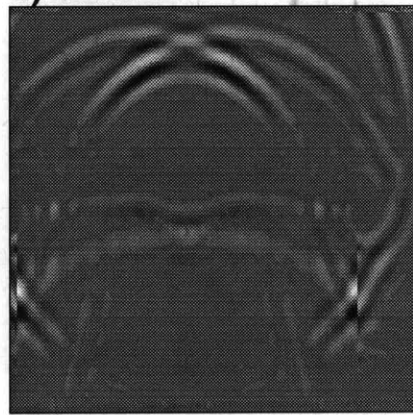


Figure 2-10: Grayscale plots showing the vertical displacement recorded at four different times for a volume source positioned above the ocean basin model.

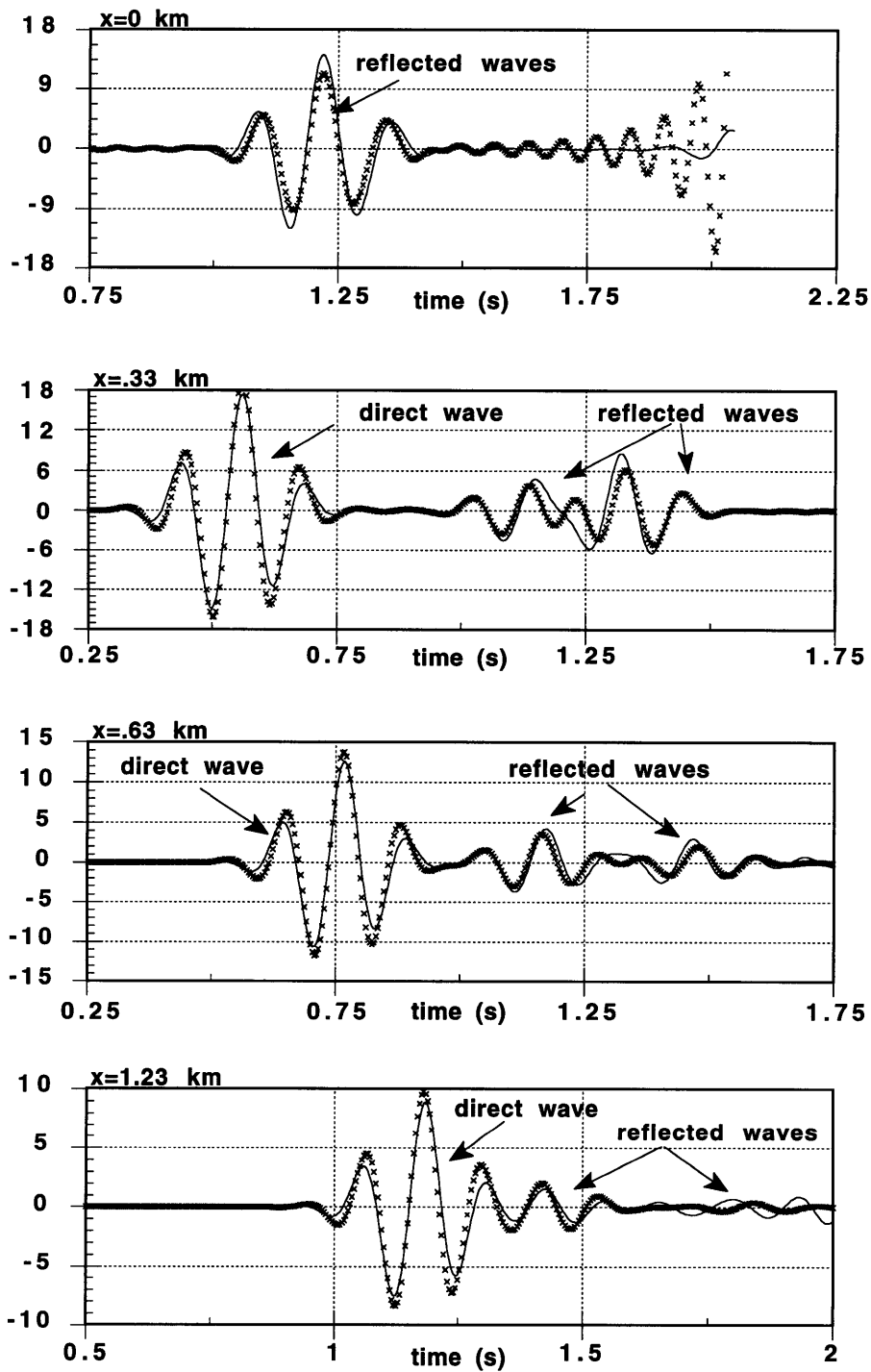


Figure 2-11: A comparison of the pressure calculated over the sinusoidal ocean basin. Both FD results (solid line) calculated on a grid with a discretization interval of 15 PPW and BIE-DWN results (crosses) are shown at four different distances from the source. Note that the exponentially growing sinusoidal noise in the DWN solution at  $x=0$  km is simply an amplification of noise which results from the large direct wave at this receiver.

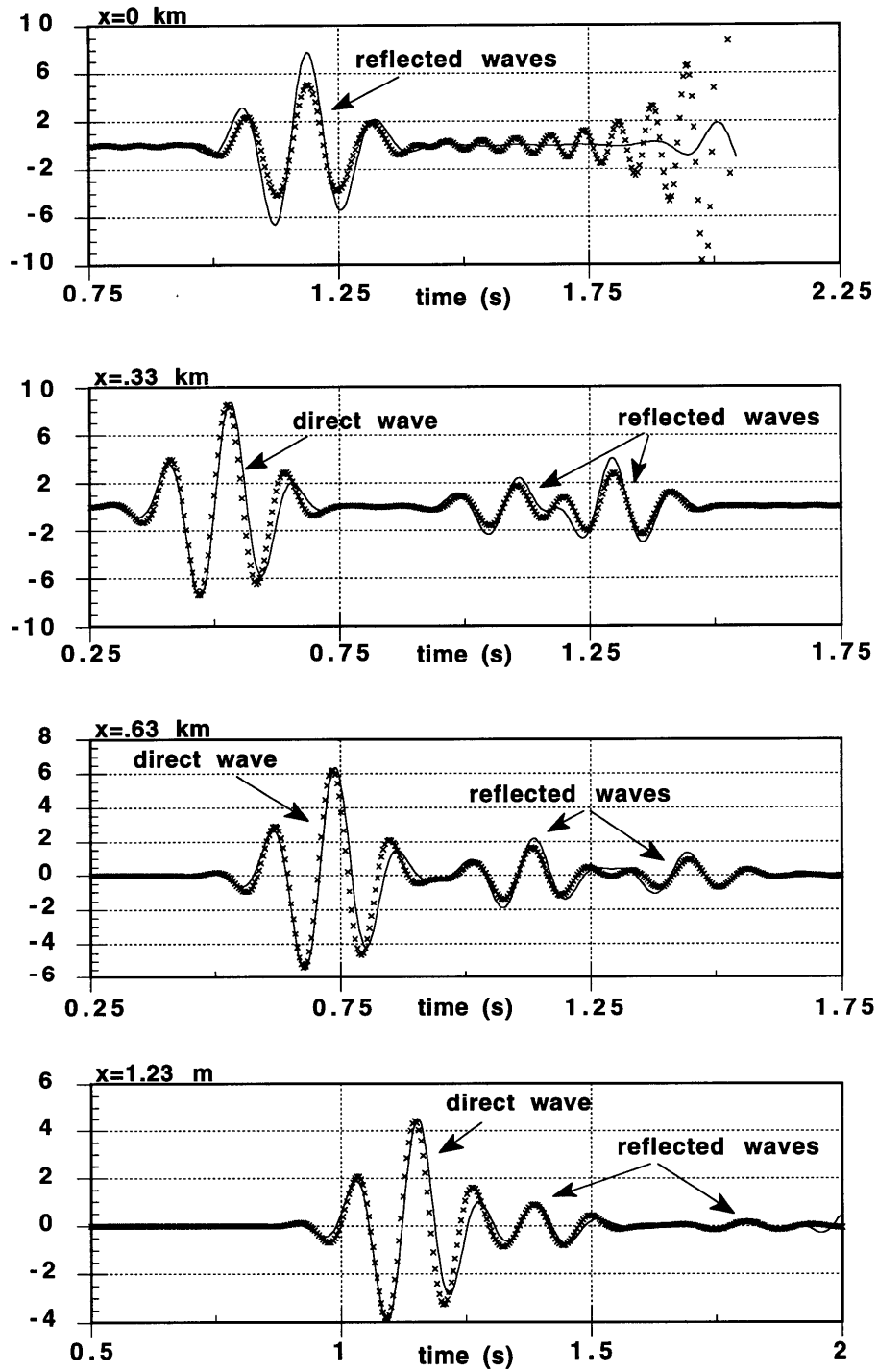


Figure 2-12: Similar to Figure 2-11, except with a sampling of 30 PPW.

## Chapter 3

# Enhanced Backscattering of Seismic Waves from a Highly Irregular, Random Interface: SH–Case

### 3.1 Summary

We begin by looking at a simpler case of seismic scattering. In this chapter we study the scattering of SH waves from a highly irregular random interface between two elastic half-spaces to determine whether the “enhanced backscattering” observed in optics can also occur for seismic waves. We approach this simplified problem with the extinction theorem utilized in Chapter 2. Combining the elastic representation theorem with the extinction theorem, we develop a surface integral representation of the total scattered displacement. The scattered displacement is then expressed

quantitatively in terms of a differential reflection coefficient (DRC). Statistically, the incoherent and coherent contributions to a mean DRC are calculated by averaging over many realizations of a randomly irregular surface. We find that the incoherent component forms the major contribution to the total mean DRC, clearly showing an “enhanced backscattered” or “retroreflective” peak which results directly from multiple scattering. The character of the peak varies strongly as a function of impedance contrast, incident angle, and *rms* slope of the interface. In each case, the peak height decreases dramatically with the decrease in impedance contrast and with the increase in incident angle. In addition, the longer the wavelength of the incident wave relative to the correlation length of the interface, the wider the retroreflective peak. Overall, this study provides a more intuitive yet quantitative understanding of multiple scattering both as a function of frequency and interface properties.

## 3.2 Introduction

Irregular interfaces may be characteristic of many boundaries in the Earth, such as the ocean floor and surface terrain along with deeper boundaries such as the Moho discontinuity and the core-mantle boundary. However, the general understanding of the scattering of seismic waves from the more highly irregular boundaries is limited because of both theoretical and experimental difficulties. The theoretical difficulty arises from surface interactions which result in nonlinear mathematical formulations and computationally intensive algorithms. Experimentally, this nonlinearity manifests itself as multiple scattering. This scattering is difficult to analyze in a simple fashion because scattered waves can travel along many different complex paths. Most research, therefore, has focused on detailed investigations of very specific interface structures. For example, Axilrod and Ferguson (1990) studied SH wave scattering from a sinusoidal grating using various discrete wavenumber techniques. Kawase

(1988) used boundary elements to look at the scattering of surface waves in a semicircular canyon. Bouchon *et al.* (1989) used discrete wavenumber to look at scattering of SH waves between layers in “synclines” and “anticlines”. Schultz and Toksöz (1991) used finite difference and laboratory model tank experiments to look at scattering from randomly distributed grooves.

Although these studies help us to understand scattering from the respective models, we must still determine the mechanisms involved in scattering from highly irregular interfaces in general. The statistical approach, currently used in optics, provides a good method for the study of general scattering mechanisms. Using this approach it has been found that when light scatters from a randomly rough interface, a large intensity of energy is directed back towards the source in the nonspecular component of the scattered field. This enhanced backscattering, which appears to be a multiple scattering effect, varies strongly in magnitude and angular width both as a function of the material and the interface properties.

In optics, experimental studies were used initially to study the phenomenon of enhanced backscattering. Statistical averaging is accomplished using a laser beam which spatially illuminates a surface containing hundreds of irregularities. The scattered waves from each irregularity smear together, forming a rough average of the total scattered field. Measuring this average scattered field at various angles from the incident point gives a mean scattered reflection coefficient. The most interesting result has been the large scattered intensity found in the direction of the incident beam (O’Donnell and Mendez, 1987; Dainty *et al.*, 1990; Mendez and O’Donnell, 1990). Ishimaru (1990) gives a good summary of the occurrences of this retroreflectance in optics and acoustics. Familiar examples include the bright ring viewed around the shadow of one’s head on grass or other vegetation, and “glory”, the bright halo which appears surrounding the shadow of an airplane viewed on an underlying cloud from an observer in the plane. John (1991) gives a good review of the more general role

that this coherent backscattering plays in electromagnetism.

Recently, efficient numerical techniques have been developed to compute the thousands of models necessary for a statistical average over an ensemble of surface realizations. Maradudin *et al.* (1990a) obtained the scattered field using Green's second integral theorem and a narrow beam source approximation. They were able to achieve high efficiency by separating the surface into small elements and approximating analytically the surface integral over each element. This approach replaces numerical integration with an analytical approximation along the surface. Using this technique to average over many surface realizations, Maradudin *et al.* (1990a) produced numerical results that closely matched experimental data.

In Chapter 2 we generalized the approach of Maradudin *et al.* (1990a) to the general seismic case of P–SV scattering from an elastic–elastic interface. In this chapter, we implement this approach to statistically study the scattering of SH waves. We use the elastic representation theorem to show that the SH case in elasticity is similar to the p-polarization case in optics. Using this technique to average over an ensemble of realizations of a randomly irregular surface, we determine the mean differential reflection coefficient (DRC) for interfaces with various statistical characteristics. We then discuss how interface slope, impedance contrast, incident wavelength relative to irregularity size, and incident wave angle affect an SH wave which interacts with and scatters from a highly irregular interface.

### 3.3 Theory

Consider the simplest case of two homogeneous, isotropic, elastic half-spaces in welded contact along an irregular interface, as shown in Figure 3-1. We assume a two-dimensional geometry with the properties invariant in the  $x_2$  direction. If no volume

sources are present in either half-space and the incident SH wave has displacement in the  $x_2$  direction, the total displacement satisfies the wave equation

$$\left(\frac{\partial^2}{\partial x_1^2} + \frac{\partial^2}{\partial x_3^2} + \frac{\omega^2}{c^{(l)2}}\right)u_2^{(l)}(\underline{x}|\omega) = 0, \quad (3.1)$$

in both media, where  $\underline{x} = (x_1, 0, x_3)$ ,  $c^{(l)}$  represents the velocity in the  $l$ th medium ( $l = 1, 2$ ), and  $\omega$  is the angular frequency. Applying the representation theorem (e.g. Aki and Richards, 1980) to this SH polarization case the displacement in both half-spaces can be expressed in the form of a surface integral

$$H[i]u_2^{(l)}(\underline{x}|\omega) = u_2^{(l)}(\underline{x}|\omega)_{incid} - (-1)^i \int_S dS(\underline{x}') [u_2^{(l)}(\underline{x}'|\omega) \mu^{(l)} \frac{\partial G_{22}^{(l)}(\underline{x}; \underline{x}'|\omega)}{\partial n} - G_{22}^{(l)}(\underline{x}; \underline{x}'|\omega) T_2^{(l)}(\underline{x}'|\omega)], \quad (3.2)$$

where  $G_{22}^{(l)}(\underline{x}; \underline{x}'|\omega)$  is the Green's function for the medium,  $T_i^{(l)}(\underline{x}|\omega)$  is the traction in the  $x_i$ -direction along the surface  $S(\underline{x})$ ,  $\mu^{(l)}$  is the rigidity, and  $H[i]$  is a function which takes a value of 1 or 0 depending on whether the point  $\underline{x}$  lies inside or outside the volume of interest, i, respectively. Requiring the Green's function to satisfy

$$\left(\frac{\partial^2}{\partial x_1^2} + \frac{\partial^2}{\partial x_3^2} + \frac{\omega^2}{c^{(l)2}}\right)G_{22}^{(l)}(\underline{x}; \underline{x}'|\omega) = -\mu^{(l)-1} \delta(x_1 - x_1') \delta(x_3 - x_3') \quad (3.3)$$

in each medium gives

$$G_{22}^{(l)}(\underline{x}; \underline{x}'|\omega) = \frac{i}{4\pi\mu^{(l)}} \int_{-\infty}^{\infty} dk \frac{e^{ik(x_1-x_1') + ik_3^{(l)}|x_3-x_3'|}}{k_3^{(l)}}, \quad (3.4)$$

where

$$k_3^{(l)} = \left(\frac{\omega^2}{c^{(l)2}} - k^2\right)^{\frac{1}{2}}, \quad \text{where } \text{Im}(k_3^{(l)}) > 0.$$

Equation (3.4) can also be written as

$$G_{22}^{(l)}(\underline{x}; \underline{x}'|\omega) = \frac{i}{4\mu^{(l)}} H_o^{(1)}\left\{\frac{\omega}{c^{(l)}} [(x_1 - x_1')^2 + (x_3 - x_3')^2]^{\frac{1}{2}}\right\}, \quad (3.5)$$

where  $H_o^{(1)}\left(\frac{\omega}{c^{(l)}}r\right)$  represents the zero order Hankel function of type 1, which can be calculated efficiently through polynomial approximations (Abramowitz and Stegun, 1964).

Incorporating the technique used by Maradudin *et al.* (1990a), we determine the scattered field resulting from the interaction of an incident SH wave with an irregular boundary. This involves combining the extinction theorem (Chew, 1990) with the representation theorem of equation (3.2). Placing the incident wave in the upper medium and concentrating on the reflected waves, we select the upper medium as the volume of interest, as shown in Figure 3-1. Similar to Huygens' principle, the extinction theorem now states that the sum of all sources along the surface separating the two half-spaces gives the displacement in the upper medium

$$u_2^{(1)}(\underline{x}) = u_2^{(1)}(\underline{x})_{incid} + \int_S dS(\underline{x}') [u_2^{(1)}(\underline{x}') \mu^{(1)} \frac{\partial G_{22}^{(1)}(\underline{x}; \underline{x}')}{\partial n} - G_{22}^{(1)}(\underline{x}; \underline{x}') T_2^{(1)}(\underline{x}')], \quad (3.6)$$

and

$$0 = - \int_S dS(\underline{x}') [u_2^{(2)}(\underline{x}') \mu^{(2)} \frac{\partial G_{22}^{(2)}(\underline{x}; \underline{x}')}{\partial n} - G_{22}^{(2)}(\underline{x}; \underline{x}') T_2^{(2)}(\underline{x}')],$$

where  $x_3 > S(\underline{x}')$  and the angular frequency,  $\omega$ , is implicit. Equation (3.6) contains four unknown functions and two integral equations.

Let the surface,  $S(\underline{x})$ , be described by the height function,  $x_3 = \zeta(x_1)$ . The normal derivative can now be expanded in the form

$$\frac{\partial}{\partial n} = ((\zeta'(x_1))^2 + 1)^{-\frac{1}{2}} [-\zeta'(x_1) \frac{\partial}{\partial x_1} + \frac{\partial}{\partial x_3}] \quad (3.7)$$

for this two-dimensional case. The two boundary conditions valid along this surface are

$$\begin{aligned} \frac{\partial u_2^{(1)}(\underline{x})}{\partial n} \Big|_{x_3=\zeta(x_1)} &= \frac{\mu^{(2)}}{\mu^{(1)}} \frac{\partial u_2^{(2)}(\underline{x})}{\partial n} \Big|_{x_3=\zeta(x_1)}, \\ u_2^{(1)}(\underline{x}) \Big|_{x_3=\zeta(x_1)} &= u_2^{(2)}(\underline{x}) \Big|_{x_3=\zeta(x_1)}. \end{aligned} \quad (3.8)$$

Substituting these conditions into the integral equations (3.6) leaves two equations and two unknown functions

$$\begin{aligned} u_2^{(1)}(\underline{x}) &= u_2^{(1)}(\underline{x})_{incid} \\ &+ \int_{-\infty}^{\infty} dx_1' [D(\underline{x}') \mu^{(1)} (-\zeta'(x_1') \frac{\partial}{\partial x_1'} + \frac{\partial}{\partial x_3'}) G_{22}^{(1)}(\underline{x}; \underline{x}') - \mu^{(1)} G_{22}^{(1)}(\underline{x}; \underline{x}') T(\underline{x}')], \\ 0 &= - \int_{-\infty}^{\infty} dx_1' [D(\underline{x}') \mu^{(2)} (-\zeta'(x_1') \frac{\partial}{\partial x_1'} + \frac{\partial}{\partial x_3'}) G_{22}^{(2)}(\underline{x}; \underline{x}') - \mu^{(2)} G_{22}^{(2)}(\underline{x}; \underline{x}') \frac{\mu^{(1)}}{\mu^{(2)}} T(\underline{x}')], \end{aligned} \quad (3.9)$$

where the two unknown functions are

$$D(\underline{x}) = u_2^{(1)}(\underline{x})|_{x_3=\zeta(x_1)}, \quad (3.10)$$

$$T(\underline{x}) = (-\zeta'(x_1)\frac{\partial}{\partial x_1} + \frac{\partial}{\partial x_3})u_2^{(1)}(\underline{x})|_{x_3=\zeta(x_1)},$$

and  $\underline{x}' = (x_1', \zeta(x_1'))$ . The first integral on the right side of (3.9) represents energy scattered into the upper half-space. The scattered displacement can now be expressed completely in the upper volume by combining (3.4) and (3.9) to give

$$u_2^{(1)}(\underline{x})_{scat} = \int_{-\infty}^{\infty} \frac{dk}{2\pi} R_p(k\omega) e^{ikx_1 + ik_3^{(1)}x_3}, \quad (3.11)$$

with the scattering coefficient

$$R_p(k\omega) = \frac{i}{2k_3^{(1)}} \int_{-\infty}^{\infty} dx_1' e^{-ikx_1' - ik_3^{(1)}\zeta(x_1')} \{i[k\zeta'(x_1') - k_3^{(1)}]D(x_1') - T(x_1')\},$$

where we have rearranged the order of integration. Given a specific incident wave, equation (3.11) expresses the scattered field everywhere in the upper medium.

We now implement a Gaussian beam approximation for the incident wave using the notation shown in Figure 3-2 (Maradudin, 1990a). This narrow beam allows the excitation of only a small segment of the irregular surface, reducing the interval of numerical integration. Since the integration over the surface in (3.9) must be taken between finite limits in the spatial domain, as described in section 3.3.1, this beam minimizes diffractions from the edges of the surface (which would otherwise result in the case of a plane wave). The Gaussian beam approximation can be written as

$$u_2^{(1)}(\underline{x})_{incid} \approx e^{i(\frac{\omega}{c^{(1)}})(x_1 \sin \theta_0 - x_3 \cos \theta_0)} [1 + W(\underline{x})] e^{-((x_1 \cos \theta_0 + x_3 \sin \theta_0)/w)^2}, \quad (3.12)$$

with

$$W(\underline{x}) = \frac{c^{(1)2}}{\omega^2 w^2} \left[ \frac{2}{w^2} (x_1 \cos \theta_0 + x_3 \sin \theta_0)^2 - 1 \right],$$

where  $\theta_0$  is the incident angle of the beam and  $w$  is the half-width of the Gaussian beam. Equation (3.12) is a good approximate solution to the wave equation provided

the condition  $\omega w/2c^{(1)} \gg 1$ , is satisfied. The condition  $\omega w/2c^{(1)} > 10$  is usually sufficient. If  $\omega w/2c^{(1)} < 10$  diffractive effects of the wave begin to spread the beam spatially and the beam approximation breaks down. This condition limits the models which we study in the next section to this higher frequency range.

To quantitatively express the scattered displacement, we turn to the differential reflection coefficient (DRC), which gives the average power flux across a unit angle relative to the average power of the incident wave. In the SH polarization case, the rate of energy flow across the plane orthogonal to the  $x_3$ -coordinate axis (horizontal plane) can be written as:

$$P_3 = -i\omega\mu^{(1)}u_{2,3}^{(1)}u_2^{(1)*}, \quad (3.13)$$

where the star represents the complex conjugate. Integrating the power of the incident beam over the horizontal plane at  $x_3 = 0$ , the time averaged power flux incident on this surface is

$$\bar{P}_{incid} = \frac{\sqrt{\pi}wL_2\mu^{(1)}\omega^2}{\sqrt{2}c^{(1)}} \left[1 - \frac{c^{(1)2}}{2\omega^2w^2}(1 + 2\tan^2\theta_0)\right], \quad (3.14)$$

where  $L_2$  is the integrated segment in the  $x_2$ -direction. Similarly, integrating over the scattered power using (3.11), the average scattered power flux takes the form

$$\bar{P}_{scat} = \int_{-\frac{\pi}{2}}^{\frac{\pi}{2}} d\theta_s P_p(\theta_s), \quad (3.15)$$

with

$$P_p(\theta_s) = L_2 \frac{\omega\mu^{(1)}}{8\pi} |r_p(\theta_s)|^2, \quad (3.16)$$

and

$$\begin{aligned} r_p(\theta_s) &= \int_{-\infty}^{\infty} dx'_1 e^{-i(\frac{\omega}{c^{(1)}})[x'_1 \sin\theta_s + \zeta(x'_1)\cos\theta_s]} \\ &\times \left\{ i\left(\frac{\omega}{c^{(1)}}\right)[\zeta'(x'_1)\sin\theta_s - \cos\theta_s]D(x'_1) - T(x'_1) \right\}. \end{aligned}$$

The differential reflection coefficient can now be expressed as

$$\frac{\partial R_p}{\partial\theta_s} = \frac{P_p(\theta_s)}{\bar{P}_{incid}} \quad (3.17)$$

$$= K_0 |r_p(\theta_s)|^2,$$

where

$$K_0(\theta_0) = \frac{1}{2(2\pi)^{\frac{3}{2}}} \frac{c^{(1)}}{w\omega} \frac{1}{[1 - c^{(1)2}(1 + 2\tan^2\theta_0)/(2\omega^2 w^2)]},$$

and  $\theta_s$  is the scattering angle shown in Figure 3-2. In this case,  $\theta_s$  is defined by the relation  $k = \frac{\omega}{c^{(1)}} \sin \theta_s$ .

### 3.3.1 Numerical Formulation: SH-case

We use the numerical techniques developed by Maradudin *et al.* (1990a) to evaluate equation (3.9). We numerically solve these integral equations by first integrating them over a finite interval,  $L$ , then converting them to a system of  $2N$  linear equations. Separating each of the integrals in (3.9) into a sum of  $N$  integrals, each integrated over an increment  $\Delta x$ , centered at the interface points

$$x_n = -L/2 + (n - \frac{1}{2})\Delta x, n = 1, 2, 3, \dots, N, \quad (3.18)$$

and evaluating the total displacement at the center of each element,  $x_m$ , the coupled equations can now be written as a sum of the integrals

$$D_{mn}^{(l)} = \int_{x_n - (1/2)\Delta x}^{x_n + (1/2)\Delta x} dx'_1 \mu^{(l)} G_{22}^{(l)}(x_m; x'_1), \quad (3.19)$$

and

$$T_{mn}^{(l)} = \int_{x_n - (1/2)\Delta x}^{x_n + (1/2)\Delta x} dx'_1 \mu^{(l)} (-\zeta'(x'_1) \frac{\partial}{\partial x'_1} + \frac{\partial}{\partial x'_3}) G_{22}^{(l)}(x_m; x'_1),$$

where we have assumed that the unknown source strengths are slowly varying over the interval of integration and we have removed them from the integrand. The surface integrals (3.9) can now be approximated as a sum of the integrals (3.19), leaving a system of  $2N$  equations with  $2N$  unknowns

$$D_m = u_2^{(1)}(x_m)_{incid} + \sum_{n=1}^N [D_n T_{mn}^{(1)} - T_n D_{mn}^{(1)}], \quad (3.20)$$

$$0 = - \sum_{n=1}^N [D_n T_{mn}^{(2)} - \frac{\mu^{(1)}}{\mu^{(2)}} T_n D_{mn}^{(2)}],$$

where  $D_n$  and  $T_n$  represent the unknown displacement and normalized stress along each of the  $N$  elements, respectively. The integrals (3.19) are now approximated to first order in  $\Delta x$  as

$$T_{mn}^{(l)} = -\Delta x \left(\frac{i}{4}\right) \frac{\omega}{c^{(l)}} \frac{H_1(\omega/c^{(l)})[(x_m-x_n)^2+(\zeta(x_m)-\zeta(x_n))^2]^{\frac{1}{2}}}{[(x_m-x_n)^2+(\zeta(x_m)-\zeta(x_n))^2]^{\frac{1}{2}}} \times \{(x_m-x_n)\zeta'(x_n) - [\zeta(x_m) - \zeta(x_n)]\}, \quad m \neq n \quad (3.21)$$

$$T_{mn}^{(l)} = \left\{ \frac{1}{2} + \frac{\zeta''(x_m)\Delta x}{4\pi\gamma_m^2} \right\}, \quad m = n,$$

and

$$D_{mn}^{(l)} = \Delta x \frac{i}{4} H_0\left(\frac{\omega}{c^{(l)}}[(x_m-x_n)^2+(\zeta(x_m)-\zeta(x_n))^2]^{\frac{1}{2}}\right), \quad m \neq n \quad (3.22)$$

$$D_{mn}^{(l)} = \frac{i}{4} H_0\left(\frac{\omega\gamma_m\Delta x}{2ec^{(l)}}\right)\Delta x, \quad m = n,$$

where we have set

$$\gamma_m = [1 + (\zeta'(x_m))^2]^{\frac{1}{2}}.$$

The singular cases, with  $m = n$ , are solved using a limiting process as the integral approaches its singular poles from above. The Hankel functions are approximated by ascending series, and all other terms in (3.19) are expanded to first order in  $\Delta x$  using Taylor expansions (Abramowitz and Stegun, 1964).

Using the approximations (3.21) and (3.22), the set of linear equations (3.20) can now be inverted for element strengths using LU decomposition followed by the back substitution of source vectors, where the source vectors depend only on the incident beam strength (see results section). The solved strengths can now be used to evaluate the reflection coefficient (3.17) using the approximation

$$r(\theta_s) \approx \Delta x \sum_{n=1}^N e^{-i(\omega/c^{(1)})[x_n \sin \theta_s + \zeta(x_n) \cos \theta_s]} \quad (3.23)$$

$$\left\{ i \frac{\omega}{c^{(1)}} [\zeta'(x_n) \sin \theta_s - \cos \theta_s] D_n - T_n \right\}.$$

### 3.4 Numerical Results

In seismic scattering studies, one generally obtains results from a specific interface. While these studies are interesting for understanding certain deterministic models and their respective scattered fields, they cannot provide a general understanding of the scattering from other rough interfaces. Since the aim of our work is to identify scattering trends that are common to many different irregular geometries, we turn to random models and a statistical analysis of the scattered field.

In optics, the most commonly modeled random surfaces are Gaussian because they can be easily represented mathematically. In this study we also adopt a Gaussian surface, having a Gaussian spatial correlation function and a Gaussian distribution about the mean. This Gaussian interface can be described by two properties: the correlation length,  $a$ , and the standard deviation in height,  $\delta$ . The correlation length corresponds approximately to the average distance between adjacent peaks and valleys along the interface and the standard deviation gives the root mean square (*rms*) deviation of the interface height from its mean, which we set to zero. The *rms* slope of the interface is given by

$$\langle (\zeta'(x_1))^2 \rangle^{\frac{1}{2}} = \sqrt{2}\delta/a = \tan \phi. \quad (3.24)$$

Averaging the scattering from a large but finite number of surface realizations provides a statistical description of the DRC. The total contribution to the DRC can then be reduced to coherent and incoherent contributions, which represent different statistical characteristics of the scattered waves. The total contribution to the mean DRC can be expressed as

$$\langle \frac{\partial R_p}{\partial \theta_s} \rangle_{tot} = K_0(\theta_0) \langle |r_p(\theta_s)|^2 \rangle, \quad |\theta_s| \leq \frac{\pi}{2}, \quad (3.25)$$

where the bracket notation represents an average over an ensemble of surface realizations. The total field contains a coherent portion which is formed by the constructive

phase interference of scattered waves between various surface realizations. This coherent contribution to the mean DRC can be written as

$$\langle \frac{\partial R_p}{\partial \theta_s} \rangle_{coh} = K_0 |\langle r_p(\theta_s) \rangle|^2, \quad |\theta_s| \leq \frac{\pi}{2}. \quad (3.26)$$

The remaining contribution is the incoherent field. The incoherent field becomes

$$\langle \frac{\partial R_p}{\partial \theta_s} \rangle_{inc} = K_0 \{ \langle |r_p(\theta_s)|^2 \rangle - |\langle r_p(\theta_s) \rangle|^2 \}, \quad |\theta_s| \leq \frac{\pi}{2}, \quad (3.27)$$

where the specular field has been completely removed with the coherent contribution. Due to the roughness of the interfaces modeled in this section, the incoherent contribution to the DRC is typically several orders of magnitude larger than the coherent contribution. This can be understood by looking at the phase difference between two waves diffracted from an incident plane wave. For an interface described by a Gaussian process with a standard deviation satisfying the relation

$$\delta > \frac{\lambda}{2 \cos \theta_0}, \quad (3.28)$$

the specular component drops off drastically, as the scattered waves are likely to accumulate a larger than  $2\pi$  phase shift in the specular direction. The interfaces presented in this paper satisfy this condition. Therefore, we only present the incoherent contribution to the DRC.

A large number of computations are now required to obtain an accurate representation of the mean DRC. In general hundreds of realizations are necessary and, taking the 250 point discretized elements used in this study, a  $500 \times 500$  matrix must be inverted for each realization. To reduce the large number of computations, we use a method where the matrix, which depends only on the interface properties, is decomposed only once. Then two source vectors, representing the Gaussian beam at incident angles of  $\theta_0$  and  $-\theta_0$ , are back-substituted into the interface matrix. Thus, the number of calculations required for two realizations is reduced by approximately one-half. In addition, for models considered in this paper, all other incident angles are

back-substituted into the same decomposed matrix. As we model five incident beam angles for one interface, this gives about a factor of 10 decrease in computation. Due to this increased efficiency, all results in this paper were obtained using a DecStation 3100, where each model represents 2000 averaged surface realizations.

In this study we vary the following parameters to delineate how they affect the mean incoherent DRC: (1) the wavelength of the incident wave, (2) the impedance contrast across the interface, (3) the mean slope of the interface, and (4) the incident beam angle. In the first case, the ratio of the incident wavelength to the spatial length of surface irregularities,  $\Lambda = a/\lambda$ , is varied. We study two wavelength ratios, corresponding to  $\Lambda \approx 1.0$  and 3.0. In the second case, impedance contrasts are varied by holding the properties of the upper layer constant while the velocity and density of the lower layer are changed. Impedance contrasts are varied to cover the spectrum of normally incident reflection coefficient values,  $R_0 = 0.33, 0.66,$  and  $0.92$ . The contrasts are chosen to be large so that a full range of enhanced backscattering can be studied. As we will show, by the time  $R_0 = 0.33$  enhanced backscattering becomes a somewhat subtle effect. These contrasts are created by varying both the velocity and density of the lower medium according to Table I.

**Table I**

model	shear velocity ( <i>m/s</i> )	density ( <i>kg/m<sup>3</sup></i> )
(1)	10000	2500
(2)	2500	2000
(3)	1600	1250
ref	1000	1000

The numbers in the left-hand column correspond to the model number labeled on

each DRC curve shown in Figures 3-3 through 3-6. In each model, the first layer has a 1000  $m/s$  velocity and 1.0 density. In the third case, different slopes are obtained by varying the *rms* slope of the interface. We study interfaces with two *rms* slopes, corresponding to  $\phi = 30^\circ$  and  $45^\circ$ . Finally, we model five incident beam angles, ranging from normal incidence to grazing angles.

Figures 3-3 through 3-6 show the incoherent contribution to the DRC for each interface tested. Each figure corresponds to a specific *rms* surface slope and incident wavelength. In each figure the five graphical diagrams represent different incident beam angles. On individual graphs, the three curves plotted represent each of the three different impedance contrasts simulated at that incident angle.

On most of the curves, the mean incoherent DRC shows a prominent peak at the angle of the incident beam. In optics this peak, which occurs at  $\theta_s = -\theta_0$ , is known as an “enhanced backscattered” or “retroreflective” peak. Recently, a number of papers have proposed that multiple scattering is responsible for this enhanced backscattering (O’Donnell and Mendez, 1987; Chakravarty and Schmid, 1986; Khmel’nitskii, 1984). Maradudin *et al.* (1990a), using a form of the Kirchhoff approximation, recently determined that retroreflectance must be caused by at least a double-scattered path.

The multiple-scattering idea is straightforward. Consider, for instance, a wave that travels into a valley of the irregular interface. If the valley sides are steep enough, a double-scattered path can be found allowing the wave to travel back towards the source. A wave traveling from the source along the time-reversed path can also send energy back to the source with the same phase, causing constructive interference. Since the surface is random, all other paths at least partially cancel each other, while the constructive interference of the time-reversed paths allows approximately twice the energy to return in the retroreflective direction. If the surface is a perfect reflector (as is the case for some optical experiments) and its slopes are steep enough,

this theory predicts that the retroreflected peak should be approximately twice as large as the background DRC. Since the elastic SH polarization case is similar to the optical p-polarization case, this explanation for the enhanced backscattering of an SH wave holds for high impedance contrasts.

### 3.4.1 Dependence of Scattering on Properties

In this section, we discuss how the wavelength of the incident wave, the impedance contrast across the interface, and the mean slope of the interface affect the mean incoherent DRC. In each case, we evaluate how the incident beam angle further affects the reflection coefficients. Referring again to Figures 3-3 through 3-6, an enhanced backscattered peak clearly exists for elastic, SH polarized waves scattered from a highly irregular interface. This peak varies dramatically with changes in interface and medium properties.

First, the shorter the incident wavelength with respect to the average wavelength of surface irregularities, the narrower the retroreflective peak. Figures 3-3 and 3-4 represent the mean incoherent contribution for a correlation length three times that of the incoming wavelength,  $a \approx 3\lambda$ . Figures 3-5 and 3-6 show the results for  $a \approx \lambda$ . The dramatic increase in the retroreflection peak width is clear. The width of the peak is a direct result of the distance over which a wave scattered at an angle  $\theta_s$  can still constructively interfere with its time-reversed partner. It can be shown (Maradudin *et al.*, 1990b; O'Donnell and Mendez, 1987), using a straightforward phase delay argument, that the angular width of the central peak is approximately equal to  $\lambda/l$ , where  $l$  is the average distance a wave propagates between two consecutive reflections on the interface. This distance, otherwise known as the “mean free path”, may be a useful descriptive feature of a rough interface. If we assume that  $l$  is approximately equal to the correlation length,  $a$ , then this equation accurately predicts the observed

increase in peak width as the incident wavelength is increased. The total angular width of the peaks ranges from an average  $18^\circ$  for  $a \approx 3\lambda$  to about  $55^\circ$  for  $a \approx \lambda$ . While this change in peak width is dramatic, the peak heights do not change significantly.

Second, decreasing the impedance contrast reduces the height of the retroreflective peak. As the impedance contrast is lowered, the retroreflective peak decreases significantly in amplitude and slightly in width. When the impedance contrast becomes very low, the peak becomes undetectable under the strength of the single scattered component of the DRC. At  $20^\circ$ , where this decrease is clearly observed, the peak becomes unnoticeable when  $R_0$  is less than 0.33. At higher incident angles the peak has already disappeared at a higher impedance contrast.

Third, increasing the incident angle while the impedance contrast is kept constant, also decreases the peak size relative to the rest of the DRC. As the angle is increased, the peak loses amplitude until it disappears. The incident angle at which the peak is no longer observable, appears to be approximately equal to the *rms* slope of the interface. For the interfaces with  $45^\circ$  *rms* slope, the peak disappears between  $45^\circ$  and  $60^\circ$  incidence. At a  $30^\circ$  *rms* slope the peak disappears at around  $30^\circ$  incidence. At least two mechanisms may be responsible for the dependence of retroreflective intensity on interface slopes. At steeper slopes, such as the  $45^\circ$  *rms* slope, shadowing may reduce retroreflective intensities as peaks shade neighboring valleys from incoming waves, inhibiting multiple scattering. Also, at smaller slopes, multiple scattered paths, which send energy back towards the source, become more difficult to find as the incident angles increase. This latter mechanism may explain why the retroreflective peak becomes smaller relative to the rest of the DRC at the lower,  $30^\circ$  *rms* slope.

While retroreflectance allows us to understand the multiple-scattered waves which are backscattered towards the source, the remaining portion of the DRC allows us to

determine how the remaining energy is scattered. Near normal incidence, the DRC shows two secondary peaks that surround the extremely strong retroreflective peak. These secondary peaks appear to be subsidiary maxima, where scattered waves have an average  $2\pi$  phase shift from their time-reversed partners. Similar to the retroreflective peak, these subsidiary peaks also become much narrower and sit a smaller angular distance away from the retroreflective peak when the incident wavelength is reduced to  $a = 3\lambda$ . No other subsidiary maxima appear to be present.

At normal incidence, the DRC does not rise above the strong retroreflective peak. However, for the cases where the normal reflection coefficient,  $R_0$ , is much less than unity, the DRC rises above the peak at larger incident angles. This is caused by the strong decrease in the backscattered component ( $-90^\circ < \theta_s < 0^\circ$ ) of the DRC along with the reduction in the relative height of the retroreflective peak. When the impedance contrast becomes low enough, the DRC curve becomes strongly skewed towards forward scattering. At  $45^\circ$  and  $60^\circ$  incident angles, the DRC becomes skewed to the point that energy is localized at large angles, with the peak energy arriving near the expected specular reflection. This suggests that large scattered reflections may be observed at large angles when the incident wave approaches grazing angles. We stress, however, that the coherent, specular component of these scattered waves is small as a result of the large surface roughness.

When  $R_0$  approaches unity, the DRC does not experience this extreme skewness. This lack of skewness appears to result from the inability of energy to penetrate the interface. This allows most of the incident energy to backscatter into the upper medium, even at larger incident angles.

### 3.5 Discussions and Conclusions

In this chapter we applied the numerical technique developed by Maradudin *et al.* (1990a, 1990b) to an SH polarized wave incident on a two-dimensional, highly irregular surface separating two elastic half-spaces. We find that the solution is similar to the results obtained by Maradudin (1990a) for the case of an incident p-polarized wave in optics, suggesting that the optical scattering mechanisms also apply in elastic theory. Numerical results, obtained by averaging over many surface realizations, show that the mean incoherent DRC is dominant. This incoherent contribution shows a multiple-scattered retroreflective peak at higher impedance contrasts. The retroreflective peak decreases in amplitude as the incident angle increases and the impedance contrast decreases. Peak width can also vary substantially. As theoretically predicted, the width increases as the incident wavelength increases relative to the correlation length of the surface. The general character of the DRC also varies strongly with changes in material and interface properties. Most interesting is the strong presence of scattered energy near the specular angle at larger incident angles and smaller impedance contrasts. This is accompanied by a dramatic decrease in backscattered energy.

This enhanced backscattering and fluctuation in the DRC may explain different observed phenomena. In ocean environments, large amplitude reflections are sometimes received at the source, giving the appearance of false obstacles along the ocean bottom. It is plausible that, if irregularities are present over a large distance on the ocean bottom, the scattered waves may be averaged spatially. This can give a large burst of scattered energy traveling in the retroreflective direction. This spatial averaging is not a new idea. In the same way that an optical laser can spatially average over irregular plates to obtain accurate experimental results and well-defined retroreflective peaks, a seismic wave may average over irregularities on the ocean

bottom causing large amplitude bursts. Similar large amplitude backscattering may also occur in the earth as waves encounter interfaces which are irregular over significant distances. Figure 3-7 shows the scattered displacement resulting from one realization of a nearly rigid interface with a  $45^\circ$  *rms* slope. The beam is incident at  $20^\circ$ . This scattered displacement demonstrates that one realization is enough to observe both strong forward scattering and backscattering. One can also identify the physical mechanism responsible for the wider, forward-scattered peak identified on most non-normal-incident DRC curves. This broad peak corresponds to the general scattering of energy about what would otherwise be a specular reflection for a plane interface. The more irregular the interface, the broader this peak becomes. Referring again to Figure 3-7, it is clear that the forward scattering can involve both single and multiple-scattered paths as much of the energy reverberates in valleys along the interface. More generally, however, we have found that forward scattered energy arises predominantly from single scattering.

The skewing of the DRC towards forward scattering at larger incident angles may explain some large amplitude reflections. It is possible that a highly irregular core-mantle boundary or Mohorovičić discontinuity may cause large reflected amplitudes in the specular direction as an incident wave approaches grazing angles. Figure 3-8 shows just one realization of a beam grazing an interface with a  $45^\circ$  *rms* slope. Even with one realization, large amplitudes appear near the specular direction.

Enhanced backscattering may also allow one to identify the statistical characteristics of surface irregularities. Since the width of the peak depends strongly on the mean free path of the surface, and thus also on the correlation length, retroreflectance may help to determine the lateral scale of surface irregularities. In addition, the angle at which retroreflectance ceases to be observable may help identify the average slope of irregularities. However, until computers become faster and less expensive to operate, a formal inversion technique is not practical.

We hope that the present analysis will stimulate further theoretical and experimental research in scattering from highly irregular interfaces. We now turn to the numerical computation of scattering from both the elastic-elastic and the acoustic-elastic interfaces. We then compare the latter case directly with ultrasonic water tank experiments.

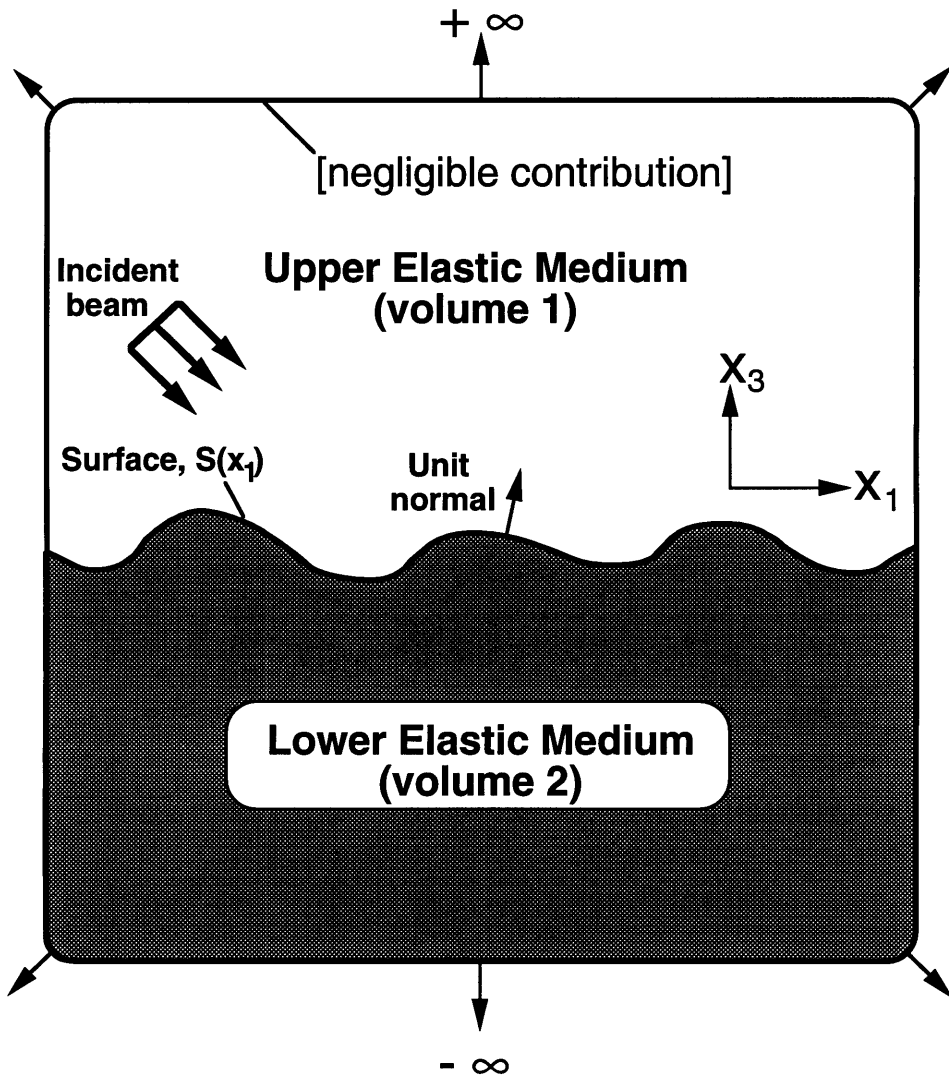


Figure 3-1: The geometry used for the development of a surface integral representation of the scattered displacement, resulting when an SH-polarized wave is incident on an irregular surface,  $S(x_1)$ . The two volumes are matched with boundary conditions along this surface while the other surfaces are assumed to have a negligible contribution to the solution. Volume 1, the upper medium, is chosen as the volume of interest.

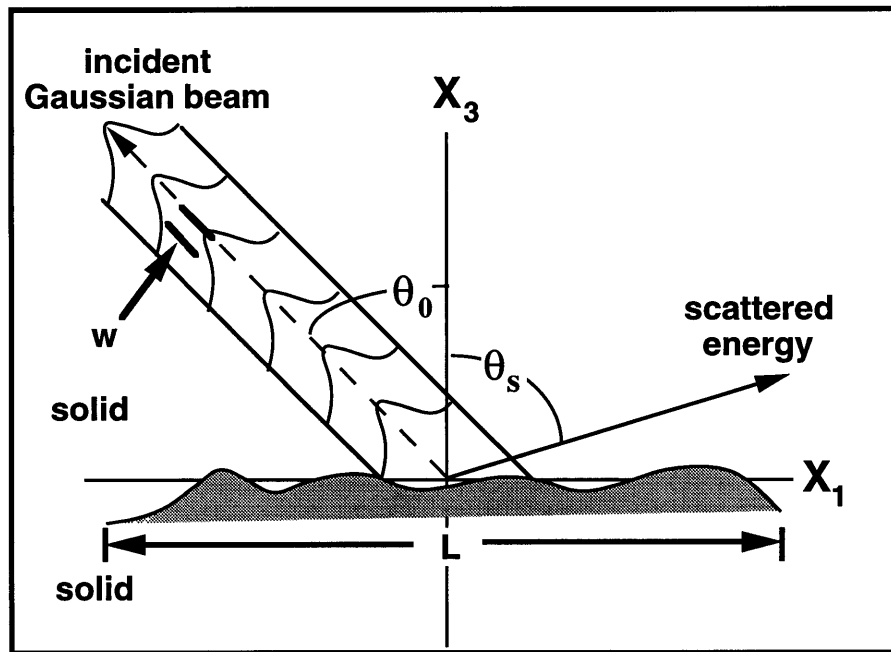


Figure 3-2: Notation used for calculating the incident beam and the resulting scattered energy.  $\theta_0$  is the incident angle,  $\theta_s$  is the scattered angle,  $w$  is the half-width of the incoming Gaussian beam, and  $L$  is the length of numerical integration.

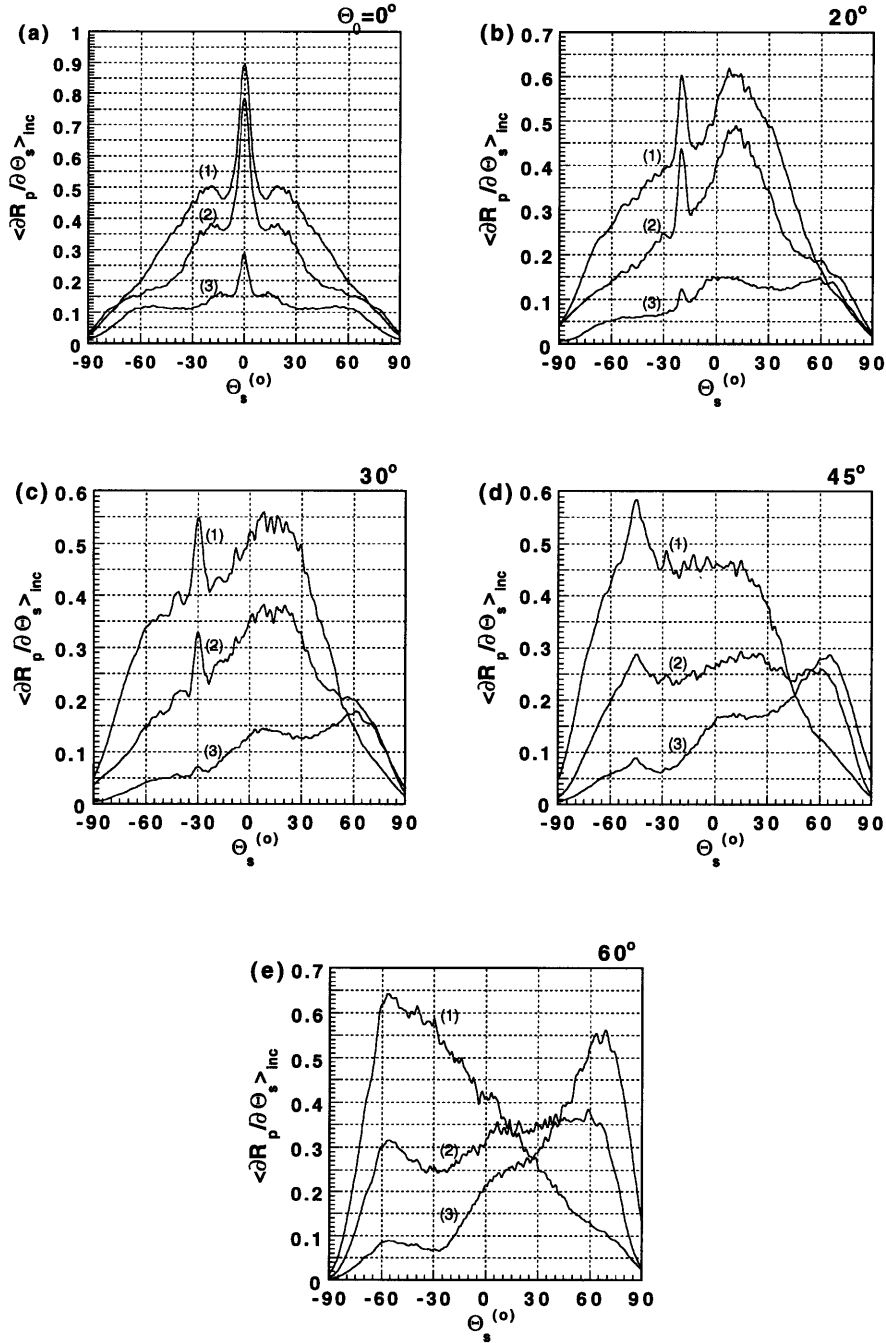


Figure 3-3: The mean incoherent DRC obtained with an incident wavelength which is one-third the interface correlation length,  $a \approx 3\lambda$ . The interface has an *rms* slope of  $45^\circ$ , where  $L=3000m$ ,  $\lambda = 62.83m$ ,  $\delta = 141.42m$ ,  $w = 450m$ , and  $a = 200m$ . Each graph represents an incident beam angle of (a)  $0^\circ$ , (b)  $20^\circ$ , (c)  $30^\circ$ , (d)  $45^\circ$ , and (e)  $60^\circ$ . The three curves plotted correspond to the physical properties given in Table I. In this case curves (1), (2), and (3) correspond to a normal reflection coefficient,  $R_0$ , equal to 0.92, 0.66, and 0.33, respectively.

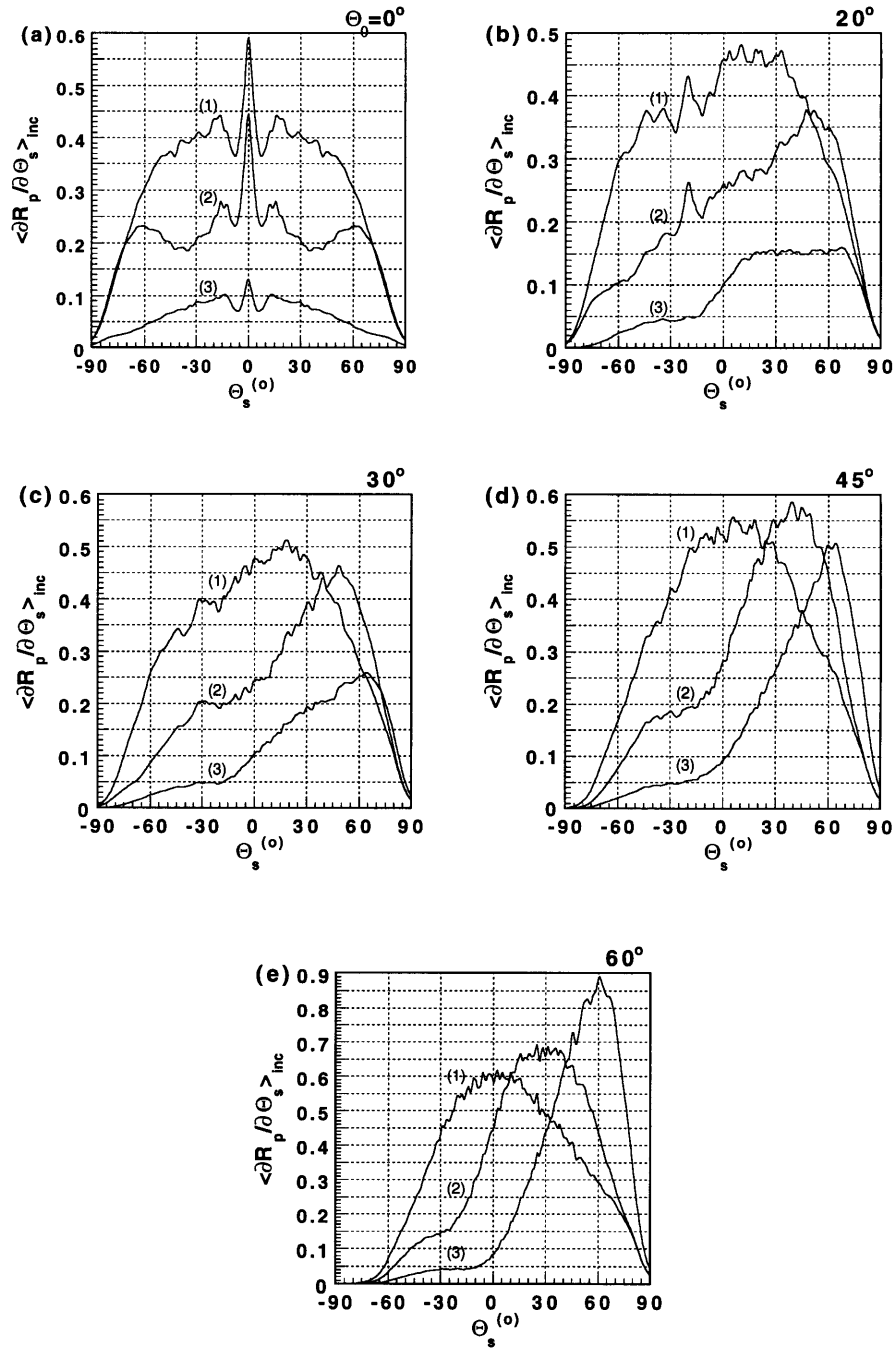


Figure 3-4: Similar to Figure 3, except the interface has a  $30^\circ$  rms slope, corresponding to  $\delta = 81.65m$ . All other parameters are the same as Figure 3.

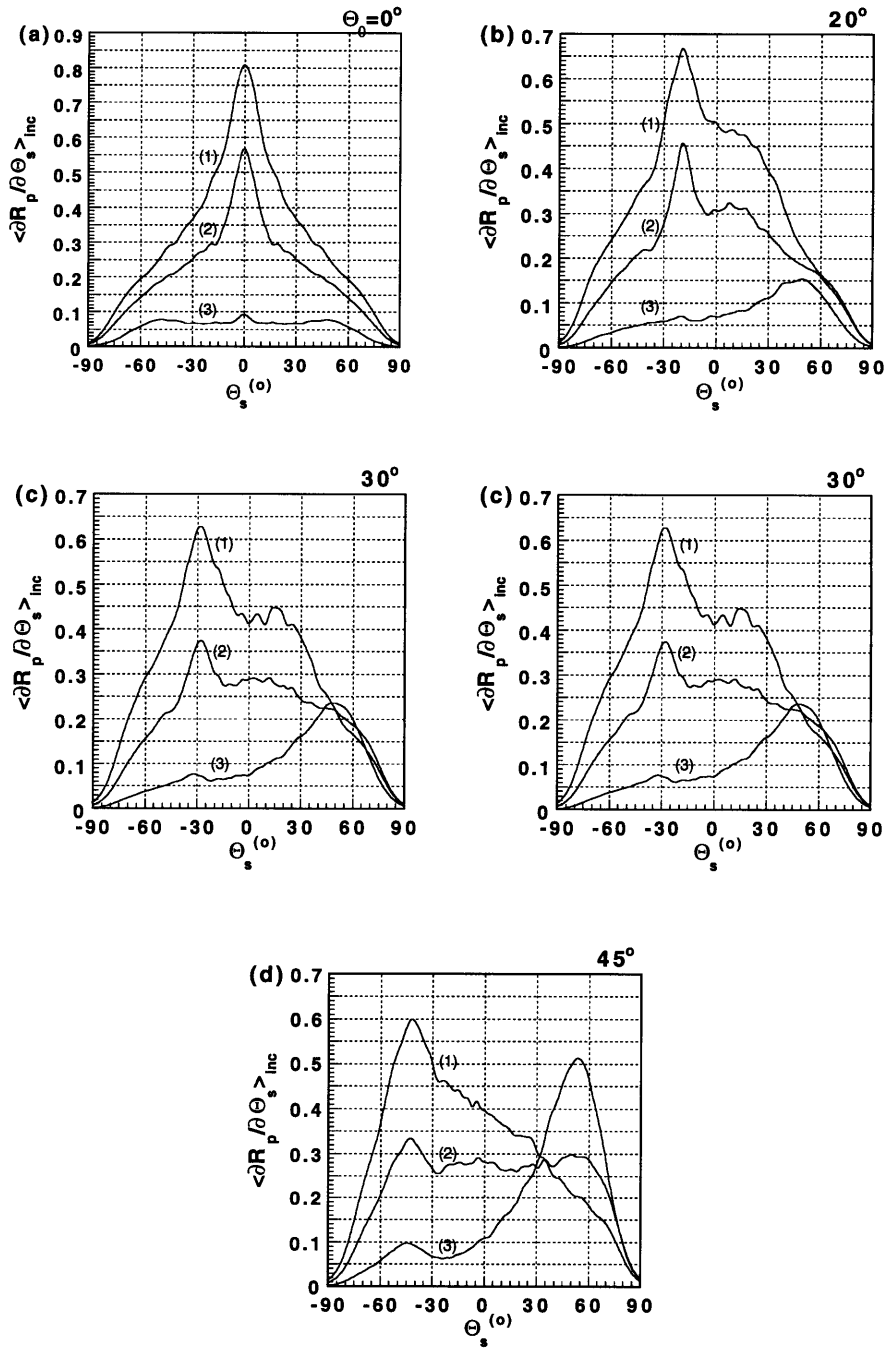


Figure 3-5: The mean incoherent DRC obtained with an incident wavelength equal to the correlation length of the interface,  $a \approx \lambda$ . The interface has an *rms* slope of  $45^\circ$ , where  $L=3000m$ ,  $\lambda = 125.66m$ ,  $\delta = 88.37m$ ,  $w = 450m$ , and  $a = 125m$ . Each graph represents an incident beam angle of (a)  $0^\circ$ , (b)  $20^\circ$ , (c)  $30^\circ$ , (d)  $45^\circ$ , and (e)  $60^\circ$ . The three curves plotted correspond to the physical properties given in Table I. In this case curves (1), (2), and (3) correspond to a normal reflection coefficient,  $R_0$ , equal to 0.92, 0.66, and 0.33, respectively.

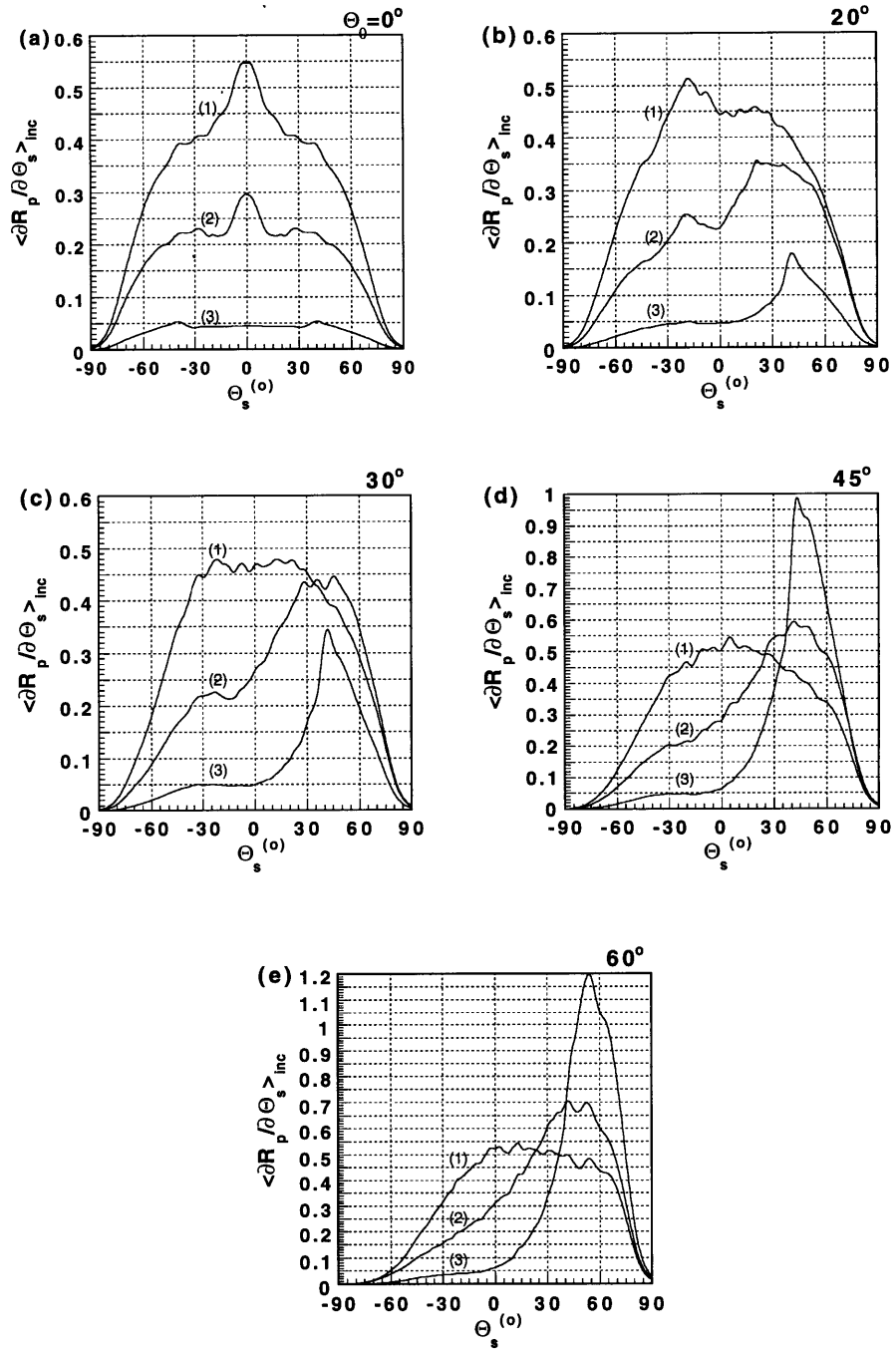


Figure 3-6: Similar to Figure 5, except for a  $30^\circ$  rms slope, with  $\delta = 51.03m$ . All other parameters are the same as Figure 5.

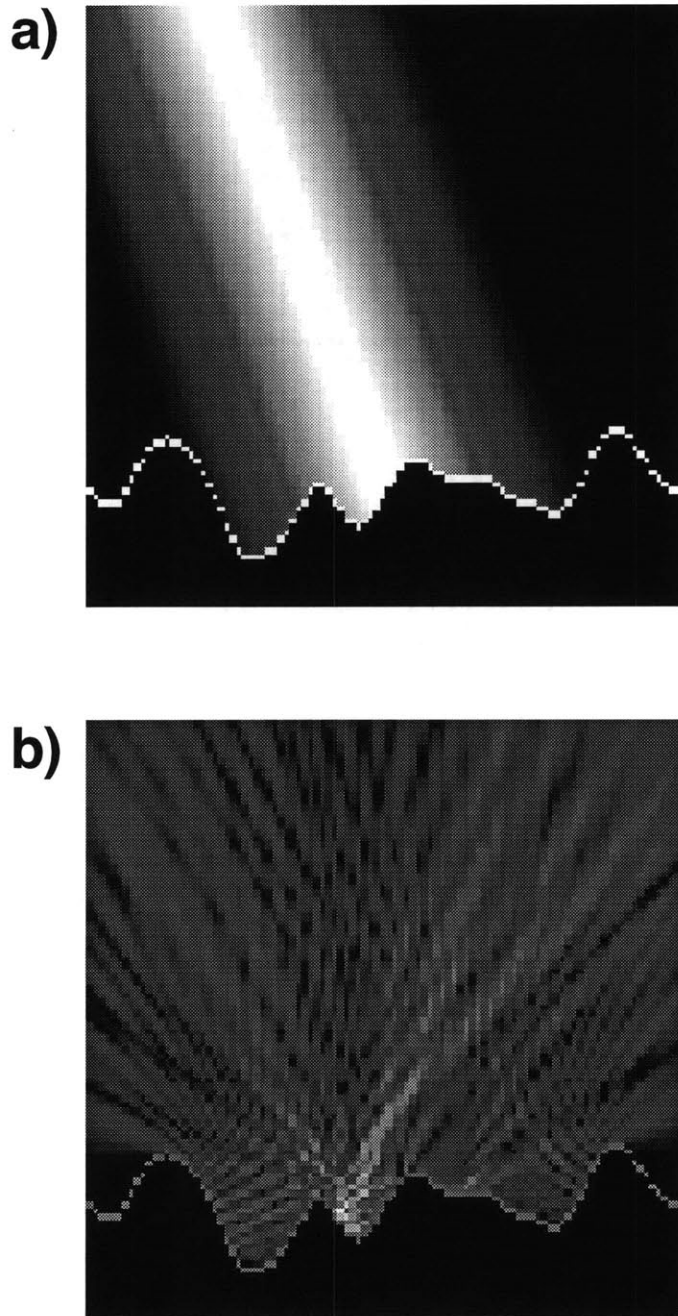


Figure 3-7: A single realization of the case shown in Figure 3b, curve (1), where the reflection coefficient,  $R_0$ , is near unity: (a) plots a Gaussian beam incident at  $20^\circ$  on an interface with  $45^\circ$  rms slope and (b) shows the resulting scattered displacement. The maximum incident amplitude is scaled to the shade of the interface in both figures.

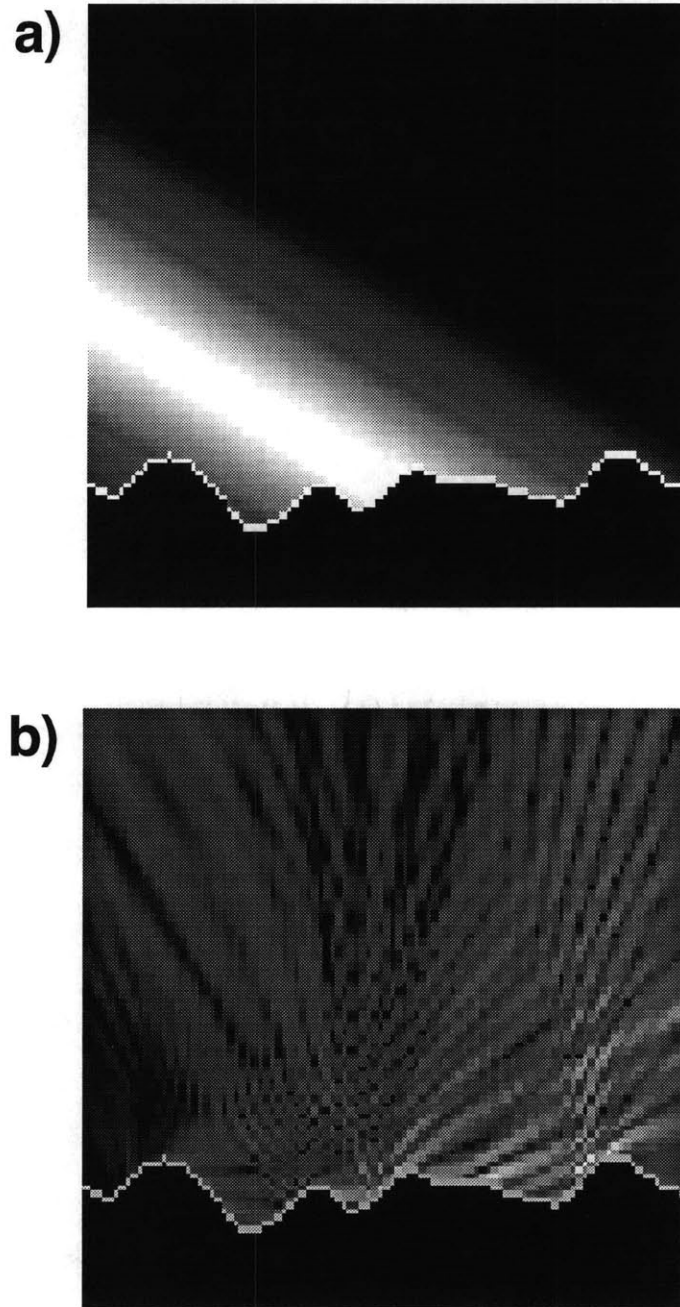


Figure 3-8: Similar to Figure 7, except for the case shown in Figure 4e, curve (3), where  $R_0$  is near .33 and (a) plots a Gaussian beam incident at  $60^\circ$ .

## Chapter 4

# Enhanced Backscattering of Seismic Waves from a Highly Irregular, Random Interface: P–SV case

### 4.1 Summary

In this chapter, we examine the scattering of P and SV waves incident on a highly irregular 2-D (the general 3-D case with one invariant direction) interface separating two semi-infinite elastic spaces to determine whether the enhanced backscattering, identified for SH waves in Chapter 3, occurs. The Somigliana identity approach of Chapter 2 is used to derive exact integral expressions for the scattered displacement produced when an incident wave having a Gaussian spatial distribution encounters a randomly irregular surface. The final set of linear equations, expressed in full analytic

form, are then inverted and a P–SV reflection coefficient is formulated.

Using a statistical approach, we elucidate the mean reflection coefficients for various irregular interfaces in the Earth’s crust and mantle. This is accomplished by varying the height and length of the irregularities with respect to the incident wavelength and varying the incident angle and impedance contrast at the interface. This analysis shows that a well defined ‘retroreflective’ peak occurs for interfaces with steep slopes and large impedance contrasts. This enhanced backscattering is observed only for P–to–P and SV–to–SV reflections, strongly supporting the optical hypothesis that multiple scattering and time–reversed paths are responsible for enhanced backscattering. We show that enhanced backscattering may play an important role at shallow, large contrast boundaries where waves can be scattered directly back at the source, greatly complicating interpretations based reflection data. In addition, we show that an irregular Mohorovičić discontinuity can destroy the specular reflection and convert most incident waves into incoherent wide–angle and post–critical energy. This may partially explain the complexities of P–coda observed in the continental crust, which we discuss in later chapters.

## 4.2 Introduction

In Chapter 3 (Schultz and Toksöz, 1993), we showed that the scattering of horizontally polarized seismic (SH) waves from highly irregular interfaces was similar to the p–polarization case of Maradudin *et al.* (1990a) and we used a similar approach to demonstrate the existence of enhanced backscattering for SH waves. This backscattering may help explain large amplitude arrivals recorded at small offsets over irregular reflectors in the crust, along with large amplitude variations recorded in mountain belt regions and other active tectonic regions. The extension of the optical hypothe-

sis of time-reversed paths (O'Donnell and Mendez, 1987; Maradudin *et al.*, 1990a) to the SH case was straightforward. Referring to Figure 1a, for instance, a wave travels into a valley of the irregular interface. If the valley sides are steep enough, a double-scattered path can be found, allowing the energy to travel back towards the source. In this case a wave traveling from the source along the time-reversed path can also send energy back to the source with the same phase, causing constructive interference in the direction of the source. Since the surface is random, all other paths at least partially cancel each other while the constructive interference of the time-reversed paths allowing additional energy to return in the direction of the source. Using simple phase arguments, we found that some of the characteristics of the retroreflective peak can also be predicted.

In the first section of this chapter, we extend the Somigliana technique of Chapter 2 to the case of P and SV waves diffracted from a highly irregular, 2-D random interface. A similar representation theorem approach has been used by Sanchez-Sesma and Campillo (1991) to model the creation and distortion of surface waves by crustal topography. However, this approach involved placing the edges of the finite interface very far away from the area of interest to avoid edge effects, greatly increasing the model size and computer run time. In this chapter, we avoid this large increase in run time by not requiring the edges of our model to be at large distances. This is accomplished by using an incident beam with a Gaussian spatial distribution which excites only a small portion of the interface. In the second section of this paper, we take the statistical approach used by Paul and Campillo (1988) one step further by computing an average reflection coefficient for various irregular crustal boundaries. This is accomplished by averaging over hundreds of realizations of waves diffracted from a given interface with Gaussian statistics. We choose to investigate a sediment-igneous contact and the Moho discontinuity with various degrees of interface roughness. The idea of time-reversed paths is then extended to this P-SV case, shown in Figure 4-1b, where wave conversions can greatly complicate the scattered waves. However, as we

will show, this more general case can be understood in a manner similar to the SH case.

## 4.3 Representation of the Scattered Energy

To determine the distribution of energy scattered from a highly irregular interface in the P–SV case, we generalize the SH plane wave decomposition approach of Chapter 3. We formulate the P–SV differential reflection coefficients (DRC) which correspond to both the dilatational (P wave) and rotational (SV wave) energy scattered from the interface. In order to reduce the length of numerical integration, we generalize the incident Gaussian beam with SH polarization, generated in Chapter 3, to the case of P and SV polarization.

### 4.3.1 The Scattered Field in Cartesian Coordinates

We begin with the model and notations developed in Chapter 2. For convenience, a summary of variables, symbols, and constants referenced throughout these chapters are given in Appendix A.

We first express the scattered displacement by performing a plane wave decomposition of the Somigliana expression (2.12) in Cartesian coordinates. Taking the dilatational and rotational potentials for a vertical and horizontal 2–D line force in the upper medium (Lamb, 1904), combined with the Helmholtz relation (2.4), the Green’s functions can be acquired in Cartesian coordinates. Substituting the corresponding Green’s functions into the integral portion of (2.12) with the aid of the constitutive relation (2.6), the total scattered field can be expressed in terms of the

plane wave decomposition

$$u_n^{(1)}(\underline{x}|\omega)_{scat} = \frac{1}{4\pi k_\beta^2} \int_{-\infty}^{\infty} dk [R_\alpha^n(k\omega) e^{ikx_1 + ik_z^\alpha x_3} + R_\beta^n(k\omega) e^{ikx_1 + ik_z^\beta x_3}], \quad (4.1)$$

assuming  $x_3 > \zeta(x_1)_{max}$ . Each plane wave corresponding to a horizontal wavenumber,  $k$ , now has an amplitude factor defined by  $R_\alpha^n(k\omega)$  and  $R_\beta^n(k\omega)$  depending on whether the wave is dilatational or rotational, respectively. All material properties correspond to the upper medium. These amplitude coefficients can be expressed as

$$\begin{aligned} R_\alpha^1(k\omega) &= \int_{-\infty}^{\infty} dx'_1 e^{-ikx'_1 - ik_z^\alpha \zeta(x'_1)} \\ &\times \left\{ \frac{\lambda}{\mu} (n_1 D_1(x'_1) + n_3 D_3(x'_1)) \left( \frac{k^3}{k_z^\alpha} + k k_z^\alpha \right) + 2 \left( n_1 \frac{k^3}{k_z^\alpha} + s n_3 k^2 \right) D_1(x'_1) \right. \\ &\left. + 2 (s n_1 k^2 + n_3 k k_z^\alpha) D_3(x'_1) - \left( i \frac{k^2}{k_z^\alpha} \right) T_1(x'_1) - (s i k) T_3(x'_1) \right\}, \end{aligned} \quad (4.2)$$

$$\begin{aligned} R_\alpha^3(k\omega) &= \int_{-\infty}^{\infty} dx'_1 e^{-ikx'_1 - ik_z^\alpha \zeta(x'_1)} \\ &\times \left\{ s \frac{\lambda}{\mu} (k^2 + (k_z^\alpha)^2) (n_1 D_1(x'_1) + n_3 D_3(x'_1)) + 2 (s n_1 k^2 + n_3 k k_z^\alpha) D_1(x'_1) \right. \\ &\left. + 2 (n_1 k_z^\alpha k + n_3 s (k_z^\alpha)^2) D_3(x'_1) - (s i k) T_1(x'_1) - (i k_z^\alpha) T_3(x'_1) \right\}, \end{aligned} \quad (4.3)$$

for the dilatational contribution to displacement where  $s$  corresponds to  $sgn(x_3 - x'_3)$ . The rotational contribution to displacement can be written in a similar form. We have defined the vertical wavenumbers as

$$\begin{aligned} k_z^\alpha &= (k_\alpha^2 - k^2)^{\frac{1}{2}}, \quad Im(k_z^\alpha) > 0, \\ k_z^\beta &= (k_\beta^2 - k^2)^{\frac{1}{2}}, \quad Im(k_z^\beta) > 0, \end{aligned} \quad (4.4)$$

where  $k$  is the horizontal wavenumber and  $k_\alpha$  and  $k_\beta$  are the total wavenumbers in the upper medium. Given the source functions  $D_n(x_1)$  and  $T_n(x_1)$  for the upper medium, the total scattered displacement can be computed. However, to determine these coefficients, the incident displacement must be specified.

### 4.3.2 Incident Beam

We implement a source wave based on a beam with Gaussian spatial distribution used in Chapter 3 (Maradudin *et al.*, 1990a; Schultz and Toksöz, 1993). This narrow beam, shown in Figure 4-2, allows for the excitation of only a small section of the interface, reducing the interval of numerical integration required. Sanchez–Sesma and Campillo (1991) have used another approach where, instead of forcing source strengths at the ends of the interface to be essentially zero, the ends of the finite interface are extended to great distances so their effects are negligible. This approach is especially useful when plane wave or more general sources are introduced. However, this approach greatly increases the interval of integration and the numerical computation time. We thus implement the beam source.

Consider the generalization of a Gaussian beam to the P–SV case. Take the following dilatational and rotational potentials

$$\Pi_h^{(1)}(\underline{x}|\omega)_{incid} = \frac{\omega W}{2\sqrt{\pi}ik_h c_h} \int_{-\frac{\pi}{2}}^{\frac{\pi}{2}} d\theta e^{-\left(\frac{\omega^2 W^2}{4c_h^2}\right)(\theta-\theta_0)^2} e^{i\left(\frac{\omega}{c_h}\right)(x_1 \sin \theta - x_3 \cos \theta)}, \quad (4.5)$$

which exactly satisfy the wave equations, (2.3), where  $\Pi_h$  corresponds to dilatational or rotational Helmholtz potentials and  $c_h$  corresponds to the respective dilatational or rotational velocity of the upper medium depending on the subscript  $h$ ;  $w$  represents the half–width of the incident beam. Differentiating (4.5) to obtain displacements and following an approach similar that in Chapter 3 (Schultz and Toksöz, 1993) results in an approximation which is equivalent to the approximation for the SH case with an additional amplitude factor multiplying the SH solution. The final approximation takes the form

$$u_n^{(1)}(\underline{x}|\omega)_{incid} \approx d_i(\theta_0) e^{ik_h(x_1 \sin \theta_0 - x_3 \cos \theta_0)[1+W(x_1, x_3)] - ((x_1 \cos \theta_0 + x_3 \sin \theta_0)/w)^2}, \quad (4.6)$$

$$W(x_1, x_3) = \frac{c_h^2}{\omega^2 W^2} \left[ \frac{2}{W^2} (x_1 \cos \theta_0 + x_3 \sin \theta_0)^2 - 1 \right],$$

where depending on the polarization (P or SV) the amplitude function can be written as

$$\begin{aligned} \text{P wave: } \quad d_n(\theta) &= (\sin \theta, 0, -\cos \theta), \\ \text{SV wave: } \quad d_n(\theta) &= (\cos \theta, 0, \sin \theta). \end{aligned} \tag{4.7}$$

This represents an exact expression for propagating P and SV source beams that have a Gaussian spatial distribution. This is most easily seen at normal incidence where the incident beam has the Gaussian form,  $\exp(-\frac{x^2}{w^2})$ , and  $w$  is clearly the half-width of the beam. This Gaussian beam satisfies the wave equation as long as  $(\frac{\omega w}{2c_h}) > 10$ . If  $(\frac{\omega w}{2c_h}) < 10$  diffractive effects begin to spread the beam spatially and the beam approximation breaks down.

### 4.3.3 The Differential Reflection Coefficient

We now represent the reflection coefficient for an irregular interface in terms of relative powers. Specifically, we derive a differential reflection coefficient (DRC), which gives the total power within a unit angle,  $d\theta_s$ , about the scattering angle,  $\theta_s$ , relative to the incident energy in the source beam. Calculating this coefficient requires knowledge of the incident and scattered energy flux across a surface.

Consider the power flux per unit area across a plane normal to the  $x_i$ -axis. This flux can be written as

$$P_i = \tau_{ij} u_{j,t}, \tag{4.8}$$

in the time-domain. The total time-averaged  $P_3$ -component of the energy flux (flux across a horizontal plane) can be written as a surface integral over the three-component of the power flux. Using the constitutive relation (2.6), the integrand can be expressed in the frequency-domain as

$$\begin{aligned} \text{Re}[-i\omega\tau_{3j}u_j^*] &= \text{Re}[-i\omega\{\mu u_{3,1}u_1^* + \mu u_{1,3}u_1^* \\ &\quad + \lambda u_{1,1}u_3^* + (\lambda + 2\mu)u_{3,3}u_3^*\}], \end{aligned} \tag{4.9}$$

where the asterisk represents the complex conjugate, and all physical quantities again correspond to the upper medium. Substituting the Gaussian source displacement (4.6) into the above equations and integrating over the plane  $x_3 = 0$  gives the final average power flux

$$P_{incid} = \frac{\sqrt{\pi} w L_2 \omega^2}{\sqrt{2} c_h} P_B, \quad (4.10)$$

with

$$\begin{aligned} P_B = & \left[ 1 - \frac{c_h^2}{\omega^2 w^2} (1 + 2 \tan^2 \theta_0) \right] [(\lambda + 2\mu) d_3^2(\theta_0) + \mu d_1^2(\theta_0)] \\ & - \left[ \left( 1 + \frac{1}{2} \frac{c_h^2}{w^2 \omega^2} \right) \tan \theta_0 \right] [\lambda + \mu] d_1(\theta_0) d_3(\theta_0), \end{aligned}$$

where  $L_2$  is an arbitrary distance integrated in the  $x_2$ -direction. In a similar fashion one can determine the total time-averaged, scattered flux crossing the plane  $x_3 = \text{constant} > \zeta(x_1)_{max}$ . Using the scattered displacement, (4.1), the time-averaged scattered flux can be written as

$$\begin{aligned} P_{scat} = & \frac{L_2 \omega}{16\pi^2 k_\beta^4} \int dx_1 \text{Re} \left[ \int \int dk dk' \right. \\ & \times \{ \mu k_z^p R_p^1(k\omega) R_p^{1*}(k'\omega) + (\lambda + 2\mu) k_z^p R_p^3(k\omega) R_p^{3*}(k'\omega) \\ & + \mu k R_p^3(k\omega) R_p^{1*}(k'\omega) + \lambda k R_p^1(k\omega) R_p^{3*}(k'\omega) \} \\ & \left. \times e^{i(k-k')x_1 + i(k_z^p - k_z^{p'*})x_3} \right], \end{aligned} \quad (4.11)$$

where the subscript,  $p$ , corresponds to  $\alpha$  and  $\beta$  for the dilatational and rotational components of the scattered energy, respectively. Using the fact that the integral over  $x_1$  results in a delta function in horizontal wavenumber then simplifying using constraint (4.4) for the respective vertical wavenumbers,  $k_z^p$ , and evaluating the power a large distance away from the interface, such that  $x_3 \rightarrow +\infty$ , one can write  $P_{scat}$  in the form

$$P_{scat} = \int_{-\frac{\pi}{2}}^{\frac{\pi}{2}} d\theta_s \bar{P}_p(\theta_s), \quad (4.12)$$

where we let  $k = \left(\frac{\omega}{c_p}\right) \sin \theta_s$ ,  $k_z^p = \left(\frac{\omega}{c_p}\right) \cos \theta_s$ , and  $dk = \left(\frac{\omega}{c_p}\right) \cos \theta_s d\theta_s$  define the scattering angle,  $\theta_s$ . Utilizing these expressions, the average scattered energy flux

passing across a unit angle in the direction  $\theta_s$  becomes

$$\bar{P}_p(\theta_s)_{scat} = \frac{L_2 \omega k_p^4}{8\pi k_\beta^4} P_p(\theta_s)_{scat}, \quad (4.13)$$

where

$$\begin{aligned} P_p(\theta_s)_{scat} = & \mu \left| r_p^1(\theta_s) \right|^2 + (\lambda + 2\mu) \left| r_p^3(\theta_s) \right|^2 \\ & + \mu \tan \theta_s \operatorname{Re}[r_p^3(\theta_s) r_p^{1*}(\theta_s)] + \lambda \tan \theta_s \operatorname{Re}[r_p^1(\theta_s) r_p^{3*}(\theta_s)]. \end{aligned} \quad (4.14)$$

Using the amplitude coefficients (4.2) and (4.3) one can write

$$\begin{aligned} r_\alpha^1(\theta_s) = & \int_{-\infty}^{\infty} dx'_1 e^{-ik_\alpha(\sin \theta_s x'_1 + \cos \theta_s \zeta(x'_1))} \\ & \times [k_\alpha \left\{ \left( \frac{\lambda}{\mu} \right) (n_1 D_1(x'_1) + n_3 D_3(x'_1)) (\sin^3 \theta_s + \sin \theta_s \cos^2 \theta_s) \right. \\ & + 2(n_1 \sin^3 \theta_s + s n_3 \sin^2 \theta_s \cos \theta_s) D_1(x'_1) \\ & + 2(s n_1 \sin^2 \theta_s \cos \theta_s + n_3 \sin \theta_s \cos^2 \theta_s) D_3(x'_1) \} \\ & \left. - i \{ \sin^2 \theta_s T_1(x'_1) + s \sin \theta_s \cos \theta_s T_3(x'_1) \} \right], \end{aligned} \quad (4.15)$$

$$\begin{aligned} r_\alpha^3(\theta_s) = & \int_{-\infty}^{\infty} dx'_1 e^{-ik_\alpha(\sin \theta_s x'_1 + \cos \theta_s \zeta(x'_1))} \\ & \times [k_\alpha \left\{ s \left( \frac{\lambda}{\mu} \right) \cos \theta_s (n_1 D_1(x'_1) + n_3 D_3(x'_1)) \right. \\ & + 2(s n_1 \sin^2 \theta_s \cos \theta_s + n_3 \sin \theta_s \cos^2 \theta_s) D_1(x'_1) \\ & + 2(n_1 \cos^2 \theta_s \sin \theta_s + s n_3 \cos^3 \theta_s) D_3(x'_1) \} \\ & \left. - i \{ s \sin \theta_s \cos \theta_s T_1(x'_1) + \cos^2 \theta_s T_3(x'_1) \} \right], \end{aligned}$$

for the dilatational power. Similar expressions can be written for the rotational power.

The DRC can finally be expressed as

$$\begin{aligned} \frac{\partial R_p}{\partial \theta_s} &= \frac{\bar{P}_p(\theta_s)_{scat}}{P_{incid}} \\ &= \frac{1}{2(2\pi)^{\frac{3}{2}}} \frac{\beta^4 c_p c_h}{c_p^4 c_h \omega w} \frac{P_p(\theta_s)_{scat}}{P_B}, \end{aligned} \quad (4.16)$$

where we have combined equations (4.10) and (4.13). This form of the DRC gives a scattered amplitude,  $RC_p = \left( \frac{\partial R_p}{\partial \theta_s} \right)^{\frac{1}{2}}$ , which is analogous to the reflection coefficients

for total displacement (e.g. Zoeppritz's equations). Given the cases we will be studying, a Gaussian beam reflected with unit displacement corresponds to a maximum value of  $RC_\alpha \approx 3.0$  and  $RC_\beta \approx 4.0$ . Although unit normalized reflection coefficients can be derived for the scattering of a Gaussian beam (see Chapter 5), the absolute amplitudes do not correspond directly to those for a scattered plane wave as the incident energy itself is different. To avoid any confusion with reflection coefficients calculated for an incident plane wave, we will present the DRC and focus our attention on the relative amounts of P and SV energy scattered from the interface.

Note that the differential reflection coefficient can be numerically evaluated using the discrete set of source strengths,  $D_i(x_n|\omega)$  and  $T_p(x_n|\omega)$ , solved for in Chapter 2. For example, the coefficient  $r_\alpha^1(\theta_s)$ , can be approximated by the discrete sum

$$\begin{aligned}
r_\alpha^1(\theta_s) = & \Delta x \sum_{n=1}^N e^{-ik_\alpha(\sin \theta_s x_n + \cos \theta_s \zeta(x_n))} \\
& \times [k_\alpha \left\{ \left( \frac{\lambda}{\mu} \right) (n_1(x_n) D_1(x_n) + n_3(x_n) D_3(x_n)) (\sin^3 \theta_s + \sin \theta_s \cos^2 \theta_s) \right. \\
& + 2(n_1(x_n) \sin^3 \theta_s + s n_3(x_n) \sin^2 \theta_s \cos \theta_s) D_1(x_n) \\
& + 2(s n_1(x_n) \sin^2 \theta_s \cos \theta_s + n_3(x_n) \sin \theta_s \cos^2 \theta_s) D_3(x_n) \} \\
& \left. - i \{ \sin^2 \theta_s T_1(x_n) + s \sin \theta_s \cos \theta_s T_3(x_n) \} \right],
\end{aligned} \tag{4.17}$$

where the other coefficients in (4.15) and the coefficients for the rotational contributions can be approximated in a similar fashion.

## 4.4 Numerical Results

In this section the statistical averaging approach of Chapter 3 allows us to identify the distribution of energy scattered from a highly irregular interface with given statistical properties. In a similar manner, by averaging many realizations of the Differential Reflection Coefficient (DRC), each generated from an interface with the same Gaussian

statistical properties, a mean DRC is determined.

Various components of this mean DRC can be computed. In general the total mean contribution to the DRC can be expressed as

$$\begin{aligned} \left\langle \frac{\partial R_p}{\partial \theta_s} \right\rangle_{tot} &= \kappa_o \{ \mu \langle |r_p^1(\theta_s)|^2 \rangle + (\lambda + 2\mu) \langle |r_p^3(\theta_s)|^2 \rangle \\ &\quad + \mu \tan \theta_s \langle \text{Re}[r_p^3(\theta_s) r_p^{1*}(\theta_s)] \rangle \\ &\quad + \lambda \tan \theta_s \langle \text{Re}[r_p^1(\theta_s) r_p^{3*}(\theta_s)] \rangle \}, \end{aligned} \quad (4.18)$$

where

$$\kappa_o(\theta_0) = \frac{1}{2(2\pi)^{\frac{3}{2}}} \frac{\beta^4 c_p c_h}{c_p^4 c_h \omega w P_B}, \quad (4.19)$$

which gives the average total power reflected into the upper medium, as a function of the scattering angle,  $\theta_s$ , given a specific incident beam. The factor,  $\kappa_o$ , is defined by expression (4.16). The angular brackets above represent averages over an ensemble of interface realizations. Averaging over this ensemble allows further separation of the total mean DRC into its more basic coherent and incoherent components. The coherent contribution to the mean DRC

$$\begin{aligned} \left\langle \frac{\partial R_p}{\partial \theta_s} \right\rangle_{coh} &= \kappa_o \{ \mu \langle |r_p^1(\theta_s)\rangle|^2 + (\lambda + 2\mu) \langle |r_p^3(\theta_s)\rangle|^2 \\ &\quad + \mu \tan \theta_s \text{Re}[\langle r_p^3(\theta_s)\rangle \langle r_p^{1*}(\theta_s)\rangle] \\ &\quad + \lambda \tan \theta_s \text{Re}[\langle r_p^1(\theta_s)\rangle \langle r_p^{3*}(\theta_s)\rangle] \}, \end{aligned} \quad (4.20)$$

gives the scattered energy for waves which on average constructively interfere between various realizations. The incoherent contribution, representing the energy for waves which do not constructively interfere from one realization to the next, can then be written as

$$\left\langle \frac{\partial R_p}{\partial \theta_s} \right\rangle_{inc} = \left\langle \frac{\partial R_p}{\partial \theta_s} \right\rangle_{tot} - \left\langle \frac{\partial R_p}{\partial \theta_s} \right\rangle_{coh}. \quad (4.21)$$

When the irregular boundaries studied in this paper are rough enough so that the coherent field is small, we will place emphasis on the incoherent contribution to the

DRC. Otherwise, for the smaller sized irregularities, such as those which might occur along the Mohorovičić discontinuity, the total contribution to the DRC is presented.

Due to the large number of realizations required for this statistical analysis, two methods are used to optimize the algorithm discussed in the previous section. First, vectorized LU-decomposition is used to solve the linear system of equations (2.19) and (2.21). Since the resulting decomposed matrix includes all information about the interface, this matrix is saved and vectors representing each incident beam angle are backsubstituted for little additional cost. For example, if 31 incident angles are modeled, a factor 31 reduction in computation time is approached. Second, if an incident beam is placed at  $-\theta_0$ , this constitutes another realization of the interface as  $\zeta(-x_1)$  becomes another random sample of the interface. The vector for this reversed beam can then be backsubstituted into the same LU-decomposed matrix, giving approximately another two-time reduction in computation time. However, in this more general case, one must be careful to reverse the horizontal component of the incident SV wave and all horizontal scattered displacements for this negative incident angle to gain a proper average. Overall, these techniques approach a factor of 62 reduction in computation time.

In the remainder of this study, we assume that the interface profile function,  $\zeta(x_1)$ , is a stationary, Gaussian, stochastic process. The mean height of the interface is set to zero

$$\langle \zeta(x_1) \rangle = 0, \quad (4.22)$$

and the deviation from this mean is defined as

$$\langle \zeta(x_1)\zeta(x'_1) \rangle = \delta^2 W(|x_1 - x'_1|), \quad (4.23)$$

where  $\langle \delta^2 \rangle = \langle \zeta^2(x_1) \rangle$  is the standard deviation from a flat interface. The interface spatial correlation function has a Gaussian form

$$W(|x_1|) = e^{(-x_1^2/a^2)}, \quad (4.24)$$

where  $a$  is the transverse correlation length. This length is a good approximation to the mean distance between adjacent peaks and valleys along the interface (Maradudin and Michel, 1990c). The root-mean-square (*rms*) slope of the interface can now be written as

$$\langle (\zeta'(x_1))^2 \rangle^{1/2} = \sqrt{2}\delta/a, \quad (4.25)$$

which is important for the characterization of interfaces in the remainder of this paper (Beckmann and Spizzichino, 1987).

We now demonstrate scattering which results from irregular interfaces with high velocity contrasts and we apply this scattering to specific regions of the Earth. We consider numerical solutions for two specific Earth boundaries that may have large irregularities. The first case is a soil-basement interface and the second is an irregular Mohorovičić discontinuity. The soil-basement interface is important in seismic “reflection” and imaging problems. In such studies a large amount of scattered energy is classified as noise. This noise can interfere with primary reflections and can completely wash out, smear, or intensify primary reflections, giving the impression that a distinct interface does not exist, is not a distinct contact, or has a higher impedance contrast than actually exists, respectively. Similar effects occur for the Mohorovičić discontinuity, where these distortions must be defined before one can understand the exact nature of various active and passive tectonic regions. This is especially true for mountainous regions and continental rift zones where large interface topography may give rise to large amplitude fluctuations.

In these two cases we select rather extreme velocity contrasts so that the various scattering phenomena which are characteristic of these boundaries may be accentuated. For the soil-basement interface, the overlying sediment is given a P wave velocity of 2000m/s, an SV wave velocity of 1200m/s, and a density of 2.0, which represents an unconsolidated or semiconsolidated sediment. The basement rock is given a P wave velocity of 6400m/s, an SV wave velocity of 3200m/s, and a density of 2.7,

representative of a mafic igneous rock. For the Mohorovičić discontinuity, we assume that the overlying crust has a P wave velocity of 6700m/s, an SV wave velocity of 3900m/s, and a density of 3.0; the mantle is given a P wave velocity of 8200m/s, an SV wave velocity of 4700m/s, and a density of 3.3, giving a clear impedance contrast across the boundary. The velocities and corresponding wavelengths for each medium are summarized in Tables I.

**Table Ia: soil–basement interface**

medium	$\alpha(m/s)$	$\beta(m/s)$	$\rho(Mg/m^3)$	$\lambda_\alpha(m)$	$\lambda_\beta(m)$
(1)	2000	1200	2.0	251.0	151.0
(2)	6400	3200	2.7	804.2	402.1

**Table Ib: Moho boundary**

medium	$\alpha(m/s)$	$\beta(m/s)$	$\rho(Mg/m^3)$	$\lambda_\alpha(m)$	$\lambda_\beta(m)$
(1)	6700	3900	3.0	935.5	544.5
(2)	8200	4700	3.3	1030.4	590.6

In Figures 4-3 through 4-8 we consider scattering of both P and SV waves from the irregular soil–basement interface. In these figures both the dilatational and rotational components of the mean incoherent DRC are plotted as a function of both incident angle ( $\theta_0$ ) and scattering angle ( $\theta_s$ ), allowing us to look at the full scattering regime for the interface of interest. In this case, backscattered energy appears on the lower half ( $\theta_s < 0$ ) of the grayscale plots. In each figure  $N_r$ , the number of surface realizations used to calculate the mean, is 1000. In Figures 4-9 through 4-15 we consider scattering

from an irregular Mohorovičić discontinuity. In these figures  $N_r$  is much smaller because fewer realizations are required to model the smaller fluctuations in the mean DRC.

#### 4.4.1 Soil–Basement Interface

Figure 4-3 gives the mean incoherent contribution to the DRC for a P wave incident on a soil–basement interface with an *rms* slope of  $30^\circ$  and the source located in the soil. This plot shows that the dilatational component of the DRC characterizes distinct scattering regimes. The presence of backscattering is clearly present, clustering about the line  $\theta_s = -\theta_0$  with approximately a  $60^\circ$  total scattering width. A narrower retroreflective peak, with width about  $40 - 50^\circ$ , also appears in the direction of the source ( $\theta_s = -\theta_0$ ). This enhanced backscattered peak loses amplitude dramatically, but retains its shape as the incident angle is increased; the peak’s definition disappears at incident angles between  $30^\circ$  and  $40^\circ$  (near the *rms* slope of the interface). Forward scattering is very small at lower angles of incidence, but increases at higher angles until it reaches the same magnitude as the backscattered energy at  $30^\circ$ –incidence. Forward scattering eventually dominates the power distribution at about  $50^\circ$ –incidence. The rotational component of the scattered waves shows no clear retroreflectance. Instead, it shows an area of negligible amplitude directed back towards the source. General backscattering on the rotational component shows a maximum at normal incidence and is negligible by  $20^\circ$ –incidence. The forward scattered intensity dominates at all incident angles greater than normal incidence and increases uniformly to  $60^\circ$ –incidence.

Figures 4-4 and 4-5 show the mean incoherent contribution to the DRC for a P wave incident on a rougher soil–basement interface which has a  $45^\circ$  *rms* slope. Incoherent scattering increases dramatically. Large backscattering appears on the di-

latational component, occurring generally over the same  $60^\circ$  zone about the retroreflective direction. The retroreflective peak retains an angular width of about  $40 - 50^\circ$ . The backscattering amplitude decreases to a minimum at  $30^\circ$ -incidence and then increases uniformly to  $60^\circ$ -incidence, while the retroreflective peak loses definition by about  $50^\circ$ -incidence. On the rotational component, scattered energy shows a much broader intensity distribution which is spread evenly over the  $0^\circ$  to  $70^\circ$  forward scattering angles. No retroreflectance is observed on the rotational component although broad angle backscattering does occur between  $0^\circ$  and  $25^\circ$ -incidence. Backscattering is negligible by  $40^\circ$  to  $50^\circ$ -incidence.

When an SV wave is incident on a soil-basement interface the forward scattering and backscattering regimes take on somewhat different characteristics. Figure 4-6 shows the mean incoherent DRC contribution for an SV wave incident on an interface with a  $30^\circ$  *rms* slope. In this case, the retroreflective peak shifts to the rotational component and becomes much narrower, with an overall width of  $25 - 30^\circ$ . The overall extent of backscattering is only about  $40^\circ$  to  $45^\circ$  wide. The retroreflective peak intensity varies in a fashion similar to the incident P case, where the intensity decreases with increasing incident angle, losing definition between  $30^\circ$  and  $40^\circ$ -incidence. Subsidiary maxima are observed at about a  $25^\circ$  angular distance from the central retroreflective peak. On the dilatational component, no retroreflectance is observable. Forward scattering appears to cover an angular width of about  $60^\circ$  surrounding the expected direction of a specular reflection, although a specular reflection is not observed due to the large irregularity of the interface. Overall, forward scattering is predominant, increasing uniformly from  $0^\circ$  to  $60^\circ$ -incident angles.

Figures 4-7 and 4-8 show the mean incoherent contribution to the DRC for an SV wave incident on a more irregular interface with a  $45^\circ$  *rms* slope. Retroreflectance again appears in the rotational component. The increased roughness allows retroreflectance to extend out to  $50^\circ$  to  $55^\circ$ -incidence. General backscattering again de-

creases continually with increasing incident angle. Subsidiary maxima extend to larger incident angles than observed for the interface with a  $30^\circ$  *rms* slope. The forward scattered energy is about  $60^\circ$  wide in the scattering angle and tends to cluster about the expected path of a specular reflection given a plane interface. Energy is also spread into the  $0^\circ$  to  $-30^\circ$  backscattering region at all incident angles measured. The dilatational component shows generally uniform scattering over most incident angles, with a slight increase in intensity when the incident angle approaches  $60^\circ$ -incidence. Again, no retroreflectance is observed, although general backscattering is detectable at incident angles less than  $25^\circ$ .

#### 4.4.2 Mohorovičić Discontinuity

In this section, various interfaces simulating a Mohorovičić discontinuity are analyzed to determine the effects irregularities may have on the mean DRC given an incident P wave. The square root of the average DRC is plotted in each figure since the amplitude fluctuations of the scattered waves can be compared more easily with field data.

We first look at the total dilatational and rotational components of the DRC for a P wave incident on a plane Mohorovičić discontinuity, shown in Figure 4-9. The total DRC consists completely of the coherent, specular reflection. The amplitude fluctuations of the specular reflection match the results of a plane layer, although the values presented here are normalized to the square root of the power of the incident wave, which is different from the amplitude normalization used with a Fourier component reflection coefficient.

Consider now a slightly irregular Mohorovičić discontinuity with an *rms* slope of  $10^\circ$ . Figures 4-10 and 4-11 show that scattered waves become distributed over a broad

range of angles centered about the specular reflection. The coherent portion of the P wave reflection, consisting of the specular reflection, decreases in amplitude by about 3 percent. The incoherent contribution consists of low amplitude waves scattered  $40 - 50^\circ$  about the specular direction at both small and large incident angles. The dilatational component also shows wide angle incoherent energy forward-scattered at angles greater than the  $54^\circ$  shear wave critical angle, as computed for a plane interface. The rotational component of the DRC shows approximately a 12 percent reduction in the specular reflection, while the incoherent contribution is spread over a similar  $40 - 50^\circ$  angular distance about the specular reflection over most incident angles.

In Figures 4-12,4-13 and 4-14,4-15 the *rms* slope of the Moho discontinuity is increased further to  $20^\circ$  and  $30^\circ$ , respectively. As the *rms* slope is increased the mean DRC changes dramatically. The specular reflection decreases at all incident angles while the incoherent contribution increases and becomes the dominant contribution to the dilatational component. By a  $30^\circ$  *rms* slope the only remaining coherent portion of the dilatational component exists for incident angles greater than  $45^\circ$ . The incoherent component is uniformly distributed over about a  $90^\circ$  range for the  $20^\circ$  *rms* slope and increases to about  $160^\circ$  for the  $30^\circ$  *rms* slope. At most incident angles the energy forward scattered at angles greater than the shear wave critical angle of  $54^\circ$  continually increases. In addition, increases in amplitude are also observable in the retroreflective direction, although retroreflectance remains almost undetectable. The rotational component shows energy focused in the forward scattered direction predominantly about the specular direction between  $0^\circ$  to  $30^\circ$ . As the interface slopes increase, the specular coefficient loses definition quickly and the incoherent contribution dominates the DRC, showing forward scattering from  $0^\circ$  to  $80^\circ$  and general backscattering.

### 4.4.3 Scattering Mechanisms

A number of optical studies have developed a simple and intuitive picture of how multiple scattering may be responsible for enhanced backscattering (O'Donnell and Mendez, 1987; Maradudin *et al.*, 1990b). To apply these ideas to an elastic-elastic interface, which includes converted P and SV waves, we consider first the simple case of SH scattering, which is analogous to the optical P polarization case. In this case, consider a multiple-scattered path which may occur along the interface as shown previously in Figure 4-1a. In this figure, a portion of an incident wave with wave vector  $\underline{k}_i$  diffracts from point 1, propagates to point 2, and finally diffracts upward into the upper medium with wave vector  $\underline{k}_s$ . If we assume an incident plane wave, some diffracted energy will also follow the time-reversed path from point 2 to 1, contributing additional energy as the final scattered wave travels away from point 1 with wave vector  $\underline{k}_s$ . The phase difference between the two time-reversed paths traveling off at  $\theta_s$  can be written

$$\begin{aligned}\Delta\phi &= \Delta\phi_i + \Delta\phi_s \\ &= \Delta\underline{r} \cdot (\underline{k}_s + \underline{k}_i),\end{aligned}\tag{4.26}$$

where  $\Delta\underline{r}$  is the vector extending from point 1 to 2. When the difference between  $-\underline{k}_i$  and  $+\underline{k}_s$  is considerable, the average of these paths scattered from the random interface to the angle  $\theta_s$  will generally cancel out and constructive interference will be negligible. Of course, if  $\underline{k}_s = -\underline{k}_i$ , the opposite is true; the phase difference goes to zero and the two time-reversed paths add constructively to give a contribution to the final average “retroreflective” amplitude.

A good approximation to the retroreflective peak width can now be obtained by averaging the phase difference and determining which scattered angles give an average phase difference less than  $\pi$ . Averaging over all scattered paths, a null in the

retroreflective peak should occur for

$$\theta_s \approx \frac{\lambda}{2\langle|\Delta\mathbf{r}| \rangle}, \quad (4.27)$$

where  $\langle|\Delta\mathbf{r}| \rangle$  is the “mean free path” or the average distance between multiply scattered points 1 and 2. The overall width of the retroreflective peak becomes

$$\Delta\theta_s \approx \frac{\lambda}{\langle|\Delta\mathbf{r}| \rangle}. \quad (4.28)$$

Using this same argument one can also predict where the subsidiary maxima will occur. These peaks should occur when  $\langle\Delta\phi \rangle$  is a multiple of  $2\pi$  or at the points

$$\theta_s \approx \frac{n\lambda}{\langle|\Delta\mathbf{r}| \rangle}, \quad (4.29)$$

where  $n$  represents the order of interference. If we take  $\langle|\Delta\mathbf{r}| \rangle \approx a$ , the results match the peak widths shown in Figures 4-5 and 4-8 to within  $5^\circ$ . The subsidiary maxima are also well predicted for  $n = 1$ .

Note that the above argument makes no reference to Gaussian statistics. As expected, the boundary is not required to have specific statistical properties. The only requirement for retroreflectance is that the irregularities are large enough for a time-reversed path to exist. In most cases, the mean free path still represents the average distance a wave travels between consecutive diffractions along the interface and remains a valid description of the lateral scale of interface irregularities.

This SH case argument is simpler than the P–SV case since no wave conversions occur along the interface. In the P–SV case, both converted P and SV waves must be considered when a wave encounters any segment of the interface. Figure 4-1b demonstrates the conversions present when a P wave encounters a valley along the interface. In this case a P wave can diffract from the interface and convert to both P and SV waves, which then travel away from point 1. Both the P and SV waves created at the 2–D interface split again at points 2 and 2' to create additional P and

SV wave components. Of course if the interface were 3-D, the case would be further complicated by conversions to P, SV, and SH waves. Although many more paths exist than in the SH case, the SH analysis can still be applied to each individual path along the elastic interface. Figure 4-16 shows the individual time-reversed paths which give constructive interference for an incident wave double-scattered along a 2-D interface. For a time-reversed path to exist, both the forward and time-reversed paths must have the same phase shift as they eventually travel away from the interface. It is clear that retroreflectance is predicted for all P-to-P and SV-to-SV paths. Figure 4-17 shows some of the many paths which do not lead to constructive interference. In general this shows that retroreflectance is not predicted for P-to-SV and SV-to-P diffraction paths. Therefore, the only predicted retroreflections should occur on P-to-P and SV-to-SV paths. In all cases studied, enhanced backscattering was not observed on both P-to-SV and SV-to-P paths in our numerical results strongly supporting this multiple scattering explanation for retroreflectance. In addition to the lack of retroreflectance, a minimum was consistently detected in the retroreflective direction. This minimum is likely due to the continuity conditions at the interface. The continuity of displacement at the boundary makes it difficult to convert the energy in the incident wave into an SV wave in the reverse direction since the polarizations are perpendicular. This absence of energy is most prominent for the interfaces with lower slopes. Some P-to-SV and SV-to-P energy is observed in the retroreflective direction as the interface is roughened, likely resulting from multiple scattering and more complex diffractive effects.

In the discussion earlier it was apparent that increasing the incident angle decreases the retroreflective peak size relative to the background energy. The incident angle at which the peak is no longer observable appears to be approximately equal to the *rms* slope of the interface. For a soil-basement interface with 30° and 45° *rms* slopes, the retroreflective peak begins to lose its definition by 30° and 45°-incidence, respectively. Two mechanisms may be responsible for this loss of peak height. First,

for retroreflectance to occur, a multiply scattered path must be found such that when a wave encounters a valley along the interface, energy can be sent back to the source. As the incident angle is increased, it becomes more difficult for the side walls of a valley to sustain such a multiply scattered path and retroreflectance diminishes. The second mechanism occurs when an interface becomes very rough. In this case the additional effect of shadowing may help break down retroreflectance. Shadowing occurs when a peak is large enough to shadow an adjacent valley from the excitation of an incident wave, not allowing energy to be multiply scattered within the valley. If a  $45^\circ$ -incident wave encounters an interface with an *rms* slope of  $45^\circ$ , large amplitude backscattering might be expected on average, as the interface slopes align. However, large amplitude backscattering is not observed. Shadowing may explain the absence of this high amplitude burst, as energy is kept from exciting much of the interface. This shadowing should become more predominant as incident angles are increased.

The future application of retroreflectance to various subsurface interfaces may allow further insight into the exact nature of the boundaries. It is clear from the above discussion that the statistical characteristics of irregularities along an interface are connected to the retroreflective properties of that interface. If the interface irregularities are close to Gaussian in nature, the transverse correlation length of the interface and the *rms* slope of the interface are tied directly to the shape and size of the retroreflective peak. Of course, before these interface properties can be determined, a valid mean DRC must be obtained over the interface.

A standard 2-D or 3-D seismic array may allow one to identify the mean reflection coefficient for a stationary, statistically irregular interface. The statistical approach discussed in the previous sections may then be a useful method for defining the geometry of various subsurface boundaries. For instance, the nature of the Mohorovičić and core-mantle boundary may be determined. The Moho discontinuity can be analyzed using deep crustal seismic profiling. If irregularities do exist along the discontinuity,

waves recorded at a given receiver will be scattered from a wider and wider zone of points along the interface as the size of irregularities are increased, as specified by Figures 4-10 through 4-15. If the interface is extremely irregular, the conversion of an incident P wave to wide-angle and post-critical energy will contribute greatly to the complexity of P coda as scattered energy remains trapped in the crust. The recent assertions that the core-mantle boundary may be highly irregular can also be analyzed. These deeper, core-mantle irregularities can be studied using earthquake or nuclear explosion sources to look at *ScS* and *PcP* core phases recorded on a large aperture seismic network (*e.g.* IRIS broadband data). If full coverage of incident angles and scattering angles can be attained, and one assumes that any core-mantle irregularities are stationary along the boundary, the presence or absence of retroreflectance may not only indicate whether irregularities exist along the boundary, but also give the scale of these irregularities.

Enhanced backscattering may also be a valuable tool in studying the ocean bottom environment. Seismic data can be acquired using a narrow beam source, created with an array of transducers similar to that used with Sea Beam data, and can be recorded with hydrophones. With the source and receiver distortions removed, retroreflectance may be used to identify the degree of ocean bottom roughness in various regions. In addition, retroreflectance may explain the presence of anomalous echo 'bright spots' recorded with sonar equipment over what appears to be an otherwise featureless sea floor.

But how many irregularities must an incident wave encounter before the general nature of the mean DRC can be resolved? This question is important to any experimental study that may try to average over the Mohorovičić discontinuity, a soil-basement interface, or any other interface which may be of interest.

If we consider the mean DRC recorded over a highly irregular soil-basement inter-

face, the resolution of the DRC increases dramatically with the number of realizations averaged. Figure 4-18 shows the total dilatational contribution to the mean DRC for a P wave incident on the interface with an *rms* slope of  $45^\circ$ , given 2 realizations, 8 realizations, and 32 realizations. At 2 realizations, enhanced backscattering is not obvious as the mean DRC fluctuates greatly over short angular distances. However, the diffracted amplitudes generally increase as they cross the retroreflective direction, suggesting that time-reversed paths are contributing additional energy. By 8 realizations the fluctuations have decreased and the general form of the enhanced backscattering has developed more clearly. Although fluctuations exist at 32 realizations, the general form of the DRC is now resolved and enhanced backscattering is clearly identifiable.

The curved streaks observed in Figure 4-18 with only a few realizations of the DRC illustrate the presence of constructive and destructive interference due to a strong form of Bragg scattering. Although the actual scattering is somewhat more involved due to multiple scattering, these energy streaks approximately follow the interference pattern predicted by the grating equation for a periodic surface where the grating equation predicts the angles of constructive and destructive interference due to scattering by adjacent peaks along the interface (Stanton, 1992). The position at which the streaks appear on the diagram is predicted by the ratio of the incident wavelength to the periodic length of the interface irregularities. In the case of a Gaussian autocorrelation function the strong presence of periodic interference is not surprising since much of its power is concentrated over a very narrow spatial wavenumber range resulting from an exponential fall-off in the wavenumber domain about the periodic length defined by  $2a$ . As observed in Figure 4-18, this periodic interference is eventually averaged out as the number of surface realizations is increased (*see also* section 4.4.4). This Bragg scattering is likely not as strong for interfaces with a more realistic autocorrelation function, since interfaces are many times fractal in nature and usually contain a much broader power spectrum than that given by the Gaussian function (*see* Chapter 5).

One can approximate the number of irregularities required for resolving enhanced backscattering by recognizing that the majority of incident energy for one realization is within a distance of  $2w$  along the interface. The number of irregularities encountered in the distance  $2w$  is approximately 3.5 for the soil–basement interface. Multiplying this by the number of realizations gives an approximation to the total number of irregularities averaged. If at 2 realizations, or 7 averaged irregularities, one is fortunate enough to choose an incident angle where a time–reversed path is set up, it is likely that higher amplitudes will be observed in the retroreflective direction. However, by 8 realizations, or 28 irregularities, time–reversed paths appear to exist for most incident angles and enhanced backscattering is clear, but still highly fluctuating in nature. By 32 realizations, or 112 irregularities, a number of time–reversed paths appear to have formed at each incident angle, constructing a good average DRC. Of course for less irregular interfaces, fewer realizations are required to resolve the reflection coefficient as the scattered intensity does not vary as dramatically from one realization to the next.

We now show that the standard deviation of a finite average of surface realizations varies inversely with the  $\sqrt{N_r}$ , explaining this rapid increase in resolution with the number of realizations.

#### 4.4.4 Accuracy of Statistical Averages

Various retroreflective peaks and general reflection coefficient trends have been identified above. It is now important to establish that these peaks are real features and not just statistical fluctuations due to the finite average of surface realizations. Given our Gaussian approach, the average DRC will converge to a probability distribution function. The difference between this function and the finite average consists of fluctuations whose size can be determined by computing their standard deviation from the

mean DRC. Utilizing the expression for the standard deviation of these fluctuations, the error of the finite average can be expressed as (Hogg and Tanis, 1983)

$$\sigma_{\langle \partial R_p / \partial \theta_s \rangle_{tot}} = \frac{1}{\sqrt{N_r}} \frac{1}{2(2\pi)^{3/2}} \frac{\beta^4 c_p c_h}{c_p^4 c_h \omega w} \frac{[\langle P_p(\theta_s)_{scat}^2 \rangle - \langle P_p(\theta_s)_{scat} \rangle^2]^{1/2}}{P_B}, \quad (4.30)$$

where we have chosen to look at the total contribution to the DRC. It is clear that the fluctuations decrease as a factor of  $\sqrt{N_r}$ .

Figure 4-19a shows a model of the mean incoherent dilatational component of the DRC for a P wave incident at 20° on a soil–basement interface. The interface has an *rms* slope of 45°. Since the interface is highly irregular and the scattered waves fluctuate greatly, 1000 realizations were averaged to determine this mean incoherent contribution. Since the coherent contribution to the DRC is negligible, the standard error of the total contribution to the DRC, (4.30), is a good estimate of the error for the incoherent contribution to the DRC. In this figure the lower curve gives the standard error of the average. The standard error is clearly much smaller than the size of the retroreflective peak, demonstrating that this peak is real and not just a statistical fluctuation.

Figure 4-19b shows the mean incoherent DRC also recorded for an incident angle of 20° over a soil–basement interface with a 30° *rms* slope, where 1000 realizations were used again. This smaller sloping interface creates a broad backscattered ridge which surrounds the retroreflective peak. This ridge is clearly within the standard deviation of the average. However, the small fluctuations at the top of the peak are approximately the same magnitude as the standard deviation, demonstrating that such small fluctuations cannot be resolved with this finite average. If more realizations were used in the average, the fluctuations in this area could be better resolved.

The above examples show that in general the larger DRC variations in this study are well within the statistical fluctuations of the finite average. If more resolution is desired, more realizations must be averaged.

## 4.5 Discussion and Conclusions

In this chapter, we have taken the complex interaction of a seismic wave with an irregular interface and reduced it to a simpler problem, giving insight into scattering mechanisms at the interface. Essentially, the case of a general incident wave has been reduced to a given frequency and incident angle. Using an incident beam and averaging over many realizations of the scattered field, we have obtained a mean reflection coefficient which quantitatively describes how energy generally diffracts from a point along an interface with given statistical properties.

We have shown that enhanced backscattering does exist for an incident P wave scattered to P waves and for an SV wave scattered to SV waves. In this section, we summarize how this enhanced backscattering and the more general trends in the DRC are affected by the wavelength of the incident wave, the impedance contrast across the interface, and the *rms* slope of the interface. In addition, we demonstrate that the variations of the retroreflective peak and the more general trends in the DRC are similar to those observed in Chapter 3 (Schultz and Toksöz, 1993) for SH scattering.

First, we find that the shorter the incident wavelength with respect to the average wavelength of surface irregularities, the narrower the retroreflective peak becomes. In the case of the incident P wave, the ratio of the incident wavelength to the correlation length of the interface,  $\lambda/\langle|\Delta_{\mathbf{r}}|\rangle$ , was approximately one, assuming  $\langle|\Delta_{\mathbf{r}}|\rangle \approx a$ . In the case of the incident SV wave with the same frequency, this ratio decreased to approximately 0.60. A similar 0.60 decrease in the retroreflective peak width is observed. This is clear from Figures 4-5 and 4-8, which show the DRC calculated at specific incident angles for the soil-basement interface with a  $45^\circ$  *rms* slope. Figure 4-5 corresponds to an incident P wave, and Figure 4-8 corresponds to an incident SV wave. The angular width of the retroreflective peak for an incident P wave is about  $40 - 50^\circ$ , while the width for an incident SV wave decreases to about  $30^\circ$ . The

relation above predicts well the decrease in peak width, assuming that  $\langle |\Delta \mathbf{r}| \rangle$  equals approximately the correlation length of the interface. Second, we find that decreasing the impedance contrast reduces the height of the retroreflective peak. Specifically, decreasing the impedance contrast from the soil–basement interface to the Mohorovičić discontinuity reduces the height of the retroreflective peak dramatically. While the soil–basement interface shows strong enhanced backscattering, the Mohorovičić discontinuity shows enhanced backscattering which is barely detectable. Third, we find that increasing the incident angle at a given impedance contrast decreases the retroreflective peak size relative to the remaining DRC. Similar to the trends in Chapter 3 (Schultz and Toksöz, 1993), the incident angle at which the peak is no longer observable appears to be approximately equal to the *rms* slope of the interface. For a soil–basement interface with 30° and 45° *rms* slopes, the retroreflective peak begins to lose its definition by 30° and 45°–incidence, respectively.

The above characteristics of retroreflectance show again that the retroreflective properties are connected directly to the statistics of an interface. Assuming a Gaussian interface, the width of the retroreflective peak is related to the transverse correlation length of the interface. In addition, the retroreflective peak becomes undetectable when the incident angle approaches the *rms* slope of the interface. Therefore, the retroreflective properties of an interface can give insight into the geometry of a given boundary.

This study deals with highly irregular interfaces of varying roughness. The models with extreme irregularity may be applicable in tectonically active areas where large Moho topography and steep crustal interfaces are the norm. Our final results show that even the most irregular of these regions can preferentially create large amplitude post–critical energy which remains trapped in the crust, potentially complicating observed coda. Note also that, in many of these regions, scattering due to irregular interfaces must be coupled with the scattering from heterogeneous media. In these

cases, Mayeda (1992) and Zeng (1991) give good reviews of current approaches to stochastic media. Additional work should also include the study of the statistical reflection coefficients in a well controlled field study. In the next chapter, we use ultrasonic laboratory experiments to isolate the scattering from an irregular interface. In this environment, this reflection coefficient approach can be rigorously tested. The results above, also formed the motivation for the analysis of crustal scattering, presented later in Chapter 6.

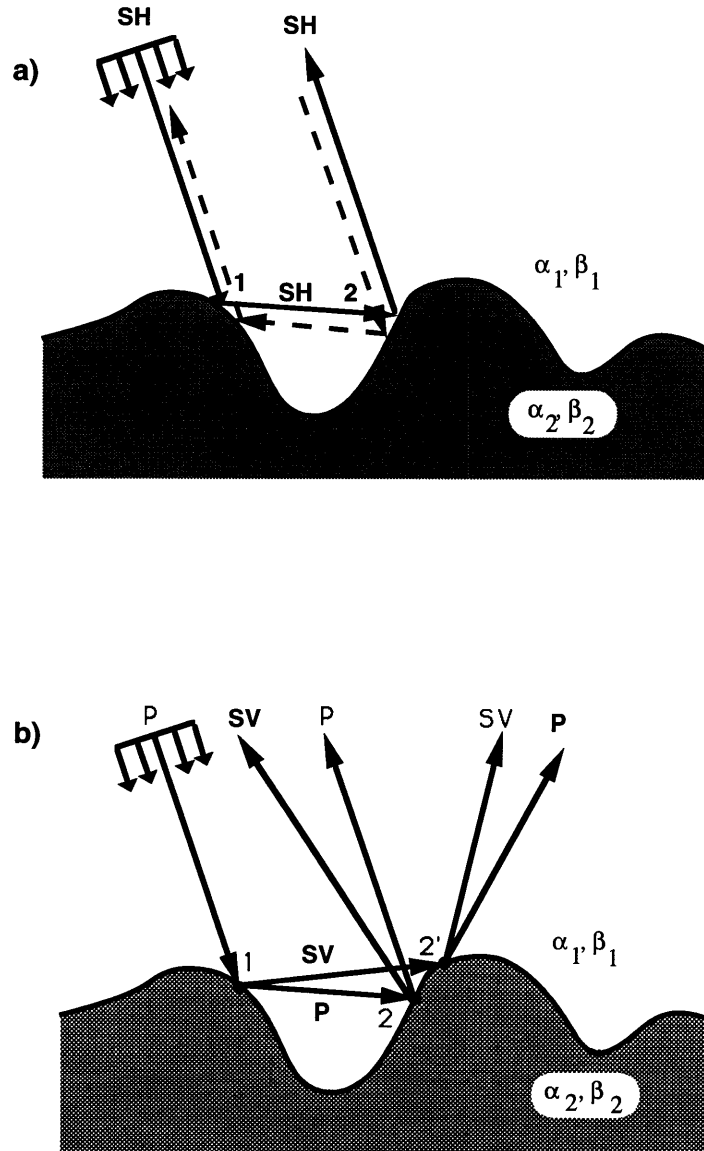


Figure 4-1: (a) a typical SH wave path created when a wave encounters a peak-valley sequence along an interface. The solid line represents a forward double-scattered path which sends energy back to the source; the dashed line represents the time-reversed path. (b) typical P-SV multiple scattered paths, given an incident P wave. This shows that the incident wave is converted at point 1 to both P and SV waves. These waves are then converted again at the second multiple scattering points, 2 and 2', showing the complexity of the multiply diffracted waves.

## SCATTERING NOTATION

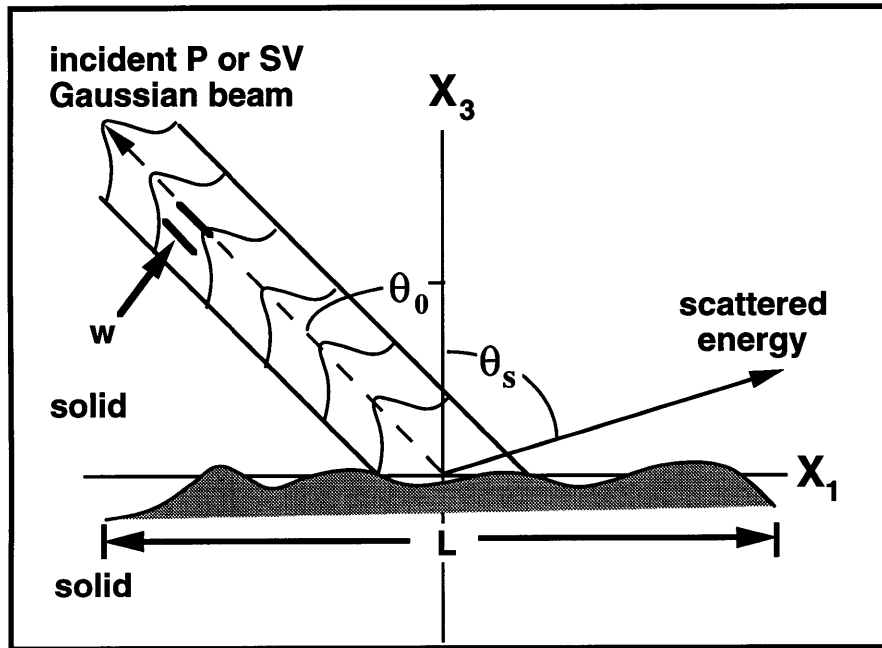


Figure 4-2: The notation and coordinate system used to generalize a Gaussian beam to the P-SV case and to calculate energy scattered from the interface.  $\theta_0$  is the incident angle,  $\theta_s$  is the scattered angle,  $w$  is the half-width of the incoming Gaussian beam, and  $L$  is the length of numerical integration.

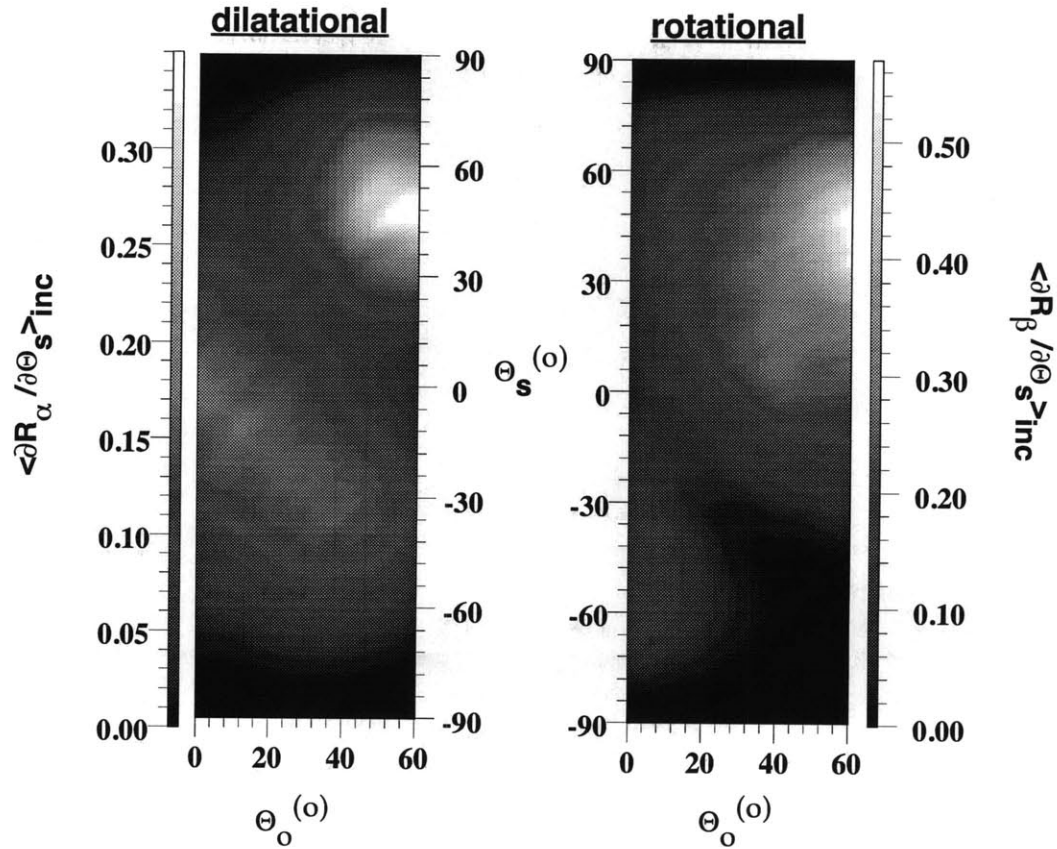


Figure 4-3: The mean incoherent DRC obtained for a soil–basement interface with the incident wavelength equal to the correlation length of the interface and  $N_r = 1000$ . The two grayscale plots show  $\langle \frac{\partial R_\alpha}{\partial \theta_s} \rangle$  and  $\langle \frac{\partial R_\beta}{\partial \theta_s} \rangle$  for the scattered P and SV waves, respectively, given an incident P wave. The interface has an *rms* slope of  $30^\circ$ , where  $L = 6600m$ ,  $\lambda_\alpha = 251m$ ,  $\lambda_\beta = 151m$ ,  $w = 900m$ ,  $\delta = 102.06m$ , and  $a = 250m$ .

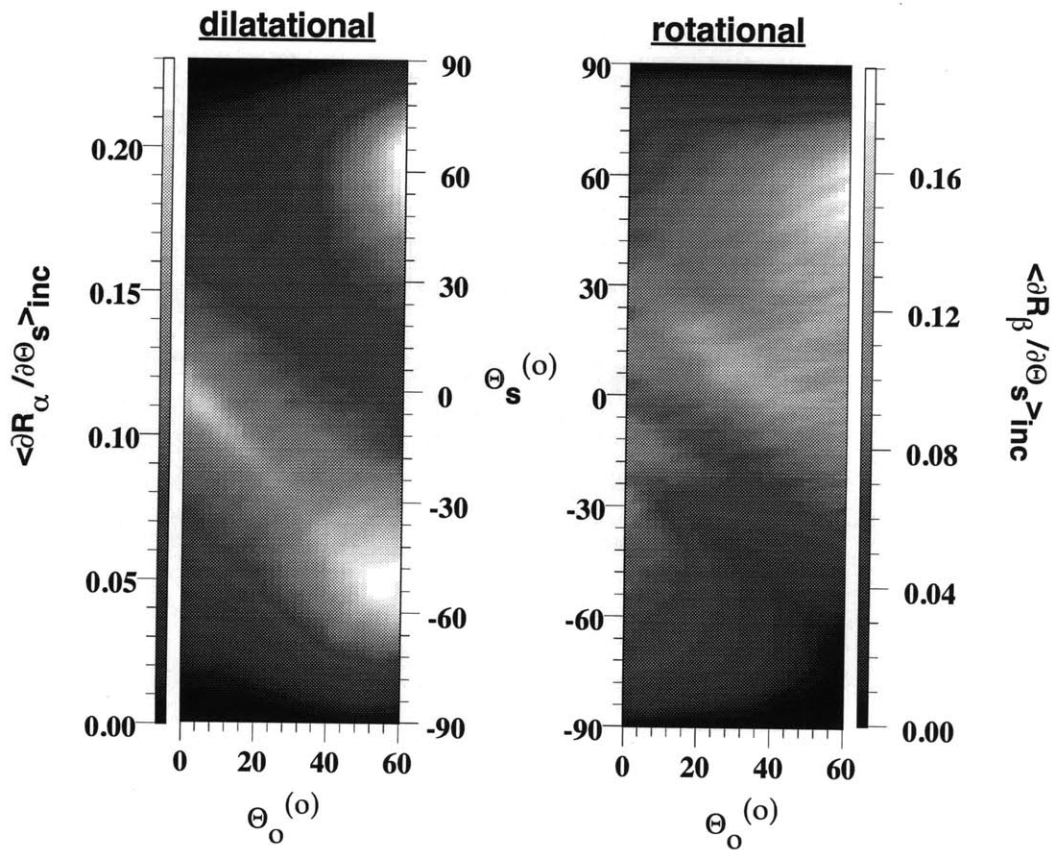


Figure 4-4: Similar to Figure 4-3, except the interface has a  $45^\circ$  rms slope, corresponding to  $\delta = 176.77m$ .

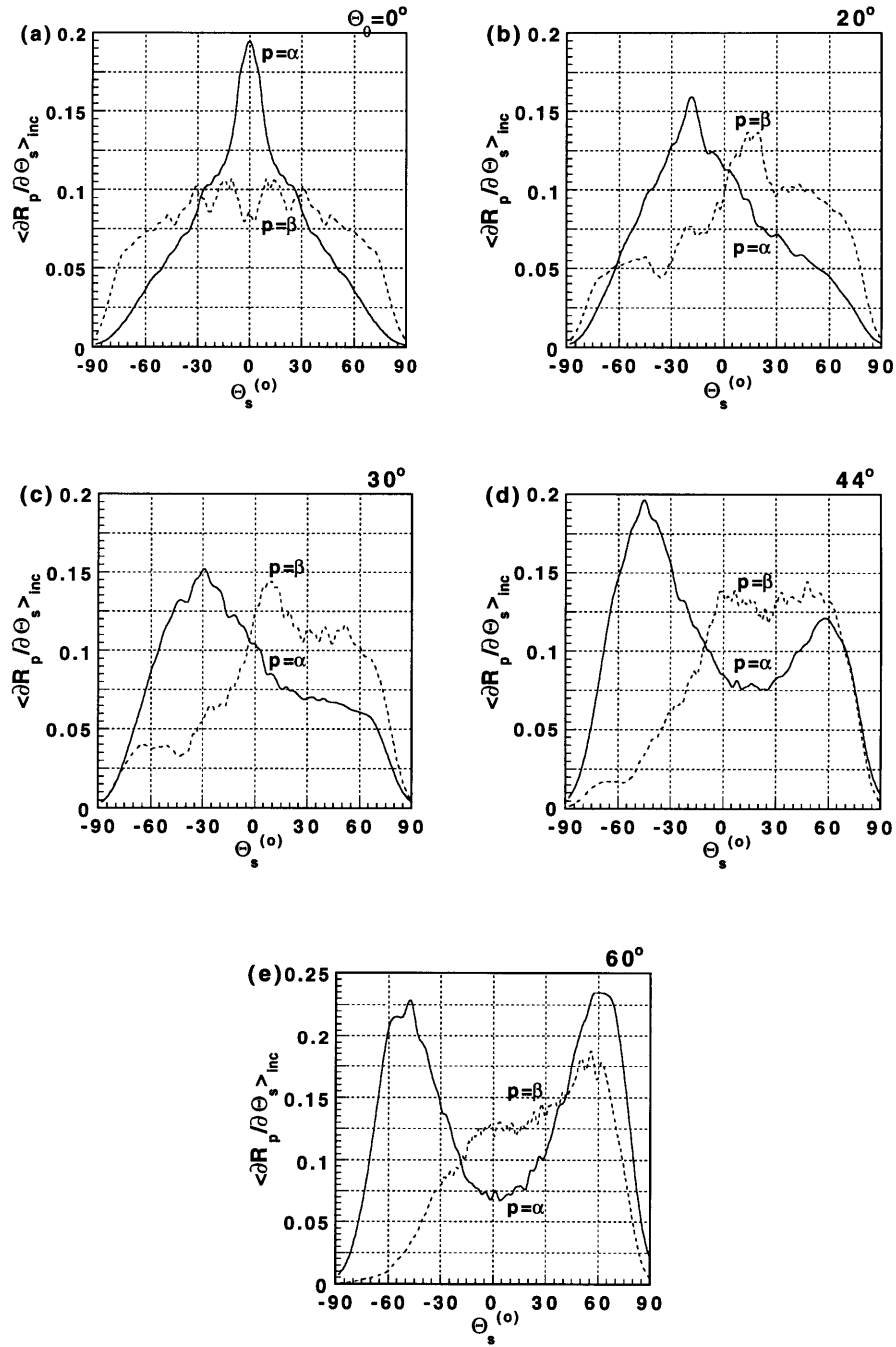


Figure 4-5: The mean incoherent DRC obtained over the soil-basement interface with an *rms* slope of  $45^\circ$  and an incident P wave with a wavelength equal to the correlation length of the interface (see Figure 4-4). Each graph represents one incident beam angle: (a)  $0^\circ$  (b)  $20^\circ$  (c)  $30^\circ$  (d)  $44^\circ$  (e)  $60^\circ$ .

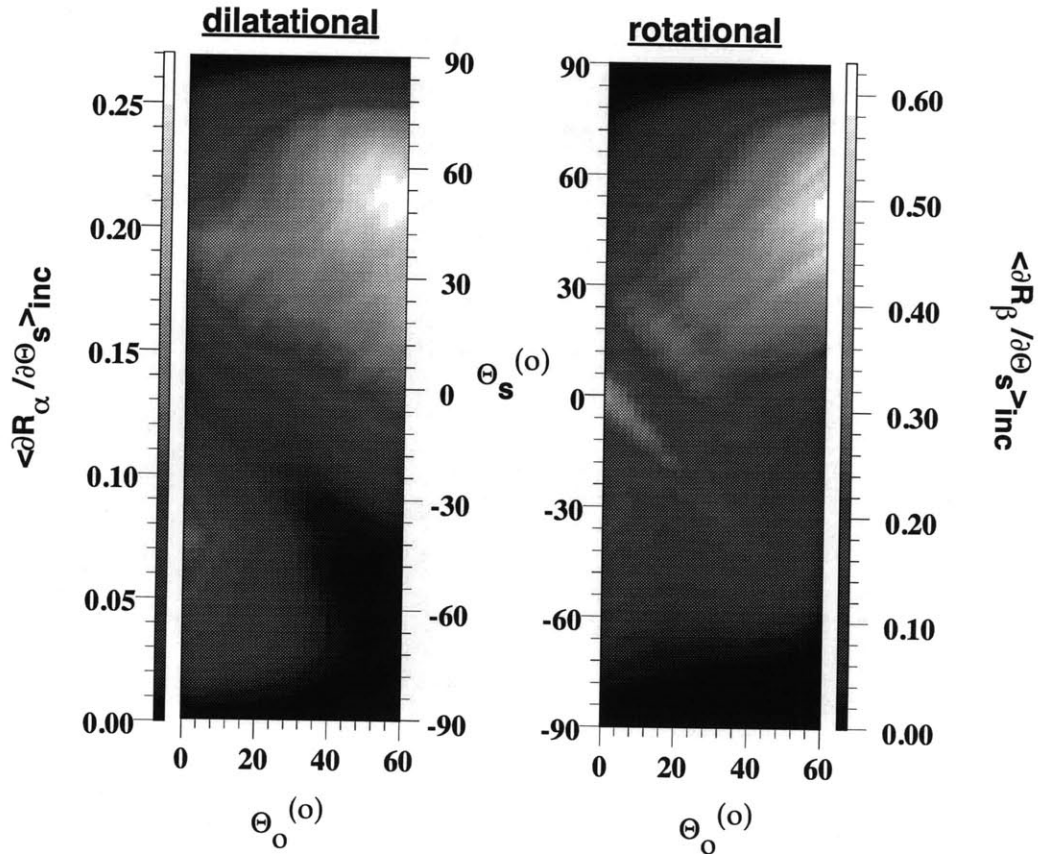


Figure 4-6: The mean incoherent DRC obtained for a soil-basement interface with the incident wavelength equal to three-fifths the correlation length of the interface and  $N_r = 1000$ . The two grayscale plots show  $\langle \frac{\partial R_\alpha}{\partial \theta_s} \rangle$  and  $\langle \frac{\partial R_\beta}{\partial \theta_s} \rangle$  for the scattered P and SV waves, respectively, given an incident SV wave. The interface has an *rms* slope of  $30^\circ$ , where  $L = 6600m$ ,  $\lambda_\alpha = 251m$ ,  $\lambda_\beta = 151m$ ,  $w = 900m$ ,  $\delta = 102.06m$ , and  $a = 250m$ .

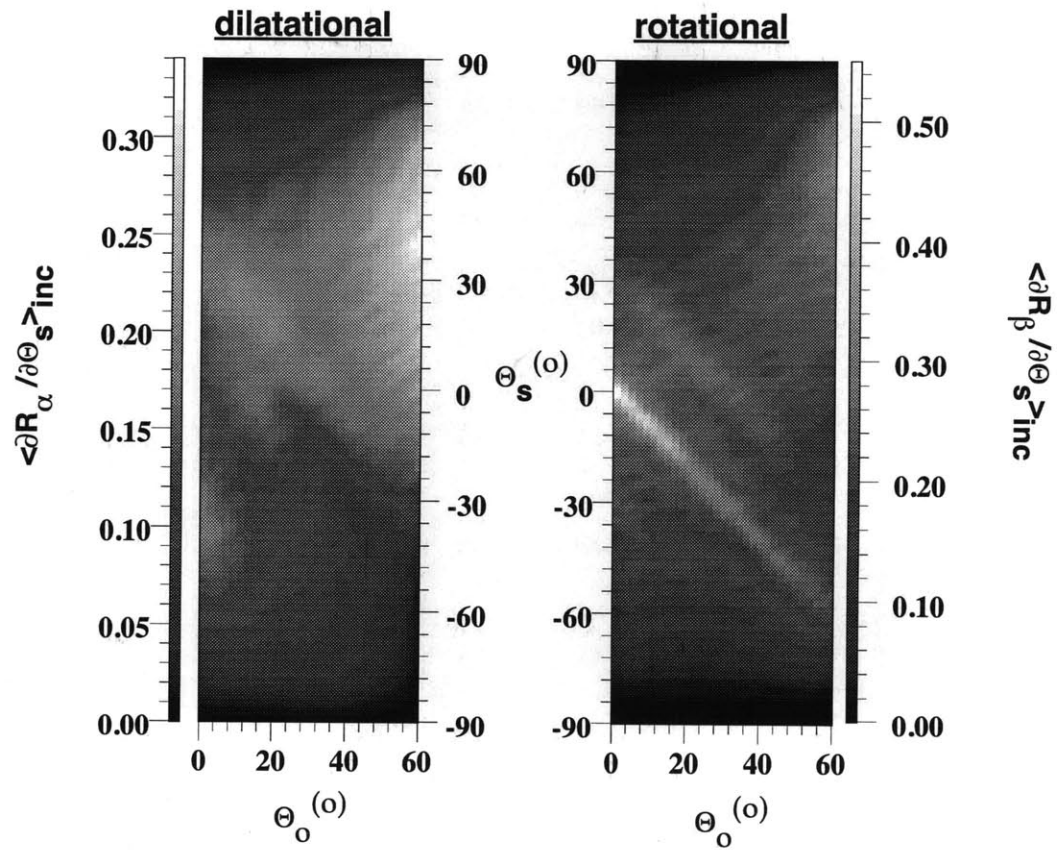


Figure 4-7: Similar to Figure 4-7, except the interface has a  $45^{\circ}$  *rms* slope, corresponding to  $\delta = 176.77$ .

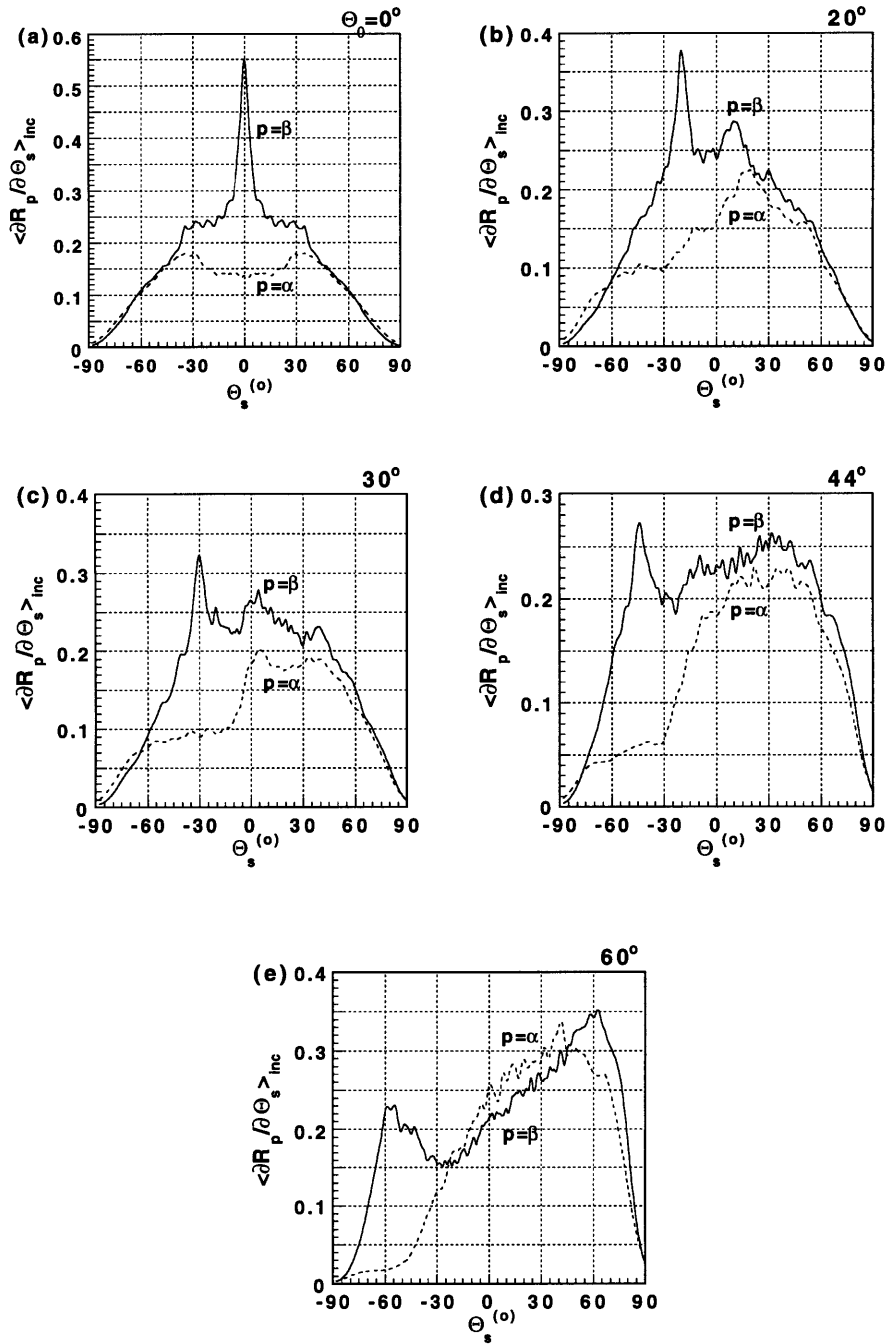


Figure 4-8: Profiles of the mean incoherent DRC obtained over the soil-basement interface with an *rms* slope of  $45^\circ$  and an incident SV wave with a wavelength three-fifths the correlation length of the interface (see Figure 4-7). Each graph represents one incident beam angle: (a)  $0^\circ$  (b)  $20^\circ$  (c)  $30^\circ$  (d)  $44^\circ$  (e)  $60^\circ$ .

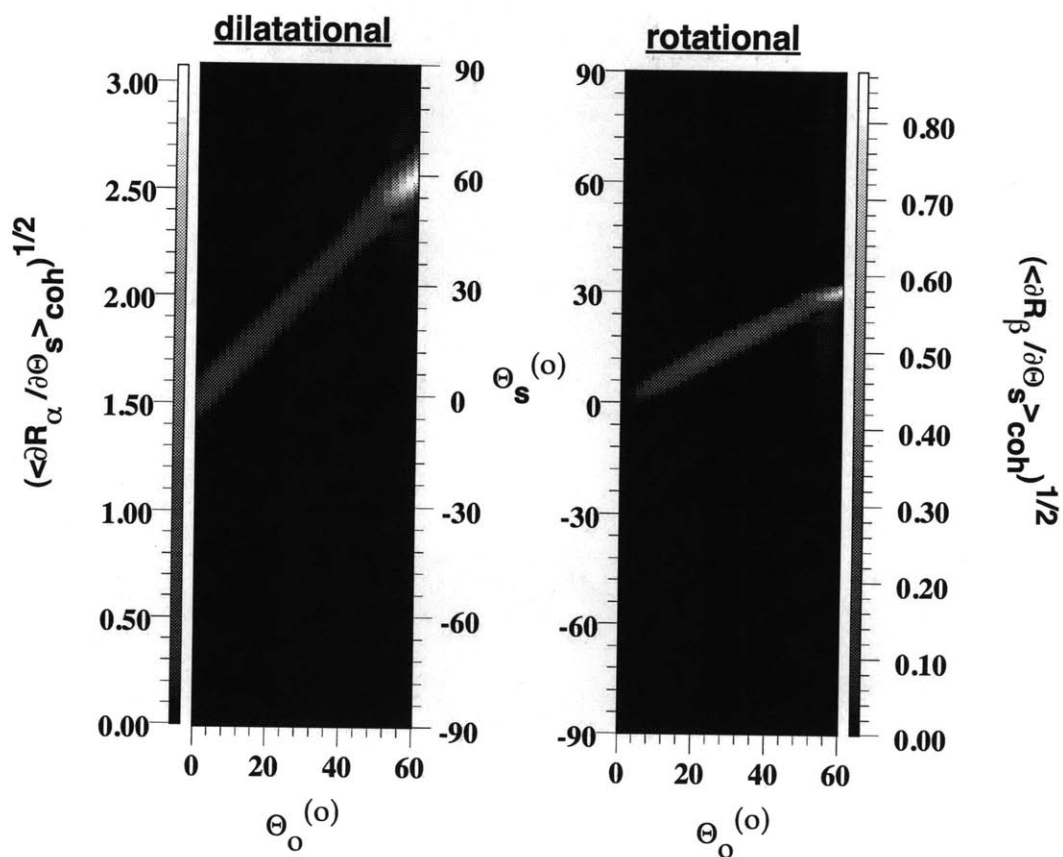


Figure 4-9: The mean total DRC obtained for a plane Mohorovičić discontinuity. Both the dilatational and rotational components of the DRC are plotted. The interface has  $L = 26.7\text{km}$ ,  $\lambda_\alpha = 935.49\text{m}$ ,  $\lambda_\beta = 544.54\text{m}$ , and  $w = 3300\text{m}$ .

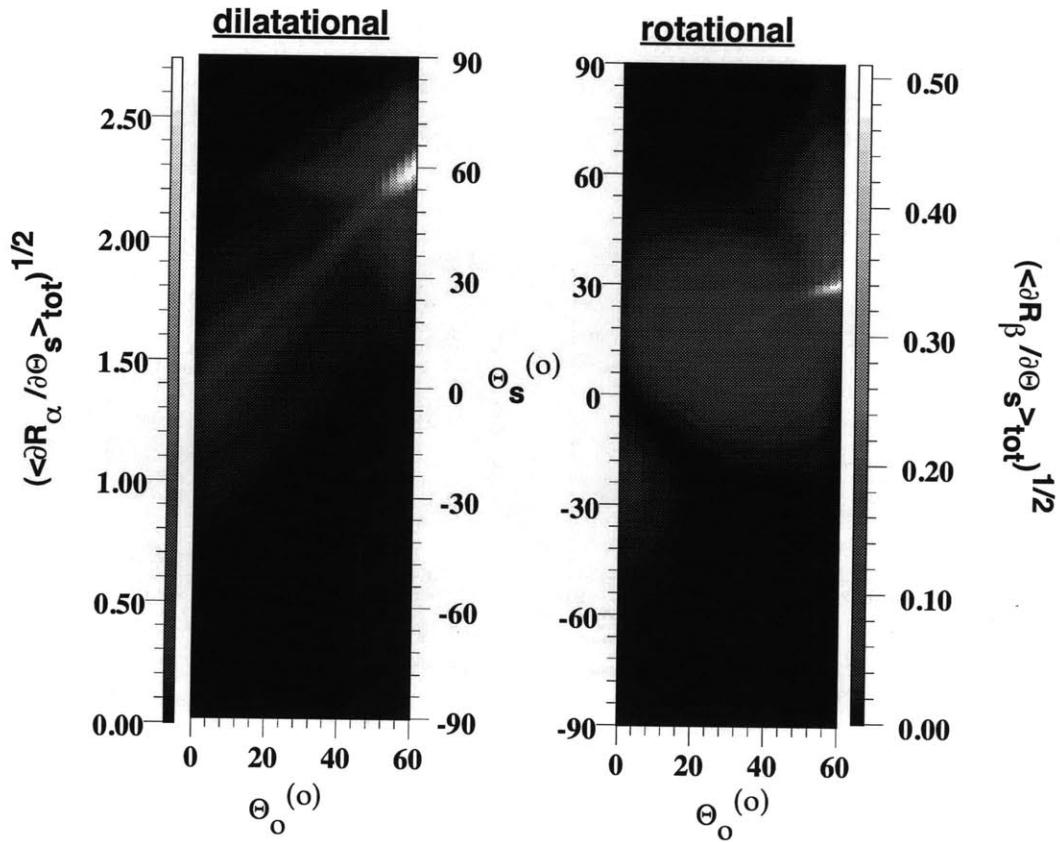


Figure 4-10: The mean total DRC obtained for a Mohorovičić discontinuity with an incident P wave having a wavelength equal to the correlation length of the interface with  $N_r = 300$ . Both the dilatational and rotational components of the DRC are plotted. The interface has an *rms* slope of  $10^\circ$ , where  $L = 26.7km$ ,  $\lambda_\alpha = 935.49m$ ,  $\lambda_\beta = 544.54m$ ,  $w = 3300m$ ,  $\delta = 115.59m$ , and  $a = 927,075m$ .

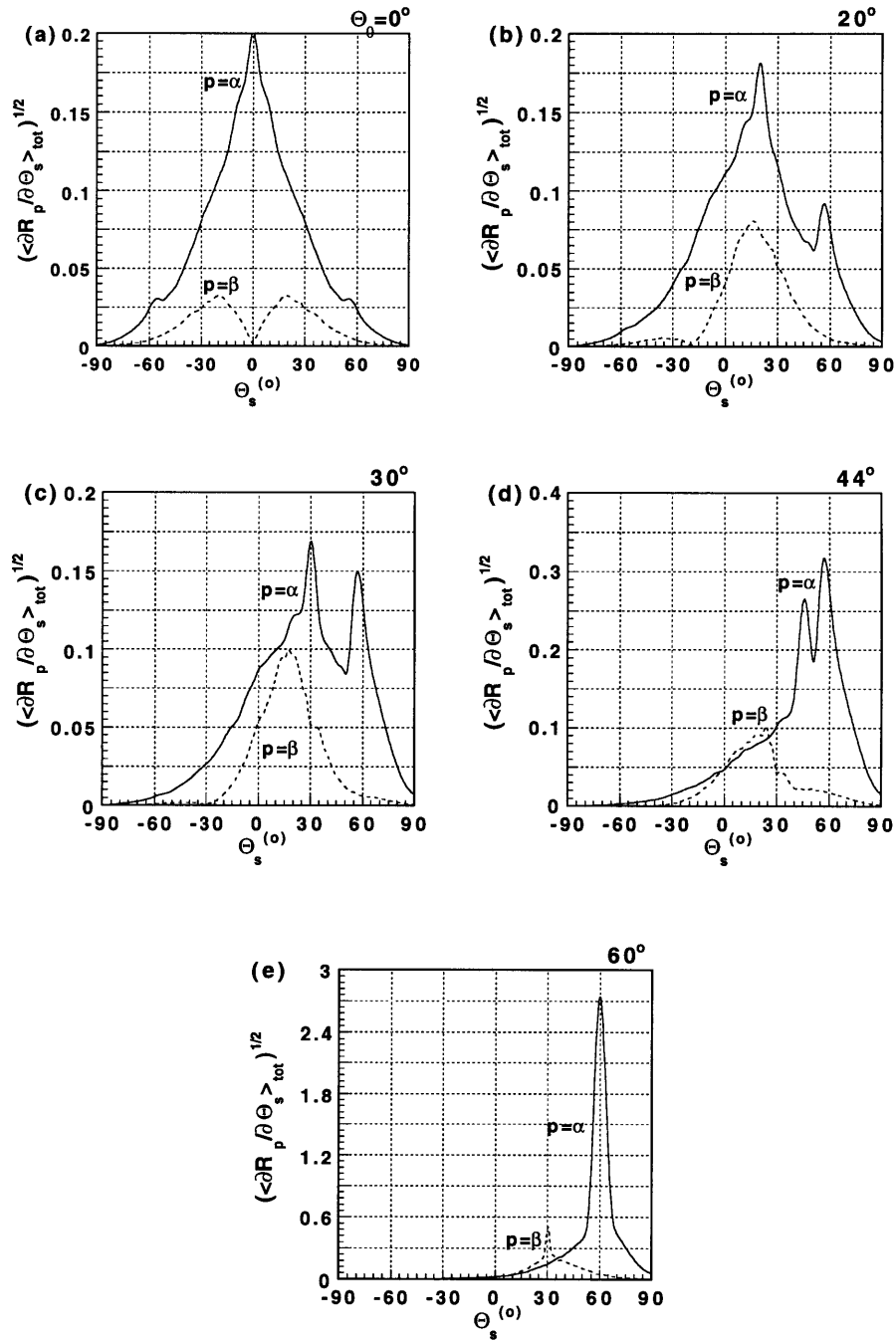


Figure 4-11: Profiles of the mean total DRC obtained over a Mohorovičić discontinuity with an *rms* slope of  $10^\circ$  and an incident P wave with a wavelength equal to the correlation length of the interface (see Figure 4-10). Each graph represents one incident beam angle: (a)  $0^\circ$  (b)  $20^\circ$  (c)  $30^\circ$  (d)  $44^\circ$  (e)  $60^\circ$ .

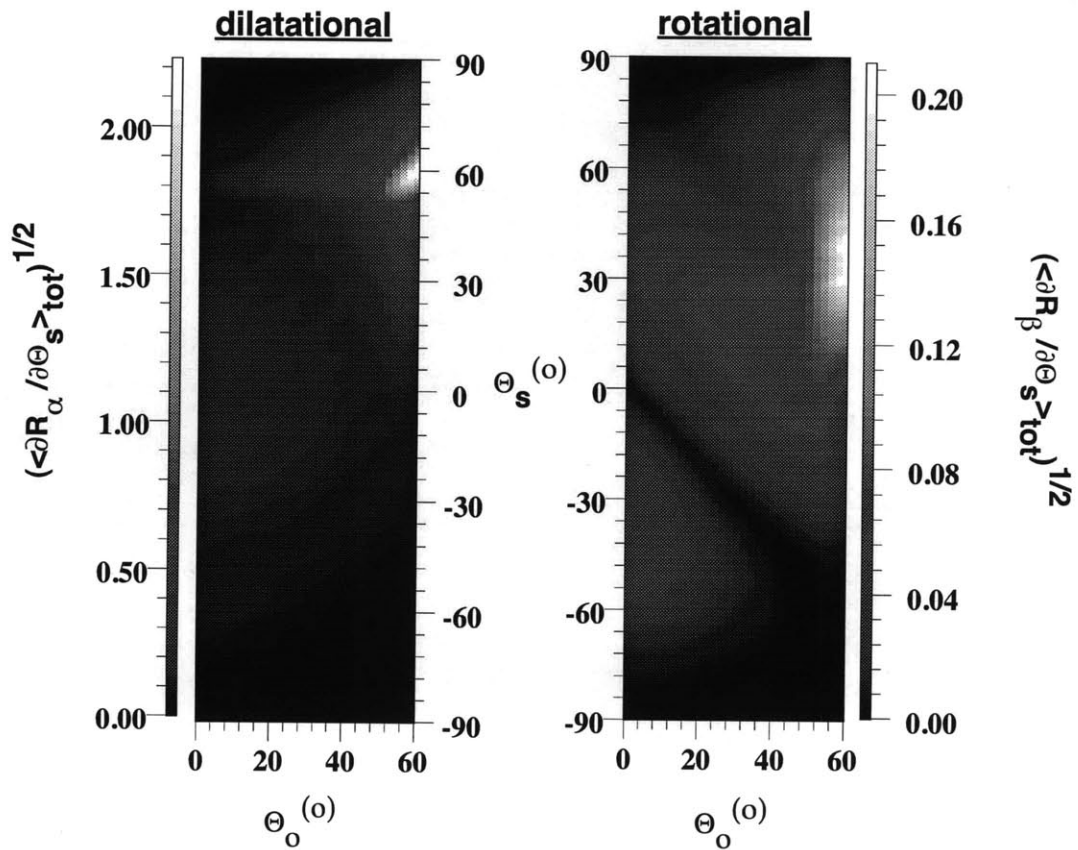


Figure 4-12: Similar to Figure 4-10, except the interface has a  $20^\circ$  rms slope, corresponding to  $\delta = 238.62m$ . The number of realizations,  $N_r$ , is 500.

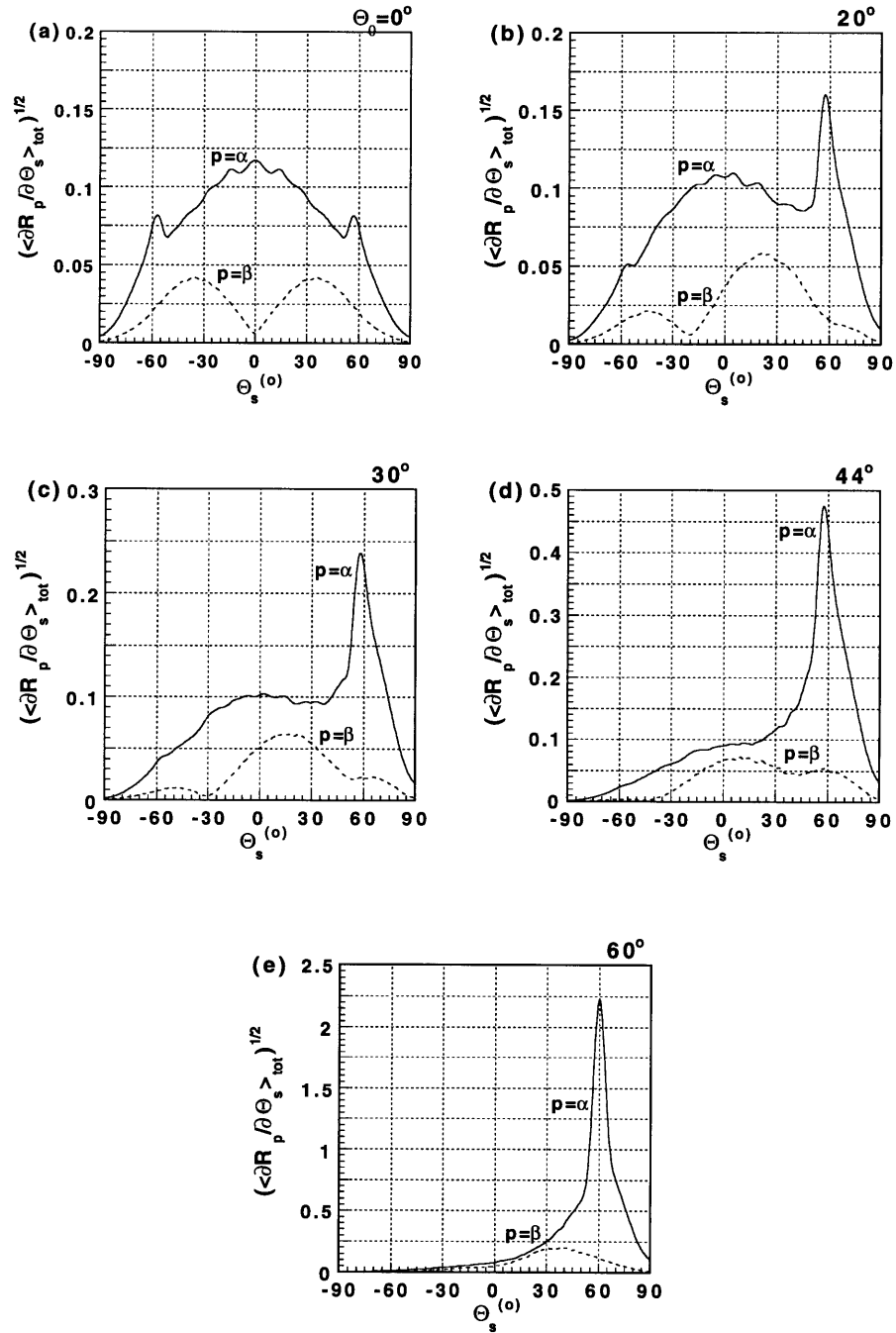


Figure 4-13: Profiles of the mean total DRC obtained over a Mohorovičić discontinuity with an *rms* slope of  $20^\circ$  and an incident P wave with a wavelength equal to the correlation length of the interface (see Figure 4-12). Each graph represents one incident beam angle: (a)  $0^\circ$  (b)  $20^\circ$  (c)  $30^\circ$  (d)  $44^\circ$  (e)  $60^\circ$ .

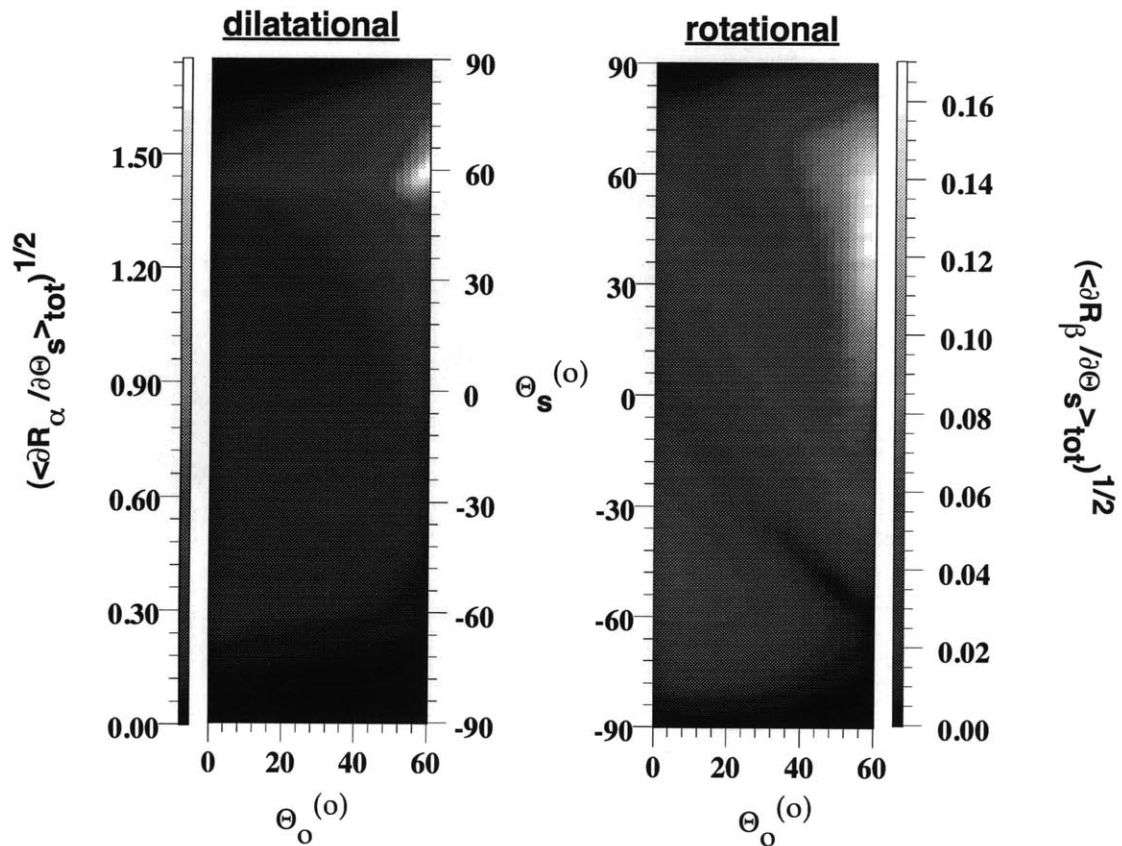


Figure 4-14: Similar to Figure 4-10, except the interface has a  $30^\circ$  *rms* slope, corresponding to  $\delta = 378.48$  m. The number of realizations,  $N_r$ , is 1000.

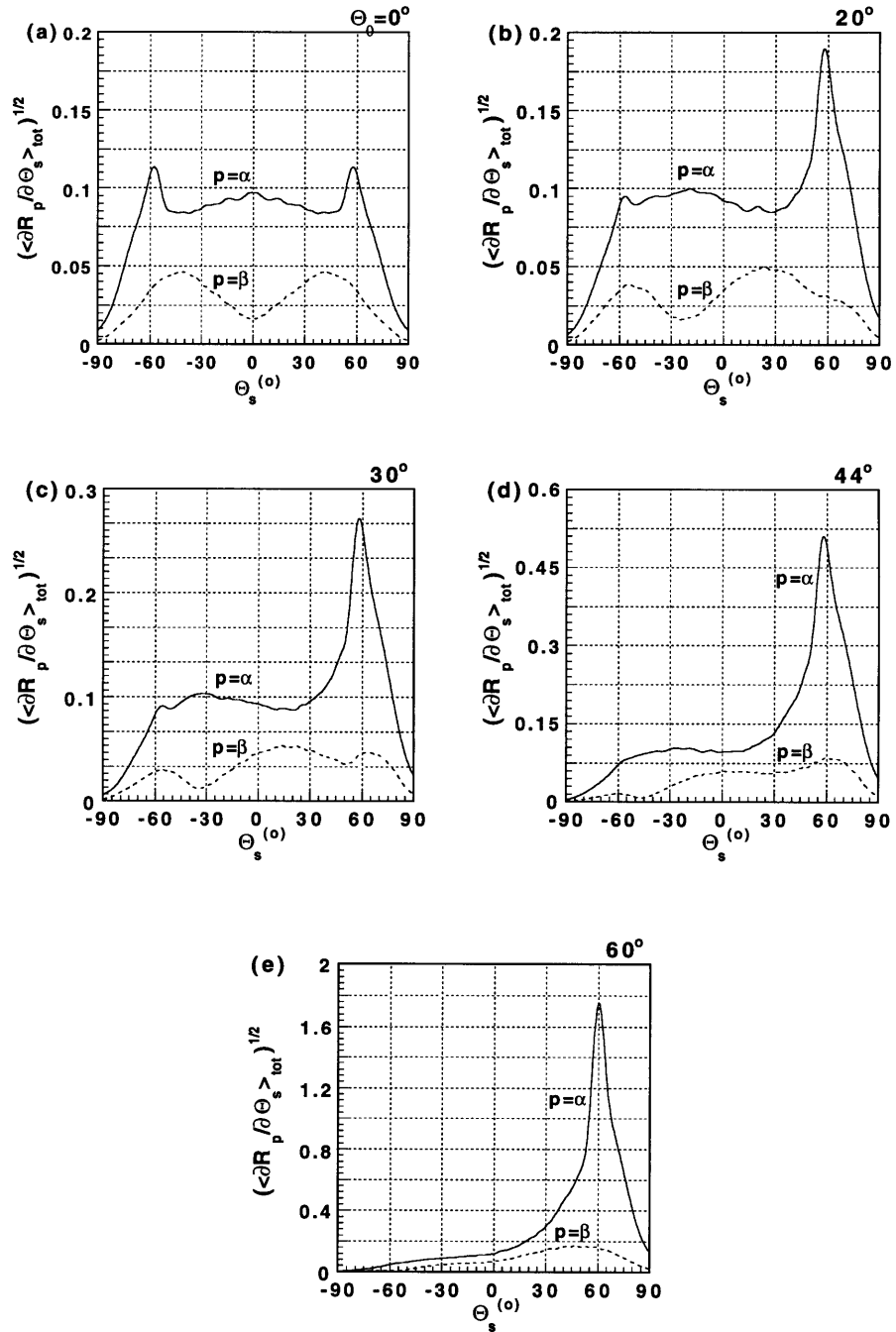


Figure 4-15: Profiles of the mean total DRC obtained over a Mohorovičić discontinuity with an *rms* slope of 30° and an incident P wave with a wavelength equal to the correlation length of the interface (see Figure 4-14). Each graph represents one incident beam angle: (a) 0° (b) 20° (c) 30° (d) 44° (e) 60°.

### Presence of Time-Reversed Wave Paths

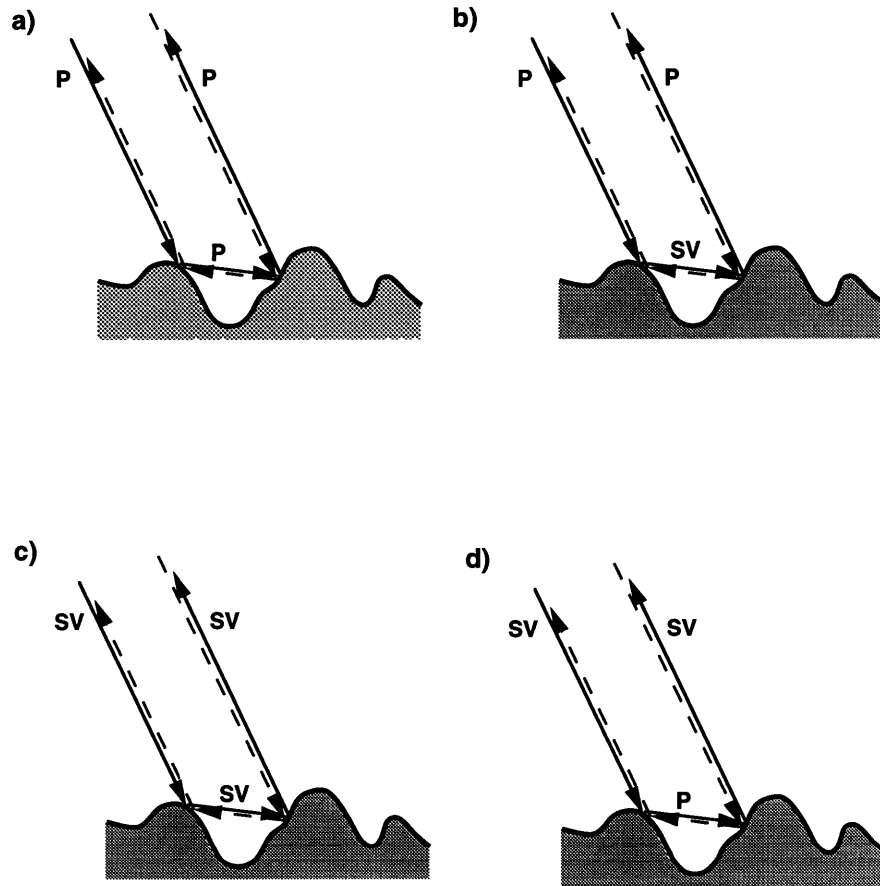


Figure 4-16: Multiple scattering scenarios which create time-reversed constructive interference in the retroreflective direction. Note that this occurs for P-to-P wave and SV-to-SV wave scattering.

### Absence of Time-Reversed Wave Paths

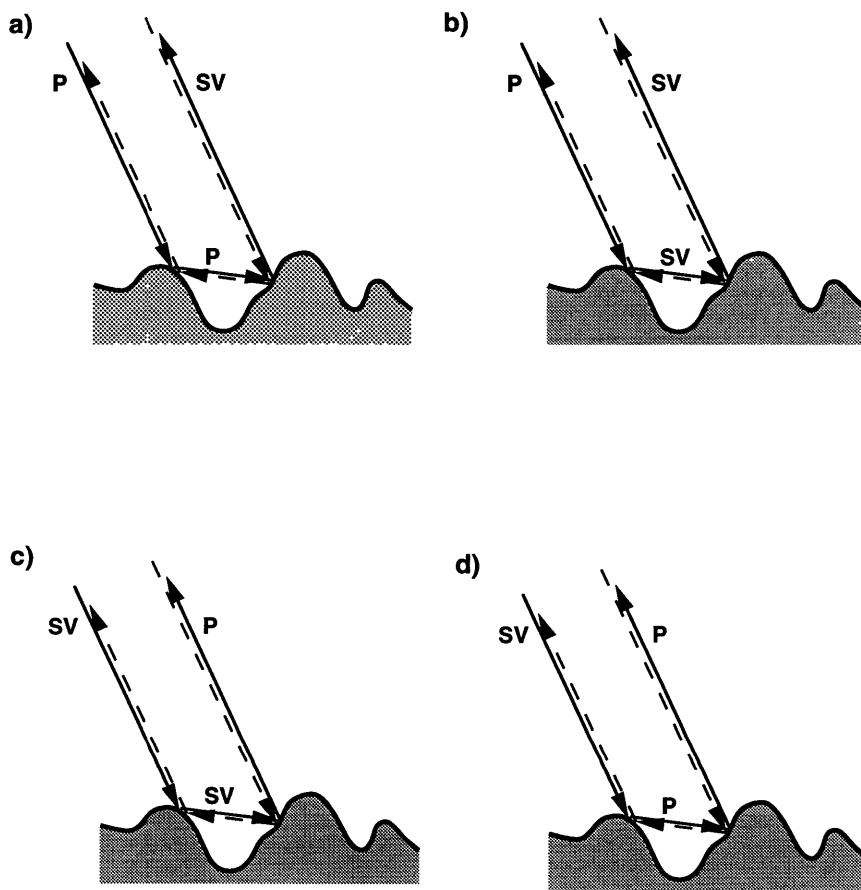


Figure 4-17: Multiple scattering scenarios which do not create time-reversed constructive interference in the retroreflective direction. Note that these occur for P-to-SV and SV-to-P wave scattering.

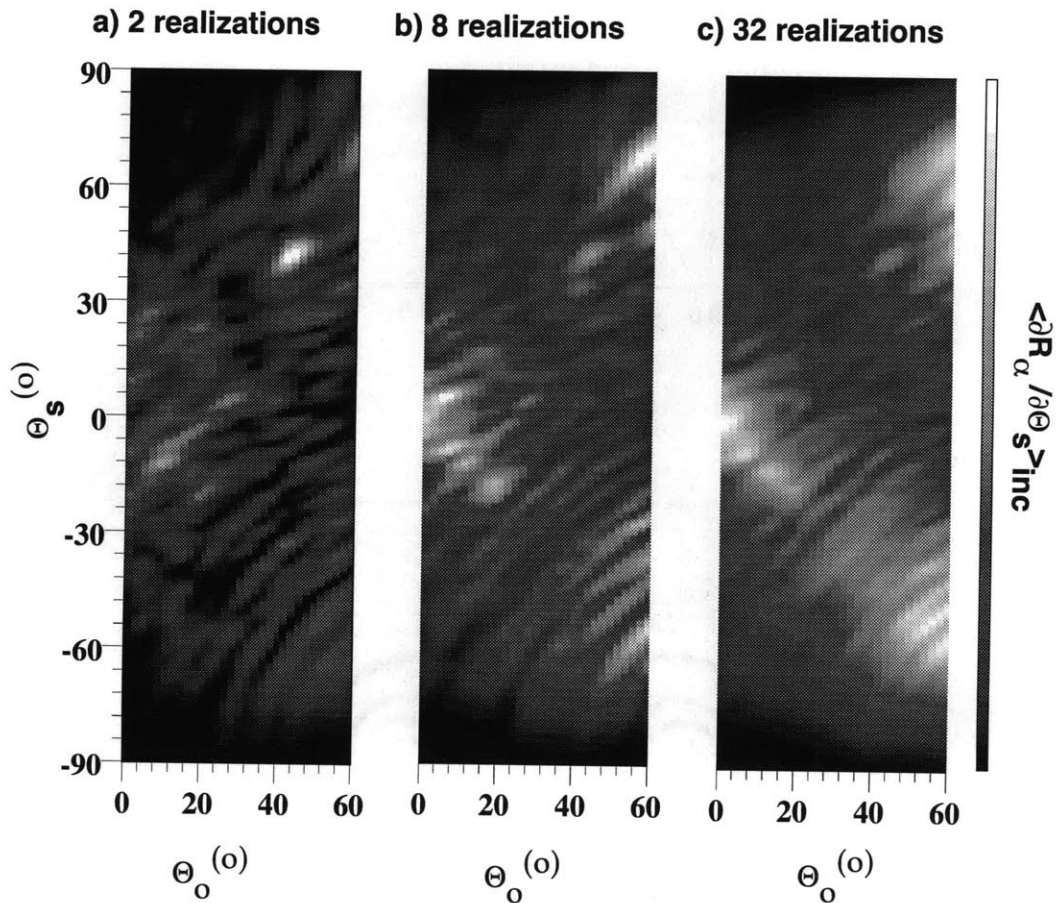


Figure 4-18: The mean incoherent dilatational contribution to the DRC for a P wave incident on a soil-basement interface given a finite average with (a) 2 realizations, (b) 8 realizations, and (c) 32 realizations. This corresponds to the case shown in Figure 4-4 and Figure 4-5.

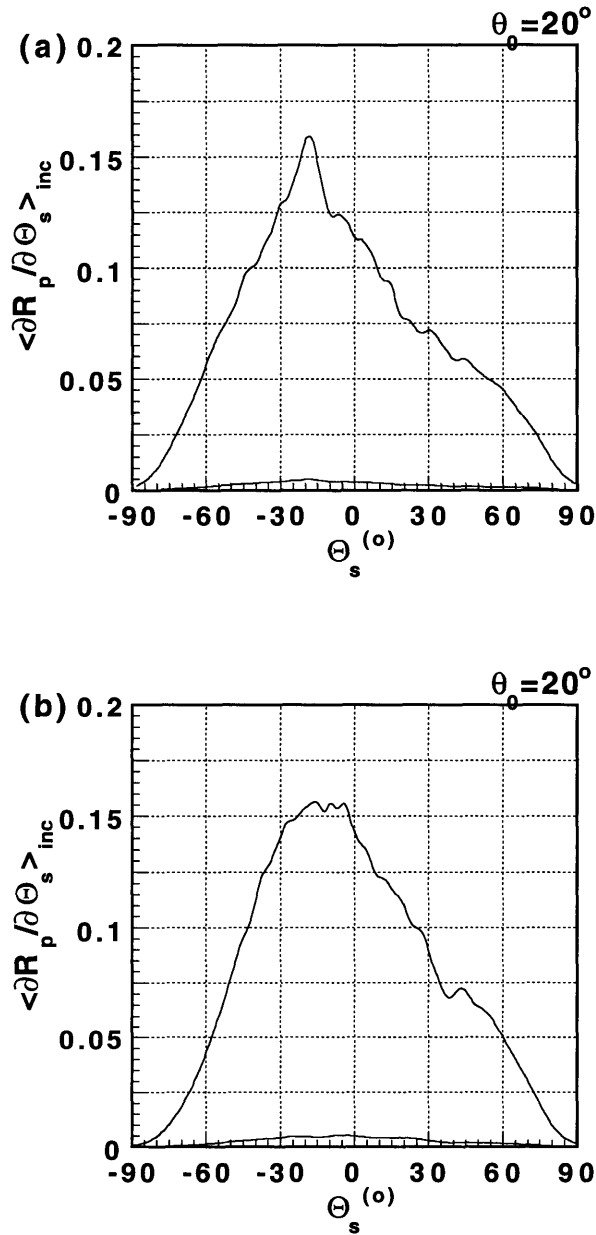


Figure 4-19: The mean incoherent dilatational contribution to the DRC for a P wave incident on a soil-basement interface. The corresponding error of the finite average used to calculate the mean is also plotted: (a) corresponds to an interface with a  $45^\circ$  *rms* slope shown in Figure 4-5 ( $p = \alpha$ ) while (b) corresponds to an interface with a  $30^\circ$  *rms* slope with ( $p = \alpha$ ).

# Chapter 5

## Experimental Study of Scattering from a Highly Irregular, Acoustic-Elastic Interface

### 5.1 Summary

In this chapter, we experimentally and numerically develop statistical models for the scattering of an acoustic P wave which is incident on a highly irregular, random acoustic-elastic interface to determine the general nature of reflected energy. We then elucidate whether or not enhanced backscattering, already identified numerically in previous chapters for acoustic (SH) and fully elastic media (P-SV), occurs. Numerically, the problem is solved in two-dimensions by coupling the representation theorem for an elastic medium and Green's second integral theorem with the extinction theorem. Exact integral expressions for the scattered pressure in the acoustic medium are then obtained, which include all converted and all multiply scattered waves at the

boundary. Experimentally, a glass etching process using photoresist templates with Gaussian statistics allows for the generation of characterized interface irregularities. In this study we generate a 3-D interface with a Gaussian correlation function and a Gaussian height distribution (surface profilometer measurements confirm this fact). Experiments were performed on a 3-D glass surface with an 'rms' slope of 30 degrees (comparable to a water-igneous contact with irregular topography) for the case of an incident wavelength with a size on the same order as the interface irregularities. The numerical models predict an enhancement of energy diffracted back towards the source. Results, obtained in our in-house ultrasonic laboratory, strongly support the presence of this retroreflective energy. In terms of general scattering, we find that, at smaller incident angles (relative to vertical), the 2-D numerical results can give insight into the 3-D experimentally observed scattering over most scattering angles. However, at larger incident angles, fundamental differences between 2-D and 3-D scattering may exist.

## 5.2 Introduction

In laboratory experiments, a lack of control over the statistical parameters of a given random model can easily produce ambiguous results. In the case of irregular interfaces, the height probability distribution and the correlation lengths of the interface may be poorly constrained, the interface statistics may show nonstationarity, and the interface may contain a wide variety of length scales. Each of these experimental uncertainties makes comparisons with numerical models difficult, if not impossible. It is the goal of this study to physically fabricate a random interface which is stationary in space, with both a simple probability distribution in height and a simple transverse correlation function. Statistical experimental results can then be easily compared with the corresponding numerical results.

The accurate physical generation of a Gaussian surface is important experimentally, since Gaussian interfaces are mathematically convenient and have been widely used up to this point in scattering studies. Many theoretical formulations in the literature apply the simple properties of a Gaussian correlation function to heterogeneities. Examples can be found in Prange and Toksöz (1990), Knopoff and Hudson (1964, 1967), Haddon (1978), and Kuperman and Schmidt (1989). However, a Gaussian autocorrelation function is a somewhat unrealistic model for many regions of the earth since a Gaussian function is continuously differentiable and has an exponential decay in spectral amplitude. This continuous differentiability and narrow wavenumber spectrum result in a very smooth model with one dominant length scale. More general fractal processes, which exhibit fluctuations on all length scales, are likely a more realistic model of true Earth structure. The most commonly utilized fractal representation is an exponential covariance function. In this case the model is continuous but not differentiable, making it a far rougher model than that given by the Gaussian function. The exponential covariance function has been utilized extensively and in many instances gives a good description of physical properties (e.g. Wu and Aki, 1985; Frankel and Clayton, 1986). Recently, Goff and Jordan (1988) have generalized the exponential function. In this case, seafloor topography was modeled as a two-point covariance function with five free parameters which describe the amplitude, orientation, characteristic wavenumbers, and Hausdorff (fractal) dimension of the topography. These self-affine surfaces, of which the exponential covariance function is a special case, have been shown to give good first order stochastic descriptions of seafloor morphology.

As a first step at modeling scattering by irregular interfaces we fabricate and physically model an irregular interface with a Gaussian correlation function. Upon evaluating the effectiveness of this experimental model in the case of the smoother Gaussian surface, more general, self-affine interface models may then be proposed. In this chapter, the statistical parameters of the interface are also chosen so that

the incident wavelength has the same length scale as the correlation length of the irregularities. In addition, the *rms* slope of the interface is chosen to be large, placing the model in a regime where approximate techniques such as the Kirchhoff, Born, and the geometrical ray approaches break down and multiple scattering mechanisms such as "enhanced backscattering" and "shadowing" play dominant roles.

What is "enhanced backscattering" from an acoustic-elastic halfspace? By definition, enhanced backscattering or "retroreflectance" is the enhancement of energy scattered back in the direction of the source. As previously discussed, O'Donnell and Mendez (1987) were the first to propose the hypothesis that time-reversed paths are responsible for enhanced backscattering. This hypothesis was further strengthened by Maradudin *et al.* (1990a) who showed that retroreflectance exists first for energy double scattered from an interface. Further support for this hypothesis was discussed in Chapter 4 where we showed that seismic scattering is consistent with the time-reversed path hypothesis. As predicted, energy enhancement was clearly observed on P-to-P and S-to-S scattering and not on P-to-S and S-to-P scattering. The idea of time-reversed paths is easily extended to the acoustic-elastic case. Take for instance the peak-valley sequence shown in Figure 5-1. If an incident P-wave, shown by the solid line, diffracts from point 1 it will propagate as a P-wave to point 2 and then diffract at some angle into the upper medium again as a P-wave. For most waves traveling away from the interface, enhancement will not occur. However, if the diffracted wave travels directly back towards the source, incident P-wave energy can be found traveling exactly along the reverse path: propagating from point 2 to point 1 and again traveling back towards the source as shown by the dashed line. In this case, the time-reversed path interferes constructively with the forward path and contributes energy towards the source resulting in enhanced backscattering. Using the simple phase argument of previous chapters, the peak width can be written as  $\Delta\theta_s = \frac{\lambda}{l}$ , where  $\Delta\theta_s$  is the angular width of the peak,  $\lambda$  is the incident wavelength, and  $l$  is the mean free path of the interface or, in other words, the average distance

a wave propagates between points 1 and 2 along the interface.

Adapting this phase approach, other path geometries may also contribute to enhanced backscattering in the case of the 3-D interfaces modeled in this chapter. For example, if a wave which encounters the interface multiply scatters from several points outside the vertical source-receiver plane and then sends energy back in the direction of the source, then a time-reversed path may be found which also sends energy back towards the source. In the same manner, many multiply scattered paths, sending energy back towards the source, can be found in the acoustic-elastic case. However, as a result of energy loss with each diffraction from the interface, due to both transmission through the interface and additional spreading, it seems reasonable that the double-scattered paths, both in and out of the source-receiver (incident) plane, will contribute the majority of retroreflective energy.

This chapter is organized as follows. The first section briefly summarizes the extension of the numerical formulations, developed in Chapters 2 through 4, to the case of scattering from a randomly irregular acoustic-elastic interface. In the second section, the physical construction of the characterized glass surface is discussed and the ultrasonic apparatus for measuring the amplitude distribution of energy scattered by the interface is described. The third section directly compares the 3-D experimental results obtained in our in-house ultrasonic water tank with the corresponding 2-D numerical results. Amplitude distributions are presented in detail and scattering mechanisms are proposed. Finally, we investigate the differences between the 2-D synthetic and the 3-D experimental data and discuss possible implications for both 2-D and 3-D scattering mechanisms.

### 5.3 Theory

The numerical approach and notation in this section follows that of Chapters 3 and 4 (Schultz and Toksöz, 1993 1994). Since the approach here is very similar to the SH and P–SV cases, we give only a brief outline of the theoretical approach. We first express the total scattered displacement at any point within two volumes of elastic material with the Somigliana representation theorem (*e.g.*, Aki and Richards, 1980). Simplifying this theorem to a 2–D case gives a set of four integral equations

$$\begin{aligned}
 H[1]u_n^{(l)}(\underline{x}) &= \int_V f_p^{(l)}(\underline{\eta})G_{np}^{(l)}(\underline{x}; \underline{\eta})dV(\underline{\eta}) \\
 &\quad - (-1)^i \int_S dS(\underline{x}') \{ [c_{ijpq}^{(l)} \hat{n}_j(\underline{x}') \partial G_{np}^{(l)}(\underline{x}; \underline{x}') / \partial x'_q] u_i^{(l)}(\underline{x}') \\
 &\quad - G_{np}^{(l)}(\underline{x}; \underline{x}') T_p^{(l)}(\underline{\mathbf{u}}^{(l)}(\underline{x}'), \hat{n}) \},
 \end{aligned} \tag{5.1}$$

where gradients are zero in the  $x_2$ –direction. Following the notation of Chapter 4 (Schultz and Toksöz, 1994a),  $T_p^{(l)}(\underline{x})$  is the traction vector along the interface in both the fluid ( $l = f$ ) and the solid ( $l = s$ ), and we have again assumed all surfaces to be far enough away so that only the surface,  $S(\underline{x})$ , separating the two volumes, contributes to the final displacement.  $G_{np}(\underline{x}; \underline{x}')$  is a Green’s function giving the  $n$ –component of displacement at  $\underline{x}$  resulting from a point force in the  $p$ –direction at  $\underline{x}'$ ,  $c_{ijpq}$  is the elasticity tensor, and  $H[i]$  is a function that takes a value of 0 or 1 depending on whether the point  $\underline{x}$  lies outside or inside the volume of interest,  $i$ , respectively. We again assume that the media are homogeneous and isotropic, so the constitutive relation can be written with the aid of the elasticity tensor as

$$\tau_{ij}(\underline{x}) = \lambda \Theta(\underline{x}) \delta_{ij} + \mu [u_{i,j}(\underline{x}) + u_{j,i}(\underline{x})], \tag{5.2}$$

where  $\Theta(\underline{x}) = u_{k,k}(\underline{x})$  is the dilatational parameter and  $\lambda$  and  $\mu$  are the Lamé parameters for the medium.

In this work the upper medium is acoustic, supporting propagation of only dilatational waves, while the lower medium is taken to be elastic. The boundary separating

these two media is shown in Figure 5-2. The boundary conditions for the resulting acoustic–elastic boundary, can be written in the general form

$$\begin{aligned}\underline{\mathbf{n}} \cdot \underline{\mathbf{u}}^{(f)}(\underline{\mathbf{x}})|_{x_3=\zeta(x_1)} &= \underline{\mathbf{n}} \cdot \underline{\mathbf{u}}^{(s)}(\underline{\mathbf{x}})|_{x_3=\zeta(x_1)}, \\ \underline{\mathbf{T}}^{(f)}(\underline{\mathbf{x}})|_{x_3=\zeta(x_1)} &= \underline{\mathbf{T}}^{(s)}(\underline{\mathbf{x}})|_{x_3=\zeta(x_1)}, \\ \underline{\mathbf{n}} \times \underline{\mathbf{T}}^{(s)}(\underline{\mathbf{x}})|_{x_3=\zeta(x_1)} &= \mathbf{0},\end{aligned}\tag{5.3}$$

where the surface profile function is taken to be  $x_3 = \zeta(x_1)$  and the unit normal vector along the interface is consistent with the previous chapters

$$\hat{\mathbf{n}} = (-\zeta'(x_1), 1)[1 + (\zeta'(x_1))^2]^{-\frac{1}{2}}.\tag{5.4}$$

The first boundary condition represents the continuity of normal displacement and the other two conditions together represent the continuity of normal stress. Referring to the requirement for continuity of normal displacement one can expand the first term of the volume integral (5.1) as

$$n_i c_{ijpq}^{(f)} u_i^{(f)}(\underline{\mathbf{x}}) = \lambda^{(f)} n_i u_i^{(f)}(\underline{\mathbf{x}}) \delta_{pq},\tag{5.5}$$

which follows from the lack of rigidity in the acoustic medium,  $\mu^{(f)} = 0$ . The last two boundary conditions in (5.3) infer the continuity of fluid pressure at the interface. Upon combining these two boundary conditions with the constitutive relation, (5.2), the traction in the solid can be expressed at the interface as

$$T_p^{(s)}(\underline{\mathbf{x}}) = S^{(f)}(\underline{\mathbf{x}}) n_p = \lambda^{(f)} \theta^{(f)} n_p,\tag{5.6}$$

where  $S^{(f)}(\underline{\mathbf{x}})$  is the fluid pressure in the fluid. Finally, referring to eq. (5.5) and comparing it with a similar expansion in the elastic medium, it is clear that the equality  $u_i^{(s)}(\underline{\mathbf{x}}) = U_i(\underline{\mathbf{x}}) = u_i^{(f)}(\underline{\mathbf{x}})$  implies that the normal displacement is continuous, or  $n_k u_k^{(s)}(\underline{\mathbf{x}}) = n_k u_k^{(f)}(\underline{\mathbf{x}}) = n_k U_k(\underline{\mathbf{x}})$ .

Taking our volume of interest to be the upper acoustic medium, placing the incident wave in the acoustic medium, and substituting the final form of the boundary

conditions (5.3), the integral equation in the lower elastic medium can be written as

$$0 = \int_{-\infty}^{\infty} dx'_1 [U_i(\underline{x}') c_{ijpq}^{(s)} n_j \frac{\partial G_{np}^{(s)}(\underline{x}; \underline{x}')}{\partial x'_q} - G_{np}^{(s)}(\underline{x}; \underline{x}') S^{(f)}(\underline{x}') n_p], \quad (5.7)$$

where the unknowns are the fluid pressure,  $S^{(f)}(\underline{x})$ , and the displacement,  $\underline{U}(\underline{x})$ , along the interface where  $S^{(f)}(\underline{x})$  should not be confused with the surface function referred to previously.

In the acoustic medium, the surface integral can be greatly simplified. Since shear waves cannot propagate in the acoustic medium, one of the two integral equations, (5.1), in the upper medium is redundant and can be combined into one equation. Take the fluid pressure in the acoustic medium,  $S^{(f)}(\underline{x})$ , which satisfies the basic wave equation

$$\nabla^2 S^{(f)}(\underline{x}) + (k_T^{(f)})^2 S^{(f)}(\underline{x}) = 0, \quad (5.8)$$

assuming no sources are present in the medium. The Helmholtz potential for the displacement,  $\phi^{(f)}(\underline{x})$ , also satisfies a similar wave equation. Operating in the frequency domain and differentiating we find that  $\phi^{(f)}(\underline{x})$  is directly related to the P wave pressure,

$$\phi^{(f)}(\underline{x}) = -(\rho^{(f)} \omega^2)^{-1} S^{(f)}(\underline{x}). \quad (5.9)$$

Using this relation, the normal displacement at the interface can be expressed as

$$\frac{\partial S^{(f)}(\underline{x})}{\partial n} = -\rho^{(f)} \omega^2 (n_k u_k^{(f)}(\underline{x})) = -\lambda k_T^{(f)2} (n_k u_k^{(f)}(\underline{x})) \quad (5.10)$$

and using the Green's function for the pressure,  $G^{(f)}(\underline{x}; \underline{x}')$ , the integral equation in the acoustic medium can be expressed with the aid of Green's second integral theorem as

$$S^{(f)}(\underline{x}) = S^{(f)}(\underline{x})_{incid} + \int_{-\infty}^{+\infty} dx'_1 [\lambda^{(f)} S^{(f)}(\underline{x}') \frac{\partial G^{(f)}(\underline{x}; \underline{x}')}{\partial n} + \lambda^{(f)2} k_T^{(f)2} G^{(f)}(\underline{x}; \underline{x}') n_k u_k^{(f)}(\underline{x}')], \quad (5.11)$$

where we have utilized (5.10). Equations (5.7) and (5.11) together consist of three integral equations with three unknown functions where these integral equations now

represent the total scattered field in the both media. Letting  $x_3 \rightarrow \zeta^+(x_1)$ , the final set of coupled integral equations can be written as,

$$S(\underline{x}) = S^{(f)}(\underline{x})_{incid} + \int_{-\infty}^{+\infty} dx'_1 [S(\underline{x}')T^{(f)}(\underline{x}|\underline{x}') - D_n^{(f)}(\underline{x}|\underline{x}')D_n(\underline{x}')], \quad (5.12)$$

in the acoustic medium, and

$$0 = - \int_{-\infty}^{+\infty} dx'_1 [U_i(\underline{x}')T_i^{n(s)}(\underline{x}|\underline{x}') - \frac{\lambda^{(f)}}{\mu^{(s)}} D_n^{(s)}(\underline{x}|\underline{x}')S(\underline{x}')], \quad (5.13)$$

in the elastic medium. We have defined

$$T^{(f)}(\underline{x}|\underline{x}') = \lambda^{(f)} \frac{\partial G^{(f)}(\underline{x}; \underline{x}')}{\partial n} \Big|_{x_3=\zeta(x_1)},$$

$$D_i^{(f)}(\underline{x}|\underline{x}') = -\lambda^{(f)} k_T^{(f)2} G^{(f)}(\underline{x}; \underline{x}') n_i \Big|_{x_3=\zeta(x_1)}, \quad (5.14)$$

$$T_i^{n(s)}(\underline{x}|\underline{x}') = T_i^{n(s)}(\underline{x}|\underline{x}') \Big|_{x_3=\zeta(x_1)}, \quad (5.15)$$

$$D_n^{(s)}(\underline{x}|\underline{x}') = \mu^{(s)} G_{np}^{(s)}(\underline{x}; \underline{x}') n_p \Big|_{x_3=\zeta(x_1)}.$$

in the respective media. The unknown source strength functions now can be expressed as a function of  $x_1$  alone

$$S(x_1) = \theta^{(f)}(\underline{x}) \Big|_{x_3=\zeta(x_1)}, \quad (5.16)$$

$$D_i(x_1) = U_i^{(f)}(\underline{x}) \Big|_{x_3=\zeta(x_1)},$$

where we have normalized the pressure term with respect to  $\lambda^{(f)}$  to ensure that the final numerical conditions are well conditioned. Once these source strength functions are determined, the scattered field in the acoustic medium can be expressed completely.

To determine the final reflection coefficient for a given interface, the final scattered displacement can be decomposed into a superposition of plane wave contributions. This is accomplished with the Cartesian coordinate form of the Green's function for an unbounded fluid space. This Green's function can be written as

$$G^{(f)}(\underline{x}; \underline{x}') = \frac{i}{4\pi\lambda^{(f)}} \int_{-\infty}^{+\infty} dk \frac{e^{ik(x_1-x'_1)+ik_3^{(f)}|x_3-x'_3|}}{k_3^{(f)}}, \quad (5.17)$$

where

$$k_3^{(f)} = ((k_T^{(f)})^2 - k^2)^{\frac{1}{2}}, \quad \text{Im}(k_3^{(f)}) > 0,$$

which corresponds to a pressure source,  $P(\underline{x}) = -\lambda^{(f)-1}\delta(x_1 - x'_1)\delta(x_3 - x'_3)$  applied at  $\underline{x}'$  in the fluid. Substituting (5.17) into the surface integral (5.12) the scattered pressure at any point  $x_3 > \zeta(x_1)_{max}$  in the fluid can be decomposed into a summation of plane waves

$$S(\underline{x})_{scat} = + \int_{-\infty}^{+\infty} \frac{dk}{2\pi k_3^{(f)}} R_f(k\omega) e^{+ikx_1 + ik_3x_3}, \quad (5.18)$$

where the amplitude coefficient takes the form

$$R_f(k\omega) = \frac{i}{2} \int_{-\infty}^{+\infty} dx'_1 [iS(\underline{x}') (k\zeta'(\underline{x}') - k_3^{(f)}) - k_T^{(f)2} (\zeta'(x'_1)D_1(\underline{x}') - D_3(\underline{x}'))] e^{-ikx'_1 - ik_3^{(f)}\zeta'(x'_1)}. \quad (5.19)$$

To reduce the computational demand of this approach, the incident wave is expressed as a narrow Gaussian beam source following Chapters 3 and 4. This again allows for a reduction in the length of integration along the acoustic boundary, since only a small portion of the interface is excited by the incident beam. The pressure of a Gaussian beam incident at an angle,  $\theta_0$ , in the acoustic medium can be written as

$$S^{(f)}(\underline{x})_{inc} = e^{ik_T^{(f)}(x_1 \sin\theta_0 - x_3 \cos\theta_0)} [1 + W(\underline{x})] e^{-((x_1 \cos\theta_0 + x_3 \sin\theta_0)/w)^2}, \quad (5.20)$$

where

$$W(\underline{x}) = \frac{1}{k_T^{(f)2} w^2} \left[ \frac{2}{w^2} (x_1 \cos\theta_0 + x_3 \sin\theta_0)^2 - 1 \right], \quad (5.21)$$

which is an approximation to the wave equation, (5.8), and is valid so long as  $\frac{\omega w}{2c} \gg 1$ , where  $w$  is the half-width of the Gaussian beam. We also express  $w = h \cos\theta_0$ , where  $h$  is the half-width of the incident beam as seen on the plane  $x_3 = 0$ .

An approximation to the Fourier reflection coefficient can now be written in terms of the amplitude coefficient, (5.19). Normalizing this amplitude coefficient by the

amplitude of the plane wave component of the incident Gaussian beam which arrives precisely at the incident angle, the reflection coefficient can be expressed as

$$R(k\omega) = \frac{|r_p(\theta_s)|}{2\sqrt{\pi}k_T^{(f)}w}, \quad (5.22)$$

where

$$r_p(\theta_s) = \int_{+\infty}^{-\infty} dx'_1 [iS(x'_1)k_T^{(f)}(\sin\theta_s\zeta(x'_1) - \cos\theta_s) - k_T^{(f)2}(\zeta'(x'_1)D_1(x'_1) - D_3(x'_1))]e^{-ik_T^{(f)}(\sin\theta_s x'_1 + \cos\theta_s\zeta(x'_1))}, \quad (5.23)$$

which is comparable in amplitude to the Fourier reflection coefficient calculated for a single incident plane wave. This normalization is different from the Differential Reflection Coefficient implemented in Chapters 3 and 4 (Schultz and Toksöz, 1993 1994). Note also that we let  $k = k_T^{(f)}\sin\theta_s$  and  $k = k_T^{(f)}\cos\theta_s$  above.

Appendix B describes how these integral equations can be solved numerically. We show that the solution over an acoustic–elastic interface can be expressed completely as a combination of the Green’s functions for the P–SV and SH cases, where the shear velocity of the SH wave is changed to the P–wave velocity of the acoustic medium, so as to reflect the acoustic Green’s function. The final coupled integral equations are then transformed to a coupled set of matrix equations and solved using LU decomposition.

### 5.3.1 Numerical Analysis

In this paper two types of interfaces are modeled numerically. Both interfaces have a Gaussian distribution about the mean, where  $\delta^2 = \langle\zeta^2(x_1)\rangle$  is the mean-square departure of the surface from flatness. The first interface studied has a correlation function

$$W(|x_1 - x'_1|) = \delta^{-2}\langle\zeta(x_1)\zeta(x'_1)\rangle, \quad (5.24)$$

described by the Gaussian function,  $W(|x_1|) = \exp(-x_1^2/a^2)$ . As shown previously, the correlation length for a Gaussian interface is approximately equal to the average distance between adjacent peaks and valleys along the interface. The interface can also be described in terms of the *rms* slope of the surface,  $\phi$ , which we will refer to often. This *rms* slope can be written as  $\phi = \tan^{-1}(\frac{\sqrt{2}\delta}{a})$ . The second surface studied has an exponential correlation function,  $W(|x_1|) = \exp(-x_1/a)$ .

Averaging over an ensemble of realizations of these surfaces, we display the final scattered pressure as a statistical average that follows the approach of previous chapters (Schultz and Toksöz, 1993 1994). The statistical characteristics of the scattered pressure is then compared with the corresponding experimental results and possible scattering mechanisms are proposed. Although the coherent and incoherent contributions to the scattered field were computed for seismic analysis, the total mean squared contribution to the reflection coefficient (RC), which includes both of the contributions, is presented in the following sections. The total mean squared contribution to the reflection coefficient (RC) can be written as

$$\left\langle \frac{\partial R_p}{\partial \theta_s} \right\rangle_{tot} = \frac{4\pi}{k_T^{(f)2} \omega^2} \langle |r_p(\theta_s)|^2 \rangle. \quad (5.25)$$

where  $k_T^{(f)2} \omega^2 \rightarrow \omega^4$ . This gives the average square pressure reflected into the upper medium as a function of the scattering angle,  $\theta_s$ , given one incident beam angle,  $\theta_0$ . The square root of the (5.25) is used for comparison with experimentally recorded amplitudes. Given this representation of the RC, a Gaussian beam which is perfectly reflected by a plane interface gives a maximum RC value of 1.

## 5.4 Experimental Procedure

The experimental approach involved submerging a solid elastic model, in this case a glass block, into an experimental water tank, essentially creating an acoustic-elastic

interface at the boundary between the block and the surrounding water. The first portion of the experiment entailed generating a block with a characterized random surface, which, if successful, would have predetermined Gaussian statistics. The second portion involved constructing a motor driven measurement device that could accurately (to within a fraction of a degree) measure various realizations of the fluid-glass boundary.

### 5.4.1 Random Interface Generation

Fabricating the randomly irregular surface was the most challenging portion of this project. Numerous irregular surfaces were designed. Models ranged from irregular distributions of glass beads to roughened cement surfaces. In addition, random distributions of gravel held together by epoxy were tested along with naturally rough granite and sandstone surfaces. Unfortunately, these models either did not give proper control over statistical parameters or were extremely heterogeneous at the ultrasonic level, making comparisons with numerical models very difficult. After much experimentation the most promising approach became the fabrication of a random glass surface using an etching procedure.

The irregular glass surface was designed using a solid glass block and a standard glass etching process. First the cylindrical glass block shown in Figure 5-3 was cast using a graphite mold. After one week of annealing the block had a final diameter of 19.5 cm and a height of 7.5 cm. The upper surface, which was exposed to air, contracted slightly due to the high expansion coefficient of soda-lime glass and resulted in a slightly concave surface. Therefore, the lower plane surface of the block was etched. The general theory behind etching a specific surface is shown in Figure 5-4. Take for instance the fabrication of the valley shown in the upper left portion of the figure. In this case, the valley is divided into a number of discrete depth intervals. Pho-

photoresist templates are designed to match the geometry of the valley at each discrete depth. The first template which contains only a small gap is glued to the smooth glass surface. The surface is then exposed to a constant pressure of high velocity particles which chip any portion of the surface not covered by photoresist. After a set time which depends on the compressed air pressure and the sand/air mixture ratio, the exposed glass is etched to a target depth. The first layer of photoresist is then removed, and the next layer is attached, exposing a larger portion of the surface to the incoming sand particles. The glass surface is exposed again to sand particles for the same amount of time. The valley is now broader and twice as deep. Adding each template in a similar manner, the desired valley is etched into the glass surface.

To achieve the desired random interface, the Gaussian surface described in the previous section was first numerically generated. Both the transverse correlation length,  $a$ , and the standard deviation of the height,  $\delta$ , of the interface were specified as 1 mm and .71 mm, respectively, giving an *rms* slope of  $45^\circ$ . After generation, the Gaussian surface was discretized into six individual depth levels, with each level's thickness equal to one standard deviation of the surface. The templates shown in Figure 5-5 were successively glued to the surface and each template was exposed to high velocity sand particles normally incident on the surface for approximately 360 s. A simple lateral sweeping motion of the sand blaster was used to cover the whole template. The blaster operated at a pressure of 125 kPa ( $\approx 18$  psi) with the glass surface 0.3 m from the nozzle of the sand blaster. In general, the correlation length of the surface was controlled by the template design and the standard deviation of the interface was controlled by the time that each template was exposed to the sand blast.

As the etching proceeded, we found that the standard deviation and correlation length were difficult to control precisely. We observed during the sand blasting process that particles impacting the surface tend to scatter many times within depressions,

generally broadening the width of the depressions. In addition, small narrow peaks tended to chip away far faster once completely exposed to the sand blast, removing the linearity assumed in the design of the surface. As we show below, this resulted in a longer correlation length than expected.

### 5.4.2 The Scattering Instrumentation

Once the irregular glass surface was created, an automated scattering apparatus was used to measure the scattering properties of the interface. The two different flat-bottomed transducers used to create a beam source were a Panametrics 12.7 mm diameter transducer (1.5 MHz,  $\lambda = 1.0$  mm in water) and a Panametrics 25.4 mm diameter transducer (0.5 MHz,  $\lambda = 3.0$  mm in water). The detectors, which were also Panametrics flat-bottomed transducers, consisted of a 6.4 mm diameter transducer (1.5 MHz,  $\lambda = 1.0$  mm in water) and a 12.7 mm diameter transducer (0.5 MHz,  $\lambda = 3.0$  mm in water), respectively. The detectors were chosen such that they were sensitive only to waves approaching nearly perpendicular to the bottom surface of the transducer, limiting the energy recorded to waves approaching in line with the transducer axis. Given the source parameters, the resulting source radiation pattern was a beam with most of the energy traveling in the forward direction. As shown in Figure 5-6 the source radiation patterns exhibited some slight spreading of the beam, although further tests showed that this did not significantly affect the results.

The experimental data was recorded in our in-house water tank, described in Appendix C. The experimental geometry used to measure the surface scattering is shown in Figure 5-7. The glass block was located at the center of the experiment and the source and detector were then stepped in a semicircle about an axis of rotation. This axis extended laterally along the irregular fluid-glass interface and perpendicular to the source-receiver plane. In each experiment the source was placed at a constant

incident angle,  $\theta_0$ , and a constant .35 m distance from the axis of rotation. The recording angle was then controlled by mounting the detector on a motor-driven, rotating arm that held the detector .30 m from the given axis of rotation. The arm was then rotated in  $0.9^\circ$  steps about this axis of rotation. Therefore, the recorded energy represents scattering in the plane of incidence (source-receiver). It is important to note that the detector occludes the source when it is near the backscattering position. This results in a loss of  $3^\circ$  to  $6^\circ$  of scattering amplitudes centered about the source position. These data points are not plotted.

The final desired measurement is the mean scattered pressure as a function of scattering angle, given a fixed angle of incidence. Since the scattering mechanisms working at the interface are a function of frequency, we are interested in measuring this scattered pressure at specific frequencies. Two different approaches to this problem can be taken. One approach is to record the scattered energy given a broad band incident wavelet and then to decompose the recorded energy as function of frequency. However, since the numerical effects of narrow band filtering are unclear, we take a second approach which involves no filtering and gives cleaner results. We introduce directly via the transducer source a monochromatic wave of a given frequency. The continuous wave is approximated by a finite sinusoid ranging between 35 and 100 cycles and the final constant amplitude of the scattered pressure is then recorded.

Given a single realization, the waves scattered from the irregular interface exhibit large fluctuations in pressure as a function of the scattering angle. It is necessary, therefore, to average experimentally as we averaged numerically so as to obtain a final mean reflection coefficient. In optical theory, averaging is accomplished by illuminating a field lens that is much larger than these fluctuations. The fluctuations, referred to as speckle in optical terminology (O'Donnell and Mendez, 1987), are integrated over a specified solid angle giving the average intensity scattered at that angle. In seismic experiments it is very difficult to use an integrating lens. This difficulty arises

mainly from the limited size and frequency range of ultrasonic experimentation. As a result, we chose to follow the numerical approach and generate different independent realizations of the interface. The pressure of waves scattered from an ensemble of interface realizations was then averaged to determine the final total contribution to the mean scattered pressure at each scattering angle.

A simple scheme was developed to generate many realizations using the same 3-D sample. In general, each realization was acquired by rotating and shifting the sample in the sequence shown in Figure 5-8. As shown, the sample was rotated by  $60^\circ$  staggered steps, followed by 1.25 cm shifts of the block which placed the axis of rotation for the source and receiver on concentric circles about the center of the glass cylinder. Since rotating the surface with respect to the incident beam formed another scattering geometry, many different realizations of the interface were obtained. This sequence of movements can easily give more than 150 different realizations of the interface. The computer controlled arm allowed for rapid acquisition of data with the reproducibility required for this averaging scheme.

Due to interest in the enhancement of energy traveling directly back towards the source, it was desirable to create a source-receiver design that retrieved energy in the occluded zone near the source. This was achieved by constructing a four-layered piezo-film receiver. The general idea behind this receiver is straightforward. Since the impedance of piezo-film is very similar to that of water, the piezo-film can be placed directly in front of the incident beam without affecting its energy. The incident beam is thus allowed to propagate to the interface, where it is then diffracted. The scattered energy traveling directly back towards the source can then be recorded as it transmits a second time through the piezo-film receiver. More precisely, a four-layered piezo-film receiver was constructed with conducting glue and an in-parallel electrical configuration. This design allowed for full control over the geometry of the receiver and also significantly increased the signal to noise ratio. The receiver

construction is discussed in detail in Appendix C. It is important to note that the piezo-film receiver is sensitive to energy arriving from both in front and behind the receiver. As a result, extreme care was taken to choose a time window of analysis which did not contain multiple scattering from the source and the tank wall. In addition, since piezo-film of this thickness (containing both an epoxy and conducting glue) does have a substantial impedance contrast with water, a resonance between the source and receiver still had to be avoided.

We stress that the data discussed in the next section represents the mean diffusely scattered signal, as a function of angle, for a fixed solid angle of data acquisition. No artificial angular factors are introduced to the data even though the apparent vertical wavelength, acting at the surface in this experiment, varies inversely with the cosine of the scattering angle. We do not place any absolute vertical scales on the data, although, for comparison, the data is normalized by the reflection coefficient (RC) calculated at normal incidence.

## 5.5 Surface Scattering Measurements

In this section we present the average reflection coefficients obtained over the roughest glass surface fabricated, thus allowing a study of the stronger forms of multiple scattering at an irregular interface. Figure 5-9a shows the target surface height distribution for this interface, independent of lateral position, and Figure 5-9b shows the histogram of the surface height, based on surface profilometer measurements of the actual surface. The surface measurements have a lateral resolution of about  $5 \mu\text{m}$ , which is within the range of accuracy required for resolving the interface statistics. These histograms show that the surface follows approximately a Gaussian probability distribution with a standard deviation of about 0.6 mm, which is close to the

target value of 0.71 mm. Figure 5-10a gives the target Gaussian autocorrelation function, and Figure 5-10b shows the the actual autocorrelation function calculated from profilometer measurements. As previously predicted, the correlation length of 1.4 mm is greater than the target value of 1 mm. Also plotted are Gaussian and exponential autocorrelation functions with the same correlation length as the data. The autocorrelation function is very close to a Gaussian correlation function at the more important, smaller lags. At larger lag distances, the surface lies directly between a Gaussian and an exponential correlation function.

Figure 5-11a gives a grayscale plot of the experimental surface based on surface profilometer measurements. Figure 5-11b plots the surface height for a profile taken across the surface, while Figure 5-11c shows a numerically generated Gaussian and exponential surface given the same standard deviation and correlation length. The numerical surface is generated in the wavenumber domain where a random height distribution is generated with a random number generator. The random distribution is filtered to achieve the desired spectrum. The random height distribution is then transformed back to the space domain resulting in the height distribution used for one interface realization (Frankel and Clayton, 1986). Although the resolution of the correlation function does make it difficult for a close comparison, upon testing various regions of the interface separately we find that the correlation function is consistently closer to the Gaussian function at small offsets. This suggests that the interface statistical properties are essentially stationary in space and tend towards the Gaussian surface. Unfortunately, the resolution of these measurements does not allow for an accurate identification of the slope of the covariance function as the offset approaches zero. Therefore, the differentiability of the experimental interface can not be verified. One should also note that, at larger offsets, the tail of the correlation function was found to fluctuate between both the exponential and Gaussian correlation functions. This long tail at larger offsets and narrowing at smaller offsets shows the difficulty in physically generating a height distribution with an exponential

fall-off in the wavenumber domain. The etching process, being a natural process, not surprisingly tends towards a rougher interface with a broader power spectrum than the targeted Gaussian. However, even with these deviations, it is clear upon referring to Figure 5-11c that the Gaussian surface matches the experimental interface well, in both the observed slopes and the lateral scale of the irregularities. Since the frequency domain amplitude spectrum of the surface varies as the square root of its covariance function in the wavenumber domain, the exponential surface should contain larger amounts of energy than the Gaussian surface at both low and high frequencies. The slower roll-off in the amplitude spectrum is clearly seen for the higher frequencies, since the exponential surface contains lower amplitude short wavelength irregularities that were not observed on the experimental surface. Although the Gaussian interface gives a good fit to the experimental data, out of interest we shall also plot the results for an exponential surface.

Based on the measurements above, the final glass interface has approximately a  $30^\circ$  *rms* slope. The slopes of this interface are quite steep and the impedance contrast at the fluid-glass interface is large as the glass interface has properties very similar to those of an igneous material (see Figure 5-3). As a result, multiple-scattering and shadowing effects can play a significant role at both small and large incident angles, and approximate linear theories, such as the Kirchhoff and Born approaches, break down. Therefore, the mean scattered pressure measured experimentally is compared with the reflection coefficients calculated with the Somigliana boundary integral technique as this approach includes all multiple scattering and wave conversions at the interface.

### 5.5.1 Case: $\lambda = 0.71a$

Figure 5-12 shows one realization of the interface given an incident pulse with a center frequency of 1.5 MHz and a half-power width of 0.25MHz. This realization corresponds to a beam impinging on the surface with an incident angle of  $20^\circ$ . The source pulse along with the pulse reflected from a plane interface are also shown, in which case energy travels only in the specular direction. Referring to the polar seismogram, it is clear that the large scale surface roughness scatters energy over most forward and back scattering angles. The energy is spread over a large time interval and amplitudes vary rapidly as a function of scattering angle. In general, it is difficult, given this single model, to determine quantitatively which scattering mechanisms are working at the surface.

Our first continuous wave analysis is carried out at 1.5 MHz, the center frequency of the seismogram above, so that  $\lambda = .71a = 1.00$  mm. Figure 5-13 shows one experimental realization of the fluid-glass surface at each of four incident beam angles:  $0^\circ$ ,  $20^\circ$ ,  $30^\circ$ , and  $60^\circ$ . Clearly the amplitudes in each realization vary strongly as a function of scattering angle,  $\theta_s$ . Averaging over a finite number of these realizations the mean reflection coefficient is obtained. The total mean reflection coefficients for both a Gaussian and an exponential surface are given in Figures 5-14 through 5-17. At the bottom of these figures, the experimental mean reflection coefficients are given along with the SD of the finite average, showing the deviation of these reflection coefficients from the final mean reflection coefficient which would correspond to a full ensemble of realizations. Negative scattering angles ( $\theta_s < 0$ ) correspond to backscattering in all plots. We also stress that given the incident wavelength, the surface is extremely irregular and the specular reflection is largely disrupted.

Figure 5-14 shows the total mean scattered pressure as a function of scattering angle given a normally incident acoustic beam. Upon comparing the numerical and

experimental data it is clear that the 2-D numerical results for a Gaussian interface can give insight into the 3-D experimental results. The fluctuations in the data are mostly within one standard deviation of the finite average. There are a number of interesting aspects in the curves. The experimental data shows a strong peak amplitude propagating back towards the source at  $\theta_s = 0^\circ$ , and this is predicted by the numerical reflection coefficient. The width of this peak is approximately  $35^\circ$ . Notice that there is also considerable scattering at all angles, dropping off linearly with increasing scattering angle. The exponential surface also predicts portions of the amplitude distribution, but the higher frequency component appears to destroy the enhancement of energy scattered back towards the source.

A similar form of scattering is exhibited in Figure 5-15 and Figure 5-16, which show the mean scattered pressure for an incident angle of  $20^\circ$  and  $30^\circ$ , respectively. Again the numerical results for the Gaussian interface are similar in nature to the experimental results. There are also some remarkable aspects to these two curves. First, both reflection coefficients contain two dominant peaks. One peak is broad and occurs in the forward scattered direction while the other peak is much narrower and occurs in the retroreflective direction,  $\theta_s = -\theta_0$ . The experimental results show a consistent, yet less distinct, peak in the retroreflective direction. The peak clearly loses amplitude as the incident angle is increased, sinking further into the surrounding reflection coefficient. A second aspect is that both curves show a strong asymmetry. However, upon comparing the curves, the 2-D numerical model shows more backscattering and less forward scattering than the 3-D ultrasonic data. This trend becomes more prominent as the incident angle is increased. The exponential curve follows the Gaussian reflection coefficient closely, although it again shows a less distinct retroreflective peak.

Figure 5-17 gives the mean scattered pressure for a beam incident at  $60^\circ$ . In this case there are no distinct signs of enhanced backscattering in either the numerical or

the experimental data. However, energy is scattered uniformly over most backscattering angles. This energy does not drop off until the retroreflective angle is exceeded in the backscattering region. Most dramatic is the continuation of the trend observed at the smaller incident angles above. Specifically, the numerical data clearly shows more backscattering and less forward scattering than the experimental data.

### 5.5.2 Case: $\lambda = 2.14a$

Figure 5-18 shows one realization of the interface given an incident pulse with a center frequency of 0.5 MHz and a half-power width of 250 kHz. This realization corresponds to a beam impinging on the surface at a  $20^\circ$  incident angle. The pulse reflected from a plane interface is shown, with the energy again arriving only in the specular direction. Referring to the scattered seismogram, it is clear that, even at this lower frequency, energy is scattered over most forward and backscattered angles. Given this one deterministic case, it is difficult to determine quantitatively the scattering mechanisms operating at this frequency or to define how these mechanisms might differ from those in the higher frequency case.

The second continuous wave analysis was carried out at 0.5 MHz, the center frequency of the seismogram above, so that  $\lambda = 2.14a = 3.0$  mm. Figure 5-19 shows one experimental realization of the fluid-glass surface at each of the four incident beam angles. Once again the amplitudes for each realization vary strongly as a function of scattering angle, although not as strongly as the  $\lambda = .71a$  case. Figure 5-20 shows the comparison between the numerical and experimental mean reflection coefficients given a normally incident beam. The 2-D numerical results for a Gaussian interface were able to predict portions of the experimental observations. In this case, much of the experimental data sits within one standard deviation of the finite-average. Comparing these curves to the curves for  $\lambda = 0.71a$ , a number of distinct differences

are apparent. Most noticeable is the widening of the retroreflective peak width from about  $35^\circ$  to greater than  $60^\circ$ . This widening is apparent in both the experimental and the numerical data. The reflection coefficient for an exponential interface again shows much lower retroreflectance than for the Gaussian interface.

Figure 5-21 and Figure 5-22 both show that the numerical results over a Gaussian interface predict the asymmetric trends in the experimental data for incident angles of  $20^\circ$  and  $30^\circ$ , respectively. However, distinct differences do occur between the two curves. First, as the incident angle increases, the 2-D numerical results again show more backscattering and less forward scattering than the 3-D ultrasonic data. A broad retroreflective peak is both predicted and observed at  $20^\circ$  and  $30^\circ$  incidence, supporting the existence of retroreflectance. Unfortunately, the height of these peaks are of the same order as the standard deviation of the experimental average, not allowing for a direct verification of retroreflectance. Numerically, the exponential interface does give rise to a retroreflective peak, although this peak is smaller than the peak predicted by the Gaussian surface.

Figure 5-23 shows the mean reflection coefficient for an incident angle of  $60^\circ$ . In this case enhanced backscattering is not predicted numerically or observed experimentally. At this lower frequency, the 2-D numerical model predicts more backscattering and less forward scattering than the 3-D ultrasonic data. In addition, the numerical model predicts a much smaller specular peak than is observed experimentally. Although the amplitudes are different, the numerical curves do predict the uniform scattering of energy into the fluid above as shown in the data.

### 5.5.3 Piezo–Film Measurements

Retroreflectance is clearly supported by the ultrasonic data above. However, the retroreflective peak height is still on the same order as the standard deviation of the finite–average in each case. This makes it difficult to verify the existence of “enhanced backscattering” absolutely. For this reason, data was recorded near the retroreflective direction using the partially transparent piezo–film receiver. The experimental procedure is described in Appendix C, while the steps for obtaining the final reflection coefficient are summarized in Figure 5-24. The final average RC observed with the piezo–film receiver is superposed on Figure 5-21. The data has been scaled to the amplitudes received with the flat–bottomed transducers. The scattered pressure was measured between the backscattering angles of  $40^\circ$  and  $5^\circ$  ( $-40^\circ < \theta_s < -5^\circ$ ), and 65 surface realizations were averaged. In this case, the size of the retroreflective peak is larger than the corresponding SD of the average. The 2–D numerical model predicts the 3–D experimental data to about one standard deviation of the finite average. A distinct peak is observed in the retroreflective direction with a slightly narrower form than the numerically generated peak. This result strongly supports the enhancement of backscattered energy due to multiple scattering from the glass interface.

### 5.5.4 General Discussion

Generally, the numerically derived mean reflection coefficients calculated over an acoustic–elastic interface show retroreflective trends similar to those observed for the SH and P–SV cases. First, the width of the retroreflective peak appears to be consistent with the multiple scattered constructive phase argument summarized in the introduction. In this case, when the wavelength is increased by a factor of three, both the numerically derived curve and the experimental data show a factor of three increase in peak width, from  $35^\circ$  at  $\lambda = .71a$  to greater than  $60^\circ$  at  $\lambda = 2.14a$ . Sec-

ond, as the incident angle is increased, the retroreflective peak amplitude tends to decrease relative to the remaining portion of the reflection coefficient. The retroreflective peak in both the experimentally and numerically derived curves disappears at an incident angle approximately equal to the  $30^\circ$  *rms* slope of the interface. Although not studied directly, it seems likely, based on the work of Schultz (1993), that the retroreflective peak height will tend to decrease as the impedance contrast is lowered and more energy is allowed to penetrate the interface. Along the same lines, the retroreflective peak amplitude is likely to diminish as the *rms* slope of the interface is decreased, since not as many time-reversed paths can be obtained with the lower slopes. Based on the modeling in this section, it appears that the distribution of amplitudes identified for the SH case should give a first order estimate of how the retroreflective peak amplitude will vary both as a function of impedance contrast and interface *rms* slope.

Interestingly, as the incident angle was increased the numerical results above consistently predicted “more backscattering and less forward scattering” than observed in the 3-D experimental results. We stress that the amplitudes for the 2-D and 3-D cases are normalized to each other at normal incidence, so that the absolute amplitude of backscattering is not given. The above statement, “more backscattering and less forward scattering”, means that backscattered amplitudes decrease and forward scattered amplitudes increase more slowly for the 2-D case than for the 3-D case. Two explanations may account for this deviation. First, the glass interface used in the experiment may not exactly follow Gaussian statistics. Therefore, the observed differences may be a direct result of differences in the statistics of the model. However, the interface statistics were well-constrained using surface profilometer measurements. A second more plausible explanation may be that the deviations represent an inherent difference between 2-D and 3-D scattering mechanisms. In the case of 2-D scattering, a peak along the interface is actually an infinite ridge extending in the  $x_2$ -direction. A wave incident on the side of this ridge has only three probable routes of getting to

the receiver located on the opposite side of the ridge. The wave can either multiply scatter within the valley, transmit through the ridge, or diffract over the very peak of the ridge. Each path may exist, but a wave loses a large amount of energy along its journey. In the 3-D case, the surface has one more degree of freedom. Therefore, at normal incidence, out of plane scattering allows energy to arrive randomly from all directions and may increase the amount of observed backscattering. As the incident angle is increased, energy also travels out of the incident plane. Unlike the 2-D interface, the 3-D nature can allow energy to pass around obstructing peaks, reducing the amount of energy backscattered as the incident angle is increased. Energy may also diffract from the flank of a nearby peak and propagate in the forward direction back into the receiver plane. In this case, out of plane scattering would work to reduce the amount of backscattering and reinforce forward scattered energy, possibly explaining the difference between the 2-D and 3-D trends. A careful analysis of scattering with a rapid 3-D numerical or experimental modeling approach should allow for the quantitative analysis of scattered amplitudes given this additional degree of freedom.

An analysis of a single numerical realization of the physical model through the use of a fourth order finite-difference algorithm, discussed in Appendix E, suggests that this extra degree of freedom increases the amplitudes recorded in the specular direction at near normal incident angles. In the cases studied in this chapter, the proper normalization of the experimental reflection coefficient could place the amplitude of the 3-D reflection coefficient as much as twice that of the numerical 2-D curve.

Upon a careful review of the numerical and experimental curves above there are finer features in the experimental data which may be of importance. For instance, the experimental observations show a distinct change in the variance of the amplitude measurements. In the case of  $\lambda = 2.14a$  the variance of the mean reflection coefficient decreases dramatically at about  $\theta_s = \pm 60^\circ$ . Within this range there is a much larger variance in the data than outside this range. This change in variance

does not appear to depend strongly on the incident angle. Although not as clear in the  $\lambda = .71a$  case, a change in the variance still appears in about the range of  $\pm 60$  to  $70^\circ$ . This suggests that the point of change is somewhat independent of the incident wavelength, at least in the frequency range studied. This change in variance appears to occur in conjunction with a sharp break and a distinct drop in the reflected amplitudes at wider scattering angles, suggesting that it may be associated with shadowing effects at the larger scattering angles. Numerically, we find that by averaging a similar number of 2-D numerical realizations, this break in the variance of the mean reflection coefficient can be predicted. If more realizations are averaged, the sharpness of the break in reflected amplitudes becomes smoothed. Surprisingly, the exponential correlation function predicts the point of this break better than the Gaussian surface. This suggests one or both of two possibilities. First, the extra degree of freedom given in the 3-D experiments may allow for scattering with an amplitude signature closer to an exponential 2-D surface. The second possibility is that the actual experimental surface has deviated enough from the Gaussian interface that it results in backscattering characteristics similar to that of the exponential interface. However, no matter which of the two models is assumed, this small variance suggests that mean amplitudes can be obtained more quickly for larger scattering angles.

Upon comparing the experimental and numerical curves, additional discrepancies can be identified between the numerically predicted and the experimentally observed amplitudes. These discrepancies may also result from the extra degree of freedom or from the small deviation of the interface statistics towards an exponential correlation function. The most prominent discrepancy is the appearance of a large amplitude specular peak at small incident angles in the 3-D data. While a peak is clearly present in the specular direction by a  $20^\circ$  incident angle in the each 3-D case, a distinct specular peak is only present for  $\theta_0 = 30^\circ$  in the  $\lambda = 2.14a$  numerical case. Discrepancies such as this can be useful for evaluating the direction of future modeling approaches and understanding the differences which might exist between scattering

by 2-D and 3-D structures.

## 5.6 Conclusions

In this chapter, we were able to generate, within reasonable accuracy, a 3-D characterized random interface. An interface with approximately a Gaussian surface height distribution and a Gaussian correlation function was generated using a glass etching procedure and photoresist templates. The resulting surface distribution was confirmed using surface profilometer measurements. Scattered pressures were then acquired over this surface and compared directly to numerical results calculated over a 2-D interface with the same statistical parameters.

More precisely, near normal incidence, we have shown that the 2-D numerical results for scattering from a randomly irregular interface, with Gaussian statistics, can give insight into the 3-D scattering observed experimentally. Numerical results predict the large amount of observed incoherent backscattering and forward scattering along with the destruction of the specular reflection at many incident angles. Most striking is the prediction of a “retroreflective” amplitude peak. The numerical results predict a decrease in the peak’s amplitude as the incident angle increases. The peak’s width is also shown to be directly proportional to the ratio of the incident wavelength and the correlation length of the interface. Experimentally, enhanced backscattering is strongly supported by observations at normal incidence and at 20°-incidence. We find that the peak’s amplitude decreases dramatically as the incident angle becomes greater than the *rms* slope of the interface. Numerical modeling of an exponential surface with the same correlation length and standard deviation as the glass interface gave results very similar to the results of the Gaussian surface, although the results showed more general backscattering. Unlike the experimental results, retroreflectance

from the exponential interface was difficult to identify in almost all cases studied. A break in variance was also observed in the experimental data. The point at which this break in variance occurred was predicted better by the 2-D exponential interface than by the 2-D Gaussian interface. This suggests that the experimental interface may have deviated far enough away from the pre-chosen Gaussian interface that the observed scattering takes on some characteristics of the exponential results. On the other hand, the geometry of the experimental interface is well constrained near a Gaussian, so this change in variance may actually be related to the extra degree of freedom associated with the 3-D experimental model.

At larger incident angles, the 2-D numerical curves deviated from the experimental curves. Specifically, as the incident angle was increased to greater than  $20^\circ$ , the 2-D models predicted more backscattering and less forward scattering than observed in the experimental data, becoming much stronger as the incident angle was increased to  $60^\circ$ . Since the surface in this experiment was well characterized, this may be the result of inherent differences between 2-D and 3-D scattering mechanisms. Relative to the energy scattered at normal incidence, the extra degree of spatial freedom associated with 3-D interfaces appears to favor the propagation of more forward scattered energy and less backscattered energy than the 2-D interfaces as the incident angle is increased. Although the fall-off in amplitudes was different between the 2-D and 3-D interfaces, the 2-D numerical results still predicted the general trend of the experimental scattering. Both results showed that at large incident angles energy is scattered uniformly over most scattering angles. This amplitude distribution would result in negative phase velocities, large phase velocities, and a large amount of interference in seismic data recorded in the fluid above. Again, at these larger incident angles, a break in variance at wider scattering angles was predicted better by the 2-D exponential interface than by the 2-D Gaussian interface.

Although tests were not carried out on epoxy surfaces in this study, an epoxy

surface was generated for the purpose of profilometer measurements. Essentially, the irregular glass surface was used as a mold. After adding a separating solution, an epoxy model was generated and separated from the glass mold. We have concluded that the glass surface can be used to make models out of different materials, each with different physical properties. Future work may, therefore, include studies to determine how the material properties affect scattering from surfaces with identical height distributions. Although in this study we chose to fabricate a Gaussian surface, the same etching process may also be used to create an interface with differing statistics. As we will show in Chapter 6, this may be important for the investigation of scattering from earth boundaries which do not follow the isotropic statistics presented in this chapter.

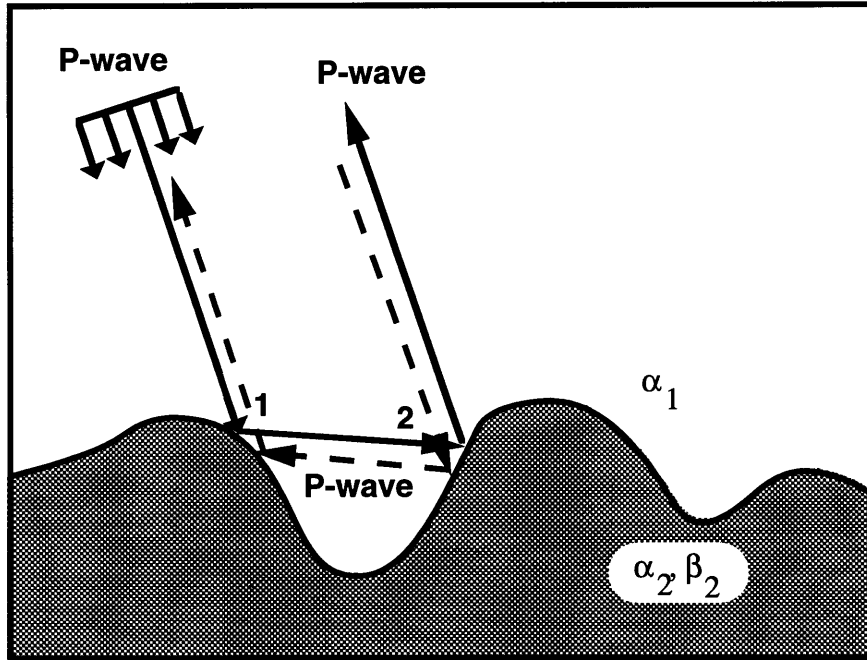


Figure 5-1: Peak-valley sequence along an interface showing an example of the time-reversed paths which lead to enhanced backscattering. The solid line shows a forward scattered path while the dashed line shows the corresponding time-reversed path. These two paths interfere constructively to give an increase in amplitude diffracted back in the direction of the source.

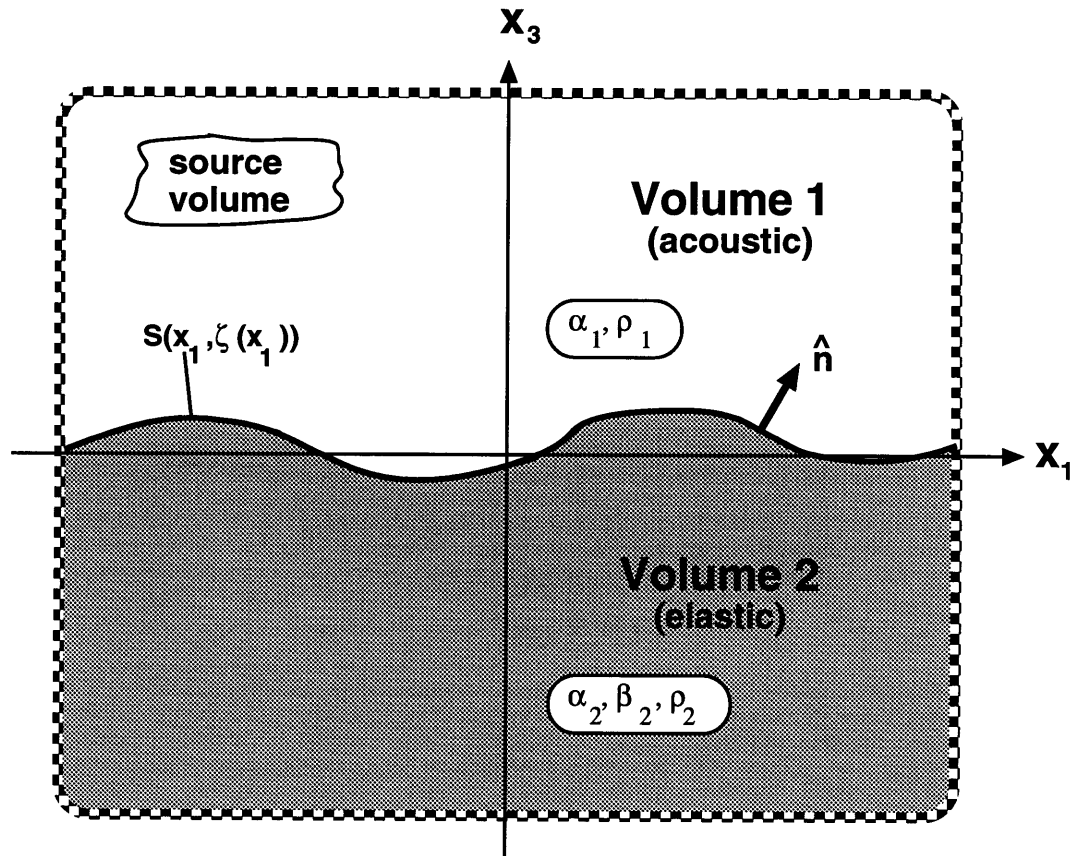


Figure 5-2: The geometry used to formulate the numerical model of scattering from a highly irregular interface. The upper acoustic volume is separated from the lower elastic medium by a highly irregular acoustic–elastic interface represented by the surface,  $S(x_1)$ .

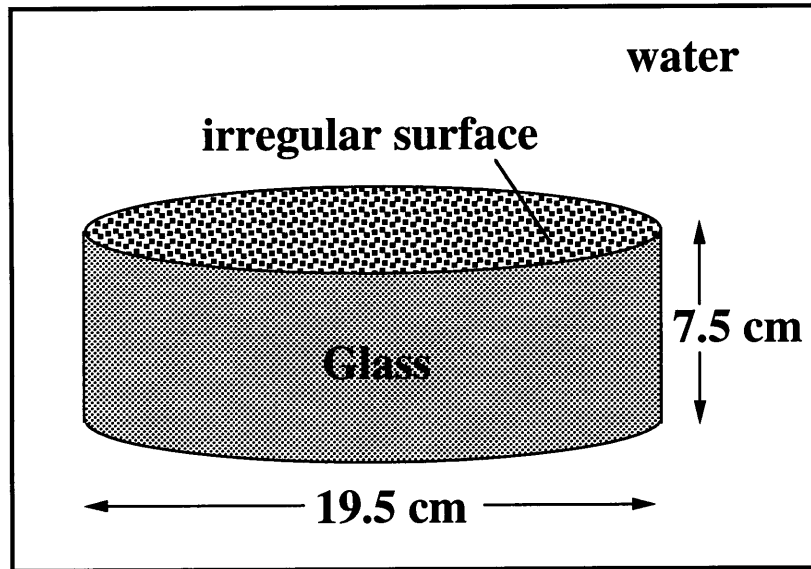


Figure 5-3: The cylindrical glass block model utilized in this study. The upper circular surface of this glass block was etched to give a randomly irregular geometry and then the block was submerged in water to create an irregular acoustic-elastic interface. Measurements show this block to have a P wave and S wave velocity of 5600 m/s and 3200 m/s, respectively. The density of the block is approximately 2.65 giving the block properties similar to that of an igneous material.

## GENERATING THE INTERFACE

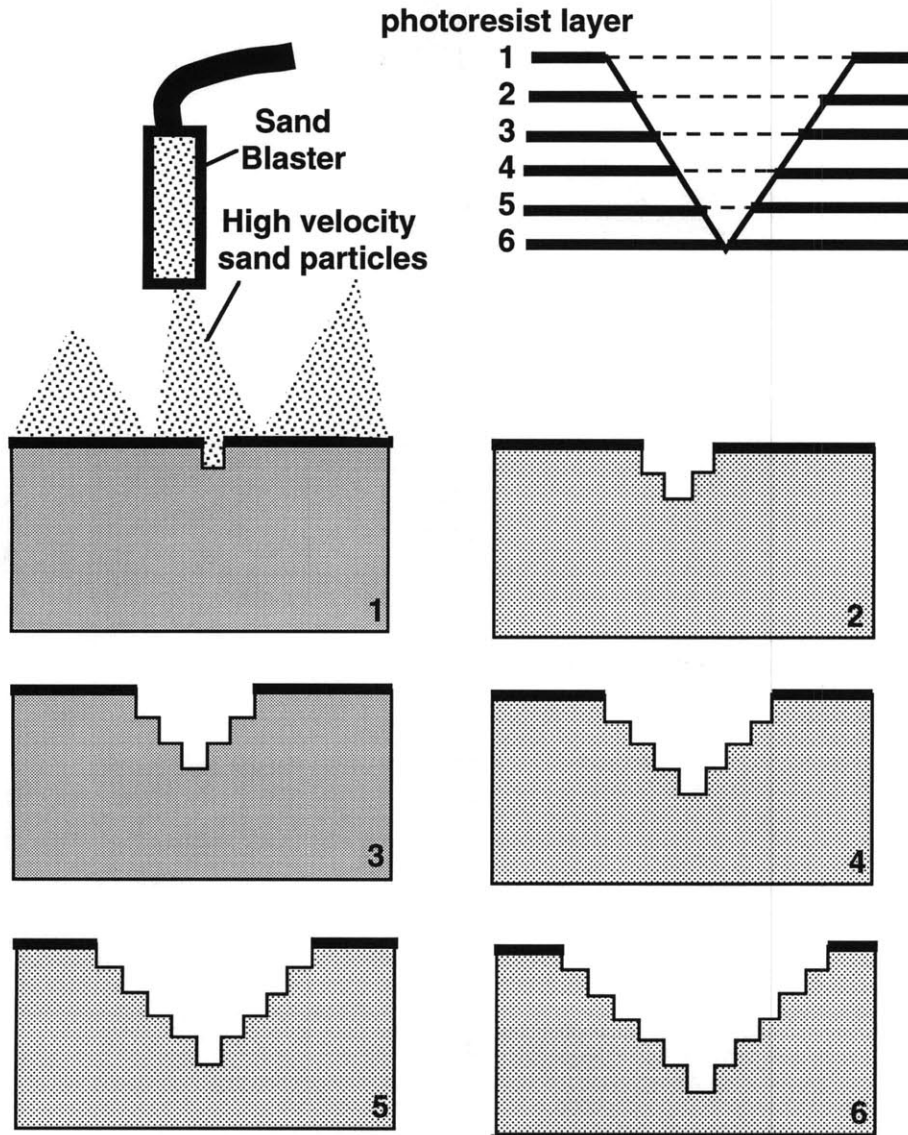


Figure 5-4: The general approach used to etch a specific surface geometry given a smooth glass surface. The valley shown above is etched in discrete levels using high velocity sand particles and a photoresist layer which shields the glass covered by photoresist from chipping. Therefore the valley is slowly deepened and broadened at each level until the desired size and shape is achieved.

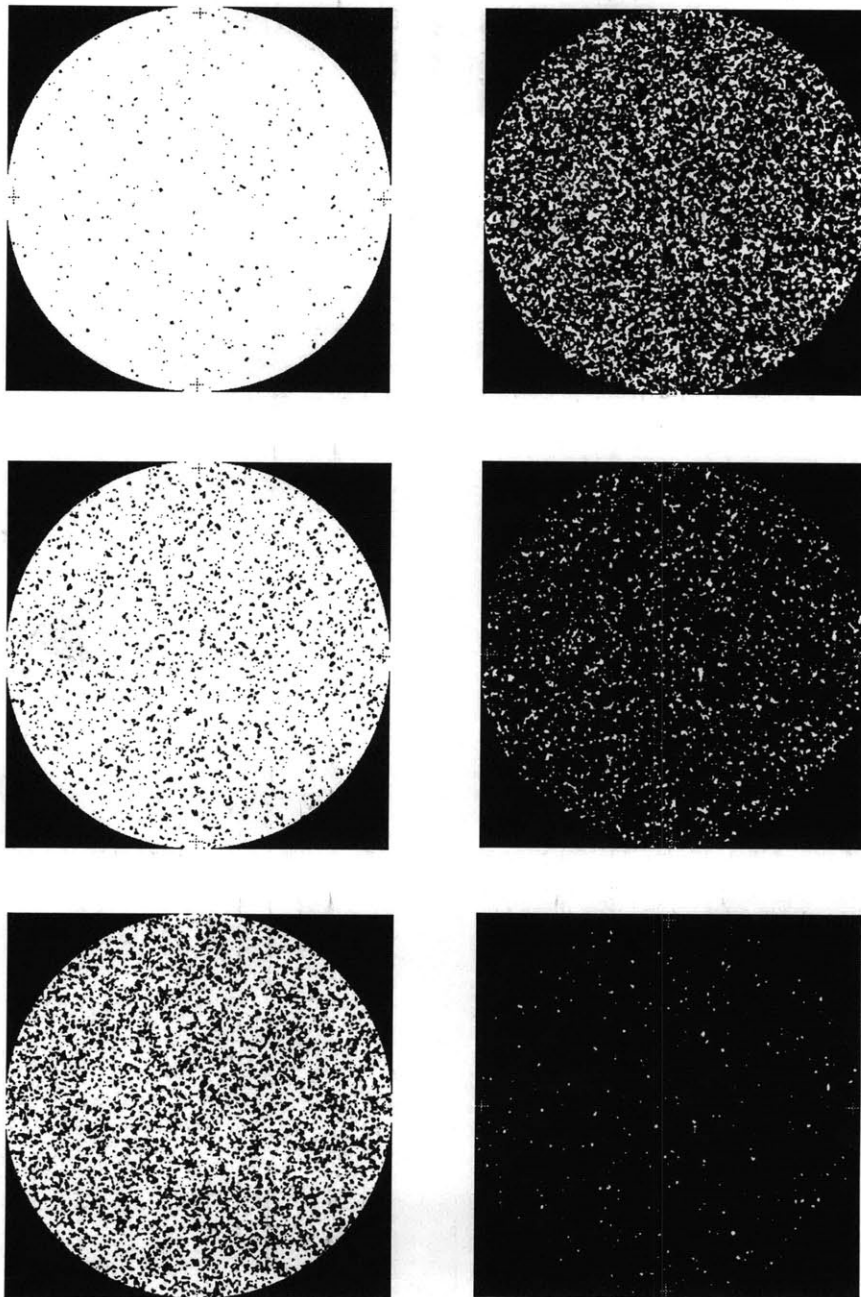
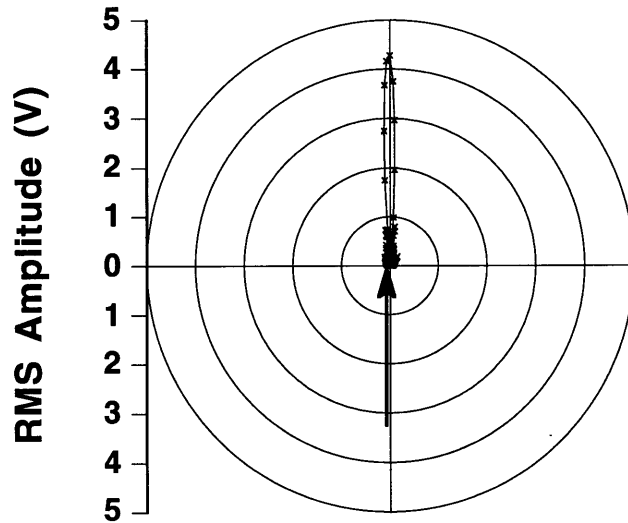


Figure 5-5: The six templates used to generate the random surface used in these experiments. Each circle has a 19.5 cm diameter to match the glass surface. Each template corresponds to one standard deviation of depth and each template was exposed to high velocity particles for the same amount of time. The numbering shows the order in which the templates were applied.

(a) **Source Radiation Pattern**



(b) **Source Radiation Pattern**

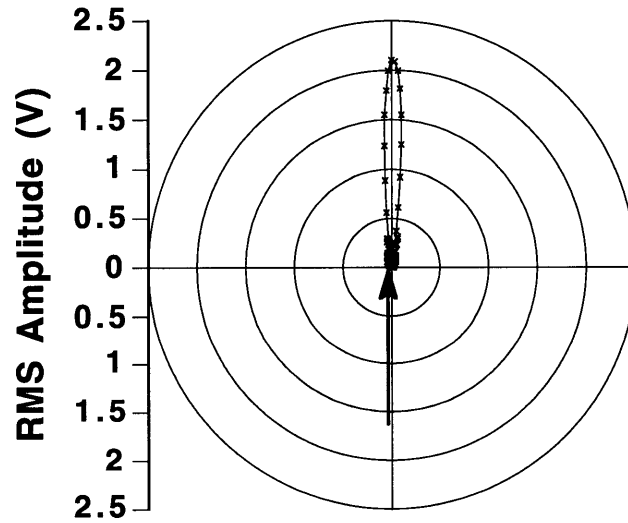
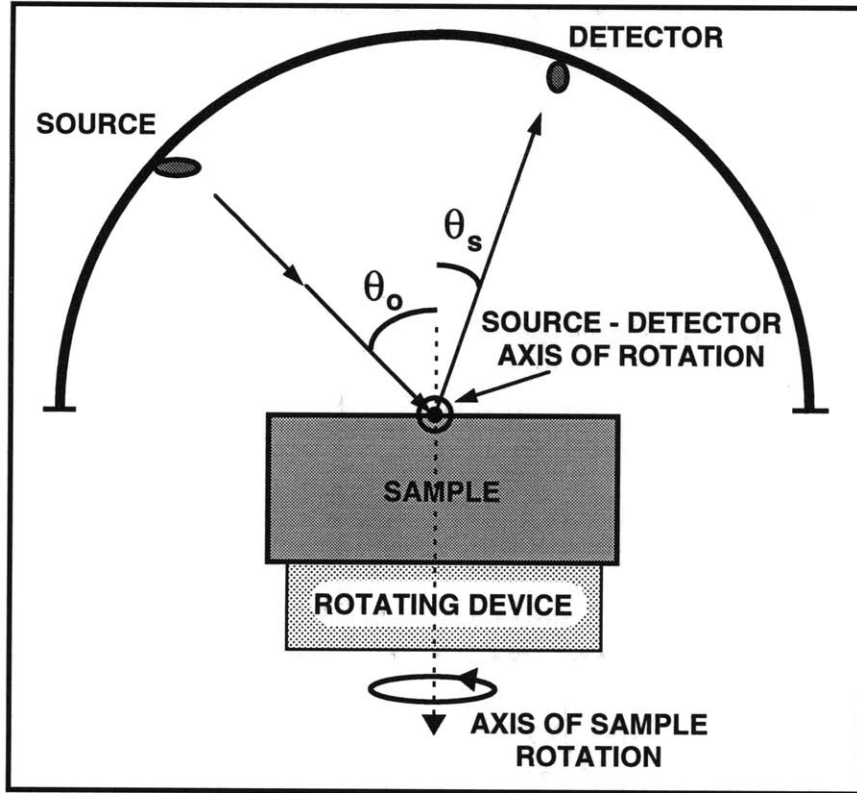


Figure 5-6: Source radiation pattern for the two flat-bottomed Panametrics transducers used in this study. Shown are the radiation pattern (a) for a 12.7 mm (1/2 in) source operating at 1.5 MHz ( $\lambda = 1.0$  mm) in water and the radiation pattern (b) for a 25.4 mm (1 in) source operating at 0.5 MHz ( $\lambda = 3.0$  mm) in water.

**SIDE VIEW**



**TOP VIEW**

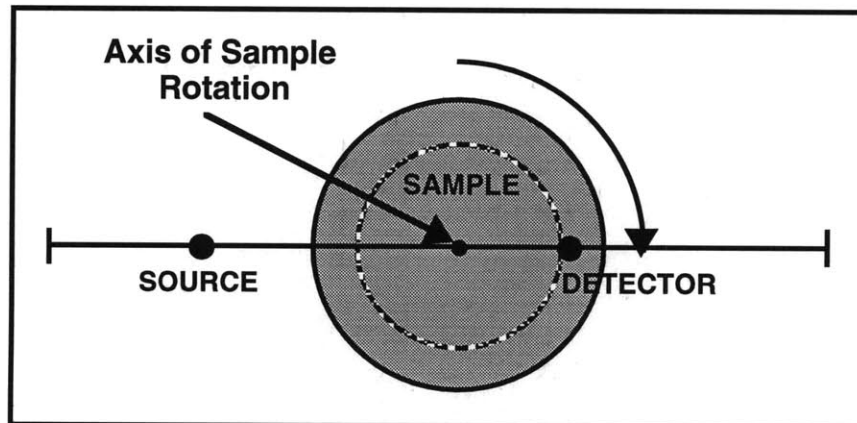


Figure 5-7: The geometry used to experimentally measure the scattering properties of a given random surface. The source is held stationary at one incident angle while the detector is stepped in a semi-circle about the random surface. This then gives one realization of that surface.

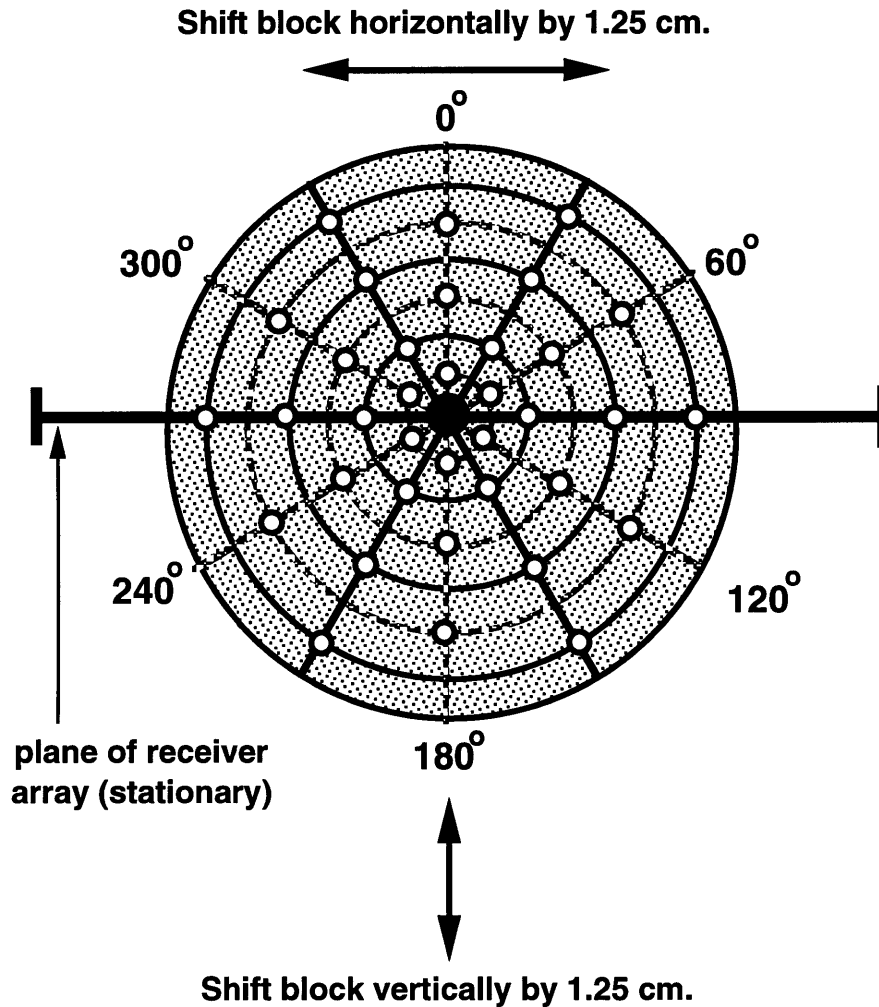


Figure 5-8: The rotation scheme used to generate many realizations of the interface. The sample is shifted left and right by 1.25 cm steps and the block is rotated by staggered 60° steps to give 6 independent realizations of the surface where the axes of rotation for the realization sit along concentric circles on the surface. This gives a total of 72 surface realizations. An additional 72 realizations can also be sampled by shifting the block up and down by 1.25 cm steps.

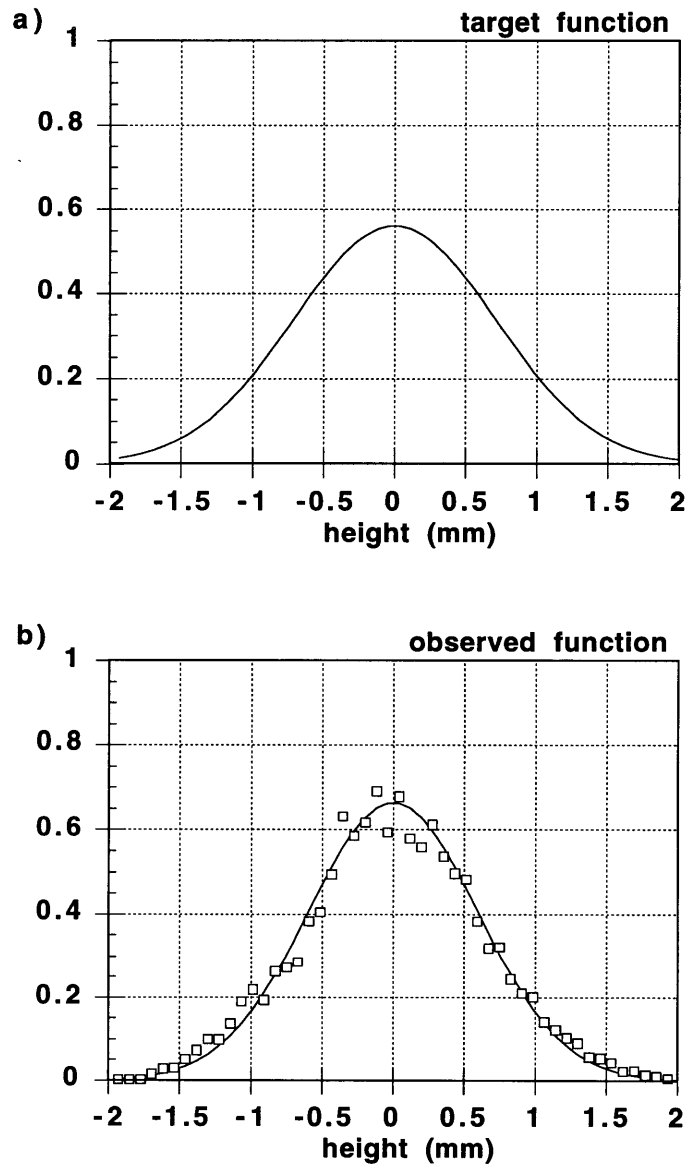


Figure 5-9: Histogram plotting surface height data. The target surface height distribution (a) is Gaussian with a standard deviation 1 mm. The surface height distribution (b) based on profilometer measurements (squares) of the glass surface is shown along with a best fitting Gaussian curve (solid line) which has a standard deviation of 0.6 mm. This histogram was plotted using 40000 surface profilometer measurements.

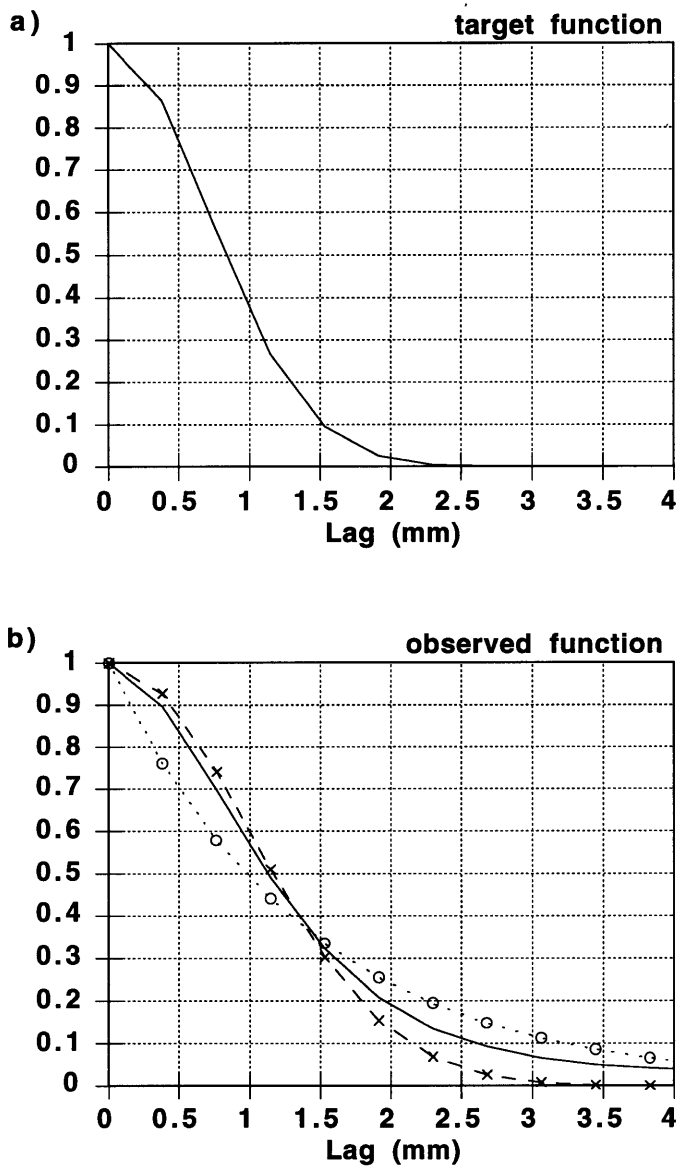


Figure 5-10: The interface autocorrelation function. The target autocorrelation function (a) is a Gaussian function with a correlation length  $e^{-1}$  of 1.0 mm. The actual autocorrelation function of the glass block (b) as calculated from profilometer measurements has a correlation length of 1.4 mm. The surface profilometer measurements (solid line) are compared with Gaussian (crosses) and exponential (circles) functions with the same correlation lengths of 1.4 mm.

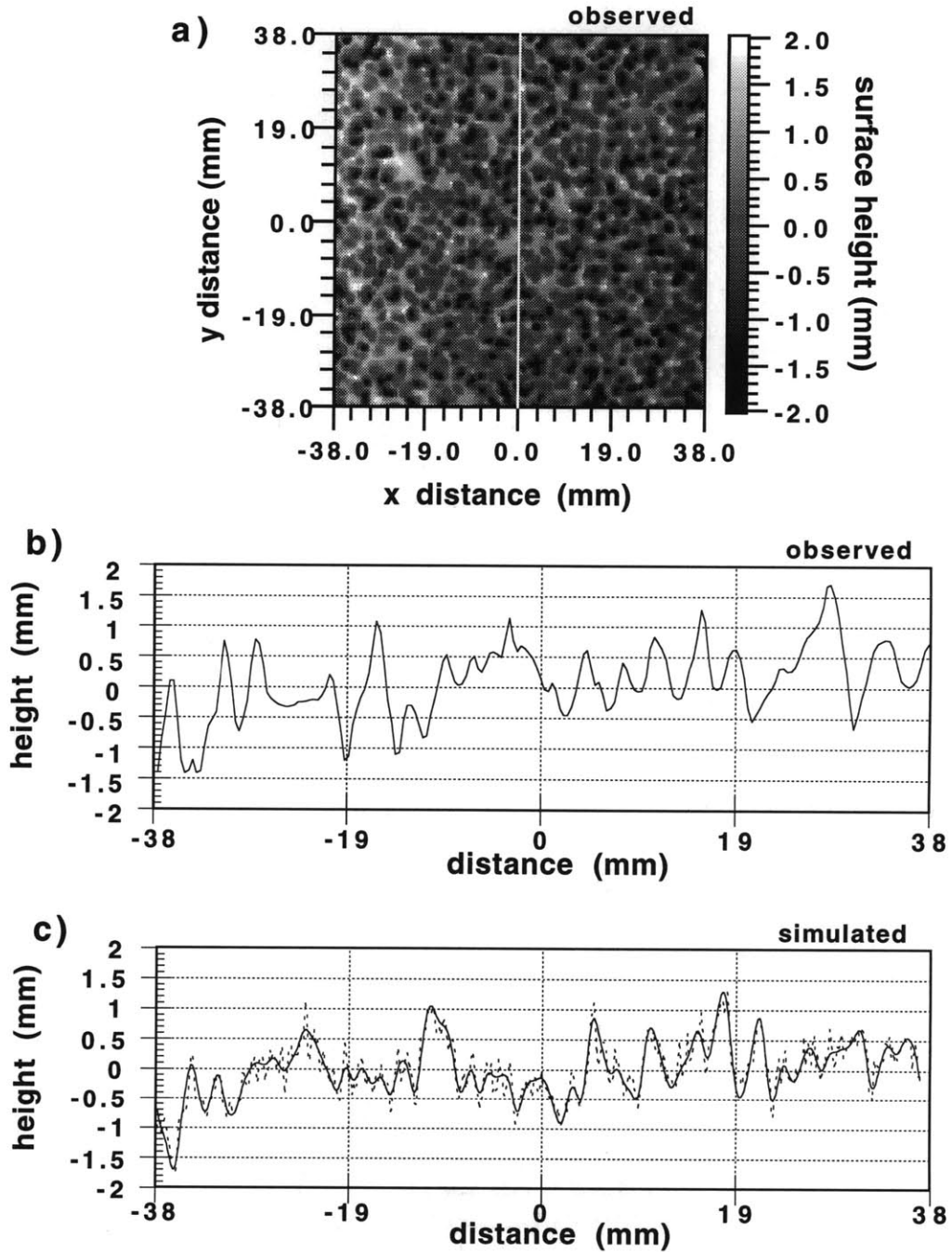


Figure 5-11: The surface height distribution based on profilometer measurements. (a) gives a grayscale plot of the surface, (b) gives a profile across the surface as marked in (a), and (c) shows a numerically generated surface with the statistics given in Figure 5-9 and Figure 5-10. Both Gaussian (solid line) and exponential (dashed line) correlation functions are shown.

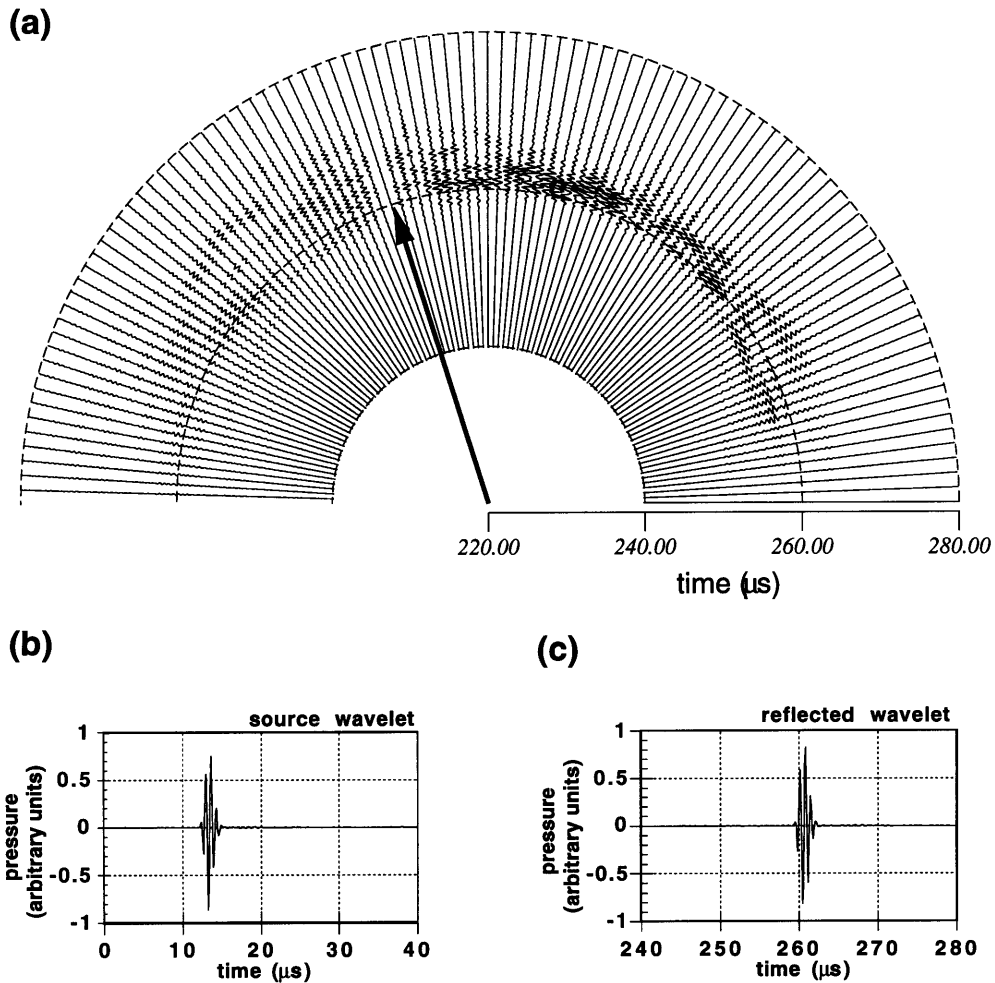


Figure 5-12: Experimental seismogram recorded over the glass model. (a) shows the seismic data recorded as a function of angle over the irregular glass surface with  $\lambda = .71a$  given an acoustic beam incident at  $20^\circ$ . The arrow shows the source direction (retroreflective angle). The source wavelet (b) and the specular reflection (c) recorded over a plane interface are also shown. In the plane layer case the only observable energy is in the specular direction.

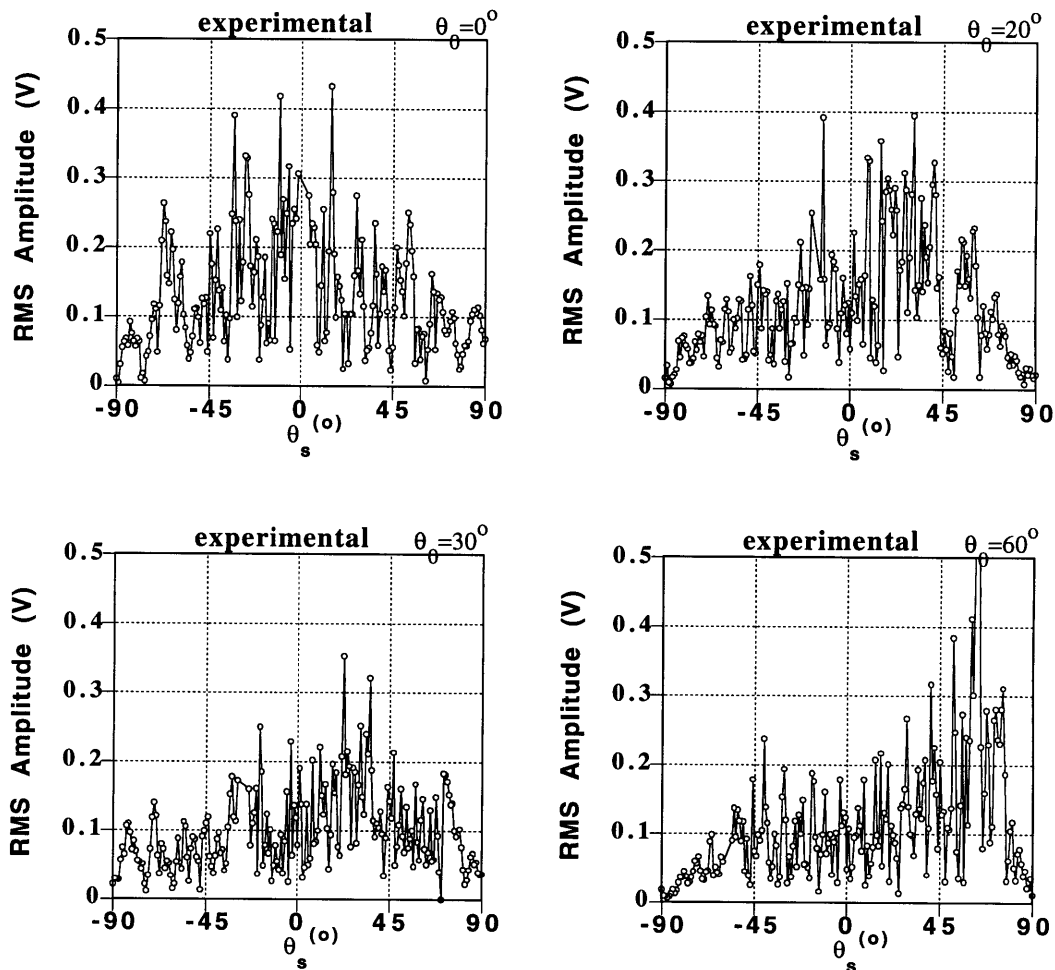


Figure 5-13: The amplitude recorded experimentally for one continuous wave realization of the fluid–glass interface given an acoustic beam incident at  $0^\circ$ ,  $20^\circ$ ,  $30^\circ$ ,  $60^\circ$ , respectively. The incident wavelength corresponds to  $\lambda = .71a$  and  $\theta_s$  is the angle of forward (positive) and back (negative) scattering.

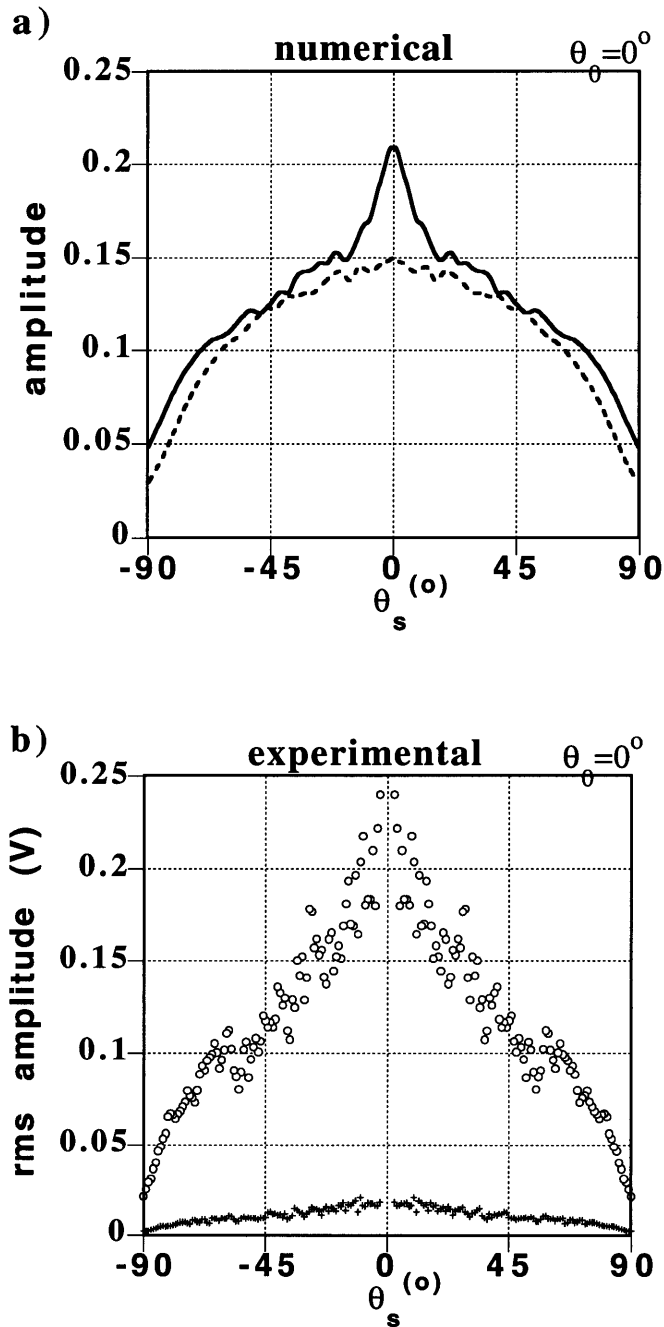


Figure 5-14: The 2-D mean reflection coefficient (a) calculated numerically over the Gaussian (solid line) and exponential (dashed line) surfaces given a normally incident source beam with  $\lambda = .71a$ . The 3-D reflection coefficient (b) recorded over the experimental interface (circles) and the standard deviation of the finite average (plus) are also shown. The experimental results correspond to 30 surface realizations.

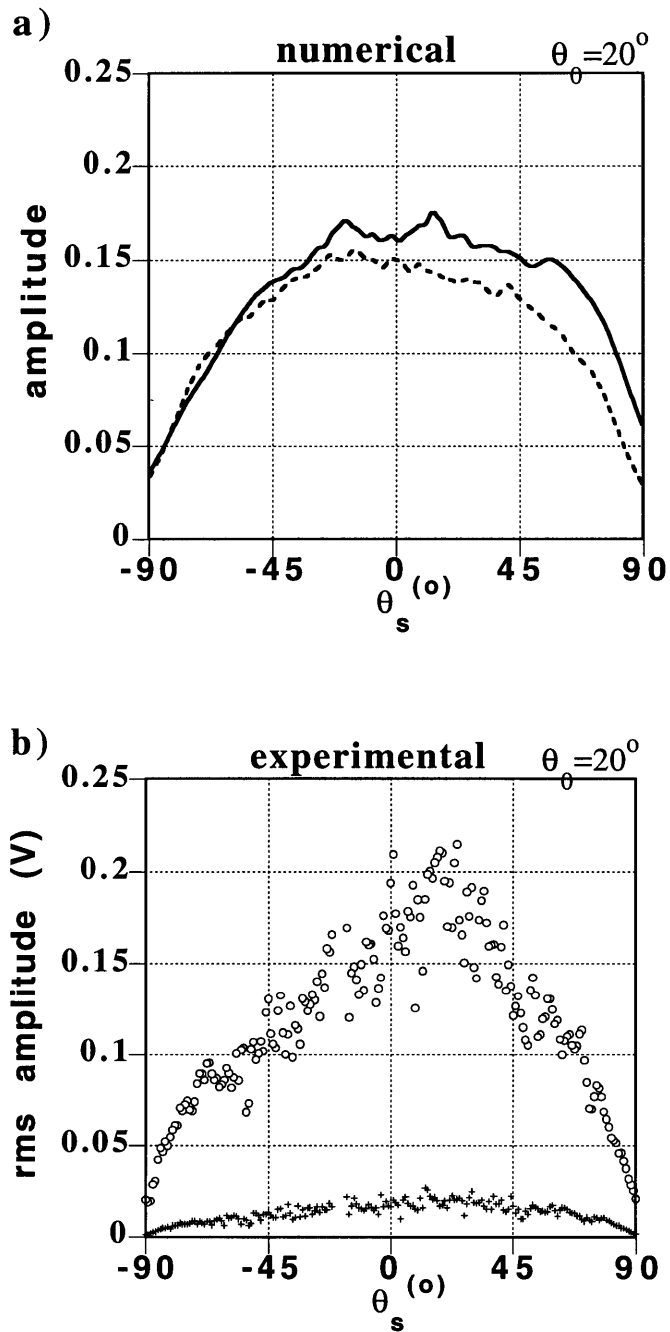


Figure 5-15: Similar to Figure 5-14, except the incident angle is now  $20^\circ$  and results correspond to 20 realizations.

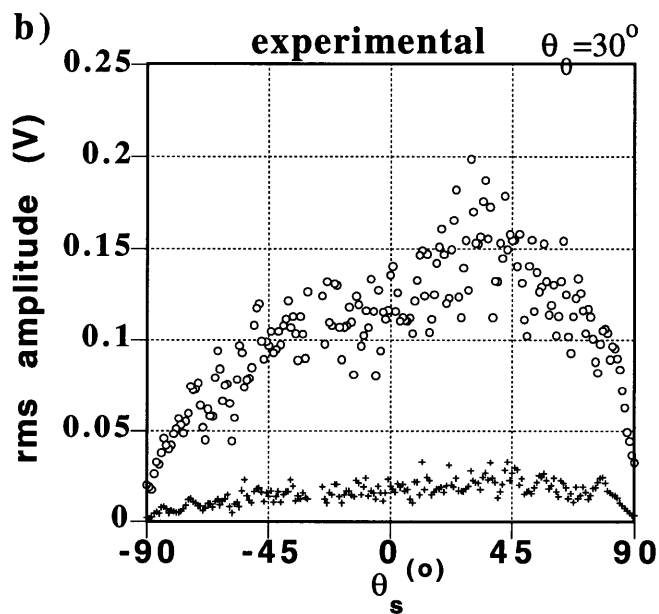
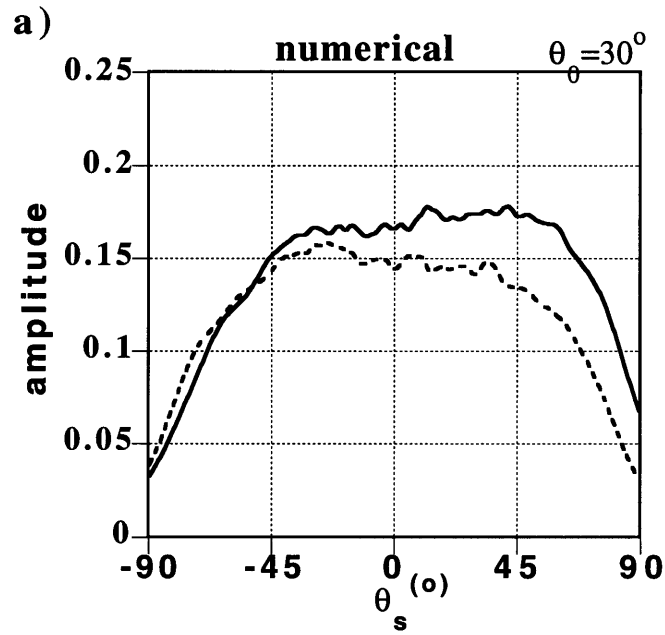


Figure 5-16: Similar to Figure 5-14, except the incident angle is now  $30^\circ$  and results correspond to 10 realizations.

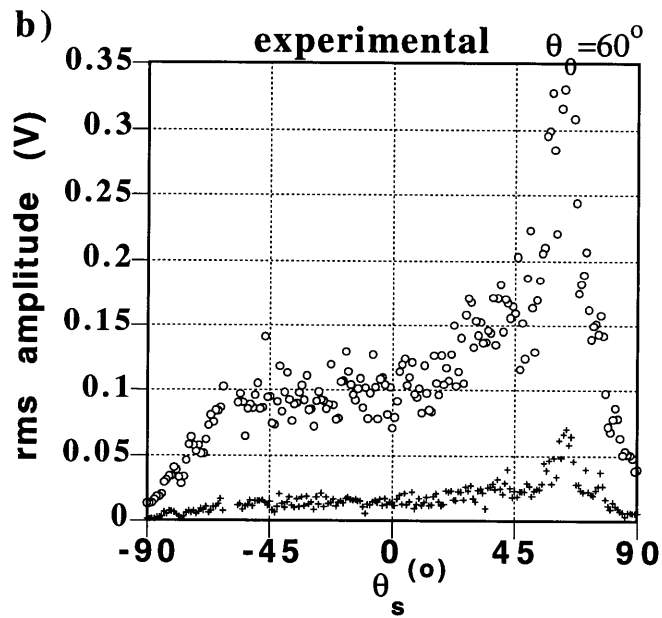
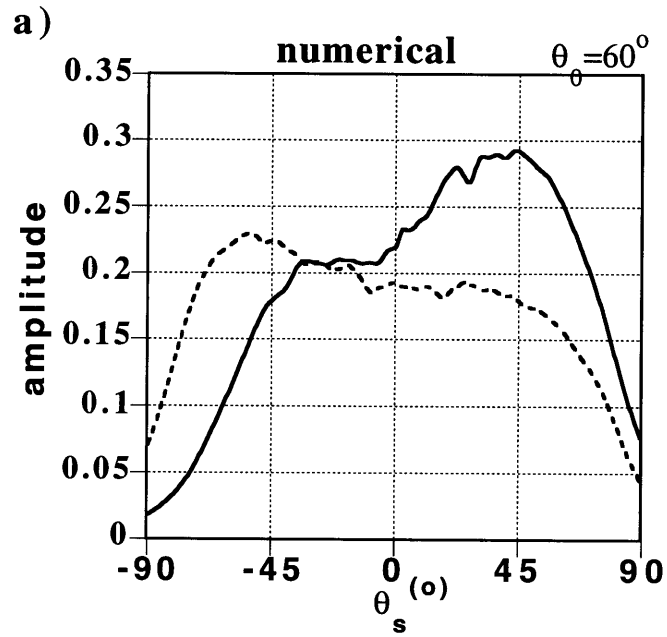


Figure 5-17: Similar to Figure 5-14, except the incident angle is now  $60^\circ$  and results correspond to 10 realizations.

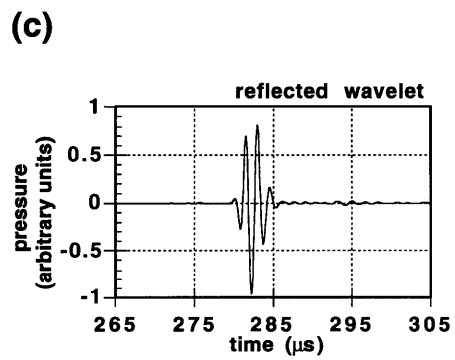
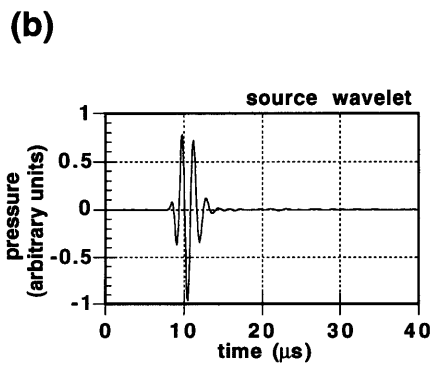
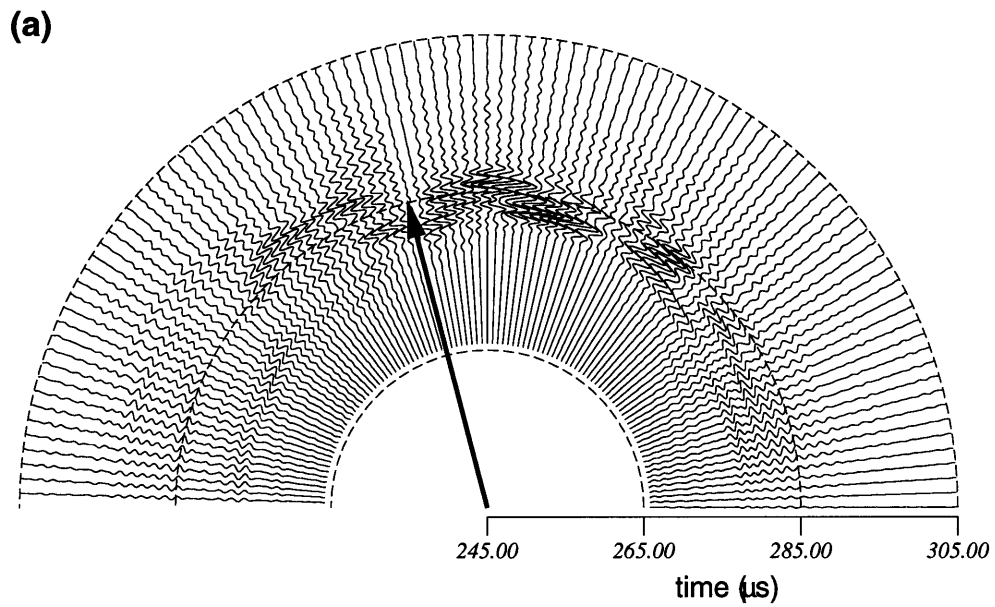


Figure 5-18: Similar to Figure 5-12, except  $\lambda = 2.14a$ .

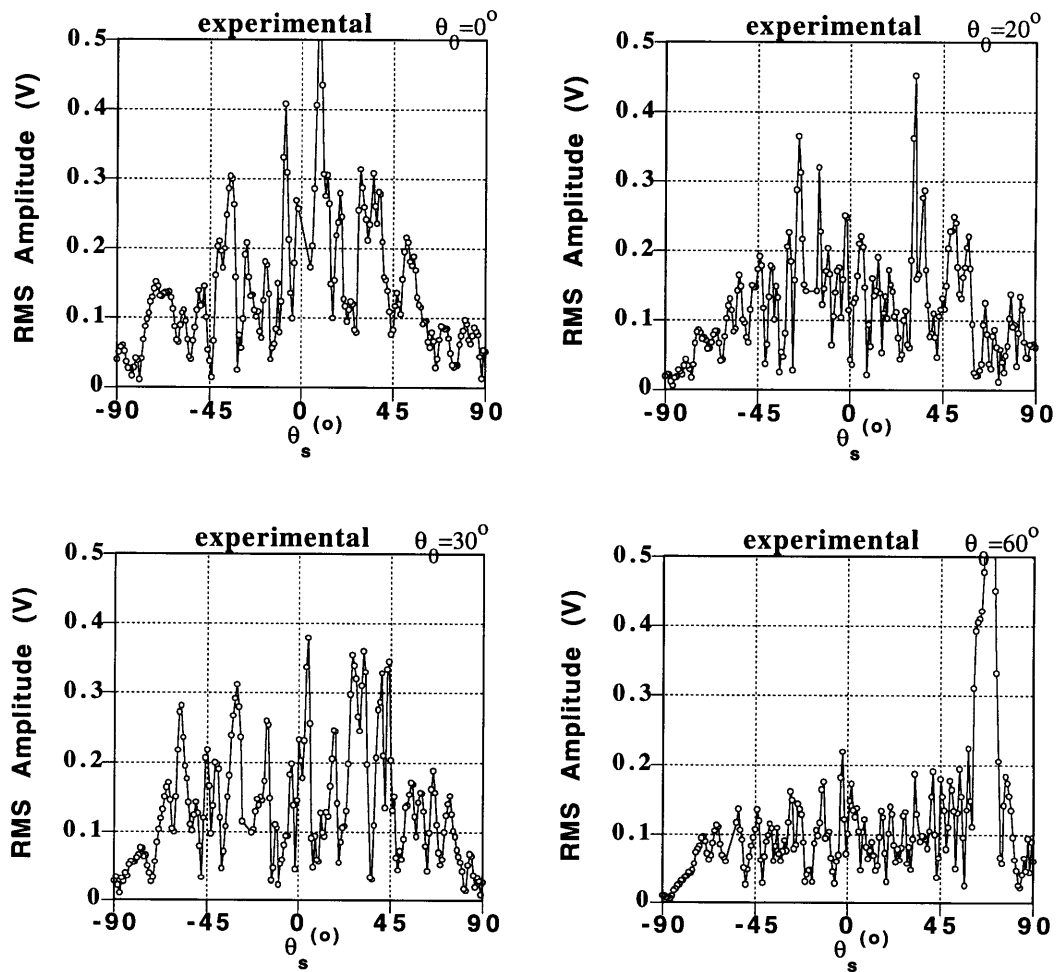


Figure 5-19: The amplitude recorded experimentally for one continuous wave realization of the fluid–glass interface given an acoustic beam incident at  $0^\circ$ ,  $20^\circ$ ,  $30^\circ$ ,  $60^\circ$ , respectively. The incident wavelength corresponds to  $\lambda = 2.14a$  and  $\theta_s$  is again the angle of forward (positive) and back (negative) scattering.

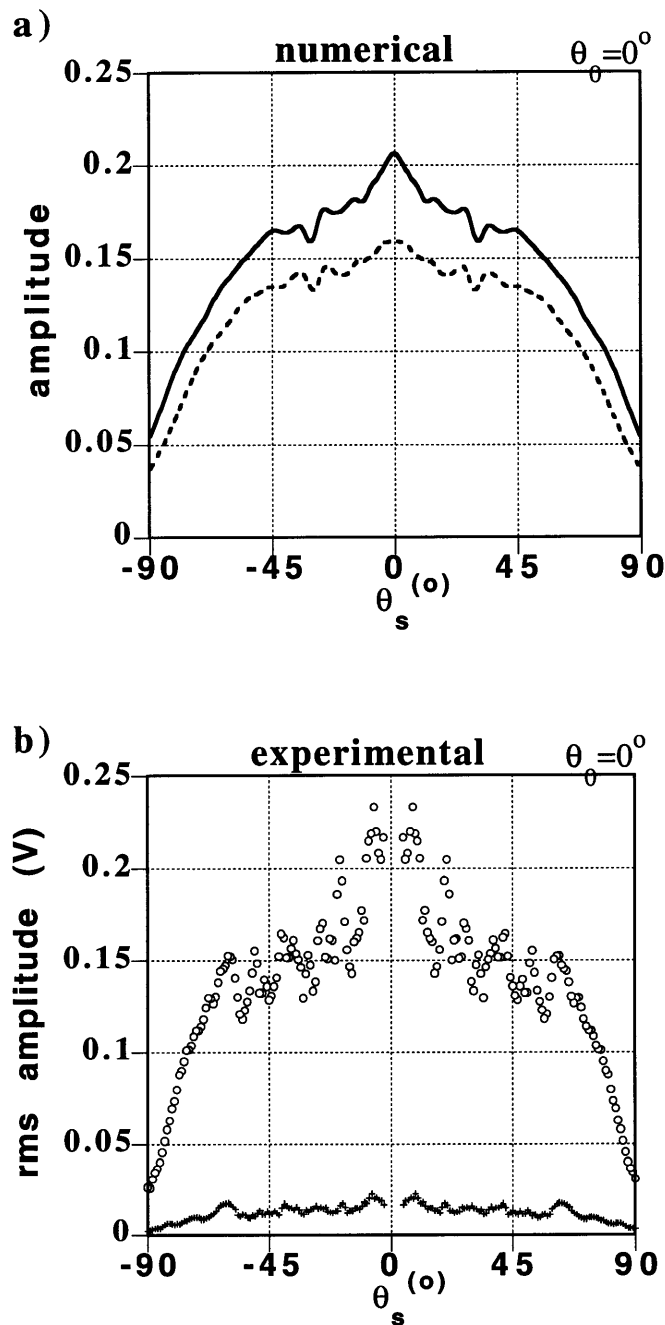


Figure 5-20: The 2-D reflection coefficient (a) calculated numerically over the Gaussian (solid line) and exponential (dashed line) surfaces given a normally incident source beam with  $\lambda = 2.14a$ .  $\theta_s$  is the angle of forward (positive) and back (negative) scattering. The 3-D reflection coefficient (b) recorded over the experimental interface (circles) and the standard deviation of the finite average (plus) are also shown. The experimental results correspond to 30 surface realizations.

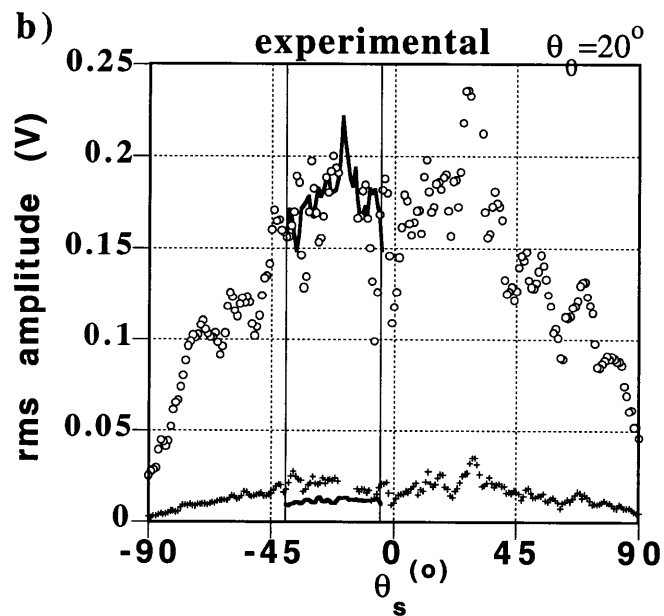
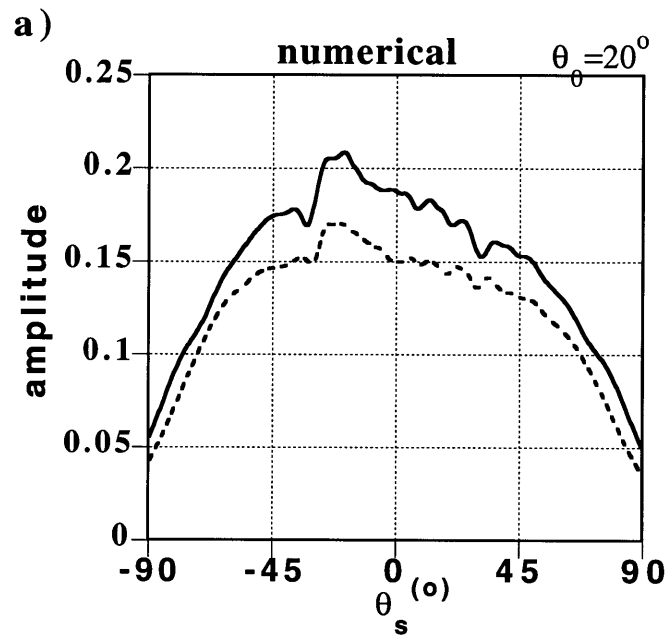


Figure 5-21: Similar to Figure 5-20, except the incident angle is now  $20^\circ$  and results correspond to 20 realizations. The solid line in (b) gives the piezo-film measurements discussed in the text.

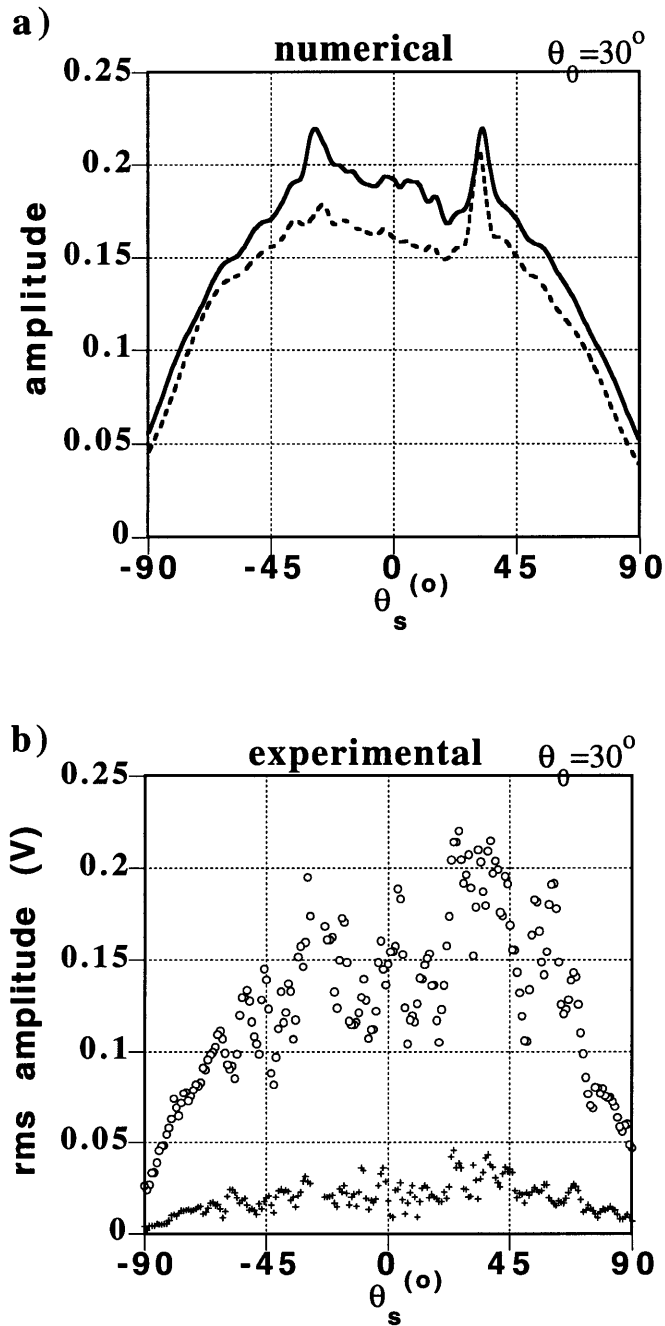


Figure 5-22: Similar to Figure 5-20, except the incident angle is now  $30^\circ$  and results correspond to 10 realizations.

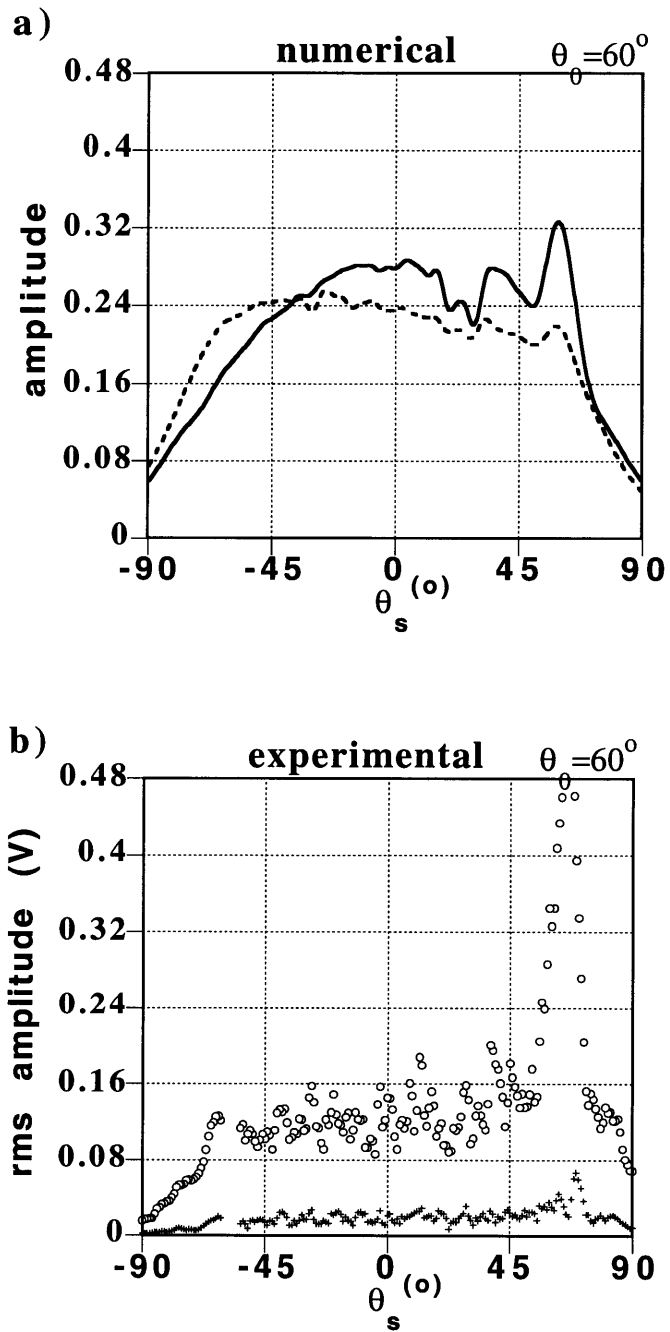


Figure 5-23: Similar to Figure 5-20, except the incident angle is now  $60^\circ$  and results correspond to 10 realizations.

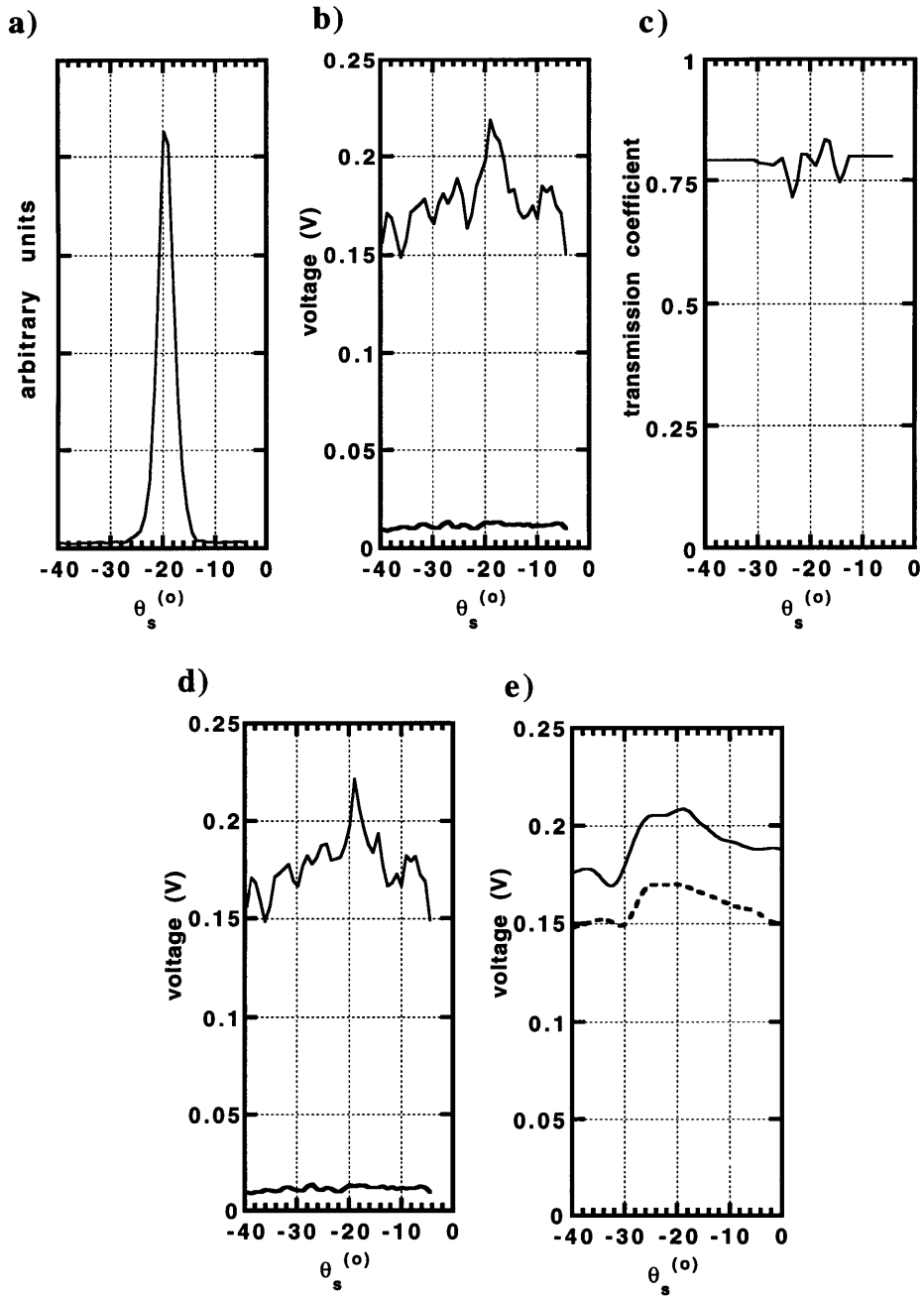


Figure 5-24: The data recorded about the retroreflection direction over the glass interface using a piezo-film receiver. Shown are (a) the incident source amplitude recorded with the piezo-film, (b) the raw data recorded using the piezo-film, and (c) the transmission coefficient of the piezo-film receiver. After making first-order corrections for the transmission coefficient of the receiver, (d) the average reflection coefficient is plotted for 65 surface realizations. The final reflection coefficient can be compared to (e) the numerically derived reflection coefficient for a 2-D Gaussian interface.

# Chapter 6

## Application to the Earth

### 6.1 Abstract

In this chapter we consider some of the implications that both the general scattering and enhanced backscattering identified in Chapters 3 through 5 may have on the propagation of seismic waves in the earth. In the first section, F–K spectra for regional P coda are presented for events recorded at the Scandinavian NORESS, FINESA, and ARCESS arrays and the New England NYNEX array. The spectra are dominated by on-azimuth energy with apparent velocities between Pn (or faster) and Lg. Following this analysis, reflection coefficients calculated with the efficient boundary integral scheme of Chapter 4 are used to study the role irregular interfaces may play in the generation of regional P coda. Specific comparisons are made between the observed P coda F–K spectrum and synthetic reflection coefficients for an irregular Moho discontinuity exhibiting various degrees of roughness. We find that observed crustal scattering in the Scandinavian and New England regions is consistent with P–P and P–SV scattering from the 2–D irregular Moho. Observed spectra are also

consistent with scattering by a 2-D irregular near surface interface. The general backscattering and enhanced backscattering predicted by reflection coefficients also suggests that irregular boundaries may generate retropropagating energy which is then favored for lateral propagation in the crust. A preliminary discussion is given on the theory of retropropagating Lg waves. Preliminary evidence for retropropagating Lg waves appears to exist in the F-K analysis of Lg coda. Further investigation into the role that irregular interfaces play in the generation of retropropagating energy is warranted, both for P and S coda. Finally, we give specific examples of ocean boundaries which might exhibit large amplitude, incoherent multiple scattering. In general, we find that the ocean bottom topography associated with active tectonic boundaries can be large enough to give rise to the scattering mechanisms identified in previous chapters. Using a very simple ultrasonic model of ocean bottom depressions, we show the importance of developing an ocean bottom model which includes a fully anisotropic distribution of topography.

## 6.2 Introduction

Previous work has shown that both regional P coda and S coda recorded in the crust are considerably more complicated than the coda predicted for a plane layered crust. The F-K analysis of Dainty and Toksöz (1990) at Scandinavian arrays has shown that at later times in S coda, energy tends to arrive from all directions to the array. This energy is consistent with the isotropic “standard model” of Aki and Chouet (1975), modified for the regional case by considering the scattering of Lg to Lg (e.g. Herrmann, 1980). Regional P coda, on the other hand, is more problematic and no single model seems to predict the observed energy. The coda is likely the result of several crustal scattering mechanisms.

The combined effect of scattering by both volume heterogeneities and irregular crustal boundaries are likely responsible for the generation of coda in the crust. Of course, depending on the region of interest, one mechanism most likely plays a more dominant role than the other. In terms of heterogeneous volume scattering models many statistical models have been proposed, usually in terms of low impedance contrast volume heterogeneities with isotropic velocity distributions similar to that of Aki and Chouet (1975). Although these isotropic models can predict energy arriving late in Lg coda, it is clear that these models have difficulty describing the form of early Lg coda and P coda at regional distances. This is not surprising as the Earth's crust generally is not isotropic, and instead takes on a velocity structure which tends to be extended laterally through the crust. Such an anisotropic velocity structure can be identified on most seismic reflection models of the deeper crust with the extreme, of course, being a layered crustal structure. So, although the isotropic models can accurately model the general fall-off of energy late in coda, it appears as though the true velocity structure of the Earth is greatly over simplified. Considering the anisotropic nature of the crust, one very promising model for crustal scattering follows from the model of Gee and Jordan (1988) which proposed an anisotropic upper mantle velocity structure based on the stochastic approach of Goff and Jordan (1988). Such a laminated, stochastic model is more geologically consistent with the crust and has the potential to explain the observed lateral variation in crustal reflectors along with the incoherent nature of P coda energy. On the other hand, sharp irregular boundaries are also identifiable in most reflection data. Given a distinct boundary, an anisotropic distribution in the boundary height may also account for the generation of incoherent scattered energy in field data and may give the appearance of discontinuous reflectors due to destructive interference effects. Although a complete scattering model which couples the two mechanisms above is beyond the scope of this study, it is clear that one can learn a great deal by studying the decoupled effect of each form of scattering. In this chapter, we study scattering from a 2-D interface to gain insight into the role

that irregular crustal boundaries can play in the generation of P coda at regional distances.

In the previous chapters we have shown that boundary integral techniques can be an effective tool in identifying the scattering mechanisms which exist at a given interface. In the first section of this chapter, we illustrate how the reflection coefficients in Chapters 3 through 5 can be used to gain insight into crustal scattering mechanisms. We first describe the general nature of regional P coda as recorded at Scandinavian (Mykkeltveit et al., 1990) and New England (Dainty and Battis, 1989) spatial arrays. The P coda is characterized in terms of the azimuth and horizontal phase velocity (angle of incidence) of energy using an F–K spectral approach. Then numerically derived reflection coefficients from earlier chapters are examined to determine whether scattering from interface irregularities is consistent with the observed F–K spectra. The comparison between reflection coefficients and F–K spectra is based on the relation  $V_{app} = V_{true}/\sin(\theta)$ , where  $V_{app}$  is the apparent (phase) velocity,  $V_{true}$  is the true velocity and  $\theta$  is the angle of propagation with respect to the vertical. In the second section, we show that enhanced backscattering from highly irregular surface topography and shallow interface topography may be partially responsible for the retropropagation of energy arriving with Lg phase velocity. Based on previous work, we look for preliminary evidence of retropropagation in the crust and determine whether this form of propagation warrants further research. In the final section, we discuss some regions where irregular ocean bottom topography may be large enough to exhibit the strong scattering mechanisms identified in previous chapters. We then show the importance of including fully anisotropic models in future analyses.

## 6.3 Crustal Scattering

Both Scandinavian and New England crustal structures have been studied in great detail using refraction profiling, wide-angle profiling and tomography, and most recently with thousands of kilometers of deep seismic reflection data (e.g. Luetgert *et al.*, 1987; Kinck *et al.*, 1991; Luosto, 1991). Although in most cases, the spatial resolution of these studies is not sufficient to identify interface irregularities over distances on the order of kilometers, these studies do show that both intracrustal interfaces and the Moho discontinuity can vary dramatically over distances on the order of tens of kilometers and, in many cases, can exhibit steep slopes which have resulted from extensive faulting and structural deformation. Structural discontinuities are also common at this scale, contributing additional energy to crustal scattering. In this section we use the reflection coefficients computed with the Somigliana approach in Chapter 4 to determine whether scattering from irregular intracrustal boundaries is consistent with incoherent energy observed in regional P coda at both Scandinavian and New England seismic arrays.

### 6.3.1 The Nature of Regional P Coda

Regional P coda consists of a train of waves between the main P and S arrivals at regional distances (100-2000 km): typical frequencies are 1-10 Hz. Explanations for P coda include the scattering of P and S waves from distributed small heterogeneities in a similar manner to S coda, and multiple crustal reflections predicted by synthetic seismogram calculations in laterally homogeneous layered media. The results of Dainty and Toksöz (1990) show that P coda cannot be explained by the same model as S coda and a composite model which includes various forms of scattering is required to explain P coda observed at arrays in Scandinavia. Such a composite

model must consider the possibility of scattering from interface irregularities. Therefore, in this section, array data are used to determine whether the scattering from an irregular Moho and irregular near surface boundaries is consistent with the observed P coda. We turn our attention to the analysis of regional P coda (100–2000 km) recorded at the Scandinavian NORESS, FINESA, and ARCESS arrays and at the New England NYNEX array. In this section, the data handling and F–K computations have been provided by Dr. Anton Dainty through the Air Force Geophysical Laboratory (AFGL, *see* Dainty and Schultz, 1993).

Figure 6-1 gives a synthetic vertical seismogram section for a plane layered crust recorded along an array of receivers at a distance of 100 to 500 km from a vertical point force applied at a depth of .04 km (from Toksöz *et al.*, 1990). The model, summarized in Table I, is based on the NORESS crustal model of Sellevol and Warwick (1971) with a quality factor  $Q = Q_{P,S}f^\zeta$ .

**Table I: NORESS Crustal Model**

Depth (km)	$V_p$ (km/s)	$V_s$ (km/s)	$\rho$ (gm/cc)	$Q_p$	$Q_s$	$\zeta$
0.0	5.2	3.2	2.6	50	25	0.5
3.0	6.0	3.5	2.7	200	100	0.8
17.0	6.51	3.8	2.9	1000	500	0.0
38.0	8.05	4.67	3.3	2000	1000	0.0

Referring to Figure 6-1, the synthetic results show that a plane layered crust results in P coda energy which will arrive on azimuth, with the predominant energy showing phase velocities between Pg and Pn. P–SV bounces are included but they have high, Pg–Pn, phase velocities. This behavior is caused by rays with multiple bounce points in the crust, mainly on the Moho and the free surface where at least one leg is P. At

larger offsets the energy in P coda converges to a Pg phase velocity. Energy is not expected at velocities lower than Pg or higher than Pn. Also, the P coda energy in this plane layer model is coherent with arrival groups that may be correlated across traces. This coherence is not observed in real seismograms.

### **6.3.2 F–K Analysis**

F–K analysis is used to determine the velocity and azimuth of the dominant and secondary energy observed in the P coda at the four arrays: NORESS, ARCESS, FINESA, and NYNEX. A summary of the events studied is given in Figure 6-2 and examples of the recorded seismograms are shown. Figure 6-3 gives an example of the processing and analysis where the seismogram corresponds to the vertical displacement recorded at the center station of NORESS. The event was a quarry blast at Titania Quarry, which is 393 km away from the array at an azimuth of 229°. The seismogram is filtered in a narrow pass-band,  $\pm 10\%$ , around a central frequency of 3 Hz and the frequency–wavenumber spectrum is calculated using the Maximum Likelihood Method (Capon, 1969). A semblance analysis for velocity was also implemented to determine the nature of P coda energy as a function of time (Dainty and Schultz, 1993).

F–K analysis of P coda energy assists in the elucidation of crustal scattering mechanisms. This preliminary analysis involved picking by hand the phase velocities and azimuthal deviations of energy peaks in the F–K spectra. The peaks were chosen based on several criteria. Generally, no more than three peaks were picked on a plot. The peaks selected were the three highest peaks, at least one contour level above the surrounding noise, and showed phase velocities faster than 2 km/sec. The largest peak was chosen as a primary peak and the remaining peaks were labeled as secondary. Figure 6-4 gives the histograms for the phase velocity and azimuthal

distribution of the data and includes both primary and secondary peaks. The peaks are cluster around the source azimuth (most peaks within  $20^\circ$ ). This contrasts with the S coda where the energy is spread over all azimuths. This F–K analysis shows energy arriving between Pg and Pn phase velocities as predicted by the plane layered geometry. Peak energy is observed at Pn phase velocity and greater. Not predicted by the plane layer model, energy arrives with slower phase velocities, between Lg and Pg, with primary peak energy arriving at Sn phase velocity. A peak number of secondary arrivals are also observed with approximate Lg velocity. Each of these slower arrivals suggests that P waves are converted during some leg of the path into post critical–shear energy which then becomes favored for lateral propagation. The semblance analysis generally confirms the F–K observations as Pn and Pg energy tends to arrive early in the P coda while Lg energy tends to arrive late. This time delay is expected with conversion to shear along at least one leg of the path. In general this F–K analysis shows that P coda energy is usually dominated by a few peaks which arrive with different phase velocities rather than a single phase velocity with the substantially different azimuths, characteristic of S coda.

This energy distribution is in agreement with the observations of Dainty and Toksöz (1990) and, similarly, we must conclude that although isotropic volume scattering models appear to be consistent with the scattering of S coda, the wide range of phase velocities and the absence of diffuse scattering over a wide range of azimuths in P coda suggests a different velocity distribution. Numerous scattering mechanisms may be responsible for the observation of slower phases in P coda at these arrays. As discussed earlier, the isotropic volume scattering model is clearly not consistent with crustal geology. In this respect, a stochastic, laminated velocity distribution, similar in nature to the structure proposed by Gee and Jordan (1988) may help explain the discrepancy between P and Lg coda. Sanchez–Sesma and Campillo (1991), among others, have also shown theoretically that even simple topographic features near an array can cause great variability in recorded amplitudes as a function of frequency,

incident angle, and receiver location with respect to the topography and observations confirm this (Bannister *et al.*, 1990; Gupta *et al.*, 1990). In addition, heterogeneities near the receiver array can play havoc with any F–K interpretation as near field interference spreads and distorts coherent arrivals on seismograms. Another mechanism which must be considered is wave conversion at irregular subsurface boundaries such as the Moho.

Assuming that this F–K analysis emphasizes energy consisting of plane wave components, therefore accentuating waves scattered at larger distances from the array, we show that the energy scattered at irregular crustal boundaries is consistent with the energy observed at the NORESS, FINESA, ARCESS, and NYNEX arrays.

### 6.3.3 The Role of an Irregular Moho

To understand the role that an irregular Moho may play in crustal propagation of energy, we utilize the Somigliana approach of Chapters 3 and 4 (Schultz and Toksöz, 1993 1994a). As we have shown, this approach models all waves scattered at an interface, including all converted, multiple scattered, and interface waves generated along the interface. The scattered energy at any point along the interface is presented in the form of the amplitude reflection coefficients, showing the average total amplitude distribution for waves propagating away from the irregular interface.

Characterizing the interface with specific Gaussian statistics the interface roughness is expressed again in terms of the standard deviation of interface height,  $\delta$ , and an autocorrelation length,  $a$ , which represents approximately the average distance between adjacent peaks and valleys along the interface. The average *rms* slope of the interface can be expressed as

$$\phi = \tan^{-1}\left(\frac{\sqrt{2}\delta}{a}\right). \quad (6.1)$$

The material parameters and statistical properties of the interfaces modeled are shown in Figure 6-5. Figures 6-7 and 6-8 overlay the statistical reflection coefficients for a P wave incident on the Moho with both a  $10^\circ$  *rms* slope and a more irregular  $30^\circ$  *rms* slope, respectively. These reflection coefficients correspond to the case  $a \approx \lambda$  presented in Chapter 4, where both reflected P and converted S amplitudes are plotted at specific incident angles, ranging from normal incidence ( $\theta_0 = 0^\circ$ ) to near grazing angles ( $\theta_0 = 60^\circ$ ). In each case the total displacement amplitude is plotted, including specular contributions. Note also that in each figure negative scattering angles,  $\theta_s$ , still correspond to backscattering.

A simplified crustal model, where a constant velocity crust is bounded by a plane free surface and an irregular Moho as shown in Figure 6-6a, can help elucidate the generation of P coda. In the case shown, an incident P wave encounters an irregular Moho, generating both P and converted S energy over a broad range of directions, including the specular direction. Referring to reflection coefficients for an irregular Moho, shown in Figures 6-7 and 6-8, it is clear that in the 3-4 Hz frequency range studied above, Moho roughness of 100-500 m over 1-2 km range can explain the observed scattering trends. P-to-P scattering at most incident angles favors a lobe of scattering with the peak amount of energy scattered at Pn phase velocity (critical angle) and a full spectrum of energy scattered between Pn and Pg phase velocities (post-critical angles) given most incident angles. This energy adds to energy arriving in the specular direction, contributing to energy arriving with Pn and Pg phase velocity. At all incident angles, P-to-S reflection coefficients show a peak amount of energy converted to phase velocities faster than Sn. At incident angles greater than  $40^\circ$ , energy is converted to post-critical shear energy. Since the peak S energy,  $V_a \geq S_n$ , leaks out of the crust, the most efficient modes of propagation are waves traveling with Sn phase velocity. Lg velocities are also favored, although less energy is converted to these waves apparently as a result of shadowing by adjacent irregularities along the interface. This distribution of energy corresponds well to the observed

data where Sn and Lg velocities are most efficient. Moving to the more irregular case of a  $30^\circ$  *rms* slope, shown in Figure 6-8, this post-critical scattering becomes more pronounced, demonstrating that larger interface roughness can give even greater preference to the propagation of Sn and Lg phase velocities in the crust.

### 6.3.4 The Role of Near Surface Intracrustal Layers

Can rough intracrustal interfaces be partially responsible for peak Sn and Lg phase velocities observed in the F-K analysis of P coda? Figure 6-6b gives an example of a simplified crustal geometry which can contribute post-critical shear energy to the lower crust. In this case, an upward propagating P wave, traveling in a constant velocity lower crust, scatters as it encounters a highly irregular soil-basement interface. Incident energy is converted into post-critical shear energy which is then favored for lateral propagation in the crust. Figure 6-9 shows the reflection coefficients for a wave incident, from the lower crust, on a soil-basement interface having an *rms* slope of  $30^\circ$ . It is clear that this interface can scatter the same order of energy as the Moho into phases which travel with Lg and Sn phase velocities and this conversion can now occur, not only at near grazing angles, but also at most other incident angles, generating additional post-critical energy in the lower crust. While the soil-basement reflection case is shown for illustration, we generally expect strongly irregular interfaces present in the near surface intracrustal region (including the free surface) to strongly influence the production of scattered energy, especially the generation of energy traveling with lower phase velocities.

Just as the scattering from the bottom of a highly irregular near surface interface can create large amplitude, post-critical energy that remains trapped in the crust, the scattering of P wave energy incident from the top of a near surface interface can also feed energy into large amplitude post-critical reflections which remain trapped in

the shallower crustal layers as shown in Figure 6-6c. Figure 6-10 shows the reflection coefficients obtained for the soil-basement interface, given a P wave incident from the soil layer. These reflection coefficients show that large amounts of scattered P and converted SV energy is scattered to post-critical angles, thus having the potential to remain trapped in the upper crustal layers unless other deviations from a plane layer geometry are encountered along their paths. This trapped energy will likely complicate the wave field observed at a nearby array. As a result of the large attenuation in these shallow layers, due to both volume scattering and intrinsic attenuation, the full effect of these waves is not likely to be observed at stations too far from the point of scattering. The reflection coefficients also show shadowing from irregularities which decreases the amount of energy traveling horizontally in the crust relatively to energy converted at angles nearer the critical angles.

The semblance analysis, an example of which is shown in Figure 6-3, suggests that energy propagating at Pn, Pg, Sn and Lg velocities (along one azimuth) may form at specific finite regions in the crust. This suggests that the Moho may contain patches of irregularities. However, the statistical approach above assumes that, on "average", with many bounces from an irregular Moho, energy will be converted to waves traveling with Pn, Pg, Sn and Lg phase velocities. Upon each bounce from a continuously irregular interface, strong amplitude fluctuations will exist in the energy scattered. These fluctuations will result in similar patchy arrivals. As a result, it is difficult to determine the lateral scale of interface irregularities based on this analysis.

The above discussion assumes a 2-D interface structure. The results for the less irregular Moho ( $\phi = 10^\circ$ ) may be compared with the 3-D single-scattering perturbation results of Prange (1989). There is a strong similarity in the scattering results over interfaces with similar Gaussian statistics. Post-critical peaks and nulls match well in both scattering angle and relative amplitudes, strengthening the assertion that 2-D scattering provides insight into the mechanisms of 3-D scattering as well.

In addition, this correspondence strongly supports a single scattering mechanism for the lobe of dilatational energy which appears at about  $\theta_s = 54^\circ$ . It is important to note, however, that multiple scattering does play a strong role even at these small *rms* slopes. For instance, single scattering theories do not predict the important mechanism of shadowing mentioned above, which works to decrease the amount of energy scattered to Pg and Lg phase velocities in the crust. Upon comparing these two models, it should be noted that the reflection coefficients presented by Prange (1989) do not include specular contributions.

The above discussion demonstrates that the reflection coefficients calculated numerically over an irregular boundary can give insight into the nature of energy propagating in forward directions away from given crustal boundaries. Having shown the effectiveness of these reflection coefficients, we now summarize a number of phenomena which may be a direct result of the backscattering mechanisms identified in the earlier chapters of this thesis. We give a brief discussion of some regions where backscattering and retroreflective mechanisms may play an important role.

## 6.4 Retropropagating Lg Waves

One direct implication of retroreflectance, identified in previous chapters, is the retropropagation of guided waves in the crust. The idea behind retropropagation can be most easily described for the simplest form of scattering, shown in Figure 6-11a. In this case, an Lg wave, propagating in a constant velocity crust, encounters an irregular topographic surface which in turn gives an enhancement of Lg energy propagating in the reverse direction of the incident Lg path. Although the case of scattering from irregular topography was not directly studied, the presence of enhanced backscattering due to topography is probable. In fact, the mechanism of enhanced backscattering

may play its strongest role at the free surface, since we have shown that the retroreflective amplitude increases as the impedance contrast at the interface is increased and the free surface is a perfect reflector. As a result, we expect a large conversion of energy to retropropagating Lg, due to this large amount of predicted backscattering and retroreflectance. In addition, an irregular free surface also has the ability to continually contribute energy into retropropagating waves since trapped waves will encounter the free surface many times during propagation. Each interaction with the surface may backscatter additional energy into retropropagating Lg.

In addition to the free surface, a near surface crustal boundary, such as the soil-basement interface, may also contribute to the retropropagation of Lg waves, as discussed in Figure 6-11b. In this case, an Lg wave propagating in a constant velocity crustal layer encounters a near surface interface, which in turn contributes energy in the reverse Lg direction. Figure 6-12a shows the mean total reflection coefficient for scattered SV waves, given an SV wave incident from the lower crustal layer. The amplitude distribution indicates a large enhancement of energy propagating in the retroreflective direction. The backscattered energy is even larger than the forward scattered energy at many incident angles and, although a distinct retroreflective peak does disappear by 30°-incidence, a large amount of backscattering is still observable at 60°-incidence. In Chapter 5 we showed that, although the reflected amplitudes for a 3-D interface may decrease more rapidly than a 2-D interface with increasing incident angles, large backscattered amplitudes are still observable at the larger incident angles. Thus, it seems plausible that a near surface interface, with either a 2-D or a 3-D geometry, can generate retropropagating Lg waves in the crust, especially for waves with wavelengths similar in size to the irregularities.

### 6.4.1 General Mechanism

Evidence of the retropropagating shear energy, traveling with Sn–Lg phase velocities, may already exist in previous analyses of the F–K spectra of Lg coda. For example, strongly backscattered shear energy can be found in the work of Dainty and Toksöz (1990). As discussed previously this work presents excellent examples of the nature of S coda, showing shear energy arriving from all directions to the seismic array. Not discussed, however, was the strong amount of energy arriving along a backazimuth to the array. Two of the five examples of Lg coda presented show the maximum amount of backscattered energy arriving almost directly along the backazimuth, with both Sn and Lg phase velocities and a signature similar to that of the energy arriving near the source azimuth in the forward direction. Figure 6-13 gives one good example from the F–K analysis of Dainty and Toksöz (1990) for energy arriving from a quarry blast at the FINESA array. This plot shows dramatic support for the presence of retropropagation of energy with Lg velocity arriving late in the Lg coda. Not only is the largest energy observed approximately along the source backazimuth, but the backscattered energy generally mimics the distribution of forward scattered energy (this is not true for the P coda window where backscattering is negligible relative to the forward scattered energy). This mimicking of the forward propagating energy is predicted from the theory of retroreflectance, since retropropagating energy will be partially formed by waves traveling forward past the array. Retropropagating waves, therefore, should travel past the array with approximately the reverse azimuth and phase velocity of the forward propagating wave. However, since large amplitude backscattering does occur over a broad range of angles about the retroreflective direction, amplitudes are not expected to mimic the forward propagating energy exactly. Also, since the required irregular boundaries are usually not encountered along all directions, the phase velocities and azimuths will not be identical to the forward traveling wave. However, based on our results, we feel that the retropropagation of seismic waves due

to retroreflectance from surface irregularities warrants future research.

Comparing the scattered amplitude distribution for an irregular Moho, it appears that irregular topography and irregular near surface layers will have a much larger affect on the retropropagation of Lg waves than the Moho. This assertion is based on a number of observations. First, when a wave encounters deeper boundaries such as the Moho, the ray path of the wave bends outwards, as shown in Figure 6-11c, to reach a post-critical angle at the Moho. The Lg waves tend to encounter the Moho at very wide angles (greater than  $\approx 54^\circ$ ), and based on the reflection coefficients for an irregular Moho, the backscattering decreases dramatically as the incident angle is increased. This is clearly seen in the reflection coefficient calculated for an SV wave incident on an irregular Moho from above, shown in Figure 6-12b. The backscattering predicted at these wider incident angles is minimal, especially with the lower impedance contrast present at the Moho boundary. However, the opposite is true for the shallower boundaries. As an Lg wave travels upward into the shallower crust, the wave path curves upward, resulting in incident angles closer to normal incidence. Based on the reflection coefficients, this will strongly increase the energy that is generally backscattered and retroreflected from the shallower boundaries, leading one to conclude that these boundaries may give the strongest contribution to Lg retropropagation. Since the incident angle is probably closest to normal incidence at the free surface, which in turn is a perfect reflector, we conclude that, given steep enough topography, this surface may give the strongest contribution to the retropropagation of Lg waves.

## 6.5 Ocean Bottom Topography

In the section above, we have shown how an F-K analysis can be used in conjunction with the mean reflection coefficients to investigate scattering within the crust. In this section, we briefly discuss how the reflection amplitude distributions identified both experimentally and numerically in previous chapters may be used to further investigate the nature of other earth boundaries. More precisely, we describe the potential application to ocean bottom scattering in rougher terrain regions, such as mid-ocean spreading ridges. We then discuss the applicability of our isotropic 2-D and 3-D models and demonstrate, with the use of a simplified ultrasonic model, the strong need to include anisotropic characteristics when studying ocean bottom topography.

The scattering mechanisms identified for a highly irregular acoustic-elastic boundary (see Chapter 5) are most applicable to the case of scattering from large scale ocean bottom topography. Based on bathymetric measurements, numerous examples of highly irregular ocean bottom topography, extending over broad regions, have been identified. For example, Hey *et al.* (1986) investigated the active oceanic, propagating rift system which separates the Cocos and the Nazca plates. Bathymetric contour maps and profiles show a 3-D topography similar in nature to the glass surface studied in Chapter 5. However, these results also show that the ocean bottom topography along this rift, rests between our numerical 2-D and experimental 3-D models, as the ocean bottom topography tends to be elongated parallel to the rift axis, in this case from east to west. The deep-tow bathymetric profiles show, that perpendicular to the general strike of the topography, variations as large as 0.1 to 0.3 km can occur over lateral distances of 0.4 km to 2.0 km, respectively. Similar degrees of irregularity have also been shown to exist in various transform regions (e.g. Madsen *et al.*, 1986). Given this scale of irregularity, the reflection coefficients proposed in this study

( $\lambda = a$ ) are applicable in the frequency range of 1.5 to 7.5 Hz, respectively, predicting both strong incoherent scattering and a potential for retroreflectance in a source–receiver plane which is perpendicular to the topographical strike. The SH results in Chapter 3, and the acoustic–elastic results in Chapter 5, predict that strong multiple scattering mechanisms can exist over a much broader frequency range than the range above. Previous perturbation analyses and experimental results (e.g. Menke, 1986, *see* Chapter 1) have also shown that single scattering can be significant, even when the incoming wavelengths are more than an order of magnitude greater than the size of interface irregularities. The exact frequency range over which scattering is dominant depends on both the statistical characteristics and the degree of roughness at the boundary. [An interesting side note: the surface profilometer approach, which utilizes a narrow laser beam and measures backscattering to determine the glass surface height distribution in Chapter 5, is analogous to the Sea Beam approach used to obtain these bathymetric images.]

Seismic refraction profiling shows that portions of the mid–ocean ridges can have a highly irregular subsurface velocity structure which mimics, to some extent, ocean bottom topography (e.g. Purdy and Detrick, 1986). This results in a highly irregular subsurface structure which may contribute additional energy to incoherent scattered energy. Refraction profiling also shows that the ocean bottom P wave velocity at the spreading axis can be as low as 2.5 to 3 km/s, which is substantially lower than the P wave velocity of glass measured in our experiments. However, the combined results and trends identified in Chapters 3 through 5 still give an approximate idea of the scattering that may occur in these regions. Generally, given large scale topography, the reflection coefficients (*see* Figures 5-12 through 5-18) predict large scale backscattering of energy into the water layer, given incident angles up to 60°. Retroreflectance may also play a strong role at the boundary, giving large amplitudes backscattered towards the source. At wider angles a uniform distribution of incoherent energy may be observed over most backscattering directions.

Recently, the azimuthal variation of the statistics of ocean bottom topography, which manifests itself as elongated topography, has been modeled in many regions with anisotropic autocovariance functions using Sea Beam data (Goff and Jordan, 1988; Goff *et al.*, 1991). This work has shown that, in many regions, sea-floor geometry is well described by second order statistics which incorporate the orientation and scale length of topographic elongations along with its fractal dimension. This work has shown how ocean bottom topography can span over seven orders of magnitude, giving a far broader range of scattering than the one observed in our studies. However, the isotropic scattering studied in previous chapters, may still give reasonable insight when the general trend of topography is perpendicular to the source-receiver plane, resulting in an approximate 2-D configuration. As one deviates from this simple 2-D configuration, extreme caution must be used, as the elongation of topography can strongly complicate the observed scattering as a function of azimuth. A simple example of these complexities can be demonstrated with the following ultrasonic experiment.

The experimental geometry is shown in Figure 6-14a where the ocean bottom is modeled by a submerged aluminum block. One realization of the scattered pressure is measured along a line of one hundred receivers which extends parallel to the ocean bottom, a distance 0.1 m above the interface, in the fluid. The receiver spacing is 3 mm. The Panametrics 6.4 mm diameter transducer, used previously as a receiver, is now used as a vertical, downward oriented source which is positioned at the first receiver. A custom made, pin tip transducer is used as the receiver. The two ocean bottom geometries shown in Figures 6-14b and 6-14c are then introduced: namely, a plane interface for reference and a very simple model of 2-D ocean bottom topography extending parallel to the axis of a mid-ocean ridge. The irregular topography consists of "V" shaped depressions. Each depression has a constant depth of 3 mm and a 60° lower acute angle. The depressions are randomly distributed with a 1 cm average spatial separation, a standard deviation from this mean of 3.0 mm, and the constraint

that depressions do not overlap. Although this is a very simplified model of sea-floor topography, which assumes that only one scale length is present and the correlation length of the topography is infinite in one direction, we will show that the results can still give a good example of the complexities which are introduced by elongated topography.

The source wavelet introduced is a narrow band pulse, with a 0–300 kHz frequency width and a peak amplitude at 185 kHz. The central wavelength in water is about 1.0 cm and the half power points of the frequency spectrum correspond to 0.5 and 1.5 cm. The size of the depressions, thus, is on the order of one-fifth to three-fifths the range of incident wavelengths. Results are averaged over 1,024 source sweeps to improve signal to noise ratios. The reader is again referred to Appendix C for further details on the ultrasonic configuration. Figure 6-15a gives the experimental pressure seismogram recorded over the plane interface. The primary reflection, a weak P head wave, and a very strong S head wave can be clearly identified. The source radiation pattern has a narrow directivity pattern, so amplitudes decay quickly with distance along the array. Figure 6-15b gives the synthetic FD results, obtained using the scheme of Virieux (1986), described in Chapter 2. As expected, these results are in good kinematic agreement with the ultrasonic results since the interface is aligned with the FD grid (see Chapter 2). Figure 6-16a and 6-16b give the 2.5-D experimental results and the 2-D numerical solution for a seismic line extending perpendicular to the strike of the ocean ridge topography. In this case, the primary reflection still dominates the seismogram, however, its amplitude now varies nonuniformly as scattered energy interacts with and trails the initial reflection. Scattered arrivals, which persist until the end of the seismogram, show both strong forward and back scattering, with the backscattered energy taking the form of point diffractions originating from the interface. Dramatically, the grooves also appear to obstruct, almost completely, S head wave propagation. This 2-D geometry most closely corresponds to the interfaces modeled in Chapter 5.

Moving the horizontal azimuth of the seismic array with respect to the topographic strike, the strong azimuthal character of scattering becomes apparent. Figure 6-17a gives the pressure seismogram for a seismic array oriented parallel to the strike of topography (running parallel to the ridge axis). This is the simplest 3-D geometry. In this case, the scattered energy takes on a different character. The primary reflection is greatly distorted by interference with secondary arrivals which consist of continuous diffractions from depressions lying outside the source-receiver plane. These arrivals have a moveout very similar to reflections from deeper layers and give the impression of subsurface reflectors. S head waves also appear to be favored for propagation parallel to the seismic array, guided by each of the elongated depressions. This results in multiple head wave arrivals, each originating from a separate depression. Each head wave arrives with a phase velocity equal to the shear velocity of the ocean bottom and each originates with a time delay corresponding to the additional distance the wave must travel to reach the respective depression. In addition, contrary to the previous case, negligible backscattering is observed in this geometry.

Studying Figure 6-17b which corresponds to the case of a seismic line oriented diagonally to the topography,  $45^\circ$  to ridge strike, we find that the nature of scattering lies in between the perpendicular and parallel cases above. Three dimensional, out of plane scattering, from the topography gives the appearance of continuous secondary arrivals which have phase velocities between those observed for the perpendicular and parallel cases. Less backscattering is observed than in the perpendicular case, and some S head wave energy can be identified only near the critical angle, as head wave energy appears to be both obstructed and guided away from the receiver plane by the topographic depressions. This distribution of scattered energy is strongly supported by F-K results which are presented in Appendix D.

The results above show that significant differences in the form of scattered energy occur as a function of azimuth as ocean bottom topography takes on an elon-

gated form. Schultz and Toksöz (1992,1994b) have quantitatively analyzed the results above, showing that amplitude variations of the primary reflection can vary significantly as a function of array azimuth. They also showed that, although amplitude errors can exist for the 30 PPW sampling of the finite grid (*see* Chapter 2), the 2-D FD results are in both kinematic and dynamic agreement with the 2.5-D experimental results. This is most likely due to the fact that the steeper slopes along the interface act only as point diffractors and not as long distance propagators of energy. The remaining plane segments of the interface which propagate energy over larger distances are aligned with the grid, propagating energy accurately.

This experiment demonstrates that the introduction of elongated topography, in itself, can greatly complicate the phase velocity and amplitude distribution of scattered energy as a function of azimuth. Most dramatic is the absence of backscattered energy propagating parallel to the topographical strike and the obstruction of head wave energy propagating perpendicular to the topographical strike. The presence of higher order statistics in the topography and a broader range of topographical scale lengths can only work to further complicate scattering. Since various scale lengths exist along the ocean bottom and general scattering may vary strongly as a function of azimuth, various levels of multiple scattering will likely exist. Understanding how retroreflectance, shadowing, and general single scattered amplitudes respond to this added complexity may give additional insight into the response of ocean bottom topography to various forms of incident energy, ranging from lower frequency teleseismic and regional events all the way to higher frequency Sea Beam energy.

## 6.6 Discussion and Conclusions

We have extended the scattered amplitude distributions from previous chapters to evaluate their implications on crustal scattering. We began by utilizing the final reflection coefficients computed with the Somigliana approach in Chapter 4 to study the P coda energy recorded at Scandinavian and New England seismic arrays. Specifically, an analysis of NORESS, FINESA, ARCESS, and NYNEX arrays using F–K spectra showed that the backazimuths of P coda energy cluster around the P backazimuth with a spread of about  $\pm 15^\circ$ . The F–K spectra contained tight peaks which do not spread over large azimuths. This contrasts with the behavior of S coda, and indicates that a model of scattering from isotropically distributed volume heterogeneities is not adequate, at least for the coherent portion of the coda. The phase velocities measured fall into three main groups: a high velocity group ( $> 7$  km/s), a Pg velocity (6 km/s) group, and a low velocity ( $< 5$  km/s) group. The high velocity group fits the multiple crustal reflection model, and is also favored by P–P scattering from a rough interface. The other velocity groups may be explained in terms of scattered, nonspecular reflections from a rough interface. Scattering from an irregular Moho and irregular near surface interfaces are both shown to be consistent with these observations. The more irregular the Moho discontinuity or intracrustal interface is, the more easily energy converts to the phase velocities observed at the arrays. In addition, a near surface interface in the shallow crust can also efficiently generate scattered energy which is favored for lateral propagation in the upper crustal layers. The effects of large attenuation in shallower crustal layers may decrease the importance of these waves. This preliminary study indicates that a composite model for scattering within the crust must consider the possibility of scattering from interface irregularities.

The retroreflectance of seismic waves predicted by the reflection coefficients for an irregular Moho and an irregular intracrustal interface suggests that interface scat-

tering can contribute energy into the retropropagation of various wave types. Lg scattering was studied specifically since energy with Lg phase velocity is preferred for propagation over significant lateral distances. The characteristics of the reflection coefficients suggest that shallow, high impedance contrast boundaries and irregular topography probably give the strongest contribution to retropropagating Lg waves. Although direct evidence for this retropropagation has not been observed, F–K plots do show the evidence of strong backscattering, warranting further research in the identification of this phenomenon. Given the 3 to 4 Hz range of frequencies studied in this chapter, the range of velocities which might be present at the interface (1.5 to 4.0 km/s), and the reflection coefficients presented, we find that near surface interface irregularities, with an average peak to peak width ranging from 0.7 to 2.3 km and a standard deviation in height ranging from 0.1 to 0.5 km, respectively, can contribute to retropropagation. Considering the lower shear velocities which might occur near the free surface, the size of surface topography required for retropropagation is somewhat smaller than that for the shallow interface. As we have shown in Chapter 3, retroreflectance can also occur over a much larger range of irregularity sizes than the  $\lambda = a$  case. Therefore, strong contributions to retropropagation can also occur for interface irregularities which are somewhat larger or smaller in size than the irregularities studied above.

Judging from surface topography near the Scandinavian arrays, it is apparent that topography will likely play its strongest role at the NORESS and ARCESS arrays as they are located in close proximity to complex fjord topography, generally lying inland on the lower foothills. Based on topographic information of this region, the topography near the array can vary by as much as 0.2 to 0.5 km over ranges of 2 to 10 kilometers, approaching the rough topography required for strong multiple scattering and retroreflectance. To the west, the fjord topography has steeper slopes, in places having elevation changes as great as 0.5 km over distances shorter than 5 km. Such large topographic variations should be optimal for the backscattering of incident

energy. The FINESA array, on the other hand, is located in the relatively flat lowlands of Finland. Changes in topography are relatively small in this region, showing a maximum change of about 0.05 to 0.1 km over a 2 to 5 km distance. Although the slopes in this region are quite steep due to glacial erosion, topography most likely plays a much smaller role at the FINESA array than at the NORESS and ARCESS arrays. Deeper crustal structure is therefore the most plausible explanation for backscattering in this region and for the possible retropropagation of energy observed for the Lg coda window in Figure 6-13.

As discussed above and in Chapter 4, the enhancement of backscattered waves in the crust can also result from multiple scattering within volume heterogeneities. Although the retropropagation of waves was discussed in this chapter with respect to irregular surfaces, retropropagation due to volume heterogeneity is also plausible and should not be ruled out. Any future study of retropropagation should consider both forms of scattering. In this sense, further work on the retropropagation of Lg waves should be conducted at the Scandinavian arrays. The general approach may include generating F–K plots for energy arriving both early and late in the Lg coda. Rotating and averaging various events may also allow for an average over many realizations of crustal scattering in these regions. Analysis of such plots can help identify the presence of retropropagating energy in the crust, elucidate any preference for this form of propagation, and determine the azimuthal distribution of retropropagation along with its dependence on surrounding crustal structure.

In the last section, we have shown that the amplitude distribution of waves scattered from highly irregular acoustic–elastic and elastic–elastic interfaces may provide a tool for understanding various ocean scattering problems. An extension of the reflection coefficient analysis of previous chapters, along with more detailed deterministic modeling, may provide further insight into the seismo/acoustic scattering which results from mid–ocean ridge topography. Although the full range of possible

applications is not investigated in this chapter, we hope that this discussion provides a basis for determining how multiple scattering may manifest itself in future applications.

**SYN. RECORD SECT., SMOOTH INTERFACES  
(TOKSÖZ ET AL., 1990)**

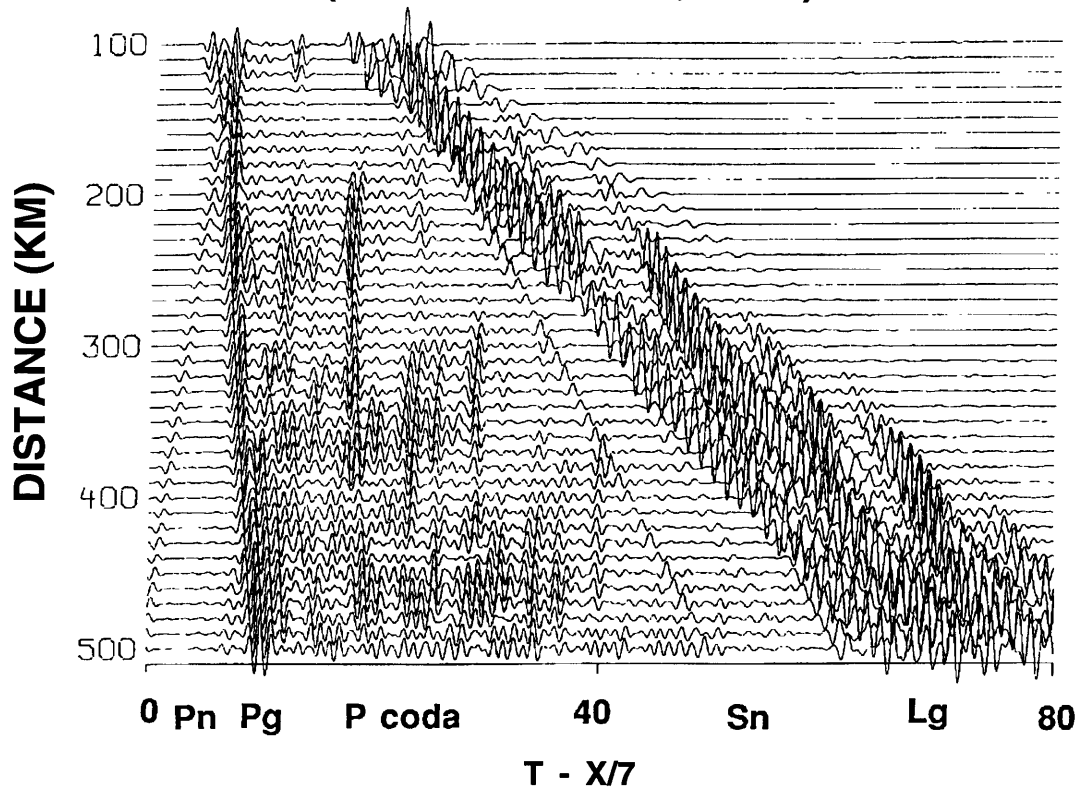
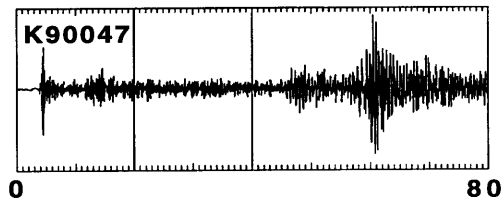


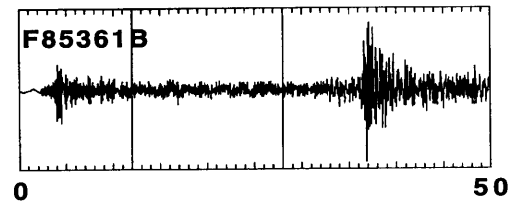
Figure 6-1: A synthetic seismogram calculated with reflectivity over a simply layered crust following a velocity model for NORESS, which is shown in the text. The various phases are labeled.

**SEISMOGRAMS:**

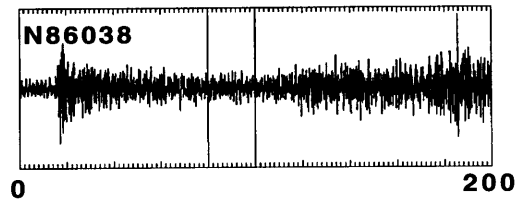
**ARCESS - 6 EVENTS (2 EARTHQUAKES,  
2 MINE BLASTS, 1 NUCLEAR TEST),  
RANGE 370-1160 KM, FREQUENCY  
CONTENT 2-10 HZ.  
EXAMPLE: 16 FEB 1990 12:39:10,  
RANGE 420 KM, KOLA MINE BLAST.**



**FINESA - 5 ESTONIAN/RUSSIAN MINE  
BLASTS, RANGE 220-340 KM,  
FREQUENCY CONTENT 2-10 HZ.  
EXAMPLE: 27 DEC 1985 12:16:49,  
RANGE 300 KM.**



**NORESS - 5 EVENTS (3 MINE BLASTS, 2  
EARTHQUAKES), RANGE 320-1070  
KM, FREQUENCY CONTENT 2-10 HZ.  
EXAMPLE: 7 FEB 1986 11:2:0,  
RANGE 1070 KM, RUSSIAN MINE  
BLAST.**



**HAVERHILL, NH - 5 REFRACTION SHOTS  
FROM THE NYNEX EXPERIMENT,  
RANGE 160-240 KM, FREQUENCY  
CONTENT 5-20 HZ.  
EXAMPLE: 17 SEP 1988 6:4:27,  
RANGE 189 KM, NYNEX SHOT 1.**

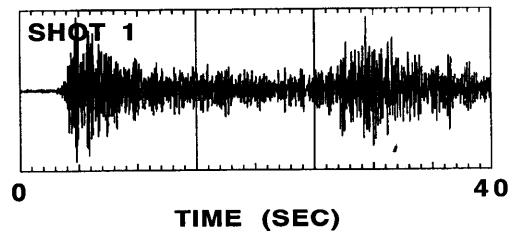


Figure 6-2: Summary of the events studied at the Scandinavian ARCESS, FINESA, and ARCESS arrays and the New England NYNESS array. Seismograms for one event at each array and an example of the P coda windows analyzed are also given.

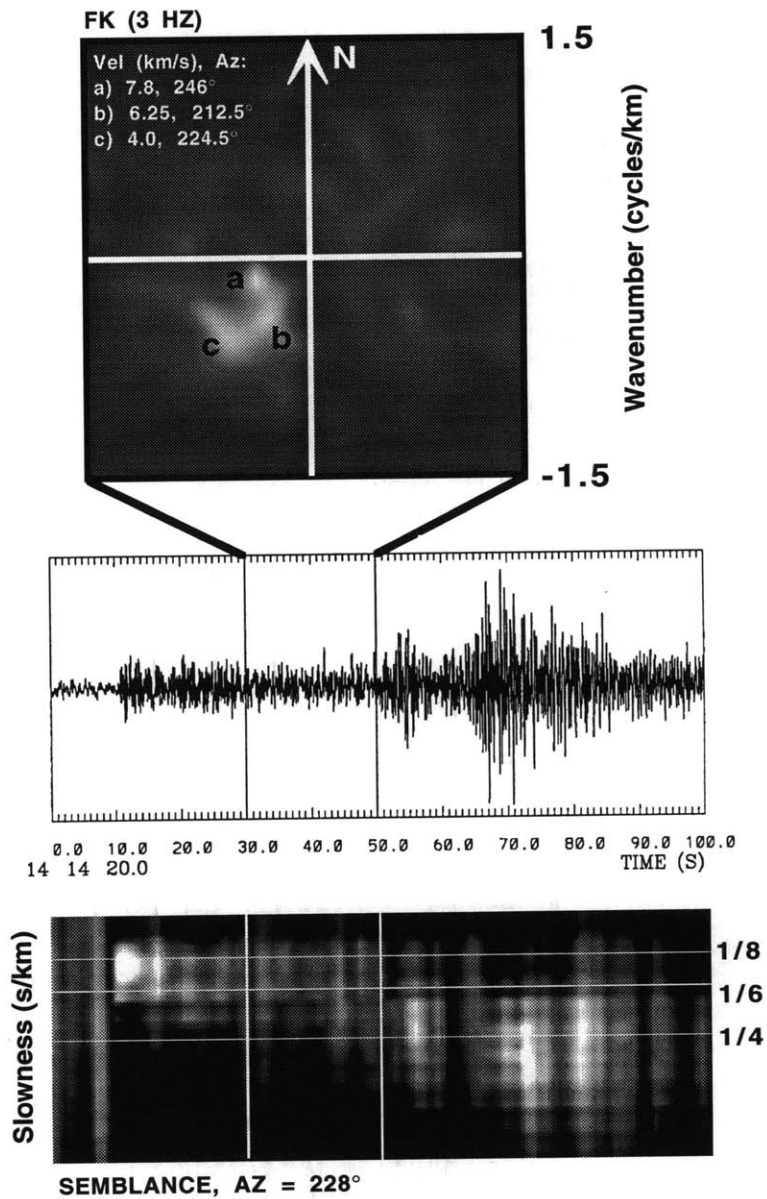


Figure 6-3: The frequency–wavenumber spectrum for the P coda window shown. The position, phase velocity, and azimuth of the primary peaks are given. Also shown is a semblance analysis for this event along an azimuth of 229° where the slowness is plotted as a function of time delay along the seismogram.

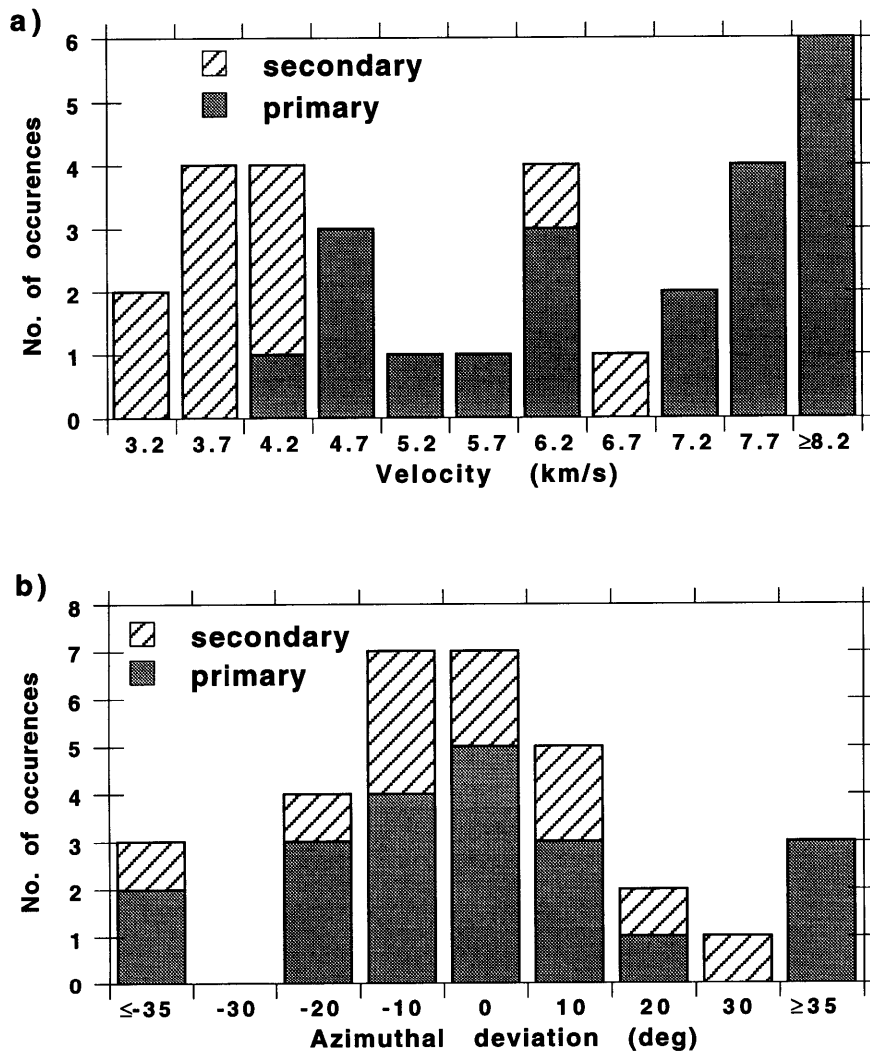
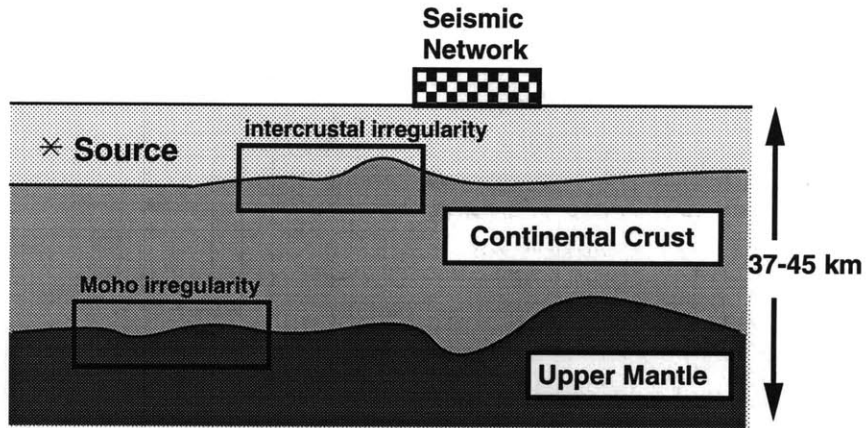
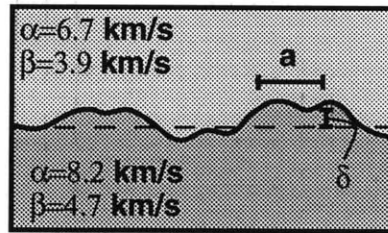


Figure 6-4: Histograms giving (a) the distribution of phase velocities and the (b) azimuthal deviation of peaks measured by hand from the F-K plots for the data analyzed at NORESS, FINESA, ARCESS, and NYNEX.



Moho irregularity:



soil--basement irregularity:

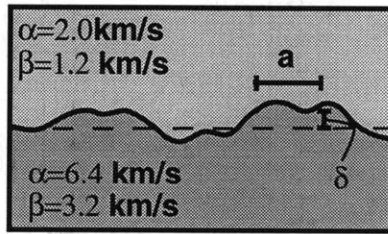


Figure 6-5: A simplified diagram illustrating the crustal geometry, where regional events are observed at various spatial arrays. The material properties used to theoretically model scattering from both an irregular Moho and an irregular intracrustal layer are given.

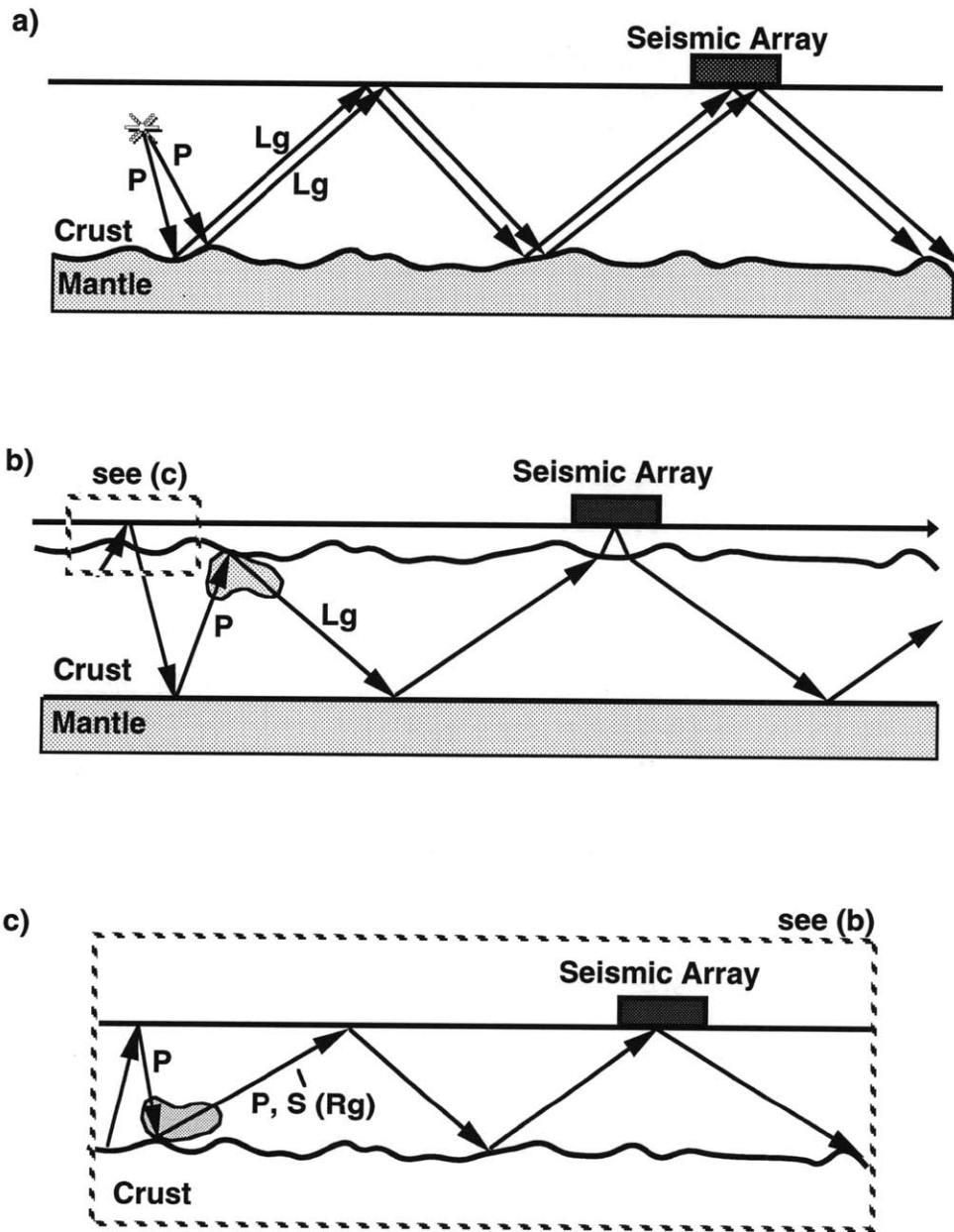


Figure 6-6: A simplified diagram showing (a) an irregular Moho and (b) a near surface, soil-basement interface generating energy which then travels with  $S_n$ -Lg phase velocities in P coda. Also shown is (c) a shallow near surface layer contributing to P and S energy which becomes trapped within a shallow surface layer, potentially complicating Rg energy recorded at a nearby seismic array.

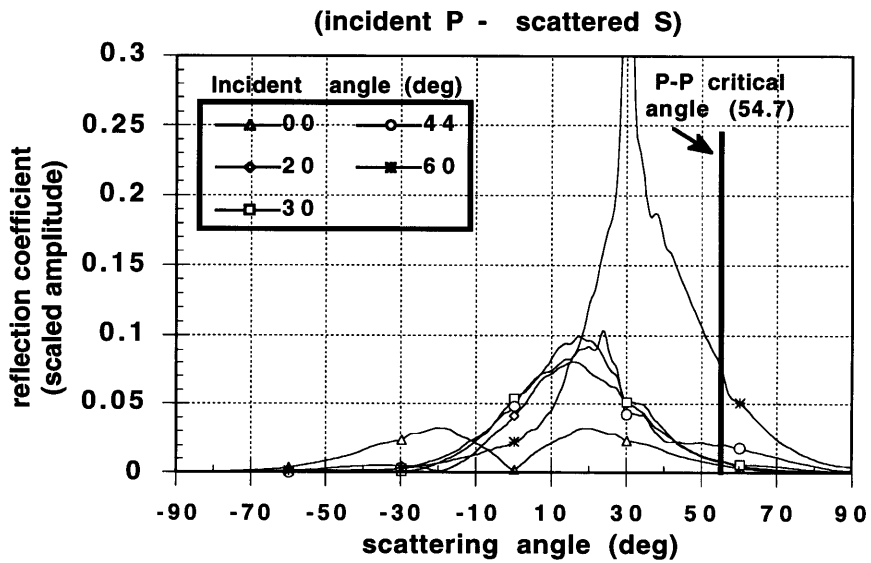
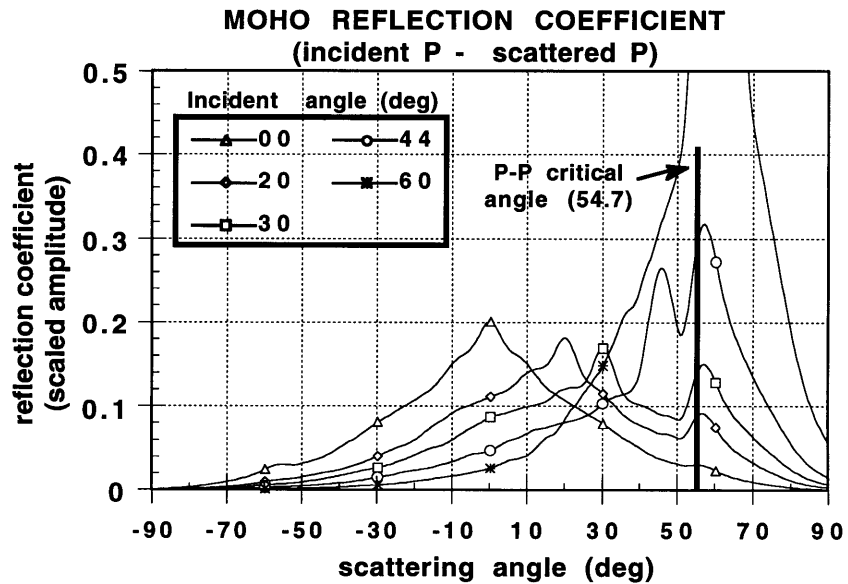


Figure 6-7: The total mean reflection coefficient calculated for an irregular Moho discontinuity with an *rms* slope of  $10^\circ$ . This amplitude distribution corresponds to a P wave incident, from the crust, onto the randomly irregular interface with the Gaussian statistics. The S-S critical angle is approximately the same as the P-P critical angle ( $\theta_c = 56^\circ$ ).

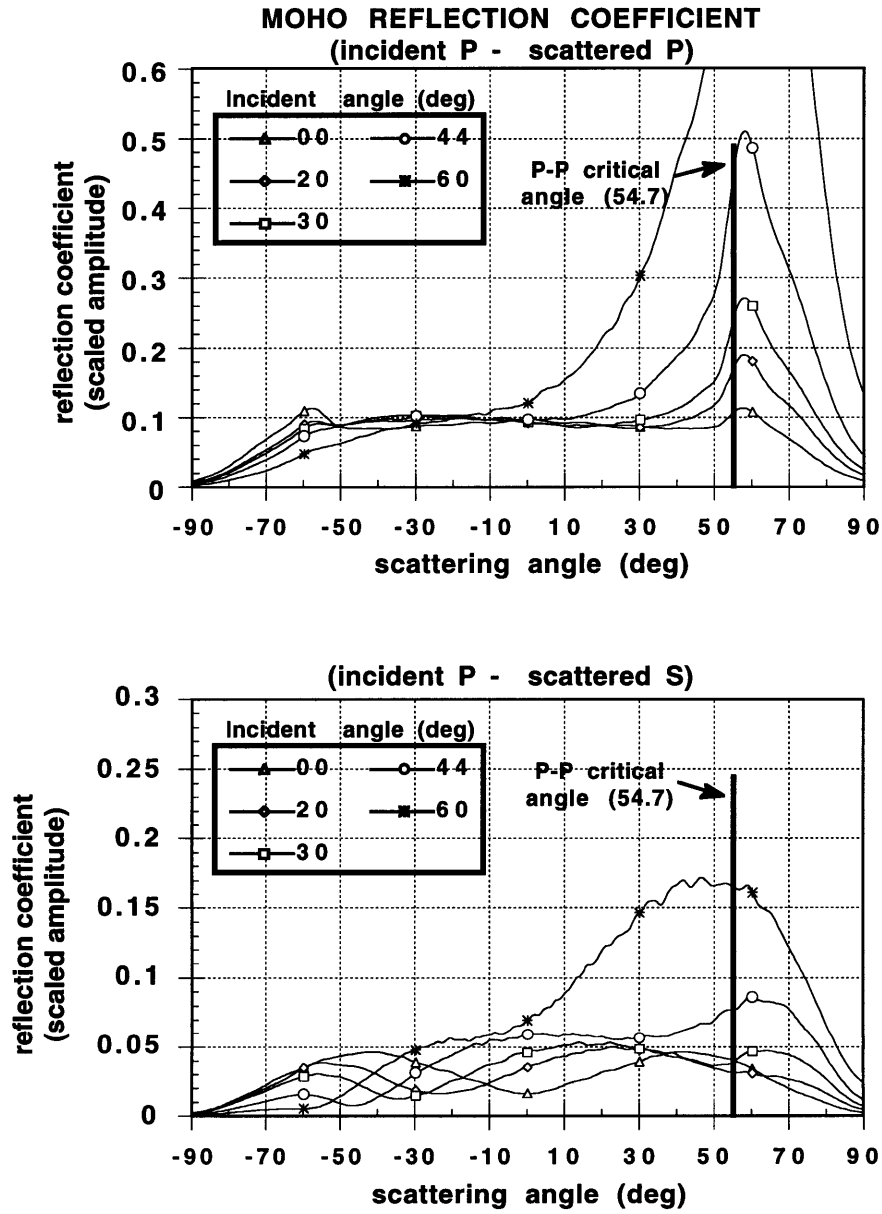


Figure 6-8: Similar to Figure 6-7, except for an interface with an *rms* slope of 30°.

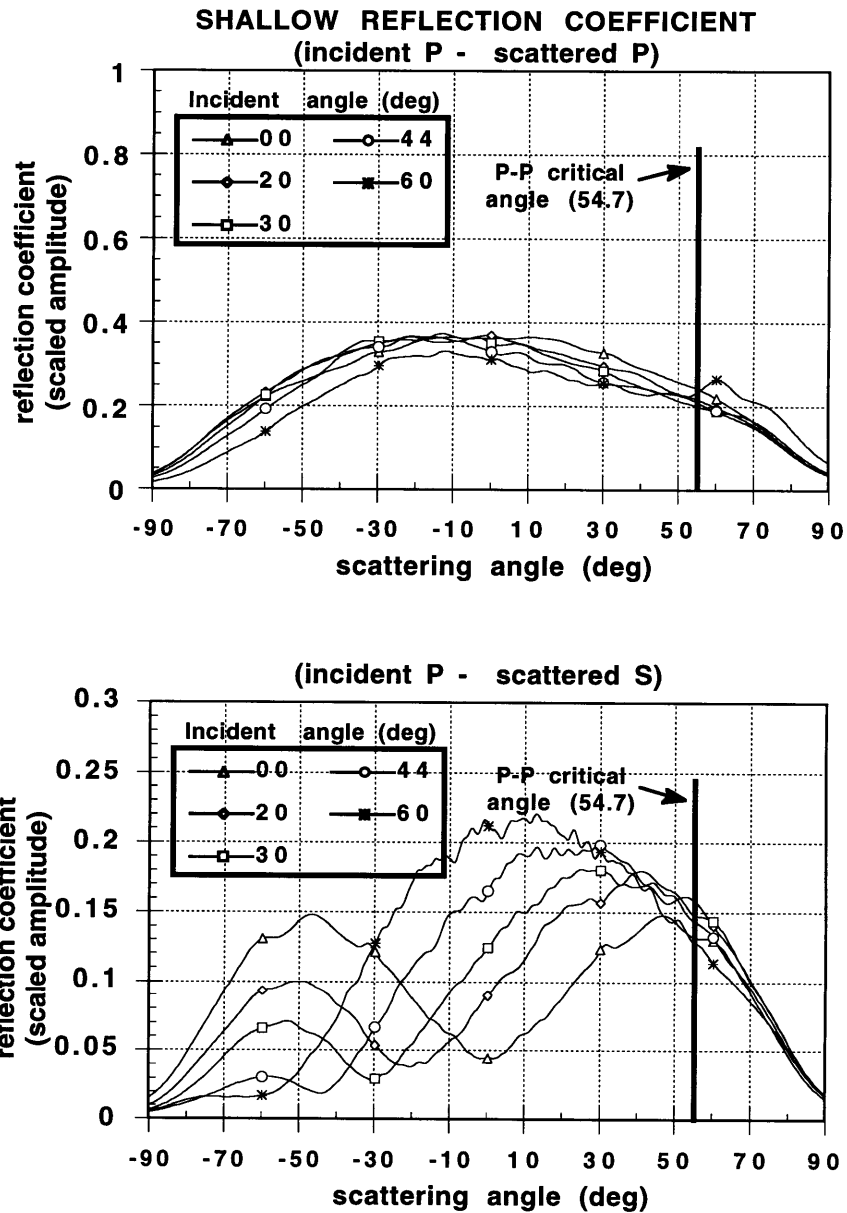


Figure 6-9: Numerical reflection coefficient calculated for a P wave incident on an irregular 2-D, soil-basement interface with a Gaussian distribution of irregularities. The wave is incident from the basement layer, and the total mean reflection coefficient is given for an interface with a  $30^\circ$  *rms* slope.

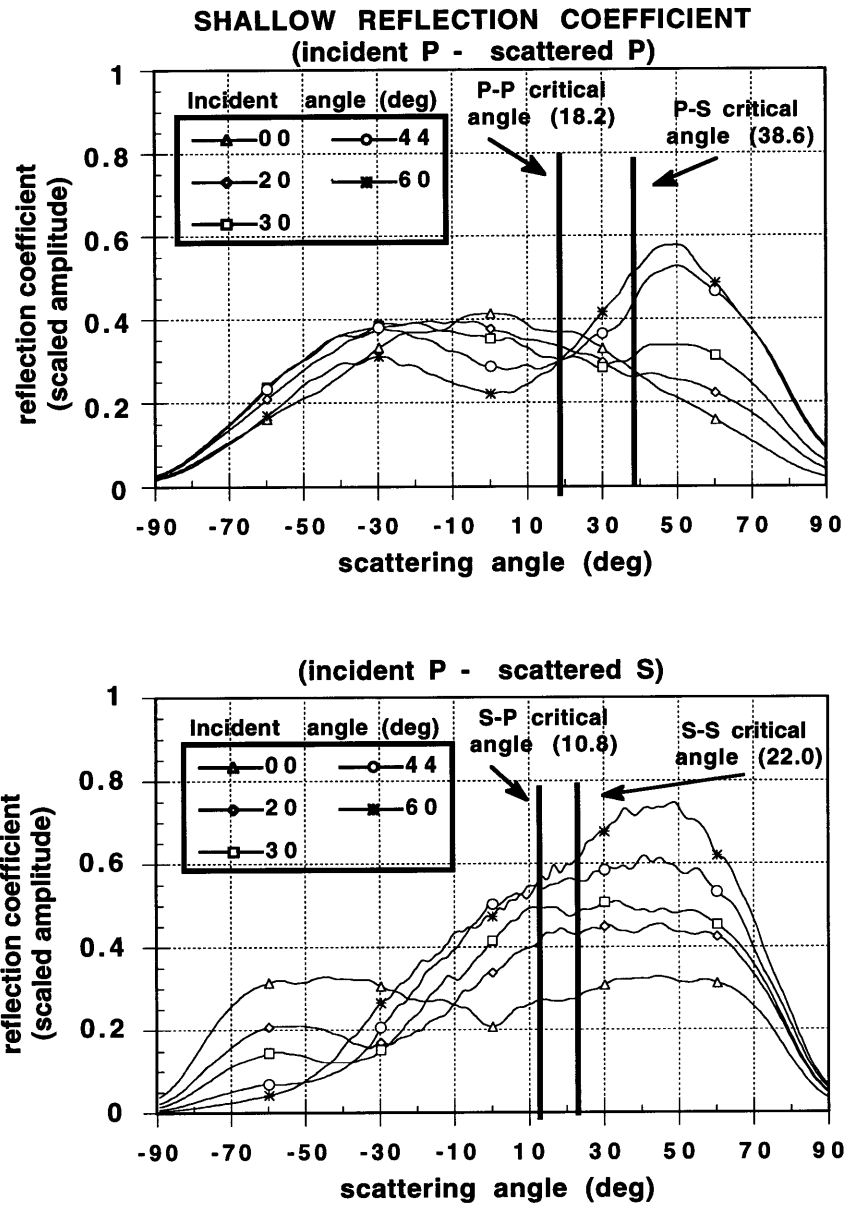


Figure 6-10: Numerical reflection coefficient calculated for a P wave incident on the irregular interface modeled in Figure 6-9. The wave is now incident from the soil layer.

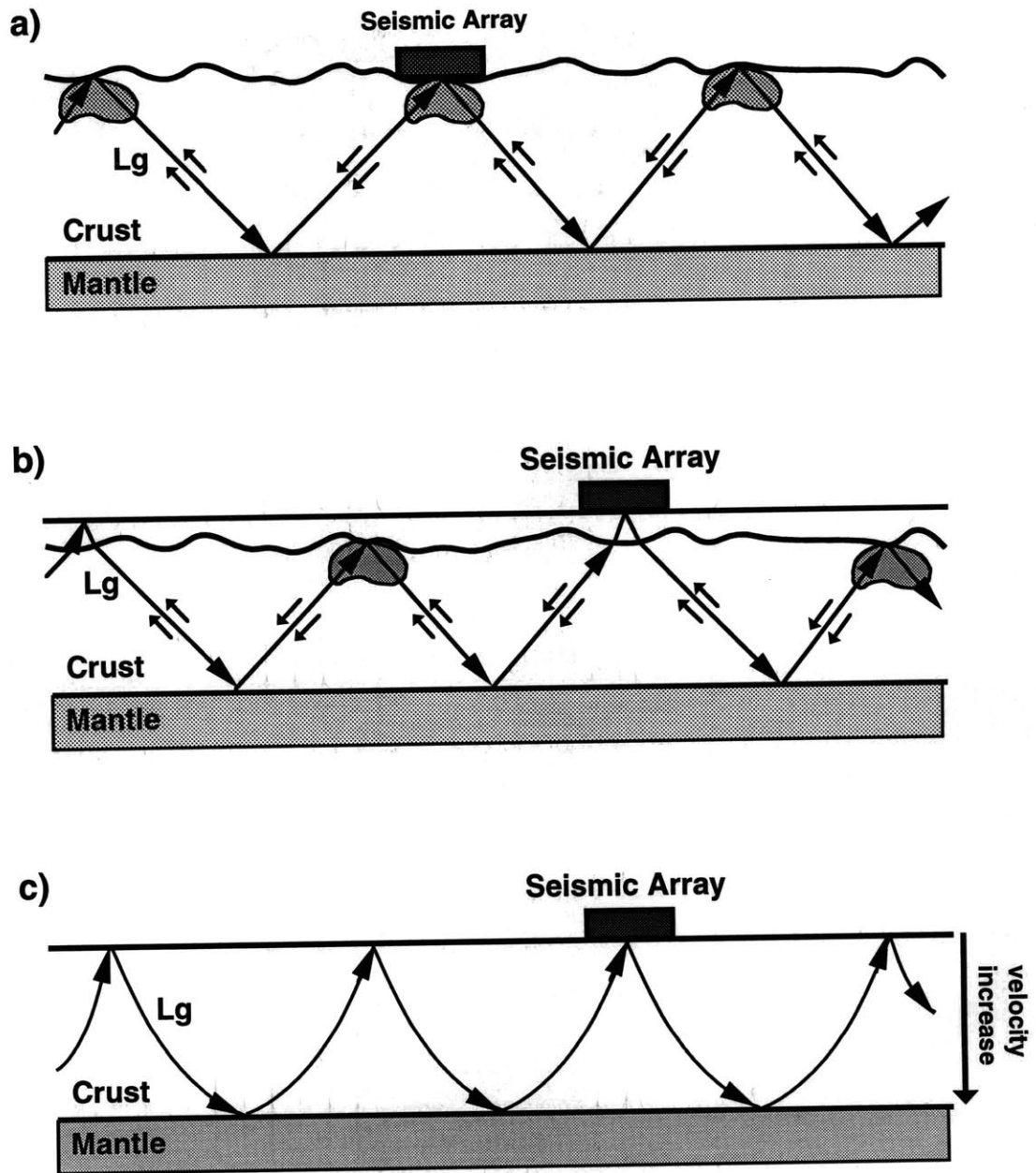


Figure 6-11: A simplified diagram illustrating both (a) irregular free surface topography and (b) a highly irregular near surface interface generating retropropagating Lg waves. A more realistic model of wave propagation in the crust must consider (c) the proper ray path curvature.

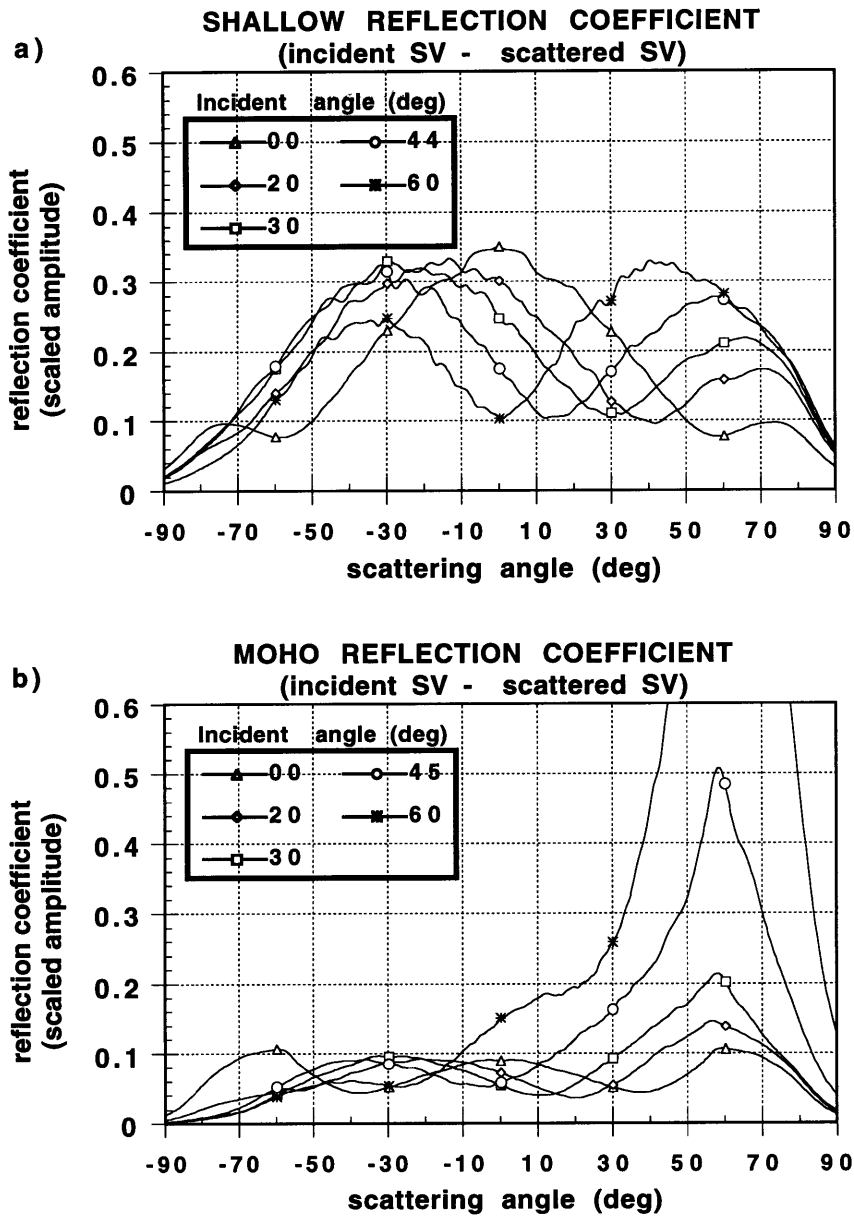
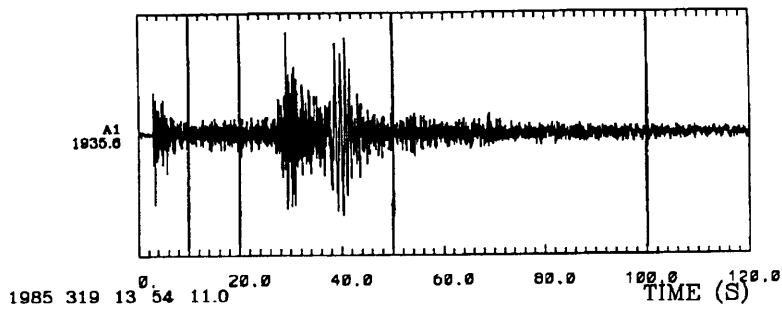
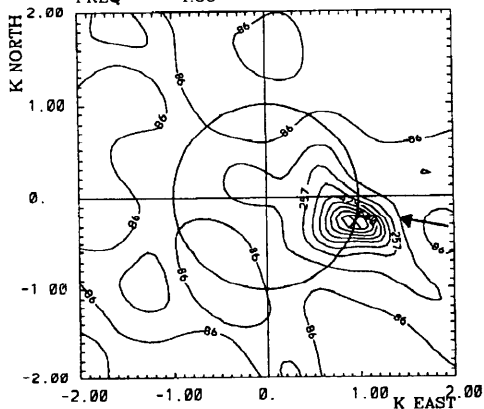


Figure 6-12: The total mean amplitude reflection coefficient for an SV wave incident on (a) the 2-D soil-basement interface from the basement layer, and (b) the 2-D irregular Moho discontinuity from the lower crust, both with an *rms* slope of 30°. Only the SV-SV component of the reflection coefficients are given, identifying the strength of backscattering.

a) 1985 DAY 319 FINESA



b) FINESA P CODA  
 VEL 4.06 AZ 105.9  
 FREQ 4.00



c) FINESA LG CODA  
 VEL 3.98 AZ 64.4  
 FREQ 3.00

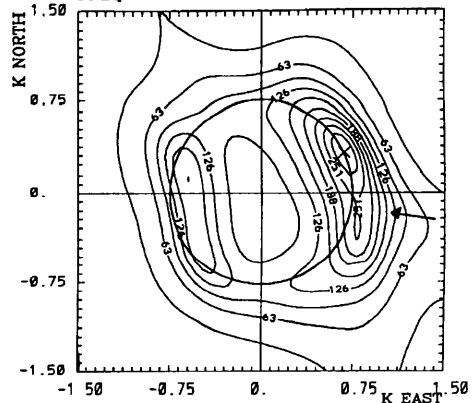


Figure 6-13: An example of (a) the seismogram recorded at a seismometer of the FINESA array along with (b) the F-K spectrum for the P coda window and (c) the F-K spectrum for the Lg coda window at a frequency of 4.0 Hz. Results correspond to a quarry blast near Leningrad (Dainty and Toksöz, 1990).

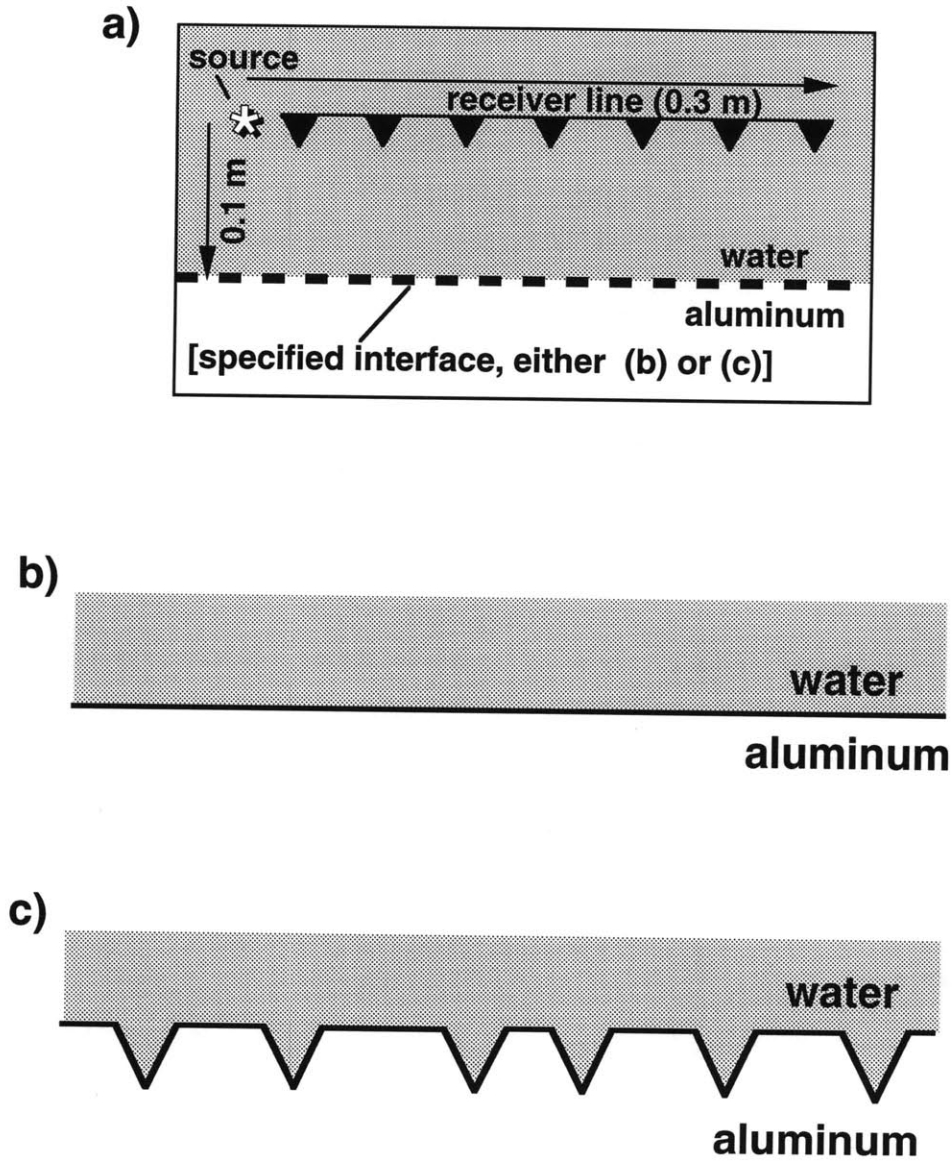


Figure 6-14: Given are (a) the experimental geometry, (b) the reference boundary, a flat ocean bottom, and (c) an irregularly grooved ocean bottom, modeled by a random distribution of grooved corrugations which cut into an aluminum surface. Each groove is 3 mm deep with a lower acute angle of  $60^\circ$ . The central incident wavelength is on the order of 1.0 cm, thus, the depth and length of a corrugation is approximately one-third the central incident wavelength. The aluminum has a 6500 m/s P wave velocity, a 3100 m/s S wave velocity, and a density of 2.7.

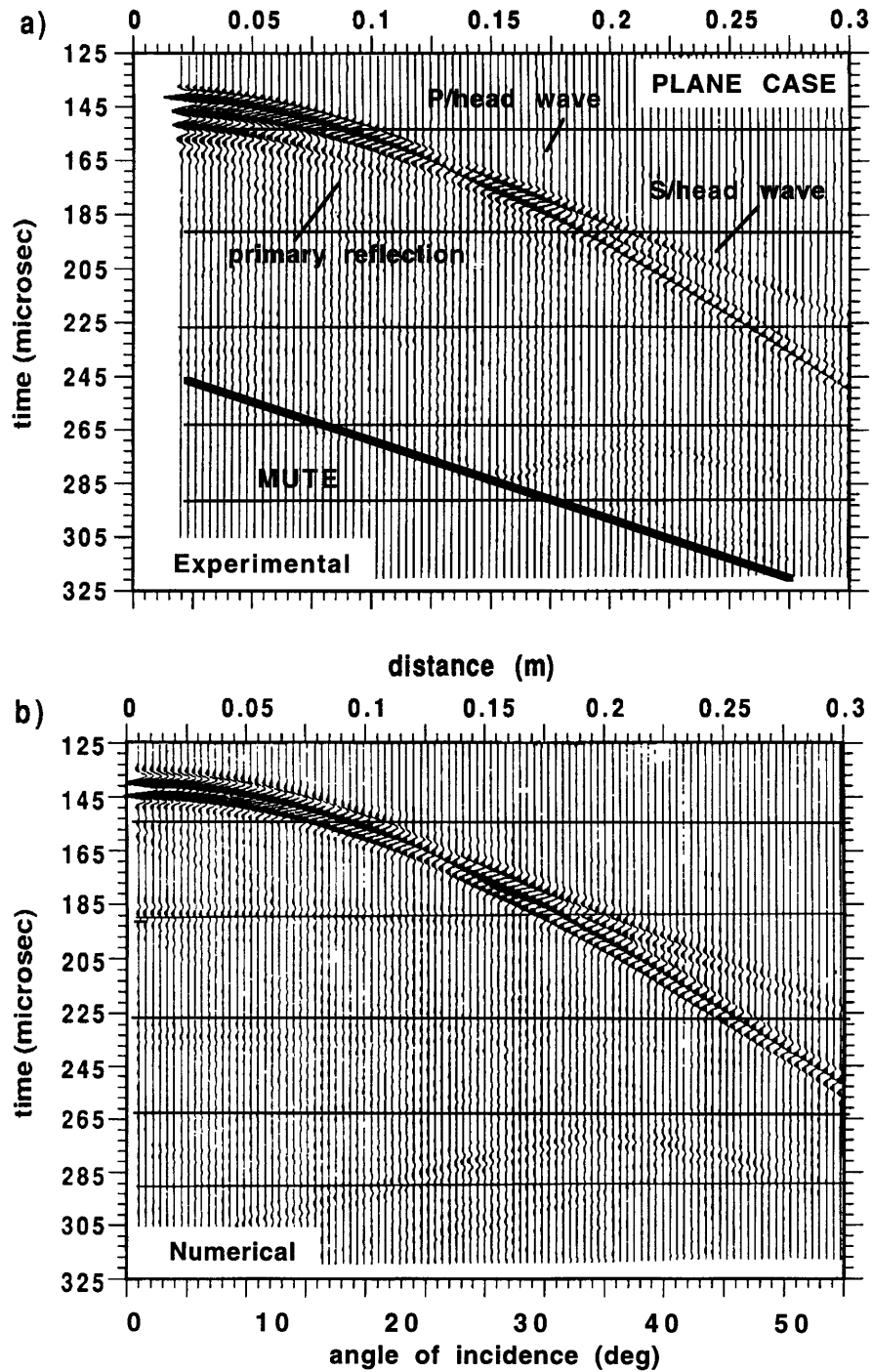


Figure 6-15: Pressure seismogram recorded in our in-house ultrasonic tank for an acoustic wave incident on a plane interface. Both (a) experimental and (b) FD numerical results are given for the same model. Arrivals are marked in (a) and in the experimental case the surface water multiple has been muted from the plot.

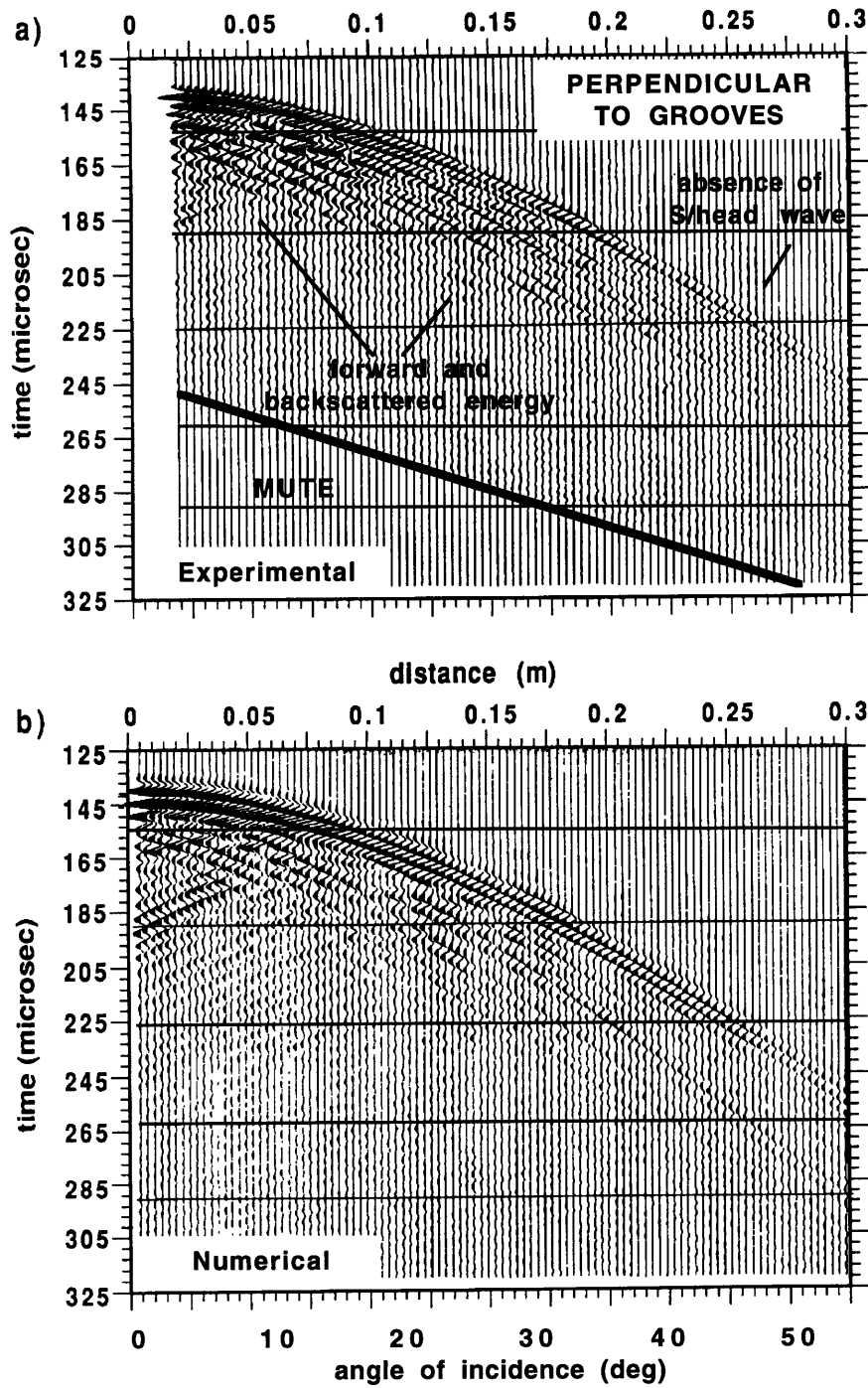


Figure 6-16: Same as Figure 6-15, except for a 2-D distribution of grooved irregularities along the interface. The seismic line extends perpendicular to the strike of the depressions.

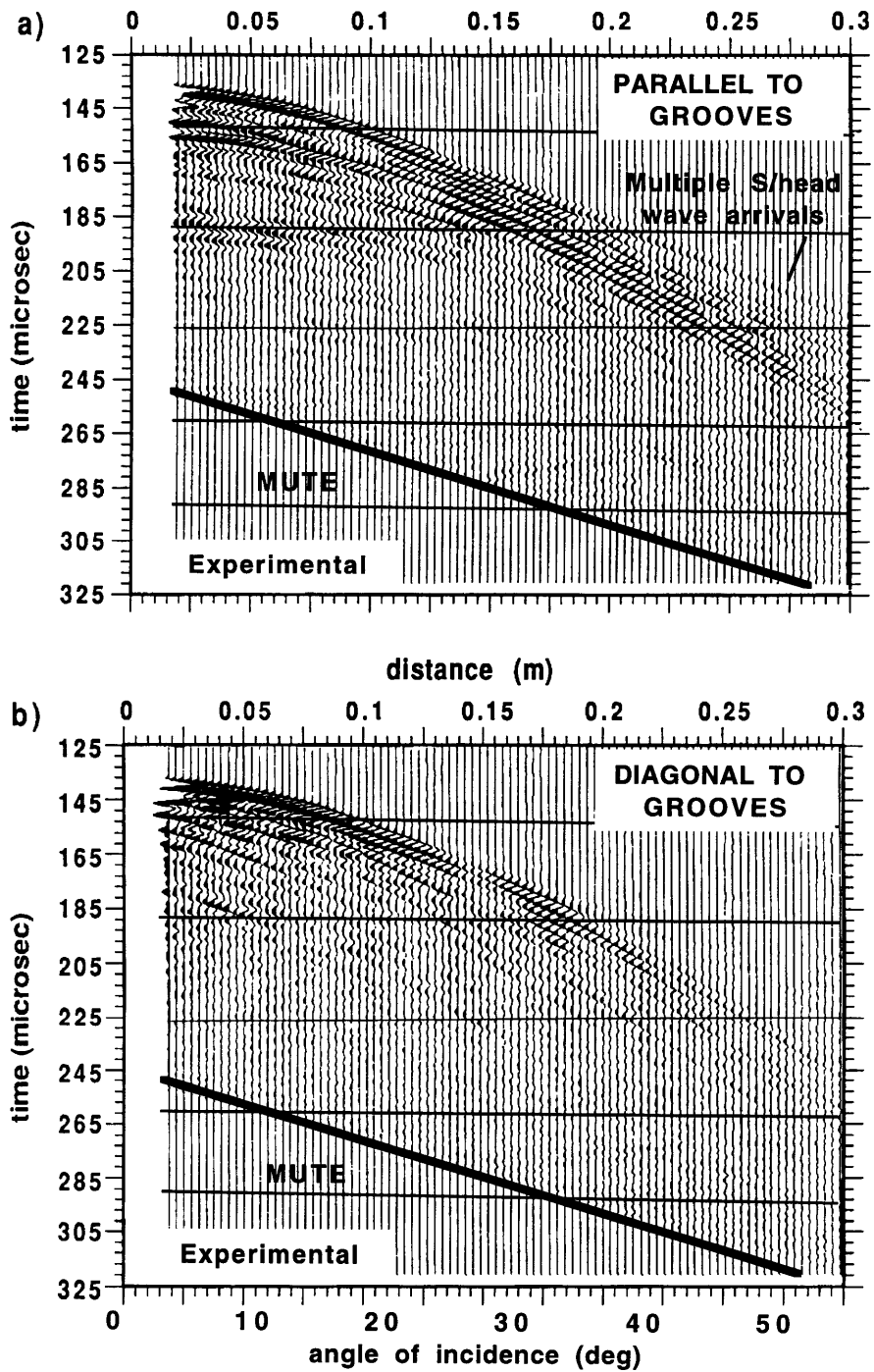


Figure 6-17: Pressure seismogram recorded experimentally over a 2-D distribution of grooved irregularities along the interface. The results are given for both a seismic line extending (a) parallel and (b) diagonal ( $45^\circ$ ) to the strike of the depressions.

# Chapter 7

## General Discussion

### 7.1 Conclusions

The goal of this thesis was to quantitatively characterize the mechanisms working to scatter seismic waves at a highly irregular random interface when the incident wavelength is on the same order as the size of interface irregularities. Scattering in this region is essential to a complete understanding of broad band seismic data. Generally speaking, the first objective of this thesis was to characterize how waves scatter from highly irregular interfaces, both as a function of material properties and interface statistics. Scattering was addressed for both solid–solid and fluid–solid boundaries. This is important for understanding the general form of energy scattered and converted at various earth boundaries. Our second objective was to identify both numerically and experimentally the enhancement of energy traveling back towards the source, otherwise known as ‘retroreflectance’, for seismic waves. The determination of how retroreflectance is related to material contrasts at the interface and the distribution of interface irregularities was of primary importance as

this gives insight into the feasibility of future field applications. Our third objective was to determine whether scattering from irregular intercrustal interfaces and an irregular Moho discontinuity is consistent with observed crustal seismic scattering. Although crustal boundaries were studied directly, the extension of this approach to other boundaries is straightforward.

More specifically, in Chapters 3 and 4 the scattering of seismic waves from a highly irregular 2-D elastic interface was expressed in terms of exact integral expressions for incident SH, P, and SV waves. In Chapter 5 a brief formulation was also given for an acoustic wave incident on an irregular 2-D acoustic-elastic interface. In each case the formulations followed the very efficient approach of Maradudin *et al.* (1990ab) where integral expressions were developed in the space-domain by combining the Somigliana identity with the extinction theorem. In the case of the acoustic medium, Green's second integral theorem was also utilized. The final numerical solution was written analytically in a very concise form where singularities were canceled using a limiting approach and the asymptotic nature of the Green's functions in cylindrical coordinates. As a result, the computational time for this algorithm was almost completely the time required to decompose the final system of coupled linear equations. Unlike most approaches which assume a plane element along the interface, we placed no constraints on the derivatives of the surface height function and determined which derivative terms must be included for first order accuracy in  $k\Delta x$ . We find that the curvature of the interface is required. Approaches which utilize a plane element require, therefore, a finer discretization so that curvature is negligible along the surface elements. Since our approach was solved explicitly in the space domain, edge effects were dealt with directly. These edge diffractions were reduced by introducing a broad incident beam, characterized by a Gaussian spatial distribution. As a result, the amplitude at the edges was reduced to a negligible value and the final solution remained analogous to the case of an incident plane wave. A plane wave decomposition of this final solution allowed the scattered energy to be expressed in terms of a determin-

istic reflection coefficient. Averaging these reflection coefficients statistically over a finite number of surface realizations, the general amplitude distribution of scattered waves was determined. Specifically, the total contribution along with the coherent and incoherent contributions to the mean reflection coefficient were studied.

In Chapter 2 the accuracy of our Somigliana approach was verified. This approach matched the results of the BIE–DWN algorithm of Paul and Campillo (1988) well up to the  $45^\circ$  slopes tested. The Somigliana approach also helped demonstrate some of the pitfalls involved with using DWN solutions in the frequency–domain to study scattering from irregular interfaces. In general, periodic effects can be strong, making interpretation of the DWN results ambiguous. The DWN approach is clearly a time–domain approach and should be used with caution in the frequency–domain. Utilizing the time–domain solution of the DWN approach and extending the algorithm to a fluid–solid boundary the accuracy and efficiency of the commonly used Virieux (1986) finite difference scheme was tested. We found that micro–roughness due to the discrete grid affected the solution strongly. Direct comparisons showed that a grid sample rate of more than 30 PPW was required to obtain the proper amplitude and phase of waves scattered from a smoothly varying interface. As a result, extremely large and computationally intensive models are required. These models were considered too demanding for the statistical approach of this study.

We find that the numerical reflection coefficients predict an enhancement of seismic waves traveling back towards the source for interfaces with steep enough slopes ( $\phi = 30^\circ$  and  $45^\circ$ ) and large impedance contrasts. This ‘enhanced backscattering’ or ‘retroreflectance’ was observed for both acoustic–elastic and elastic–elastic boundaries, giving strong support to the hypothesis of ‘time–reversed paths’ proposed in optical theory. The strongest support came from P–SV scattering where interference between various converted waves could be used to test this hypothesis. The observed enhancement of energy for P–to–P and SV–to–SV wave scattering and the

absence of enhancement for P-to-SV and SV-to-P conversions was consistent with this coherent scattering argument. The properties of the retroreflective peak were also well predicted by a straightforward interference argument. First, we found that the width of the retroreflective peak is approximately proportional to the ratio between the incident wavelength and the ‘mean free path’ of the interface, where, in the double scattering case, the mean free path is simply the average distance between the two multiple scattering points along the interface. Given an interface with Gaussian statistics, the mean free path is approximately equal to the correlation length of the interface,  $a$ . Second, we found that the peak height decreases relative to the remainder of the reflection coefficient as the impedance contrast at the interface decreases. This made retroreflectance difficult to detect in the case of scattering from boundaries with low impedance contrasts, such as the Moho discontinuity. Finally, we found that the retroreflective peak height tended to decrease as the incident angle was increased, suggesting the presence of “shadowing” and the inability of energy to find “time-reversed” paths at higher incident angles. As a result of these multiple scattering mechanisms, the retroreflective peak was difficult to detect when the incident angle became greater than the *rms* slope of the interface.

Our analysis shows that the properties of the retroreflective peak are related to the statistical properties of the interface. In the case of a Gaussian interface, the width of the peak is directly related to the correlation length of the interface and the incident angle at which retroreflectance becomes unobservable is roughly related to the *rms* slope of the interface. These relations may give an estimate of interface roughness in situations where retroreflectance can be observed. It is important to note that this analysis is not restricted to Gaussian statistics. In the case of interfaces with differing statistics, the mean free path of the given interface can still be determined.

In Chapter 5 reflection coefficients were measured experimentally over a characterized acoustic-elastic interface in our in-house ultrasonic water tank. First a

characterized random interface with a Gaussian correlation function ( $a = e^{-1} = 1.4$  mm) and an *rms* slope of  $30^\circ$  was generated using a glass etching process and numerically generated photoresist templates. The uniform statistics of the resulting glass interface allowed for a well controlled experiment where 2-D numerical reflection coefficients could be compared directly with 3-D experimental results. We found that the 2-D numerical reflection coefficients gave insight into the 3-D experimental scattering. Near normal incidence the reflection coefficients predicted the general falloff in scattered amplitudes as a function of scattering angle. As the incident angle was increased, the reflection coefficients also predicted the general asymmetry of the experimental amplitudes. Strikingly, however, as the incident angle was increased the 2-D numerical model predicted a slower fall off in backscattering and a slower increase in forward scattering than observed in the experimental results. In addition, we find that the scattering predicted by a 2-D numerical interface with an exponential correlation function was more consistent with an observed change in variance of the experimental data than the Gaussian correlation function. Future work may show that these effects are indeed a basic difference between 2-D and 3-D scattering mechanisms. The ultrasonic results also strongly supported the existence of ‘retroreflectance’, or the ‘enhanced backscattering’ of seismic waves, as an enhancement of energy scattered back towards the source was consistently observed at smaller incident angles. The strongest support for retroreflectance was obtained with a partially transparent piezo-film receiver which allowed energy to be studied directly in line with the source given a  $20^\circ$  incident angle. Averaging over 65 surface realizations, a distinct retroreflective peak was clearly observed. Unfortunately, the more detailed properties of the peak could not be identified experimentally as they were within the statistical error of the finite average. Future work with a faster, more automated ultrasonic apparatus may give further insight into these properties.

In Chapter 6 the numerically generated reflection coefficients were used to give insight into possible scattering mechanisms in the crust. We have shown that scattering

from an irregular Moho is consistent with the P coda energy observed at NORESS, FINESA, ARCESS, and NYNEX arrays. An F–K analysis of P coda at regional distances showed that energy with both Lg and Sn phase velocities arrives late in the P coda and is inconsistent with scattering from a plane layered crust. We found that the numerical reflection coefficients corresponding to an irregular Moho with a  $10^\circ$  *rms* slope are consistent with these observations when incident angles approach  $60^\circ$ . The reflection coefficients predict a conversion of incident P wave energy to post-critical shear energy which should arrive late in the P coda. In addition, modeling of an intercrustal interface with both a  $30^\circ$  *rms* slope and a larger impedance contrast than the Moho, demonstrated that intercrustal interfaces can potentially convert more than an order of magnitude greater energy into post-critical shear energy. Conversion can also occur at any incident angle. This agreement between energy distributions shows that any composite model for crustal scattering should not immediately rule out the possibility of scattering from both irregular intercrustal boundaries and an irregular Moho. We have also shown that the strong backscattering and retroreflectance predicted by the reflection coefficients may contribute to various modes of propagation in the earth. We find that scattering from a highly irregular Moho, near surface interfaces, and surface topography can contribute to the retropropagation of crustal waves, especially Lg. Reflection coefficients show that the Moho can contribute some energy into these retropropagating phases. However, based on our understanding of how the scattered amplitudes vary with interface properties, we find that irregular near surface interfaces and irregular topography can give a far greater contribution to these phases. Although the retropropagation of waves with Lg phase velocity has not been previously proposed, we have shown that portions of the F–K analysis of Lg coda by Dainty and Toksöz (1990) are consistent with the theory for retropropagation and further study of this phenomenon is warranted. Finally, we have shown that multiple scattering may play an important role in regions which exhibit large interface topography, such as mid-oceanic ridges. We find that full 3–D models which

include the anisotropic nature of ocean bottom topography and the characteristics of scattered energy as a function of azimuth are essential to the future investigation of these boundaries.

## 7.2 Future Work

Future work will include an attempt to further accelerate the Somigliana boundary integral approach through a conjugate gradient iterative approach to the matrix solution. We have already found that using the biconjugate gradient approach with forced sparsity based on amplitude can greatly increase the efficiency of these boundary integral routines. We are confident that this will allow for the modeling of general 3-D scattering in which case the general differences between 2-D and 3-D scattering can be effectively studied. In addition, we should be able to accurately study the scattering of teleseismic waves which travel through an irregular Moho discontinuity and an irregularly layered crust. The further study of the retropropagation of various modes of propagation in the crust is also well warranted. As discussed in Chapter 6 the stacking of energy from various events from a full range of azimuths should allow for an identification of any favored retropropagation in the crust. Given more data, an analysis of retropropagation as a function of both azimuth and arrival time may allow for a mapping of regions with large backscattering potential. In direct applications, amplitude versus offset analysis has become an important tool in current exploration projects. The boundary integral approaches developed in this thesis can be used to directly study the effects of interface roughness on amplitude versus offset records. In addition, the coupling of irregular boundaries with various types of crustal inhomogeneities, more specifically, with an anisotropic fractal velocity distribution, will allow for a more realistic model of P and S coda observed in the crust.

The multiple scattering mechanisms identified in this study may also be applicable to other regions of the earth. There are numerous examples of regions which might exhibit strong scattering mechanisms. For example, in addition to the case of ocean bottom topography proposed in Chapter 6, ocean surface topography may also give rise to the strong forms of scattering identified in earlier chapters. Most applicable is scattering by the ice-water interface which exists along the bottom side of a rough ice canopy. This case corresponds to the scattering by an acoustic-elastic interface investigated in Chapter 5.

Investigations have shown that rough ice cover can take on various degrees of roughness. On the one hand, specific measurements in Arctic regions show that rough ice cover can be rather subdued. Measurements by DiNapoli and Mellan (1985) have shown that, in certain regions, the topography on the bottom surface of the ice cover is on the order of  $\delta = 1.9$  m and  $a = 44.8$  m. The topography on the upper surface, although not measured, is even smaller. The correlation function for the ice depth exhibits an autocorrelation function which lies between a Gaussian and an exponential function, thus, slopes are probably steeper than the  $3.4^\circ$  *rms* slope calculated using Gaussian statistics. Even so, the multiple scattering mechanisms associated with more irregular boundaries do not appear to play a significant role, and this small order of roughness can be successfully modeled with various perturbation approaches (e.g. Kuperman and Schmidt, 1989). On the other hand, large scale topography can still exist. Large features such as ice keels, on the order of 40–60 m in depth, have been identified and are relatively common (DiNapoli and Mellan, 1985). Striations or grooves in the ice surface corresponding to cracks and other discontinuities, such as the semi-circular topographic depression modeled by Gerstoft and Schmidt (1991), can also result in large scale topography over short distances. In these instances, the larger slopes required for multiple scattering may be attained. In cases where these topographic features are distributed over some distance of the ice-water or ice-air surface, scattering mechanisms similar to the retropropagating phases and locked

mode conversions proposed for an irregularly layered crust may also exist, providing some insight into scattering and reverberation within the ice and water layers.

Another boundary of interest is the core–mantle boundary (CMB). Given that the statistics of a highly irregular interface can be tied to an interface’s retroreflective properties, we would like to be able to say that the scattering mechanisms identified from our study could give additional insight and perhaps conclusive evidence for the presence of irregularities along the CMB. However, upon reviewing the literature, we find that this is somewhat unlikely since it appears that only a small degree of CMB roughness is required to explain observed core phases.

The nature of the CMB has been investigated extensively. Doornbos (1978), utilizing the perturbation results of Kennett (1972), showed that irregularities, which exhibit heights on the order of several hundred meters and lateral scale lengths on the order of 10 to 20 km, can generate PKP precursors observed in the data. His work also showed the same ambiguity encountered throughout our study. Namely, that scattering from an irregular boundary can give results similar in nature to scattering from volume heterogeneities which have similar scale lengths. More specifically his results show that scattered energy, responsible for both PKP and PKKP precursors, may be the result of either an irregular CMB, a distribution of heterogeneities in the D” layer, or a combination of both forms of scattering. Ultrasonic experiments conducted by Menke (1986) are in agreement with these results. Menke used a thin aluminum plate model to show that irregularities at the core surface, if they exist, can not have radial variations greater than a few hundred meters. If larger scale irregularities were present, PcP amplitudes would be substantially different from observed values at periods of 4 to 40 s. The hypothesis of a slightly perturbed CMB boundary was further constrained by Doornbos (1988), who, using an approximate form of the extinction theorem, was able to incorporate various degrees of interface interaction. His results showed that multiple scattering does not significantly alter

the energy scattered by an irregular core–mantle boundary. This leads us to conclude that, although the core–mantle boundary exhibits a large impedance contrast which is optimal for enhanced backscattering, the absence of large slopes along this boundary will result in insignificant levels of retroreflectance.

We should note, nevertheless, that if retroreflectance from this region were observed, this would strongly suggest a highly irregular CMB since retroreflectance from volume heterogeneity in D" is very unlikely, at least if the heterogeneity consists of the small variations in physical parameters (up to a few percent) required to model both precursor energy (Doornbos, 1978) and observed primary and secondary arrivals from this region (Vidale and Benz, 1993).

# Appendix A

## Key of Variables, Symbols, and Constants: P–SV case

### Variables

$\underline{x} = (x_1, x_3)$	2–D Cartesian coordinate system
$S(\underline{x})$	general 2–D description of the interface
$\zeta(x_1)$	parameterization of the surface, $S(\underline{x})$
$\hat{n}(x_1)$	unit normal to the surface, $S(\underline{x})$
$\omega$	angular frequency
$N$	normalization of the normal vector $\underline{n}$
$\alpha^{(l)}$	P wave velocity
$\beta^{(l)}$	SV wave velocity
$\phi^{(l)}(\underline{x} \omega)$	dilatational Helmholtz potential
$\psi^{(l)}(\underline{x} \omega)$	rotational Helmholtz potential
$\underline{u}^{(l)}(\underline{x} \omega)$	displacement
$\underline{u}^{(1)}(\underline{x} \omega)_{incid}$	incident wave displacement in upper medium
$T_i^{(l)}(\underline{x} \omega)$	traction vector
$\tau_{ij}^{(l)}(\underline{x} \omega)$	stress tensor
$\rho^{(l)}$	density
$\lambda^{(l)}, \mu^{(l)}$	Lamé parameters
$f_i^{(l)}(\underline{x} \omega)$	body force
$H[i]$	volume function
$t$	time
$G_{np}^{(l)}(\underline{x}; \underline{x}')$	Green's function for a force at $\underline{x}'$

**Variables-continued**

$V(\underline{x})$	volume of integration
$D_i(x'_1)$	displacement along the interface
$T_p(x'_1)$	traction along the interface
$D_p^{n(l)}(\underline{x} x'_1)$	displacement resulting from a body force
$T_i^{n(l)}(\underline{x} x'_1)$	traction resulting from a body force
$c_{ijkl}^{(l)}$	elasticity tensor
$k$	horizontal wavenumber
$k_\alpha^{(l)}, k_\beta^{(l)}$	total wavenumbers note: $k_\beta^2 = (k_z^\beta)^2 + k^2$
$R_\alpha^n(k\omega)$	amplitude coefficients for dilatational plane waves
$R_\beta^n(k\omega)$	amplitude coefficients for rotational plane waves
$s$	equivalent to $sgn(x_3 - x'_3)$
$c_h$	velocity of incident wave
$\Pi_h^{(1)}(\underline{x} \omega)_{incid}$	Helmholtz potential for incident wave
$\theta_s$	scattering angle along interface
$\theta_0$	incident angle of a Gaussian beam
$w$	half-width of a Gaussian beam
$d_n(\theta_0)$	amplitude function for Gaussian elastic beam
$L_2$	arbitrary length of integration in the $x_2$ -direction
$P_i$	power flux per unit area
$P$	total power crossing a unit area normal to the $x_3$ -direction
$P_p(\theta_s)_{scat}$	power crossing a unit angular area about the scattered direction $\theta_s$
$\frac{\partial R_p}{\partial \theta_s}$	Differential Reflection Coefficient (DRC)
$L$	length of numerical integration along the interface
$\Delta x$	interface element length in $x_1$ -direction
$x_n$	discrete location of an element along the interface
$x_m$	interface position for evaluation of displacement
$T_{i0}^{n(l)}(x_m x_n)$	value of traction integrated over $\Delta x$ increment
$D_{p0}^{n(l)}(x_m x_n)$	value of displacement integrated over $\Delta x$ increment
$H_m(k_p r)$	Hankel function of $m$ th order and first kind
$\gamma$	direction cosines
$r$	radial distance from element point to evaluation point
$W( x_1 )$	interface spatial correlation function
$a$	lateral correlation length for the interface
$\delta$	standard deviation of the interface
$N_r$	number of realizations for finite average

## Variables-continued

$\sigma$	standard deviation of the finite average
$\Delta\phi$	total phase difference between two time-reversed paths
$\Delta\phi_i, \Delta\phi_s$	phase difference due to the incident and scattered wave
$\Delta\mathbf{r}$	vector from multiple scattering point 1 to 2
$\mathbf{k}_i, \mathbf{k}_s$	wavenumber vectors for incident and scattered waves
$\Delta\theta_s$	width of the retroreflective peak

## Symbols

$(l)$	superscript corresponds to medium $l$
*	represents the complex conjugate of a variable
$\langle - \rangle$	an average over an ensemble of realizations
<i>incid</i>	corresponds to the incident wave
<i>inc, coh, and tot</i>	correspond to incoherent, coherent, and total, respectively
<i>rms</i>	corresponds to “root mean square”
FD	corresponds to “finite-difference”
DWN	corresponds to “discrete wavenumber”
BIE-DWN	corresponds to “boundary integral equation-discrete wavenumber”
PPW	corresponds to “points per wavelength”

## Constants

$\gamma =$	1.781072418
$e =$	$e^1$

# Appendix B

## Numerical Formulation: Acoustic–Elastic Case

Following the approach of the previous chapters, we numerically solve the integral equations (5.12) and (5.13) by first integrating them over a finite interval,  $L$ , then converting them to a set of  $3N$  linear equations. Separating each of the integrals into a sum of  $N$  integrals, each integrated over an increment  $\Delta x$ , centered at the interface points we can express (5.13), which represents the scattered displacement in the lower medium, as a sum over integrals centered at the points

$$x_n = -L/2 + (n - \frac{1}{2})\Delta x, \quad n = 1, 2, 3, \dots, N. \quad (\text{B.1})$$

Evaluating the total displacement at the center of each element,  $x_m$ , the integral approximations can be written as

$$T_{i0}^{n(s)}(x_m|x_n) = \int_{x_n - \frac{\Delta x}{2}}^{x_n + \frac{\Delta x}{2}} dx'_1 T_i^{n(s)}(x_m|x'_1), \quad (\text{B.2})$$
$$D_{p0}^{n(l)}(x_m|x_n) = \int_{x_n - \frac{\Delta x}{2}}^{x_n + \frac{\Delta x}{2}} dx'_1 D_p^{n(l)}(x_m|x'_1),$$

which we solved for in Section 2.3.1 for  $k\Delta x$  very small. The reader should refer to Section 2.3.1 for a full review of the numerical formulations.

In the acoustic medium the integrals which we must approximate analytically can, assuming that the source amplitude functions 5.16 are slowly varying along the interface, be written as

$$T_0^{(f)}(x_m|x_n) = \int_{x_n - \frac{\Delta x}{2}}^{x_n + \frac{\Delta x}{2}} dx_1' T^{(f)}(x_m|x_1'), \quad (\text{B.3})$$

$$D_{i0}^{(f)}(x_m|x_n) = \int_{x_n - \frac{\Delta x}{2}}^{x_n + \frac{\Delta x}{2}} dx_1' D_i^{(f)}(x_m|x_1'),$$

and it can be easily shown by letting  $x_3 = \zeta(x_1) + \epsilon$  and integrating all terms corresponding to first order in  $k_T^{(f)}\Delta x$  in the limit as  $\epsilon \rightarrow 0^+$  that the boundary integral formulation in the fluid can be represented as a simple combination of both the elastic approximation made in Section 2.3.1 and the SH approximation made in Section 3.3.1. In the acoustic medium the Green's function terms are written as

$$\begin{aligned} D_i^{(f)}(\underline{x}|\underline{x}') &= \lambda^{(f)} k_T^{(f)2} G^{(f)}(\underline{x}; \underline{x}') n_i \\ T^{(f)}(\underline{x}|\underline{x}') &= T^{(SH)}(\underline{x}|\underline{x}') [\mu^{(SH)} \rightarrow \lambda^{(f)}] \end{aligned} \quad (\text{B.4})$$

where the traction term is identical to the SH traction term with  $\lambda^{(f)}$  in the fluid substituted for  $\mu$  in the SH case. In the elastic medium these terms can be written as

$$\begin{aligned} D_n^{(s)}(\underline{x}|\underline{x}') &= \mu^{(s)} G_{np}^{(s)}(\underline{x}; \underline{x}') n_p \\ T_i^{n(s)}(\underline{x}|\underline{x}') &= T_i^{n(s)}(\underline{x}|\underline{x}') \end{aligned} \quad (\text{B.5})$$

where the traction term is just that of the P-SV case. The displacement term is a function of the elastic Green's function developed in the P-SV formulations. In the case of integrating over singularities, expressing the integrands as a combination of Taylor and asymptotic series expansions, keeping terms up to order  $k_T^{(l)}\Delta x$ , and integrating over  $\Delta x$  gives a solution which reduces to a simple combination of the

SH and P-SV solutions. This includes the first term in (B.5) which multiplies an additional normal function. A direct substitution from Sections 3.3.1 and 2.3.1 gives the final linear system of equations which is then solved.

# Appendix C

## Ultrasonic Design

All experiments were done in our in-house ultrasonic water tank laboratory. Ultrasonic water tank modeling is a powerful tool as real field situations can be scaled down by four to five orders of magnitude and studied in a well controlled laboratory environment. The first section of this appendix describes the ultrasonic configuration. The second section describes in detail the construction of a four layer piezo-film receiver.

### C.1 Ultrasonic Water Tank Design

A diagram of the experimental setup is shown in Figure E-1. A solid elastic model is submerged in a water tank measuring 1.0 m by 0.5 m by 0.5 m in height. An ultrasonic wave is generated at a given source transducer with an input voltage from a Hewlett Packard 3048A function generator. For voltage output above  $\pm 5$  V a Hewlett Packard 467A Power Amplifier was utilized to obtain a  $\pm 10$  V of output. The source function generator was used to create a finite length sine wave

with a specific frequency and a finite number of cycles. The input wave, received with a corresponding piezoelectric material, is amplified from 40 to 60 db with a Panametrics 5660B preamplifier.

In the case of the finite pulse seismograms, a Krohn-Hite 3202R high-low cut-off filter was applied to the input signal. In the continuous wave study the input voltage was increased and the filter bypassed to remove any distortion it may cause. Signal to noise ratios were improved by stacking recorded signals (usually 8 stacked shots). The final signal was then digitized by a Data Precision DATA 6000 digital oscilloscope with 12-bit amplitude resolution. Although the system can simulate a full 3-D seismic study using six automated step motors, this study was carried out with only one motor. The receiver was connected rigidly to a rotating arm and then rotated in a semicircle about a rotation axis in  $.9^\circ$  steps. The digitizer and the step motor controller are interfaced with an IBM PC-AT computer through an IEEE-488 interface bus. The final digitized data is stored in the IBM PC-AT and following the experiment, is transferred to a Digital DECstation 5000/25 machine. The total time required to record and transfer the pressure recorded for a single realization of an interface was on the order of one hour.

## **C.2 Piezo-film Receiver**

In designing an experiment which can study the energy scattered at and near retroreflective angles (energy traveling back towards the source) one must be able to place a receiver very close to the source. There are a number of approaches which allow recording directly in this region. One approach involves making the source and receiver as small as possible, thus reducing the receivers interference with the source beam. As the source and receiver become smaller, more information can be recorded

near the retroreflective angle. A second approach is to use a focused acoustic beam with its focus close to the receiver. In this case the beam is narrowest near the receiver, allowing measurements very near the source angle. A third approach involves using an acoustic beam splitter which reflects incident energy arriving from beside the experiment towards the interface. This beam splitter then allows a portion of the diffracted energy to pass back through as the energy diffracts towards the source, allowing energy to arrive at the receiver which is directly in line with the incident angle. The fourth approach is to create a piezo-film receiver which is partially transparent to acoustic energy. This allows much of the source energy to propagate through the receiver, diffract from the interface, and return to the receiver where the diffracted energy is then recorded in the direction of the source. Unfortunately, the first two approaches are not applicable to this study. The first option is not practical since the size of the source transducer is required to be larger than a certain limit to propagate a narrow acoustic beam. The second option is also difficult to implement because of the water tank dimensions. If the beam is focused on a receiver located only a short distance away the beam spreading becomes too large. We choose the fourth approach since it is most easily implemented.

The following discussion gives the detailed design of a partially transparent piezo-film receiver. Figures E-2(ac) show a detailed view of the piezo-film receiver configuration. In the case of a single piezo-film layer, the film is placed between two silver conducting layers. Since the signal is received only from areas covered by conducting metal, it is advantageous to apply the metal coating as a liquid glue which allows for full control over the receiver's shape and its sensitivity. In this study the conducting element was given the same circular shape as the flat-bottomed transducers described in Chapter 5. Due to the low sensitivity of one layer of piezo-film it is desirable to stack multiple layers. However, there is a balance between the thickness of the receiver and its impedance contrast. As more piezo-film layers are stacked the impedance of the stack increases quickly. For this study, a four layer stack, shown

in Figure E-2(c), using  $110\mu$  film was optimal. The final thickness of the piezo film is approximately  $550\mu$  thick with a transmission coefficient at normal incidence of approximately 0.78. This leaves the piezo-film with a .22 reflection coefficient. As a result, reflected energy does reverberate between the source and receiver retaining a very high amplitude. A recording window was chosen such that it did not include any of this reverberative energy.

The final sheet, measuring .25 m by .12 m, was supported by a thin metal frame around the edges. In addition to supporting the film, this frame bent the sheet to the curvature of the semicircle about which the receiver was stepped. This guaranteed that the source beam was normally incident on the film during receiver rotation, therefore reducing any source beam distortion created by oblique incidence.

As this is a new transducer design, the receiver properties were studied. Figure E-4 shows the receiver sensitivity pattern as a function of incident wave angle, with an incident frequency of 500 kHz. The stacked piezo-film receiver has a very directed sensitivity pattern which is similar in nature to the flat-bottomed transducers with the same diameter. The piezo-film also appears to have a broad frequency response making it a very powerful tool. In addition, this element may be used successfully in rock physics to record on curved surfaces by gluing the film directly to the rock surface. This avoids the problem of transducer coupling encountered with a flat-bottomed transducer.

# Appendix D

## F–K Analysis of Ultrasonic Data

An F–K analysis of the scattered energy generated by the distribution of ocean bottom depressions, shown in Figure 6-14, supports the interpretation in Chapter 6 that scattered energy is dominated by both diffractions and S head waves which are radiated by each of the depressions. Figure E-5a gives the F–K plot for the energy reflected from a plane interface. The spectrum is dominated by the high amplitude reflection which arrives with a high phase velocity at small offsets. To determine the nature of the coda, the primary reflection is removed and the trailing coda are examined.

Figure E-5b-d show the F–K spectra for the cases of a seismic array oriented perpendicular, diagonal, and parallel to the depressions along the interface. These plots support the assertion that the coda show the largest amount of backscattering in the perpendicular case, as each depression acts as a point diffractor (although forward propagating energy is greater than back propagating energy). The energy in general arrives over a full range of phase velocities and approaches the water velocity in both the forward and back scattering directions. As the receiver array is moved

towards the parallel case, backscattering decreases and forward scattering increases. The phase velocities also increase, until finally, in the parallel case, backscattering becomes nonexistent and forward propagating energy arrives predominantly with large phase velocities ( $V_{app} \geq 3$  km/s). This energy corresponds to continuous diffractions from each of the depressions, giving the appearance of subsurface reflectors. Owing to the geometry, the diffractions arrive with a moveout similar to that of the primary reflection with their large amplitude and high phase velocity at smaller offsets dominating the F–K spectra.

Figure E-6a-d show the F–K spectra for the case of large offset. In this case, an F–K analysis was performed on the traces recorded at a distance of 0.15 to 0.3 m (the last 50 traces). The primary wave and S head wave arrivals were included in the analysis. Figure E-6a shows the case of a plane reflector. The spectrum is dominated by the primary reflection, arriving with a phase velocity near that of water, and the large amplitude S head wave, arriving with a velocity of about 3 km/s. The remaining plots, which correspond to the various orientations of the seismic array, show dramatically the destruction of the S head wave in both the perpendicular and diagonal cases. Most dramatically, in the parallel case, the spectra show an enhancement of energy arriving with phase velocities near the shear wave velocity of the solid. This peak in the spectrum, which are larger than the peaks in the plane interface case, strongly supports the presence of additional guided S head waves, each generated by an individual depression along the interface.

# Appendix E

## 2-D vs 3-D Acoustic-Elastic Comparison

In this section, the reflections from an interface with both a 2-D and a 3-D distribution of irregularities are modeled to determine both quantitatively and qualitatively the differences in the nature of 2-D and 3-D scattering. Figure E-7 gives the model geometry. In this case, the interface height is described by the Gaussian autocorrelation function introduced in Chapter 5. In the 2-D model, the topography is simply made invariant in the third direction (perpendicular to the vertical plane). The standard deviation of the interface is 40.8 m and the correlation length is 100 m. The fluid is given the properties of water while the solid is given the physical properties of glass given in Chapter 5.

The recording geometry consists of a volume point source placed in the fluid 0.6 km above the interface. One hundred receivers are placed in the fluid starting 200 m in front of the source with a 20 m spacing. The propagating wavefront is modeled with a fourth-order staggered grid FD algorithm. Cheng (1994) gives a full description of

the accuracies and structure of this algorithm. The center source frequency is 7.5 Hz, giving a center wavelength which is equal  $2a$ , where  $a$  is the correlation length of the interface.

The seismograms plotting the total pressure recorded in the fluid over both the 2-D and 3-D interfaces are given in Figure E-8. In the 2-D case, the primary reflection can be seen arriving at about 1 s. The amplitude of this reflection varies dramatically as a function of distance along the profile. Scattering takes the form of simple diffractions which appear to originate along the interface from areas of high curvature. Some multiple scattering can also be identified at about 2 s, delayed by almost 0.7 s from the primary reflection. The nature of the 3-D scattering is somewhat different. Energy clearly arrives from outside the sagittal plane, greatly increasing the length of the coda trailing the primary reflection. This occurs both at near normal incident angles and at wider angles. It is clear that scattering from irregularities outside of the sagittal plane can contribute a great deal of energy to the seismogram.

Figure E-9 gives the FK spectra for the seismograms recorded over the 2-D and 3-D interfaces. The FK spectra for the 2-D interface clearly shows that similar amounts of both backscattered and forward scattered energy are present in the seismogram. This distribution is supported by the numerical mean reflection coefficients presented for the 2-D interface in Chapter 5 which show similar amounts of forward scattering and backscattering. The F-K spectra for the 3-D interface also shows a large amount of both forward and back scattered energy. However, the forward scattered energy appears to be dominant. This might suggest that more forward scattering appears to exist. However, one must remember that it is possible for energy which is diffracted back towards the seismic line from a side scatterer to appear with only a positive horizontal wavenumber. Thus, in the 3-D case, out of plane scattering can give the appearance of more forward scattering and less backscattering.

Figure E-10 gives the rms amplitude for the first cycles of the primary reflection. This plot clearly shows that the extra degree of freedom associated with the 3-D interface geometry can result in a larger contribution of scattered energy in the sagittal plane. In this case, the 3-D variation of the interface topography results in about a two-time increase in the immediate vicinity of the primary reflection at near normally incident angles. This gives a first estimate of the scaling differences between the 2-D and 3-D reflection coefficients presented in Chapter 5.

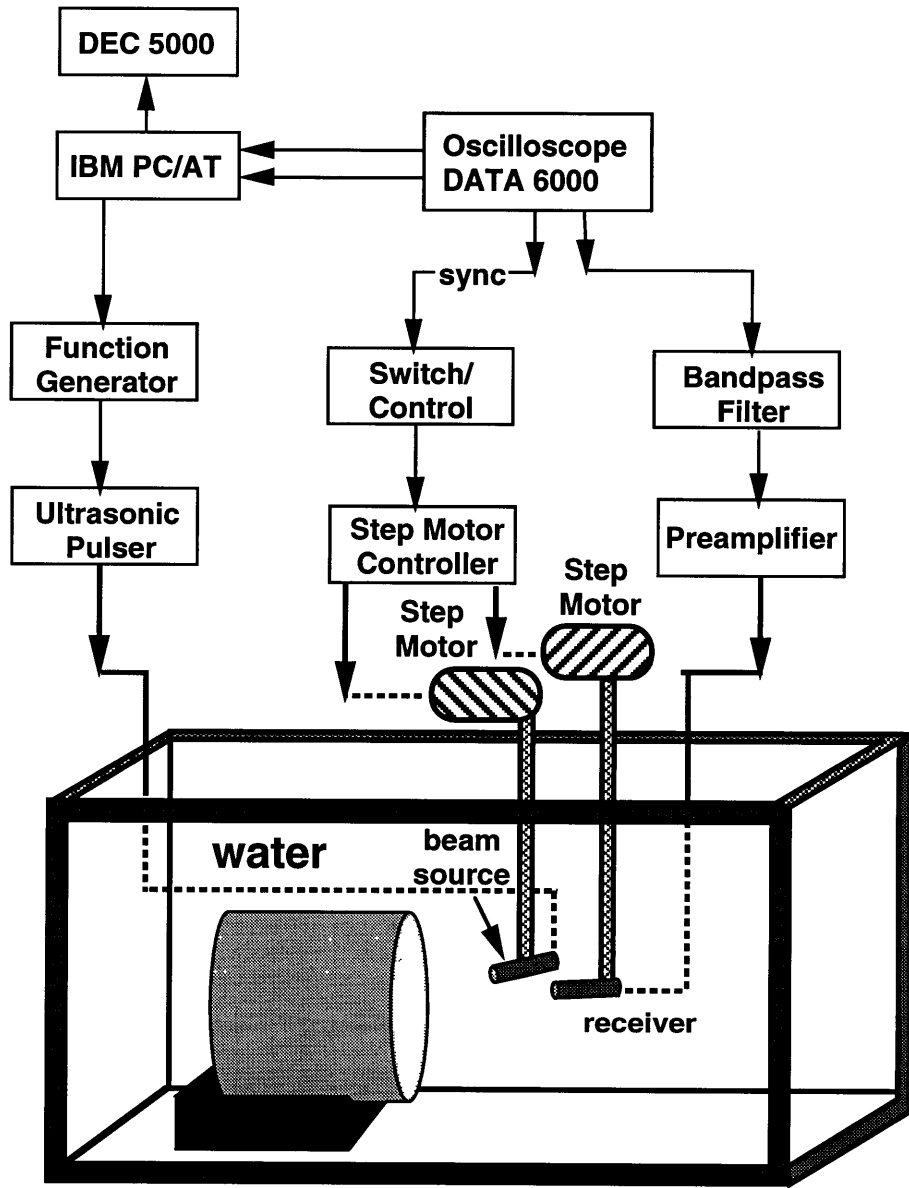


Figure E-1: The ultrasonic water tank configuration. The finite pulse measurements utilized the band-pass filter while the continuous wave measurements bypassed the filter, but used a power amplifier to increase the signal to noise ratio. In this case the power amplifier replaced the ultrasonic pulser.

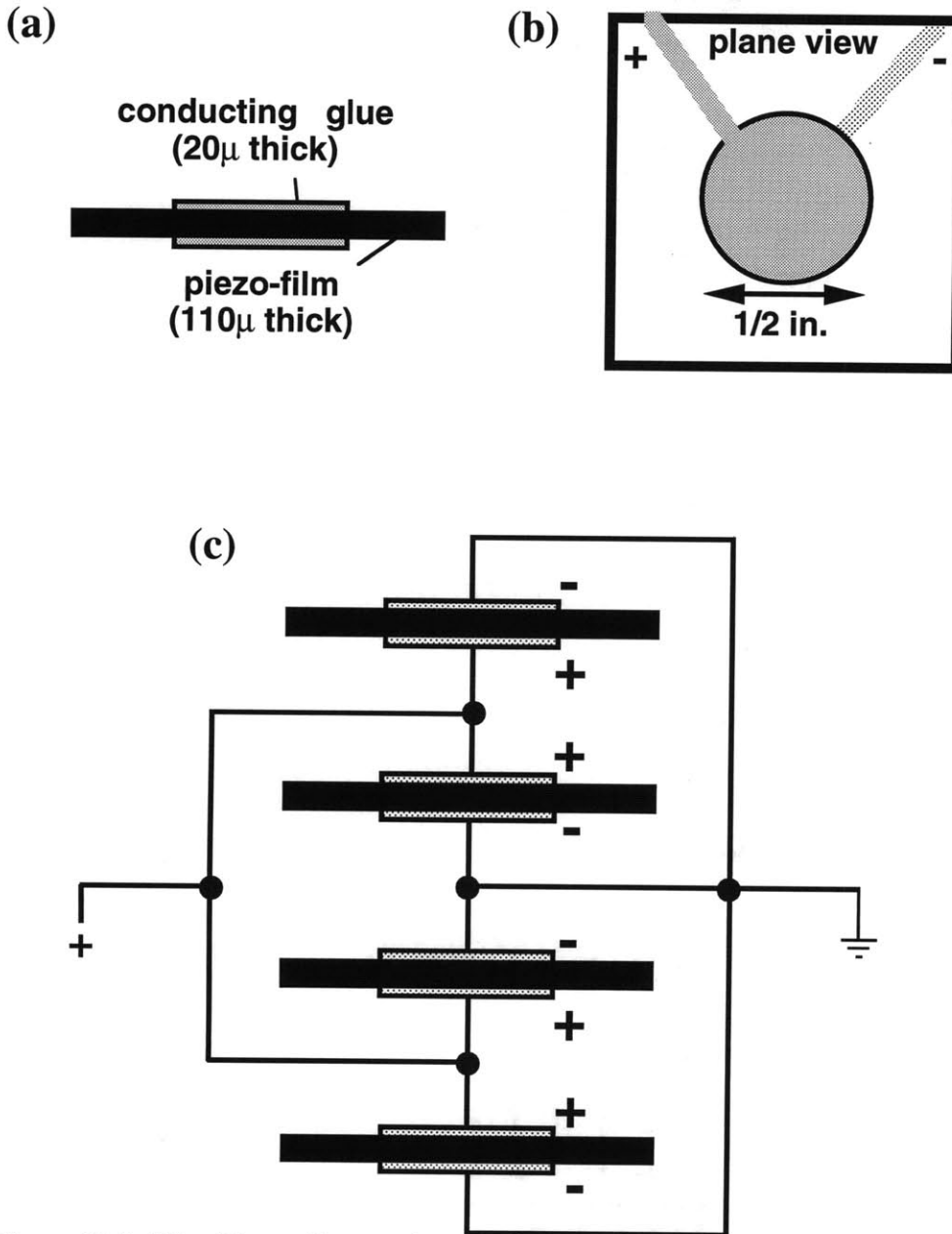


Figure E-2: The Piezo-film receiver with 4 layers of piezo-film stacked together with thin epoxy layers. (a) the piezo-film sandwiched between two thinner layers of conducting glue which carry current from the film. (b) the plane-view geometry of the receiver which has a circular geometry with a 1.25 cm diameter, and (c) the parallel connection of these piezo-elements which results in a four time increase in current output.

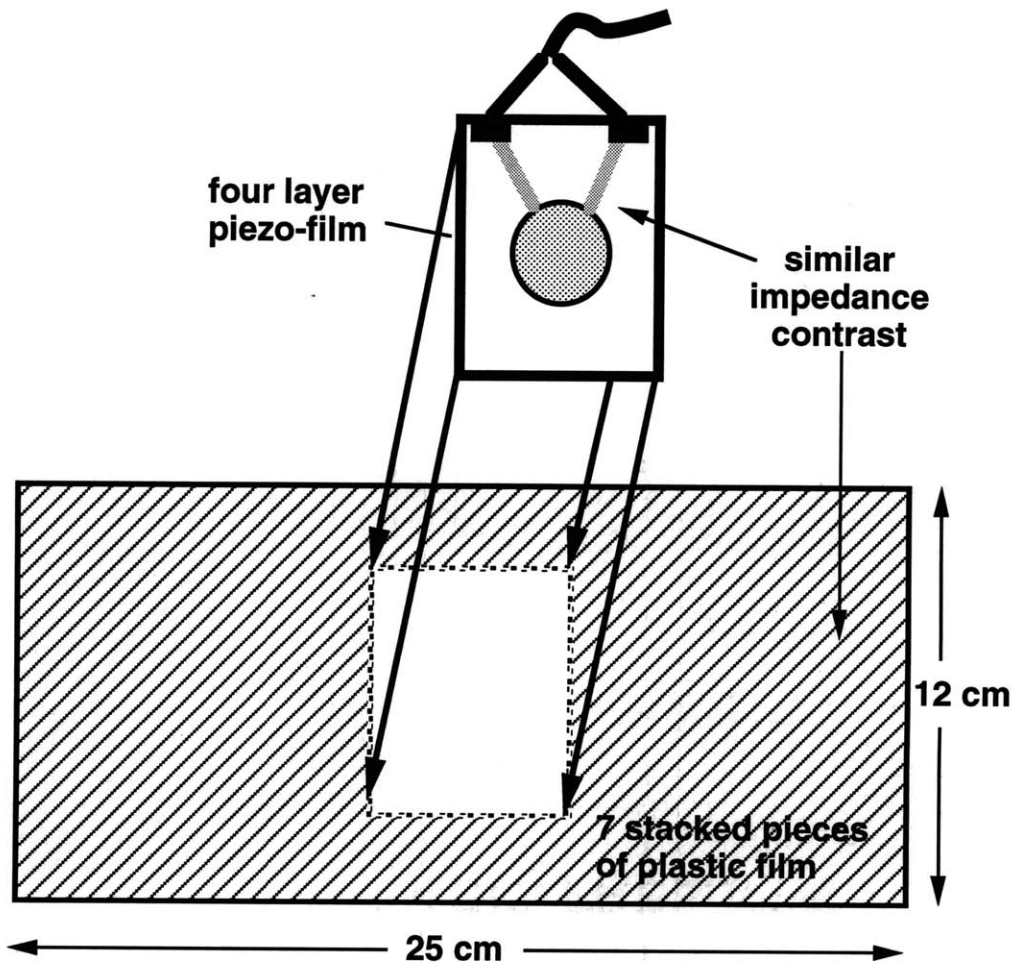


Figure E-3: Geometry of the piezo-film sheet. The piezo-film element is inserted into of a larger sheet of stacked plastic layers to reduce diffractions from the edge of the receiver element. The sheet of plastic layers was created by stacking  $110\mu$  thick layers until the impedance contrast matched that of the piezo-film.

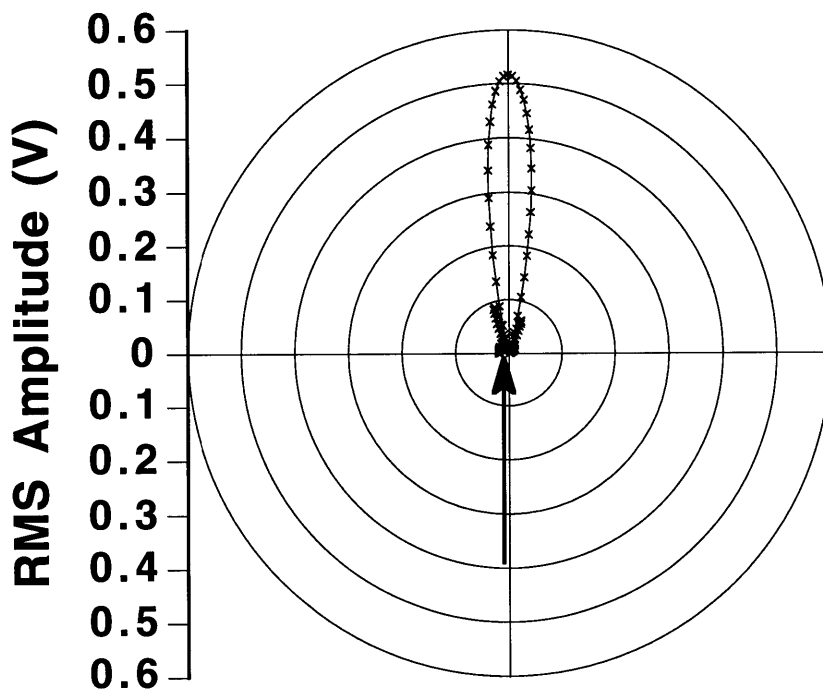


Figure E-4: The sensitivity pattern of the four layer piezo-film receiver at 500 kHz.

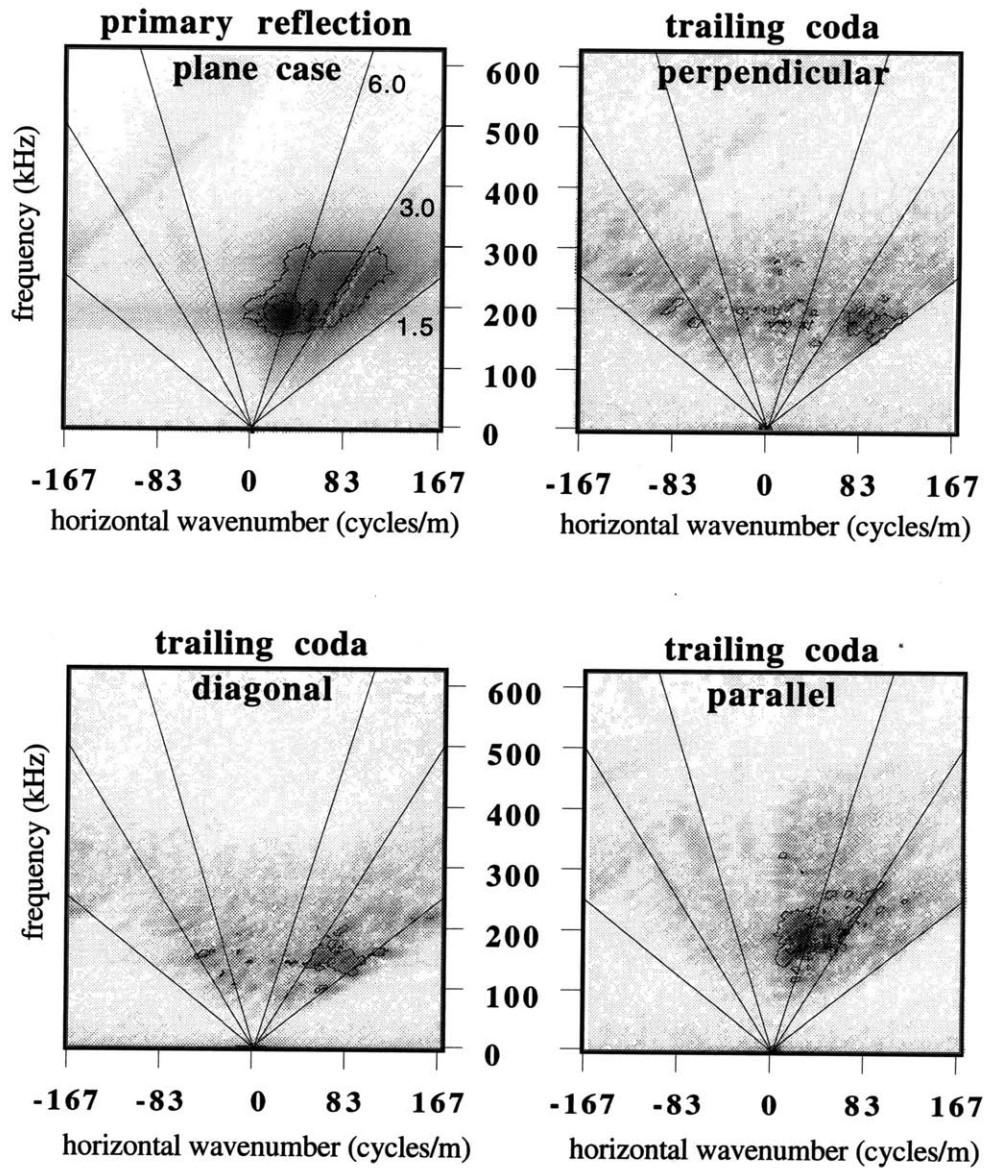


Figure E-5: FK spectrum of ultrasonic laboratory data. The first diagram shows the FK spectra for the plane reflector case, including the primary wave and all other arrivals. The latter three cases show the spectrum for coda trailing generated by scattering from the depressions shown in Figure 6-17. The cases of the seismic array aligned perpendicular, diagonal, and parallel to the grooves are given.

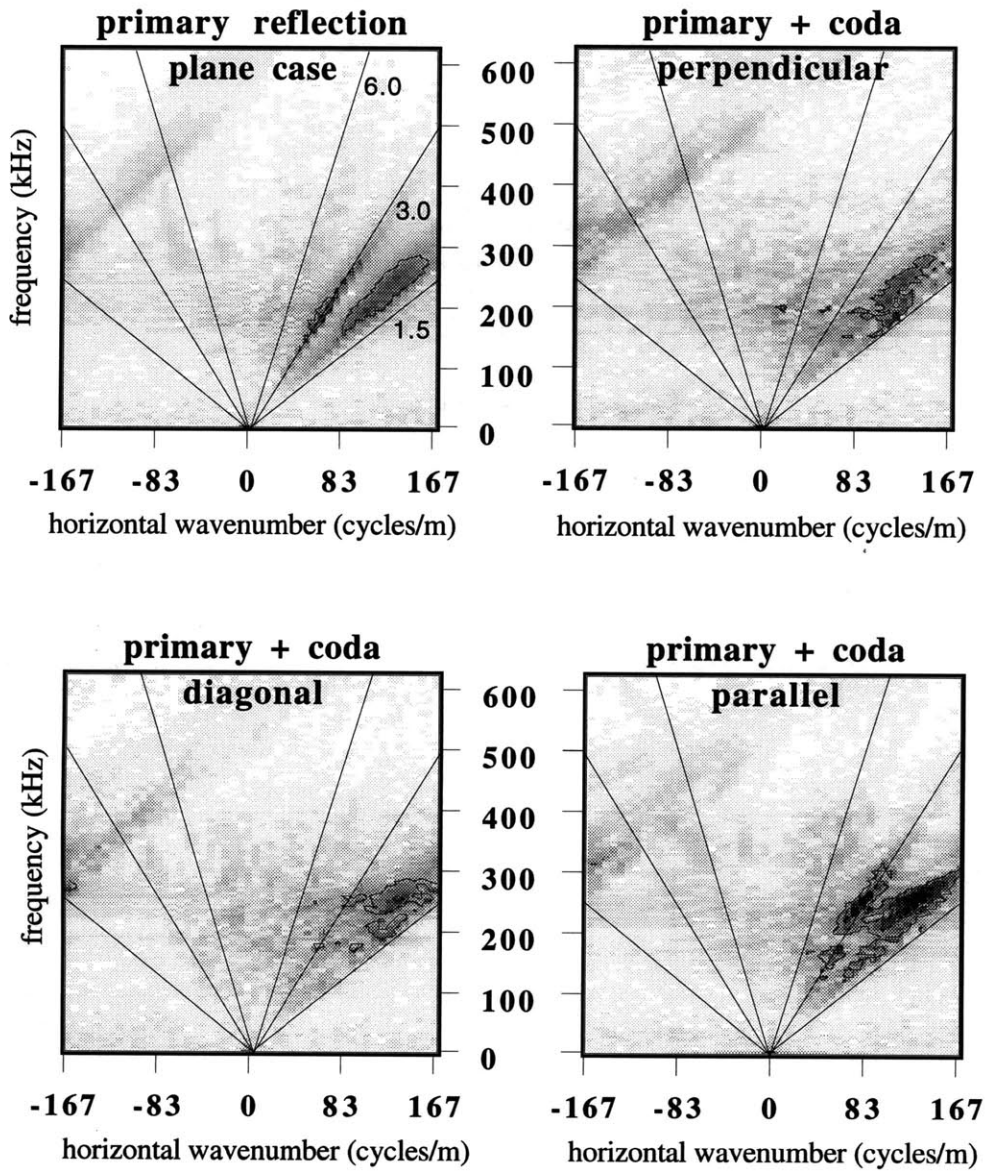


Figure E-6: FK spectrum of ultrasonic laboratory data. Each diagram is plotted for the final 50 traces of data (wide angle arrivals) in Figure 6-15 through Figure 6-17. The first diagram shows the FK spectrum for the primary and refracted waves generated by a plane interface. The latter three cases correspond to scattering by the topographic depressions shown in Figure 6-14. The cases of the seismic array aligned perpendicular, diagonal, and parallel to the depressions are presented.

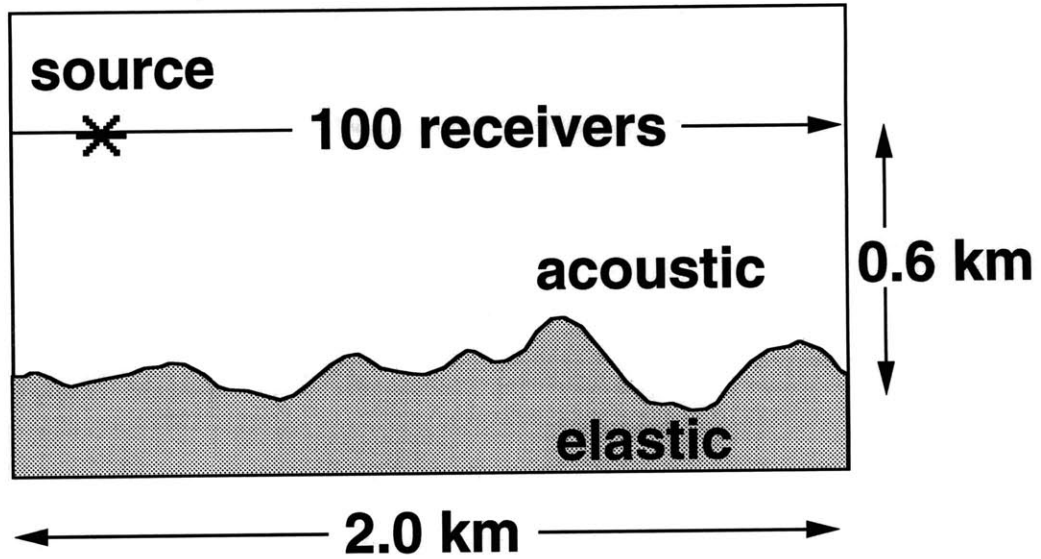


Figure E-7: FD model geometry in the vertical plane of the source and receiver. In the 2-D model, the topography is invariant in the third direction (perpendicular to this vertical plane). An explosive volume source is placed in the acoustic medium and 100 receivers are placed along a line perpendicular to the strike of the 2-D interface irregularities. The P wave velocity of the fluid is that of water and the P wave and S wave velocities in the solid are 5600 m/s and 3200 m/s, respectively. The density of the solid is 2.65.

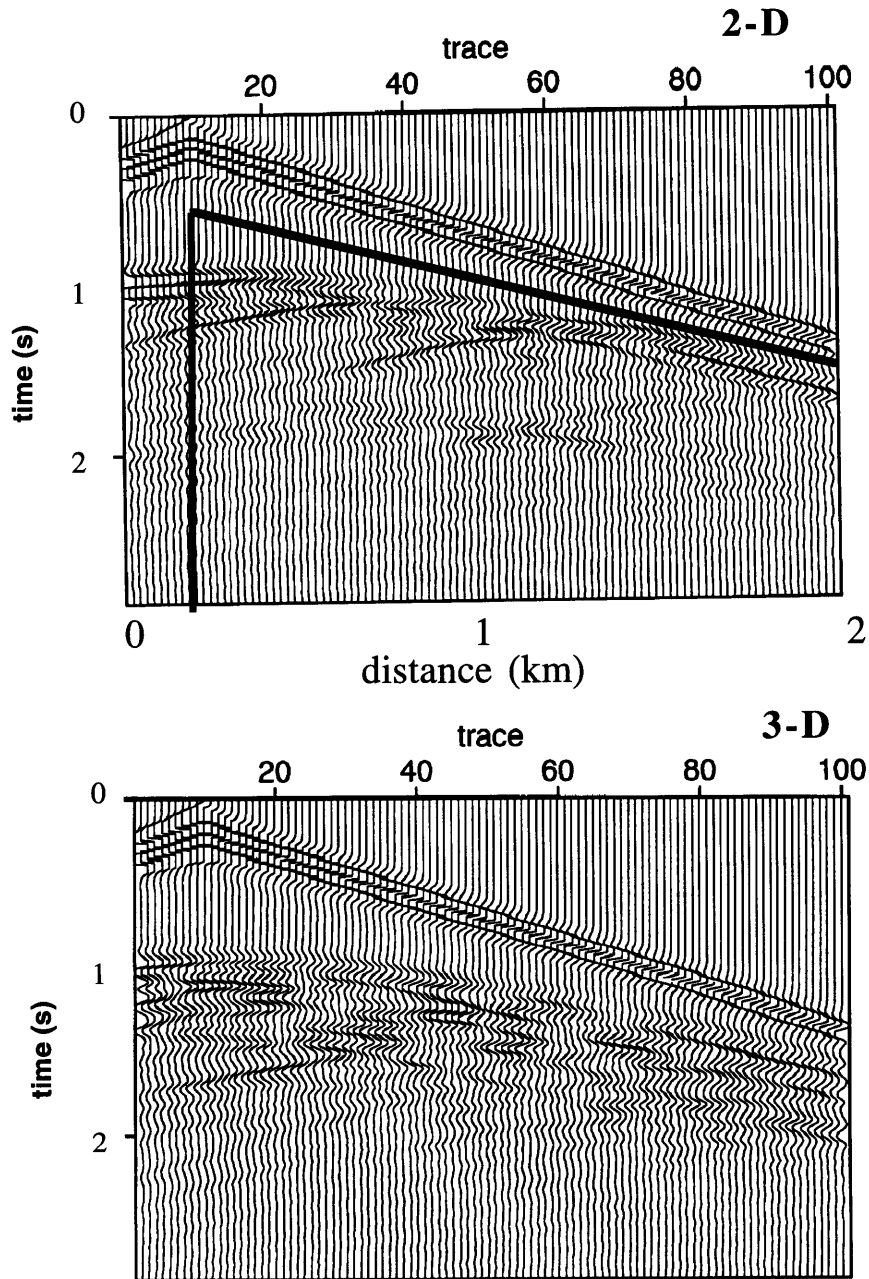


Figure E-8: Synthetics calculated using a 3-D FD algorithm. The upper seismic data corresponds to the case of 2-D irregularities which are invariant in one direction. The seismic line is perpendicular to the strike of the irregularities. The lower seismic data corresponds to the case of a full 3-D distribution of irregularities. The solid line shows the section of the coda windowed for the FK analysis shown in Figure E-9

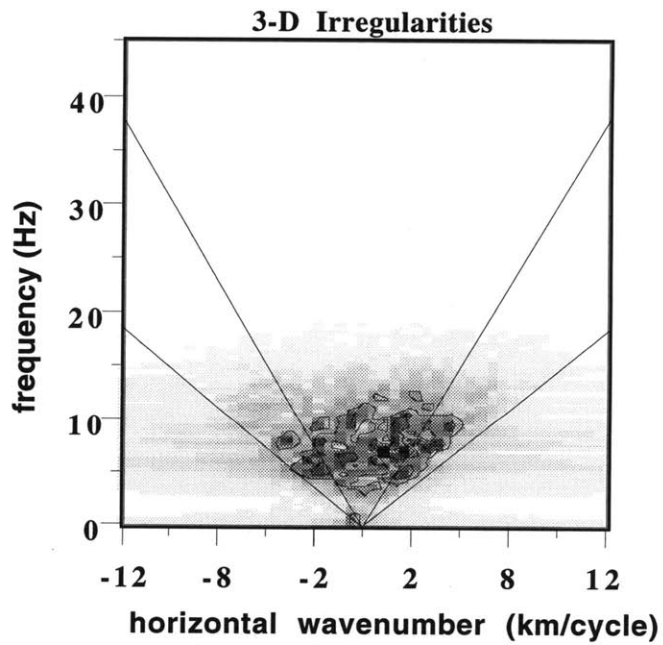
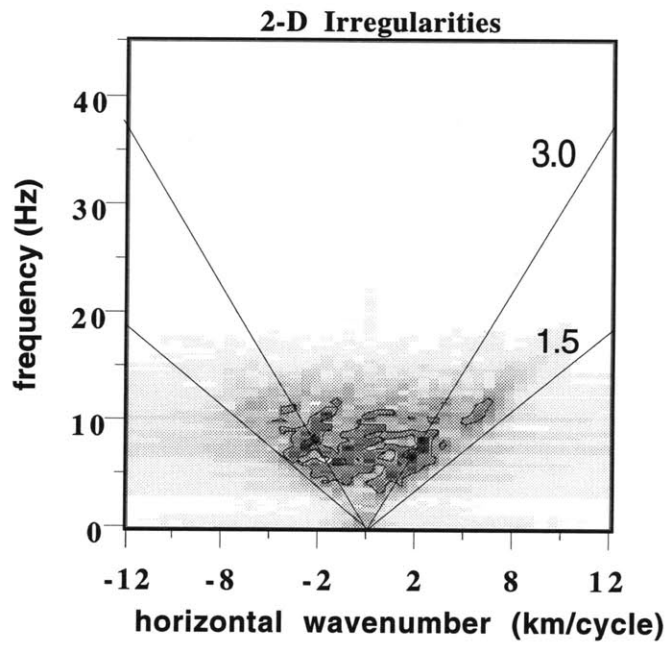


Figure E-9: FK spectrum of the windowed coda recorded along the line of receivers over the (a) 2-D and (b) 3-D distribution of irregularities shown in Figure E-8.

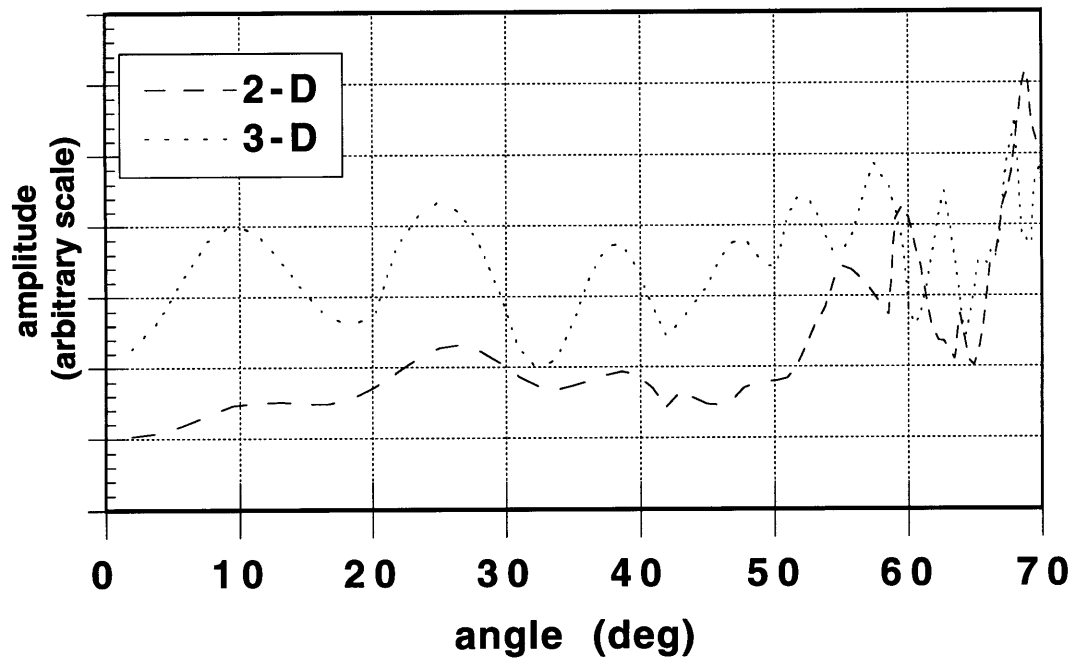


Figure E-10: Plot illustrating the amplitudes of the waves reflected from the interface given both the 2-D and 3-D variation along the interface. The amplitudes for the first few cycles of the primary reflection are given.

## References

- Abramowitz, M. & Stegun, I.A., 1964, Handbook of Mathematical Functions, Dover Publications, New York, NY (sections 9.1.3,9.1.10–11,9.1.27,9.1.30,9.4.1–6).
- Abubakar, I., 1962a, Reflection and refraction of plane SH waves at irregular interfaces, I, *J. Phys. Earth*, **10**, 1–14.
- Abubakar, I., 1962b, Reflection and refraction of plane SH waves at irregular interfaces, II, *J. Phys. Earth*, **10**, 15–20.
- Aki, K. & Chouet, B., 1975, Origin of coda waves: source, attenuation, and scattering effects, *J. Geophys. Res.*, **80**, 3322–3342.
- Aki, K. & P. Richards, 1980, *Quantitative Seismology—Theory and Methods*, W. H. Freeman, San Francisco, 721–796, 1980.
- Asano, S., 1960, Reflection and refraction of elastic waves at a corrugated boundary surface. Part I, *Bull. Earthq. Res. Inst*, **38**, 177–197.
- Asano, S., 1966, Reflections and refraction of elastic waves at a corrugated interface: *Bull. Seism. Soc. Am.*, **56**, 201–221.
- Axilrod, H.D. & J.F. Ferguson, 1990, SH-wave scattering from a sinusoidal grating: An evaluation of four discrete wavenumber techniques, *Bull. Seism. Soc. Am.*, **80**, 644–655.
- Bannister, S.C., Husebye, E.S., & Ruud, B.O., 1990, Teleseismic P coda analyzed by three-component and array techniques: deterministic location of topographic P-to-Rg scattering near the Noress array, *Bull. Seism. Soc. Am.*, **80**, 1969–1986.
- Bayer, G., & Niederdränk, T., 1993, Weak localization of acoustic waves in strongly scattering media, *Phys. Rev. Let.*, **70**, 3884–3887.
- Beckmann, P., & Spizzichino, A., 1987, in *The Scattering of Electromagnetic Waves from Rough Surfaces*, Artech House, Norwood, MA (185–194).

- Bouchon, M. & Aki, K., 1977, Discrete wavenumber representation of seismic source wave fields, *Bull. Seism. Soc. Am.*, **67**, 259–277.
- Bouchon, M., 1985. A simple, complete numerical solution to the problem of diffraction of SH waves by an irregular surface, *J. Acoust. Soc. Am.*, **77**, 1–5.
- Bouchon, M., Campillo, M., & Gaffet, S., 1989, A boundary integral equation-discrete wavenumber representation method to study wave propagation in multilayered media having irregular interfaces, *Geophysics* **54**, 1134–1140.
- Campillo, M., 1987, Modeling of SH wave propagation in irregularly layered medium, application to seismic profiles near a dome, *Geophys. Prospect.*, **35**, 236–249.
- Campillo, M., & Bouchon, M., 1985, Synthetic SH seismograms in a laterally varying medium by the discrete wavenumber method: *Geophysics*, **83**, 307–317.
- Capon, J., 1969, High-resolution frequency-wavenumber spectrum analysis, *Proc. IEEE*, **57**, 1408–1418.
- Chakravarty, S. & A. Schmid, 1986, Weak localization: the quasiclassical theory of electrons in a random potential, *Phys. Rep.*, **140**, 193-236.
- Cheng, N., 1994, Borehole Wave Propagation in Isotropic and Anisotropic Media: Three-Dimensional Finite Difference Approach, Thesis: Massachusetts Institute of Technology, Department of Earth, Atmospheric and Planetary Sciences.
- Chew, Weng Cho, 1990, In *Waves and Fields in Inhomogeneous Media*, pp. 431–443, Van Nostrand Reinhold, New York, NY.
- Condat, C.A., & Kirkpatrick, T.R., 1987, Observability of Acoustical and Optical Localization, *Phys. Rev. Lett.*, **58**, 226–229.
- Dacol, D.K. & Berman, D.H., 1988, Sound scattering from a randomly rough fluid-solid interface, *J. Opt. Soc. Am.*, **84**, 292–302.
- Dainty, A.M., & Schultz, 1993, Reflections and the nature of P coda, *1993 AGU, MSA, GS Joint Spring Meeting*, Paper No. **S41A–16**.

- Dainty, J.C., M.J. Kim, & A.J. Sant, 1990, Measurements of angular scattering by randomly rough metal and dielectric surfaces, in *Scattering in Volumes and Surfaces* (M. Nieto-Vesperinal and J.C. Dainty, Eds.), pp. 143–155, North-Holland, Amsterdam.
- Dainty, A.M., & Toksöz, M.N., 1990, Array analysis of seismic scattering, *Bull. Seism. Soc. Am.*, **80**, 2242–2260.
- Dainty, A.M., & Battis, J.C., 1989, Variation in apparent azimuth of arrivals at a small aperture array in New England, *EOS, Spring AGU*, **S42A-03**, p.400.
- DiNapoli, F., & Mellan, R.H., 1985, Low frequency attenuation in the Arctic Ocean, in *Ocean Seismo-Acoustics*, edited by T. Akal and J.M. Berkson (Plenum, New York).
- Doornbos, D.J., 1978, On seismic-wave scattering by a rough core–mantle boundary, *Geophys. J. R. astr. Soc.*, **53**, 643–662.
- Doornbos, D.J., 1988, Multiple scattering by topographic relief with application to the core–mantle boundary, *Geophys. J. Int.*, **92**, 465–478.
- Dougherty, M.E., & Stephen, R.A., 1987, Geoacoustic scattering from seafloor features in the ROSE area, *J. Acoust. Soc. Am.*, **82**, 238–256.
- Dougherty, M.E., & Stephen, R.A., 1991, Seismo/acoustic propagation through rough seafloors, *J. Acoust. Soc. Am.*, **90**, 2637–2651.
- Frankel, A., & Clayton, R., 1986, Finite difference simulations of seismic scattering: implications for the propagation of short–period seismic waves in the crust and models of crustal heterogeneity, *Journ. Geophys. Res.*, **91**, 6465–6489.
- Gaffet, S. & Bouchon, M., 1989, Effects of 2–D topographies using the discrete–wavenumber–boundary integral equation method in P–SV cases, *J. Acoust. Soc. Am.*, **85**, 2277–2283.

- Gee, L.S. & Jordan, T.H., 1988, Polarization anisotropy and fine-scale structure of the Eurasian Upper Mantle, *Geophys. Res. Let.*, **15**, 824–827.
- Gerstoft, P., & Schmidt, H., 1991, A boundary element approach to ocean seismoacoustic facet reverberation, *J. Acoust. Soc. Am.*, **89**, 1629–1642.
- Goff, J.A., Jordan, T.H., Edwards, M.H., & Fornari, D.J., 1991, Comparison of a stochastic seafloor model with SeaMARC II bathymetry and Sea Beam data near the East Pacific Rise, 13°–15°N. *J. Geophys. Res.*, **96**, 3867–3885.
- Goff, J.A., & Jordan, T.H., 1988, Stochastic modeling of seafloor morphology: inversion of sea beam data or second-order statistics, *J. Geophys. Res.*, **93**, 13,589–608.
- Gupta, I.N., Lynnes, C.S., & Wagner, R.A., 1990, Broadband F–K analysis of array data to identify sources of local scattering, *Geophys. Res. Let.*, **17**, 183–186.
- Haddon, R.A.W., 1978, Scattering of seismic body waves by small random inhomogeneities in the earth, *NORSAR Sci. Rep.*, **3-77/78**, Norw. Seismic Array, Oslo.
- Herrmann, R.B., 1980, Q estimates using the coda of local earthquakes, *Bull. Seism. Soc. Am.*, **70**, 447–468.
- Hey, R.N., Kleinrock, M.C., Miller, S.P., Atwater, T.M., & Searle, R.C., 1986, Sea Beam/Deep–Tow investigation of an active oceanic propagating rift system, Galapagos 95.5°W, *J. Geophys. Res.*, **91**, 3369–3393.
- Hogg, R. & Tanis, E., 1983, *Probability and Statistical Inference*, MacMillan, sect. 7.3.
- Ishimaru, Akira, 1990, Experimental and theoretical studies on enhanced backscattering from scatterers and rough surfaces, in *Scattering in Volumes and Surfaces* (M.Nieto-Vesperinal and J.C. Dainty, Eds.), pp. 1–15, North-Holland, Amsterdam.
- John, S., 1991, Localization of Light, *Phys. Today*, **44**, 32–40.

- Kawase, H., 1988, Time-domain response of a semi-circular canyon for incident SV, P and Rayleigh waves calculated by the discrete wavenumber boundary element method, *Bull. Seism. Soc. Am.*, **78**, 1415-1437.
- Kawase, H. & Aki, K., 1989, A study on the response of a soft basin for incident S, P, and Rayleigh waves with special reference to the long duration observed in Mexico City, *Bull. Seism. Soc. Am.*, **79**, 1361-1382.
- Kennett, B.L.N., 1972, Seismic wave scattering by obstacles on interfaces, *Geophys. J. R. astr. Soc.*, **28**, 249-266.
- Khmel'nitskii, D.E., 1984, Localization and coherent scattering of electrons, *Physica*, **126B**, 235-241.
- Kinck, J.J., Husebye, E.S., & C.E.Lund, 1991, The South Scandinavian crust: structural complexities from seismic reflection and refraction profiling, *Tectonophysics*, **189**, 117-133.
- Kirkpatrick, T.R., 1985, Localization of acoustic waves, *Phys. Rev. B*, **31**, 5746-5757.
- Knopoff, L., & Hudson, J.A., 1964, Scattering of elastic waves by small inhomogeneities, *J. Acoust. Soc. Am.*, **36**, 338-343.
- Knopoff, L., & Hudson, J.A., 1964, Frequency dependence of amplitudes of scattered elastic waves, *J. Acoust. Soc. Am.*, **42**, 18-20.
- Kuga, Y., & Ishimaru, A., 1984, Retroreflectance from a dense distribution of spherical particles, *J. Opt. Soc. Am.*, **A1**, 831-835.
- Kuperman, W.A., & Schmidt, H., 1989, Self-consistent perturbation approach to rough scattering in stratified media, *J. Acoust. Soc. Am.*, **86**, 1511-1522.
- Lamb, H., 1904, On the propagation of tremors at the surface of an elastic solid, *Phil. Trans. Roy. Soc. London, Ser. A*, **203**, 1-42.
- Lavender, A.R., & Hill, N.R., 1985, P-SV resonances in irregular low velocity surface layers, *Bull. Seism. Soc. Am.*, **75**, 847-864.

- Lindman, E., 1975, Free-space boundary conditions for the time dependent wave equation, *J. Comp. Phys.*, **18**, 66–78.
- Luetgert, J.H., Carol, M.E., & Klemperer, S.L., 1987, Wide-angle deep crustal reflections in the northern Appalachians, *Geophys. J.R. astr. Soc.*, **89**, 183–188.
- Luosto, U., 1991, Crustal structures of Easter Fennoscandia, *Tectonophysics*, **189** 19–27.
- Maradudin, A.A., Michel, T., McGurn, A.R., & Méndez, E.R., 1990a, Enhanced backscattering of light from a random grating, *Annals of Physics*, **203**, 255–307.
- Maradudin, A.A., E.R. Mendez, & T. Michel, 1990b, Backscattering effects in the elastic scattering of P-polarized light from a large amplitude random grating, in *Scattering in Volumes and Surfaces* (M.Nieto-Vesperinal and J.C. Dainty, Eds.), pp. 157–174, North-Holland, Amsterdam.
- Maradudin, A.A., & Michel, T., 1990c, The transverse correlation length of randomly rough surfaces, *J. Stat. Phys.* **58**, 485–501.
- Mayeda, K., & Koyanaga, S., 1992, A comparative study of scattering, intrinsic, and Coda  $Q^{-1}$  for Hawaii, Long Valley and Central California between 1.5 and 15.0 Hz, *J. Geophys. Res.*, **97**, 6643–6659.
- McGurn, Arthur R. & Alexei A. Maradudin, 1985, Localization effects in the scattering of light from a randomly rough grating, *Phys. Rev. B*, **31**, 4866–4871.
- Madsen, J.A., Fox, P.J., & Macdonald, K.C., 1986, Morphotectonic fabric of the orozco transform fault: results from a sea beam investigation, *J. Geophys. Res.*, **91**, 3439–3454.
- Mendez, E.R. & K.A. O'Donnell, 1990, Scattering experiments with smoothly varying rough surfaces and their interpretation, in *Scattering in Volumes and Surfaces* (M.Nieto-Vesperinal and J.C. Dainty, Eds.), pp. 125–141, North-Holland, Amsterdam.

- Menke, W., 1986, Few 2–50 km corrugations on the core–mantle boundary, *Geophys. Res. Lett.*, **13**, 1501–1504.
- Müller, G., 1985, The reflectivity method: a tutorial, *J. Geophys.*, **58**, 153–174.
- Mykkeltveit, S., Ringdal, F., Kuaerna, T., & Alewine, R.W., 1990, Application of regional arrays in seismic verification research, *Bull. Seism. Soc. Am.*, **80**, 1777–1800.
- O’Donnell, K.A. & Mendez, E.R., 1987, Experimental study of scattering from characterized random surfaces, *J. Opt. Soc. Am.*, **4**, 1194–1205.
- Ogilvy, J.A., 1987, Wave scattering from rough surfaces, *Rep. Prog. Phys.*, **50**, 1553–1608.
- Paul, A. & Campillo, M., 1988, Diffraction and conversion of elastic waves at a corrugated interface, *Geophys.*, **53**, 1415–1424.
- Prange, M. & Toksöz, M.N., 1990, Perturbation approximation of 3-D seismic scattering, *Geophys. J. Int.*, **101**, 713–738.
- Prange, M., 1989, Seismic wave scattering from rough interfaces, Thesis: Massachusetts Institute of Technology, Department of Earth, Atmospheric and Planetary Sciences.
- Purdy, G.M. & Detrick, R.S., 1986, Crustal structure of the Mid–Atlantic ridge at 23°N from seismic refraction studies, *J. Geophys. Res.*, **91**, 3739–3762.
- Randall, C., 1989, Absorbing boundary condition for the elastic wave equation: Velocity-stress formulation, *Geophys.*, **54**, 1141–1152.
- Rayleigh, J.W.S., 1894, *The Theory of Sound*, 2nd ed., vol II, p. 89, Macmillan; New York: Dover, 1945.
- Sanchez–Sesma, F.J. & Campillo, M., 1991, Diffraction of P, SV, and Rayleigh waves by topographical features: A boundary integral formulation, *Bull. Seism. Soc. Am.*, **81**, 2234–2253.

- Schultz, C.A. & M.N. Toksöz, 1991, Seismic wave scattering from a randomly grooved interface: ultrasonic modeling and finite difference calculation, in *Abstracts of the American Geophysical Union: Fall Meeting*, **S21A-03**, 82.
- Schultz, C. & Toksöz, M.N., 1993, Enhanced backscattering of seismic waves from a highly irregular interface: SH case, *Geophys. J. Int.*, **114**, 91–102.
- Schultz, C.A. & Toksöz, M.N., 1994a, Enhanced backscattering of seismic waves from a highly irregular interface: P–SV case, *Geophys. J. Int.*, in press.
- Schultz, C.A. & M.N. Toksöz, 1994b, Reflections from a randomly grooved interface: ultrasonic modeling and finite-difference calculation, *Geophys. Prosp.*, in press.
- Sellevoll, M. & Warrick, R., 1971, A refraction study of the crustal structure in Southern Norway, *Bull. Seism. Soc. Am.*, **61**, 457–471.
- Singh, S.J. & Sikka, J.S., 1988, On 2–D dynamical dislocations, *J. Phys. Earth*, **36**, 27–41.
- Stanton, T.K., 1992, *Personal contact*, Woods Hole Oceanographic Institute (WHOI).
- Stephen, R.A., 1984, Finite-difference seismograms for laterally varying marine models, *Geophys. J. R. astr. Soc.*, **79**, 185–198.
- Stephen, R.A., 1988a, A review of finite difference methods for seismo-acoustics problems at the seafloor, *Review of Geophysics*, **26**, 445–458.
- Stephen, R.A., 1988b, Lateral heterogeneity in the upper oceanic crust at DSDP Site 504, *J. Geophys. Res.*, **93**, 6571–6584.
- Toksöz, M.N., Cheng, N., Dainty, A.M., & Mandal, B., 1990. Regional seismograms: attenuation, scattering and anisotropy. Proc. 12th Ann. DARPA/GL Seis. Res. Symp., pp. 166-176.
- Tsang, L., & Ishimaru, A., 1984, Backscattering enhancement of random discrete scatters, *J. Opt. Soc. Am.*, **A1**, 836–839.

- Vidale, J.E., & Benz, H.M., 1993, Seismological mapping of fine structure near the base of the Earth's mantle, *Nature*, **361**, 529–532.
- Virieux, J., 1986, P-SV Wave Propagation in heterogeneous media: Velocity-stress finite-difference method, *Geophysics*, **51**, 889–901.
- Virieux, J., 1984, SH wave propagation in heterogeneous media: velocity–stress finite–difference method, *Geophysics*, **49**, 1933–1957.
- Wu, R., & Aki, K., 1985, Scattering characteristics of elastic waves by an elastic heterogeneity, *Geophysics*, **50**, 582–595.
- Zeng, Y., Feng, S., & Aki, K., 1991, Scattering wave energy propagation in a random isotropic scattering medium: 1. Theory, *J. Geophys. Res.*, **96**, 607–619.